SCUOLA DI DOTTORATO
UNIVERSITÀ DEGLI STUDI DI MILANO-BICOCCA

Dipartimento di / Department of

FISICA G. OCCHIALINI

Dottorato di Ricerca in / PhD programma FISICA e ASTRONOMIA Ciclo / Cycle 29

Curriculum in (se presente / if it is) ASTRONOMIA

The road to the red sequence via secular and environmental processes: insights from the local Universe

Cognome / Surname Consolandi Nome / Name Guido

Matricola / Registration number 702272

Tutore / Tutor: Giuseppe Gavazzi

Cotutore / Co-tutor: Massimo Dotti
(se presente / if there is one)

Coordinatore / Coordinator: Marta Calvi

ANNO ACCADEMICO / ACADEMIC YEAR 2015/2016

The Road to the red sequence

via secular and environmental processes: insights from the Local Universe.

Guido Consolandi

Doctor Philosophiæ (Ph.D.) in Astronomy and Astrophysics

University of Milano-Bicocca

Cover page: *False color mosaic of the barred spiral galaxy NGC 1300 and of the edge-on spiral galaxy UGC 6697.*

Guido Consolandi

The road to the red sequence via secular and environmental processes: insights from the Local Universe.

SUPERVISOR:
Giuseppe Gavazzi

CO-SUPERVISORS:
Massimo Dotti

University of Milano-Bicocca | Department of Physics G. Occhialini
Milan, Italy

"Every student who enters upon a scientific pursuit, especially if at a somewhat advanced period of life, will find not only that he has much to learn, but much also to unlearn."

– Sir John Frederick William Herschel

Contents

Abstract **I**

1 Introduction **1**
1.1 The morphological classification of galaxies 2
1.2 Objective morphology 6
1.3 Colors and stellar masses 9
1.3.1 The color magnitude 12
1.3.2 Relations with the gaseous component 13
1.3.3 Ionized Gas. 19
1.3.4 Star formation 22
1.4 Kinematics - Longslit Spectroscopy and IFUs 24
1.5 Bars 27
1.5.1 Consequences on the gas 29
1.5.2 Observational evidences 30
1.6 The environment 33
1.6.1 Evidences of environmental evolution 35
1.7 Environmental processes 39
1.7.1 Tidal interactions 39
1.7.2 Hydrodynamical interactions 40
1.7.3 A new golden-age 44
1.8 Evolution 45
1.8.1 This work 47

2 Samples **49**
2.1 The SDSS sample 49
2.2 The Hα3 sample 53
2.3 The Herschel Reference Survey sample. 53

3 Bar-quenching **55**
3.1 Star formation rate at z=0 55
3.2 The star formation rate as a function of redshift 58
3.3 Strong bars and bulges as a function of M_* 63
3.4 Bar-driven star formation quenching 68
3.4.1 Comparison with hydrodynamical simulations 68
3.4.2 Dynamical model for the sSFR-quenching cosmic evolution 75
3.5 Discussion 77

4 The effect of bars on gas as seen by *Herschel* **81**
4.1 The *Herschel* Reference Sample 82
4.2 Results 83
4.3 Discussion and conclusions 86

5 Galaxy colors in the local Universe **89**
5.1 Photometry 91
5.1.1 Magnitudes 91
5.1.2 The color magnitude diagram 97
5.2 Radial Color profiles 100
5.2.1 Templates 102
5.3 Dissecting the color-magnitude relation 105
5.3.1 Nuclei 106
5.3.2 Bulges, Bars and Disks 109
5.4 Discussion 110
5.4.1 Nuclei 112
5.4.2 Bulges, Bars & Disks 113

6 The colors of bars **117**
6.1 The automatic classification 117
6.2 Comparison with visual classifications 118
6.3 The local bar fraction 121
6.4 Tilted color profiles of barred galaxies 122

7 Ram Pressure stripping: U6697 **129**
7.1 Observations . . . 133
7.2 Data reduction & analysis . . . 133
7.2.1 Emission line measurements . . . 136
7.2.2 Absorption line measurement . . . 139
7.3 Results - Flux and Kinematics of gas and stars . . . 139
7.3.1 Velocities . . . 141
7.3.2 Onboard and stripped gas . . . 147
7.4 Excitation mechanisms . . . 151
7.4.1 Line ratio maps . . . 151
7.4.2 Spatially resolved BPT diagrams . . . 156
7.5 The HII regions . . . 160
7.6 Discussion . . . 163
7.6.1 Which process is driving the stripping? . . . 163
7.6.2 The tail(s) . . . 167

8 Summary and conclusions **171**
8.1 The bar quenching . . . 172
8.2 The colors of Bar quenching . . . 175
8.3 The stripping of UGC-6697 . . . 177

Appendices **179**

Appendix A Automated photometry and isophotal fitting **179**
A.1 The method . . . 179
A.1.1 Image preparation, target detection and masking . . . 180
A.1.2 Petrosian radius and photometric extraction . . . 181
A.1.3 Errors . . . 183
A.2 Isophotal fitting and tilted color profiles . . . 184
A.3 Bar detection . . . 185

Appendix B Single velocity component fitting **187**
B.1 One component line ratios . . . 187

Appendix C Illumination correction details **191**

Abstract

The evolution of galaxies can be thought as the result of the cumulative effects of two broad classes of processes: (i) secular (internal) processes determined by the very nature of the galaxy, and (ii) external processes that are determined by the environment in which the object is embedded. In this thesis I face both aspects of galaxy evolution. Among secular processes, I investigated the effects of stellar bars on the gaseous components of galaxies and their consequences on their evolution. In particular I show how bars affect both the ionized and cold gas in two different samples: the sample of the Halpha3 survey, an Halpha imaging survey of galaxies selected from ALFALFA in the Local and Coma superclusters; the Herschel Reference Sample, a representative sample of 323 local galaxies observed with the space-based Herschel observatory sensitive to the far-infrared emission of dust, a good tracer of cold gas. Owing to the Halpha3 data I demonstrate that main sequence barred galaxies have specific star formation rate suppressed with respect to pure disks. Here I propose a simple model in which bars drive the evolution of disk galaxies. Hydrodynamical simulations indeed show that a barred potential funnels the gas inside the corotation radius toward the center of the galaxy where it reaches high densities, cools and can be consumed by a burst of star formation. At the same time the dynamical torque of the bar keeps the gas outside the corotation radius in place, cutting the gas supply to the central region that consequently stops its star formation activity. Taking advantage of the images of the HRS sample, we show the evidences of such quenching. The aforementioned model is further tested by studying the stellar population properties of galaxies belonging to a sample of 6000 galaxies extracted from SDSS. To this aim, I designed in-house IDL codes that automatically perform aperture photometry and isophotal fitting recovering reli-

able magnitudes, colors, ellipticity, position angle (P.A.) and color profiles. The automatic procedure is complemented by an automatic bar finder able to extract a fairly pure sample of barred galaxies on the basis of their P.A. and ellipticity profiles. The analysis of color profiles show that disk galaxies have their central regions redder (therefore quenched) than their outer regions and that this is more evident at high mass. The high local bar fraction that we extrapolate as well as the analysis of the average color profile of barred galaxies shows the strong contribution of bars to the observed colors. In a second part, I present the work done in the field of environmental processes. The work is focused on the analysis of the observations, carried on with the IFU MUSE, of a system belonging to the nearby galaxy cluster A1367. These observations mosaicked the galaxies UGC-66967 and CGCG-97087N, two galaxies suffering ram pressure stripping and that have possibly interacted, as hinted by the presence of gas in the region between them. Owing to in-house automatic Python codes and by comparing the gas velocities to the stellar kinematics, we could separate the emission of the ionized gas in a stripped component and a component still attached to the potential of the galaxy. While the gas onboard the galaxy shows low velocity dispersions and ionizations states consistent with photoionization by stars, the stripped gas is more turbulent and ionized by shocks. The HII regions that formed in the tail of UGC-66967 (but are absent in the tail of CGCG-97087N) are systematically found in regions where the velocity dispersion of the gas is lower than 50 km/s, while the stripped gas show typical velocity dispersions about or greater than 100 km/s.

Chapter 1

Introduction

Galaxies are gravitationally bound systems containing different amounts of stars, gas in different phases, dust, and dark matter. They span a wide range of luminosities, thus masses. Such distribution is well approximated by a Schechter function of the form:

$$n(L)dL = n\left(\frac{L}{L^*}\right)^{\alpha} e^{\frac{L}{L^*}} d\left(\frac{L}{L^*}\right), \tag{1.1}$$

where the parameters n is the number density, α the power law slope for low luminosities (L), and L^* is the luminosity break after which the distribution decreases exponentially. Typical values for α lie in the range $-1.5 < \alpha < -1$ while the exponential break (expressed in magnitudes) is found between $-23 < M^* + 5logh50 < -20$ in B-band (Schechter, 1976). The derived masses range of galaxies span from $\approx 10^6 M_\odot$ and $\approx 10^{12} M_\odot$.
Galaxies are virialized systems whose virial equilibrium is sustained either by the rotation of stars and gas around a common axes (i.e., a rotating disk) or by the chaotic motion in a triaxial geometry. They are one of the best tracers of the baryonic distribution in the Universe and they harbor the molecular clouds where new stars born. Galaxies contain different populations of stars, objects well approximated by a black-body emission that peaks at a wavelength that depends exclusively on their surface temperature. Their color is therefore univocally determined by their surface temperature which depends on their luminosity (thus mass). Massive stars have typical surface temperature $T_s \approx 10^4$K

and their emission peaks in the blue region of the visible spectrum or in the UV. They are characterized by short lifetimes and are therefore young objects. Low mass stars have low surface temperatures, red colors, and lifetimes comparable to the Hubble time. Their emission peaks in the red end of the optical spectrum and in the near-infrared (NIR). Therefore, when looking at a galaxy, in absence of non-stellar component, different colors reflect different stellar populations.
The spectrum of stars is characterized by the continuum emission of the black body and by many absorption lines due to the transition of atoms in stellar atmospheres.
Gas is the fundamental ingredient to form new stars and is present in galaxies in different phases (ionized, neutral, molecular) in different proportions. The interstellar medium (ISM) is mainly composed of gas, principally hydrogen that we detect in its atomic phase (HI) by detecting the radio emission line at 21 cm while, in the molecular phase it is usually observed indirectly. As a matter of fact, the cold molecular gas is observed detecting transition lines of the CO molecules. These molecules are associated to the presence of H2 that is quantified by the mean of an empirical conversion factor. Across the galaxy, the cold gas, if present, can collapse and form new stars. The newborn population containing hot massive stars ionizes the surrounding gas that emits lines. In the local Universe, the best tracer of the ionized gas is the first line of the Balmer series, the Hα line at 6562.82$\mathring{A}$.
A small percentage of the total mass of a galaxy is represented by dust which is easily revealed in the optical as black filaments that obscure stellar light along the line of sight. The absorbed radiation is subsequently re-emitted at much greater wavelength, in the Far Infrared (FIR) and sub-mm region of the electromagnetic spectrum.
During the last century, a lot of effort has been put in trying to characterize galaxies in order to put constrain on their evolution which, to date, is still poorly understood.

1.1 The morphological classification of galaxies

The most accessible information in a galaxy is its morphological appearance. The structure of a galaxy reflects the way matter assembled and the first approach in the study of galaxies is to study their different visual morphologies.

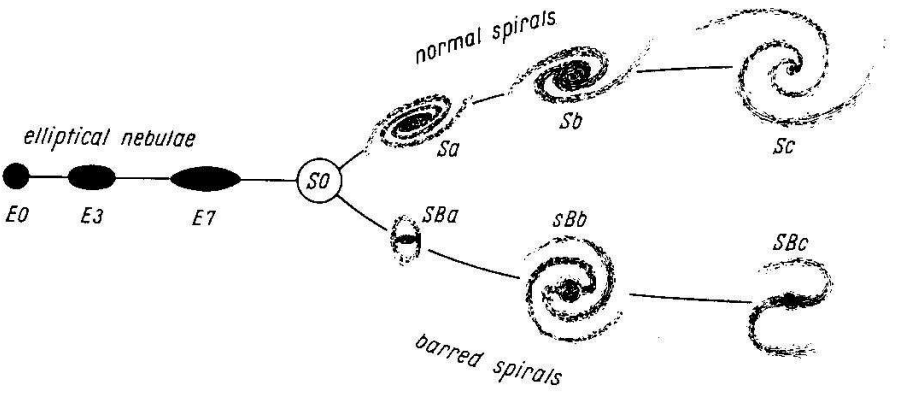

Figure 1.1: The Hubble tuning fork for the morphology classification of galaxies. From left to right are displayed Elliptical galaxies (E, black ellipses), lenticulars (S0) and spiral galaxies, divided into barred (SB) and non barred (S).

The seminal work of Edwin Hubble in (1936) *The realm of nebulae* was the first to propose a classification to characterize the properties of galaxies based on their optical appearance. This was later revisited and expanded by Sandage (1961) and de Vaucouleurs (1959). With respect to other classifications proposed (see for example those by Morgan, 1958; Bershady et al., 2000), the merit of the extended Hubble classification was that it did not try to account for every superficial detail, but kept his classes broad enough that the vast majority of galaxies could be sorted into one of his proposed bins (Sandage, 1975). As a matter of fact, this classification prevailed and is the most widely used. In particular, some of the classes introduced by the early work of E. Hubble became standard in galaxy evolution studies.

The classification scheme is summarized by the worldwide famous tuning fork (Hubble, 1936) displayed in Fig. 1.1. From left to right, the classification discriminates between ellipticals (E), lenticulars (S0) and spirals (S). The first were further differentiated by their ellipticity (with a number ranging from 0 to 7). On the other hand, the sequence of spirals splits in two branches (one for barred and the other for normal disks) each of them divided in different classes indicated with a letter ranging from a to d, depending on the degree of aperture of the spiral arms and on the dimensions of the central bulge. The extension of

this classification (de Vaucouleurs, 1959) introduced the possibility to classify in more detail disk galaxies. This classification distinguished between normal disk spiral galaxies (from Sa to Sd) and blue irregular objects without evident spiral arms such as the categories magellanic spirals (Sm) and irregulars (Irr). Furthermore the letters r, B and A are used to indicate the presence of ring-like structures, bars, and ansae respectively.

More generally, the extended Hubble classification distinguished two fundamental categories: *late-type* galaxies (LTGs) and *early-type* galaxies (ETGs). The first one embraces the classes of spirals and irregular galaxies while the other the classes of ellipticals and lenticulars. These names reflected the evolutionary path[1] that Hubble had in mind but the division was based solely on the morphology of galaxies. Surprisingly as data were gathered through the years, it became evident that this classification correlates with other physical parameters such as the star formation rate or gas fraction. In facts Spiral and Irregular galaxies that are characterized by a disk-like or irregular shape have considerable amount of dust and cold gas that allows the star formation to proceed vigorously. On the contrary, ellipticals and lenticulars are amorphous, smooth objects, characterized by an elliptical shape containing little to no gas and dust, thus with negligible levels of star formation.

Since then, the creation of classes around shared morphological characteristics has become a common practice and in particular the subdivision in early and late type system is the most general and widely used method to classify galaxies in the study of galaxy evolution. Nevertheless the morphological characterization has two limitations: it has to be done individually and is a somewhat subjective measure.
The first problem implies that small teams of astronomers, similar to the ones that classified few hundreds/thousands of objects in the early surveys (Sandage, 1961; de Vaucouleurs et al., 1991), cannot perform the classification within the large, modern surveys that embrace millions of galaxies. A possible solution is to involve in the classification process as many persons as possible and then average the votes. In this sense, the modern era of the World Wide Web has provided the unprecedented chance to gather the classifications of

[1] Hubble speculated that galaxies evolve from the class of early type to the class of late type, inversely to the path imagined nowadays.

Figure 1.2: (Top) The spiral galaxy Messier 95, an example of a barred-ring galaxy (SBrb) according to de Vaucouleurs (1959). (Bottom) The elliptical galaxy (E) Messier 86.

hundreds of thousands of participants. This is the case of the *GalaxyZoo project* (Lintott et al., 2008) which provides visual morphological classifications for nearly one million galaxies, extracted from the Sloan Digital Sky Survey (SDSS). This achievement was made possible by inviting the general public to visually inspect and classify these galaxies via the internet. The data for this project was collected via a website. Volunteers users were first "trained" by reading a brief tutorial giving examples of each class of galaxies and then asked to classify new objects. Apart from the large number of participants, the inclusion of non-astronomers has also some other advantages. For example, although morphological classification is traditionally performed in gray-scale images in order to avoid a possible bias imposed by the well-known color-morphology relation, the idea to involve non-astronomers ensures that only a negligible percentage of participants is aware of the color-morphology relation thus allowing to let participants classify color composites (RGB) images. These images possess the large dynamic range necessary for the identification of faint features and are therefore perfect for the scope.

However such an approach is still affected by large uncertainties mainly because the possible biases introduced by the great variety of different participants are difficult to quantify. The great number of persons involved requires efficient organization as well as sufficient time to let everybody complete their part. Therefore the other possible solution is to create objective selection criteria of different morphological types based on measurable quantities.

A lot of effort has been put in linking the morphology, e.g *early*- and *late*-types, to parameters with empirical relations that can later be used as proxy of the morphology. These studies opened the possibility to develop algorithms that are able to automatically perform a morphological classification guided by as many as possible objective proxies of morphology (Scarlata et al., 2007; Fasano et al., 2012).

1.2 Objective morphology

Many parametrical and non-parametrical techniques have been studied to extract quantities that characterize the structure of galaxies. Many of these parameters are correlated between them as well as with the morphological type. Therefore, these correlations are particularly useful when dealing with

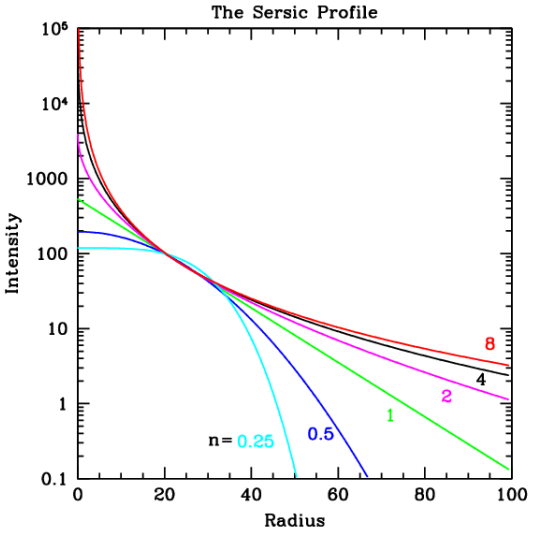

Figure 1.3: Different Sérsic profiles color coded according to their Sérsic index.

the large datasets of the large surveys or at high redshift where the key morphological differences that are likely attributable to evolution are inaccessible because of the angular resolution.

One of the first approaches in the objective classification of galaxies was the surface brightness radial profile fitting technique introduced by de Vaucouleurs (1959). Radial surface brightness profiles can be extracted integrating light in annular apertures of increasing radius and centered on the galaxy. de Vaucouleurs (1959) noticed that profiles can be modeled with three different functions: an exponential function ($I(R) \propto \exp -R$) typical of disks; a de Vaucouleur function ($I(R) \propto \exp -R^{1/4}$) typical of ellipticals; and a function that is the sum of the previous two, typical of spirals hosting a central bulge. These were later generalized in a single function called the Sersic function (Sérsic, 1963, 1968):

$$I(R) = I_e \exp -b_n[(\frac{R}{R_e})^{1/n} - 1], \tag{1.2}$$

where I_e is the effective intensity, R_e the effective radius (the radius containing half the total luminosity of the galaxy), n the Sérsic index. The term b_n is

not a parameter but is instead dependent on the third model parameter, n, that describes the shape, i.e. the concentration, of the light profile. The variation of the light profiles as a function of n is shown in Fig. 1.3. For n$>$ 2 the profiles show an evident central cusp indicative of an higher light (thus mass) concentration in the center of the galaxy and is typical of ETGs and especially elliptical galaxies. Lower values of the Sérsic index are instead characteristic of LTGs and in particular of irregular galaxies and/or disks without a central bulge. Normal spiral galaxies however are better represented by the sum of two Sérsic functions: one that models the central part of the galaxy with a n$>$ 2 an the other modelling the outer wings of the distribution, namely the disk, with a low Sérsic index (n$\sim$ 1).

Modern computational techniques and technologies allow for more complicated methods such as the two dimensional surface brightness fitting. Codes such as GIM2D (Simard, 1998) or GALFIT (Peng et al., 2010) are able to fit the image of a galaxy with the 2D model that better approximate the distribution of light with a combination of known functions (such as the Sérsic function) expressed in two dimensions. The possibility to decompose the galaxy light distributions in different analytical components allows to quantify the relative importance of bulges with respect to disks in LTGs by measuring the B/D or B/T parameter, i.e the ratio between the luminosity of the bulge and the disk/total luminosity. This correlates with parameters such as color and mass although with considerable scatter (Simard et al., 2011; Mendel et al., 2014). However, as pointed out by Laurikainen et al. (2005) the simple bulge + disk models are not adequate for dwarfs and irregular galaxies.

Therefore, along with these methods, also non-parametric approaches have been proposed to characterize the structure of galaxies without assuming a particular analytical function for the galaxy's light distribution. One of the most popular parameter system adopted at high redshift is the concentration, asymmetry, and clumpiness (CAS) system developed by Conselice (2003), inspired by other seminal works by Abraham et al. (1996), Takamiya (1999), Bershady et al. (2000). The concentration is the ratio between the radii containing different amount of the total light in a given band. There are different definition in the literature such as the ones of Bershady et al. (2000), i.e. the ratio between the radii that enclose 80% and 20% of the total galaxy light, or the one of de Vaucouleurs (1977) that defined the concentration index C31 as the ratio between the radii that enclose 75% and 25% of the total galaxy light.

The asymmetry parameter quantifies the degree to which the light of a galaxy is rotationally symmetric, measured from the residuals of the difference between the image of a galaxy and the same image rotated by 180^o (Conselice, 2003). Finally the clumpiness parameter is a measure of the amount of light in small scale structures.

1.3 Colors and stellar masses

Other parameters are linked to the physical properties of the galaxy such as its stellar and gaseous mass, star formation rate (SFR), age.

An important parameter is the color of a galaxy, i.e. the ratio between the fluxes in two different bands. It reflects the dominant stellar population in a galaxy and correlates with morphology as highlighted by the pioneering works by Humason (1936); Hubble (1936); de Vaucouleurs (1961) and the many recent works such as Strateva et al. (2001); Scodeggio et al. (2002); Gavazzi et al. (2010). As a matter of fact at visible length the dominant contributors are the intermediate-type main sequence stars (from A to F) and G-K giants (Kennicutt, 1998). Therefore the integrated colors are determined by the ratio of the population of young ($<$ 1Gyr) and old ($3 - 15$ Gyr) stars, making possible to use the observed colors to estimate the fraction of young stars. In general, ETGs are characterized by red colors suggestive of old stellar population dominating the emission of Es and S0s. LTGs are instead blue, thus harboring a young stellar population, with the exception of the central bulge of spiral galaxies that is red and dominated by old stellar populations (McDonald et al., 2011). Thus, the total color correlates to the concentration of galaxies as well: ETGs are red and show on average higher values of C31 and Sérsic index while LTGs are blue and less concentrated. This is well summarized by the Fig. 1.4 by Scodeggio et al. (2002) where the authors plot these quantities together. As a matter of fact, highly concentrated galaxies (C31>4) are exclusively found at high luminosity and at red colors (B-H>3). The separation in different morphological classes highlights that the red, concentrated objects are mostly ETGs.

As shown in the upper right panel of Fig. 1.4 the color of a galaxy is also correlated to the total infrared luminosity which is proportional to the total stellar mass. Starting from the knowledge of stellar evolution and assuming

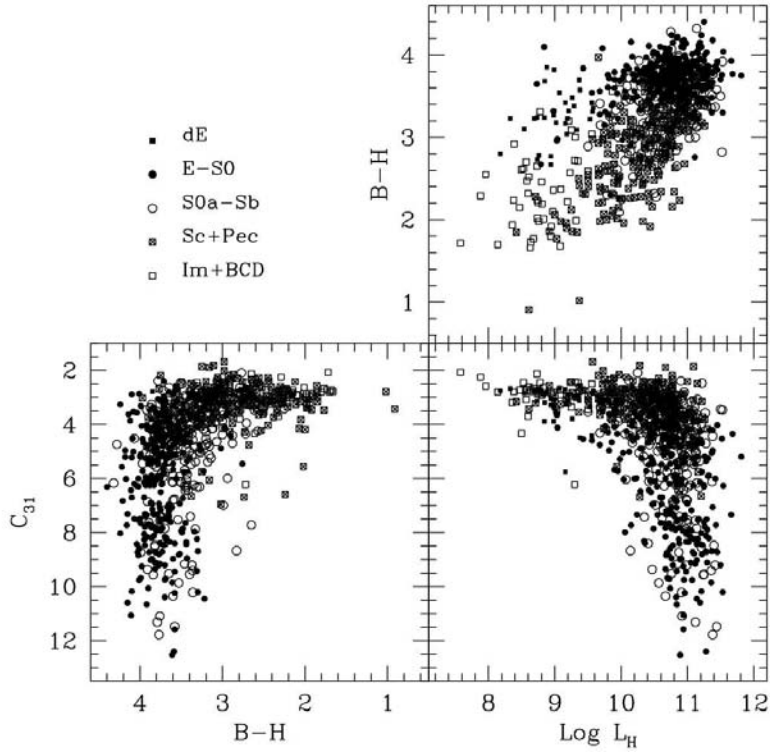

Figure 1.4: The relation between C31, color and total H-band luminosity taken from Scodeggio et al. (2002).

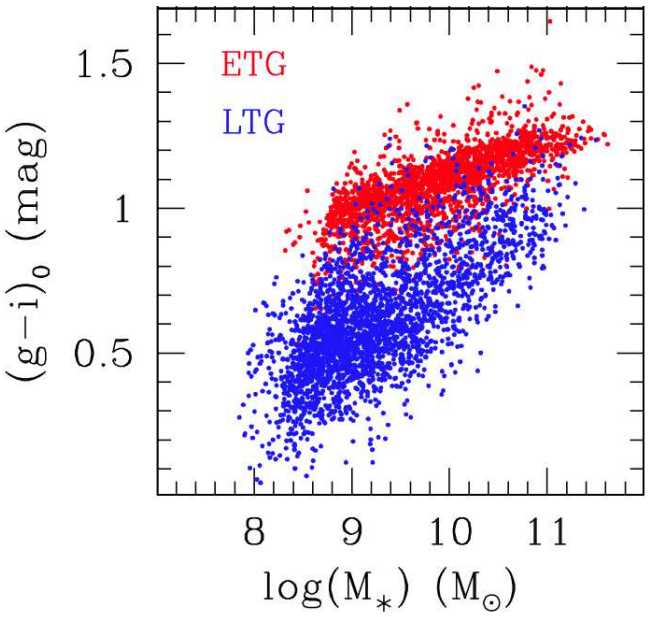

Figure 1.5: The color magnitude diagram of a sample of galaxies belonging to the local and Coma superclusters. On the y-axes the g-i color and on the x-axes the stellar mass. Blue dots represents LTGs and red dots ETGs.

an initial mass function, it is possible to calibrate relations for the mass-to-light ratio in a given optical/NIR band as a function of optical/NIR colors. Hence the total stellar mass can be analytically derived, starting from the total galaxy luminosity in a given band and its color (Zibetti et al., 2009). The stellar mass may be the most fundamental parameter describing present day galaxies (Gavazzi et al., 1996; Scodeggio et al., 2002; Fontanot et al., 2009). In the last decades a large observational effort has been put in constraining the dependence on stellar mass of galaxy evolution. Many physical and structural parameters of galaxies correlate with mass, pointing at it as a fundamental driver of galaxy evolution.

1.3.1 The color magnitude

The color of galaxies is correlated to their total stellar mass and to the morphological type. As a matter of fact, early multi-wavelength studies by Faber (1973), Visvanathan & Sandage (1977), Aaronson et al. (1981) suggested the existence for E and S0s of a color-magnitude relation with a shallow slope and a small intrinsic scatter. Similarly, other authors stated that spiral galaxies follow a color magnitude relation with a much greater intrinsic scatter (Chester & Roberts, 1964; Visvanathan & Griersmith , 1977; Griersmith, 1980). However these pioneering studies were based on limited samples of only tens or at most hundreds of objects which prevented conclusive statistical analyses. With the advent of the Sloan Digital Sky Survey (SDSS York et al., 2000) Strateva et al. (2001), using an unprecedented sample of 147920 galaxies, definitely demonstrated the bimodal distribution of galaxy colors and luminosity, with a clear separation between star-forming blue LTGs and passive, "red and dead" ETGs.

Since 2001, this bimodality in the galaxy distribution has been observed in many different regimes of density (Baldry et al., 2004; Kauffmann et al., 2004; Gavazzi et al., 2010) at different redshifts (Bell et al., 2004; Xue et al., 2010) suggesting an evolutionary path of galaxies from the "blue cloud" of star forming galaxies to the red sequence of "dead" galaxies. The color-magnitude relation for the (g-i) color index is displayed in Fig. 1.5 and shows that on average the galaxy population is twofold at almost all range of masses: ETGs, in red, form a tight sequence with a shallow slope, called the red sequence; LTGs distribute instead along the so-called blue cloud that overlaps the red sequence at high masses, suggesting a more advanced evolution for high mass LTGs.
In between the two distributions there is a zone characterized by a lower density of objects, called the "Green valley". Such region is thought to embrace galaxies that are in the process of quenching their star formation and are about to reach the red sequence (Bell et al., 2004). While the red sequence and the blue cloud are exclusively populated by ETGs and LTGs, respectively, almost at all mass, recent studies have highlighted that the green valley population is heterogeneous and comprehends both early and late-type galaxies that follow different quenching mechanisms (Schawinski et al., 2014).

1.3.2 Relations with the gaseous component

One of the most striking differences in ETGs and LTGs is their interstellar medium (ISM) and in particular their gaseous content: ETGs have low amounts of gas as testified by the low or null levels of H2, HI and Hα detected in such systems (Knapp et al., 1985; Roberts & Haynes, 1994; Cappellari et al., 2011); LTGs are instead characterized by considerable fractions of gas in all its phases. The HI mass is evaluated from the integrated flux of the finestructure emission line at 21 cm of the neutral hydrogen

$$M_{HI} = 2.36 \times 10^5 D^2 \int SdV, \tag{1.3}$$

where D is the distance in Mpc and $\int SdV$ is the flux of the HI line in $\mathrm{Jy\ km\ s^{-1}}$. The properties of the gaseous content of galaxies were investigated in early works embracing few hundreds of galaxies by Haynes & Giovanelli (1984), Knapp et al. (1985). Immediately emerged the fact that ETGs were characterized by considerably lower amounts of gas with respect to LTGs and, when present, the gas often surrounded the optical diameter of ETGs suggesting an external origin (e.g. a recent merger, van Driel & van Woerden, 1991; Roberts & Haynes, 1994). On the other hand, the gas fraction in LTGs was not constant and the advent of large HI survey such as GASS (Catinella et al., 2010) and ALFALFA (Giovanelli et al., 2005), definitely demonstrated with sufficient statistic that among LTGs the gaseous content scales with stellar mass and color: in general, more massive, red LTGs retain lower percentages of gas with respect to low mass LTGs. Fig. 1.6 shows the percentage of HI retained in LTGs as a function of the stellar mass of galaxies computed by Huang et al. (2012). From low mass to high mass, galaxies appear increasingly depleted: while low mass galaxies have an HI mass equivalent to their stellar content, massive galaxies only have $\approx 10\%$ of their stellar mass. A clear decreasing trend of the gas fraction ($\mathrm{M}_{HI}/\mathrm{M}_*$) is also observed from blue to red systems.

To quantify the degree of depletion of a galaxy Haynes & Giovanelli (1984) have defined the HI deficiency parameter ($< Def >$):

$$< Def >= log[M_{HI}(T,D)]_0 - log[M_{HI}(T,D)_{obs}], \tag{1.4}$$

i.e. the logarithmic difference between the observed HI mass (M_{HI}) and that expected for a galaxy of same linear diameter (D) and morphological type (T).

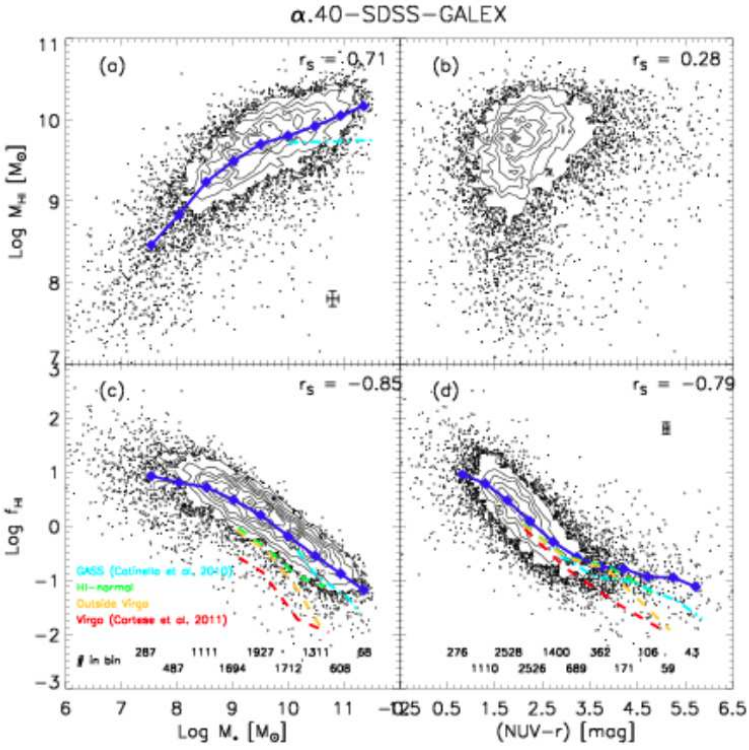

Figure 1.6: The HI mass (top) and HI mass fraction (bottom) of the ALFALFA sample (blue), published in Huang et al. (2012), as a function of stellar mass (left), and color (right). Cyan, green, yellow and red points represents the points of the GASS survey by Catinella et al. (2010), HI normal galaxies, galaxies outside Virgo, and galaxies Inside Virgo, respectively.

Along with the atomic phase of Hydrogen also the molecular phase (H2) of Hydrogen is dependent on mass and morphological type. Molecular hydrogen is the coldest component of a galaxy's gas reservoir and the component most directly linked to the possibility for the galaxy to form new stars, as it traces the cold molecular clouds that collapse, forming new stars. Such component is typically observed indirectly because of the absence of a permanent electric dipole moment and of bright rotational transitions in the H2 molecules. Thus H2 is derived from the emission associated to rotational transitions of the CO molecules (emitting at mm wavelengths) as $N_{H2} = I_{CO}X_{CO}$, where N_{H2} is the molecular hydrogen column density, I_{CO} the CO line intensity and X_{CO} is an empirical conversion factor which is expected to vary with the physical properties of the ISM (Boselli et al., 2002; Sandstrom et al., 2013). The dependence on such properties is still debated and some authors adopt a constant value for all galaxies (Sanders et al., 1984; Strong et al., 1988), namely the one observed in the solar neighborhood. Nevertheless calibrated relations exist to take into account variations of the conversion factor in different galaxies as a function of their luminosity (Boselli et al., 2002; Obreschkow & Rawlings, 2009; Feldmann et al., 2012).

Recent surveys such as the *Herschel* Reference Survey (HRS, Boselli et al., 2010) and the COLD GASS (Saintonge et al., 2011) have settled the relation with mass, color, concentration and surface mass density also for molecular gas. Fig. 1.7 shows the scaling relations obtained by Boselli et al. (2014) for the HRS for the total gas (H2+HI, top row), H2 (central row), and H2/HI fraction (bottom row). Although the fraction of H2 with respect to HI (third row) is mildly correlated with mass and has a very large scatter, the dependencies on mass of the molecular gas fraction (second row, M_{H2}/M_*) is remarkably similar to the one in HI. The combination of H2 data with HI (top row), gives a global scaling of the gas in galaxies with stellar mass: more massive galaxies have already consumed a considerable fraction of their reservoir, contrary to their lower mass counterparts. It follows that galaxies that are more concentrated, red, and with higher stellar surface mass densities retain lower global gas fractions than more diffuse, blue, low mass systems. While HI is characterized by a distribution typically larger than the optical extent the CO emission is more concentrated in the internal regions of galaxies (Kenney & Young, 1989, , see also Fig. 1.9).

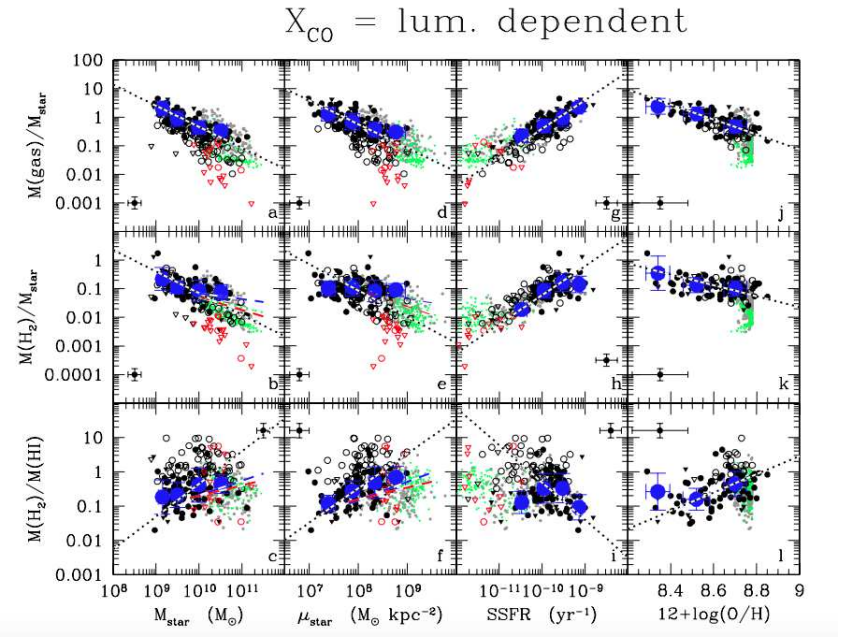

Figure 1.7: The scaling relations with mass, surface mass density, SSFR, and metallicity for H2+HI (Top row), H2 and H2/HI from Boselli et al. (2014).

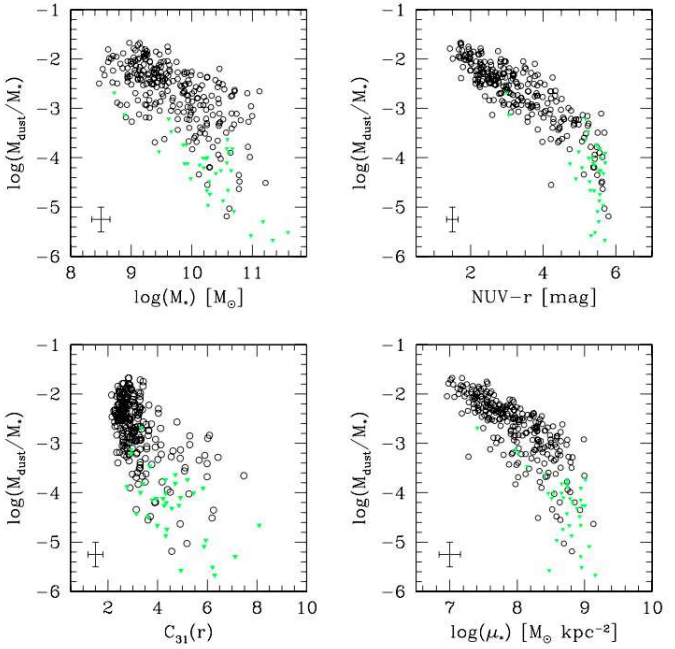

Figure 1.8: The dust scaling relations with mass, NUV-r color, concentration and stellar surface mass density evaluated by (Cortese et al., 2012) among the *Herschel* Reference Sample. Green triangles represent non detected galaxies while black circles the detections.

During stellar evolution, metals are produced in stars by stellar nucleosynthesis and are redistributed in the ISM by supernovae explosions and stellar winds. The aggregation of metals forms dust grains that are distributed inhomogeneously in galaxies. They are generally associated to the gaseous component and are indirect tracers of the cold gas distribution. The grains of dust have typical dimensions ranging from few hundreds of $\mathring{A}$ to $\sim 100\mu m$ and are principally made of hydrocarbon and silicate particles.

Because of their dimensions they absorb preferentially the UV and photons of the blue region of the visible spectrum primarily emitted by the hot, massive young stars. The absorbed radiation is subsequently re-emitted in the far-infrared ($\sim 3\mu\mathrm{m} - 1\mathrm{mm}$) region of the electromagnetic spectrum. They

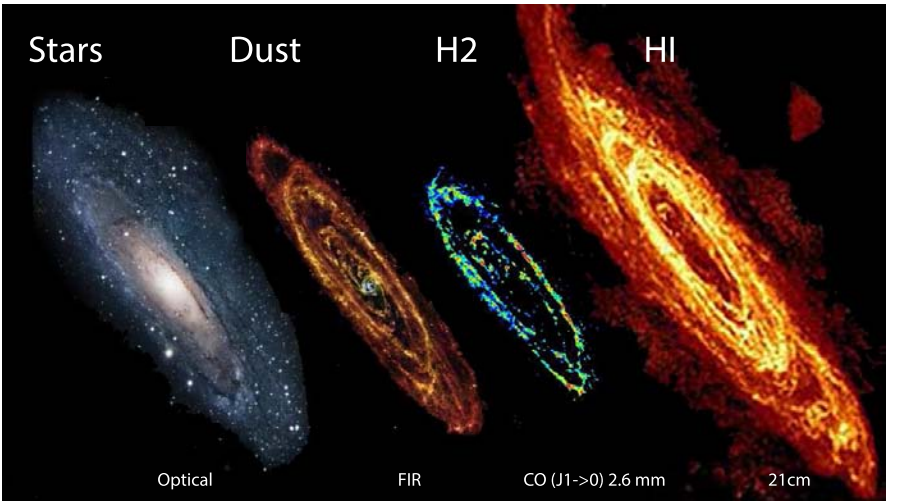

Figure 1.9: From left to right: Optical RGB, FIR (HRS, PACS+SPIRE), CO (J$-$ $>$ 0), and HI (21 cm) map of the Andromeda galaxy on the same scale. The image show how the different cold phases of the ISM distribute. In particular, the HI has the largest distribution while the dust map in the FIR is remarkably similar to the one of the molecular gas traced by CO.

are embedded in the cold gas component which prevents their destruction by the hot gas (Clemens et al., 2010) and hence their distribution is similar to the H2 distribution. Dust grains are also thought to be a catalyzer for the formation of molecular hydrogen molecules and are able to prevent its dissociation by the radiation fields of stars (Hollenbach & Salpeter, 1971), thus contributing to the regulation of star formation. Recent works such as da Cunha et al. (2008) have indeed shown the tight relation standing between the mass of dust as evaluated from its FIR emission and the star formation of galaxies.
The dust fraction (i.e., the percentage of dust with respect to the stellar mass) is anticorrelated to the stellar mass in a similar fashion to the gaseous component (Cortese et al., 2012, see Fig. 1.8), confirming a tight relation between the gas and dust abundances.

1.3.3 Ionized Gas.

Dust and Hydrogen, are fundamental drivers of the process of star formation which is therefore, in general, possible only in LTGs. While sustaining the star formation the newborn hot, massive stars emit UV photons able to photoionize the surrounding medium. Hence a considerable fraction of the hydrogen inside a galaxy is ionized (HII) and it is detected observing the many nebular emission lines emitted at different wavelengths from the Lyman limit to NIR. The ionized gas appears as diffuse with very bright compact knots, that represent the so-called HII regions, the loci where the star formation is actually taking place.

In these regions of strong photoionization, the nebular emission is primarily dominated by the Hydrogen recombination lines of the Lyman and Balmer series which are the brightest. In particular, one of the best tracer of the ionized gas (at least in the local Universe) is the first line of the Balmer series (Hα). This is the brightest line of the Balmer series and falls in the visible part of the spectrum and thus it is easily traced with optimal spatial resolution from groundbased optical telescopes. Other ions, less abundant than Hydrogen like N,O, He, and S, emit lines at "prohibited" wavelengths, i.e. wavelengths that cannot be observed in a laboratory because of the high densities that highly collisionaly deexcite the gas. The ratio of both Hydrogen and prohibited line fluxes ratio gives important clues about the physical state of the ionized interstellar medium:

Temperature & Density This two quantities can be measured from the energetic levels of a single atom. Among forbidden lines of a single ion, some are very close in wavelength while others are much more separated, reflecting a wider separation in the energy of the level occupied by the electrons.
The ratio of the emission of two levels/lines that are well separated is proportional to the probability that electrons occupy one or the other level and this is dependent on the temperature. Typical diagnostics used to evaluate temperatures are the ratios ([NII]$\lambda6548$+[NII]$\lambda6583$)/[NII]$\lambda5755$, ([OIII]$\lambda5007$+[OIII]$\lambda4959$)/[OIII]$\lambda4363$, ([SIII]$\lambda9531$+[SIII]$\lambda9569$)/[SIII]$\lambda6312$.
Conversely, the ratios of lines that are close in the electromagnetic spectrum are regulated by the collisional excitation and deexcitation of the two levels

which depends on electron density. Hence to derive electron density suitable ratios are [SII]λ6716/[SII]λ6731 and [OII]λ3729/[OII]λ3727 (Osterbrock & Ferland, 2006). These relationships have been well tested within the Galaxy but suffer some limitations in extragalactic sources as many weak lines are hardly detected (for example [OIII]λ4363).

Metallicity & Abundances Once the density and temperature are known, the abundance ratio between two ions can be determined from the relative intensity between measured lines. Nevertheless the temperature and density are not always well constrained or measurable directly from the emission lines. Hence abundance and metallicity can then be derived from empirical relations between different emission line ratios and metallicities calibrated via direct measures in large samples of Galactic HII regions. The emission line ratios most commonly adopted are O32 ([OIII]λ5007/[OII]λ3727), N2 ([NII]λ6584/Hα), O3N2 (([OIII]λ5007/Hβ)/([NII]λ6584/Hα)). However measuring galaxy metallicity is still a focus of current effort in research and a common agreement on the best calibration has not been reached yet (Curti et al., 2016).

Absorption The ratio between the Hα and Hβ has a theoretical value from case B recombination, that depends weakly on density and temperature in the low density limit at T=10^4K (Osterbrock, 1989). As a consequence, the variation from the theoretical value (Hα/Hβ =2.86) can be attributed to attenuation due to dust absorption.

In general, most line ratios vary over a wide range of values depending on parameters such as the metallicity and ionization parameter, which identifies the strength of the ionizing source. Taking advantage of radiative modern models of photoionization, some authors were able to reconstruct how line ratios vary as a function of metallicity and ionization parameter. Hence combining spectroscopic observations and models, these authors have proposed diagnostic diagrams that can separate the ratios typical of regions ionized by the radiation field of stars from ratios that need other ionizing sources to be explained (e.g. the accretion of material onto a supermassive black hole).

As a matter of fact, photoionization by stars is not the only source of ionization in galaxies. The strong ionizing radiation emitted by the activity of the supermassive black hole residing in the center of most massive galaxies

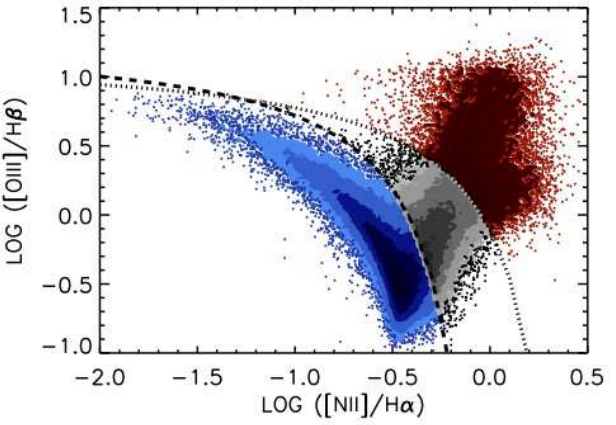

Figure 1.10: The BPT diagram: In Blue the sequence of star forming regions, red the ratios corresponding to AGN emission and in gray the composite region.

represents an alternative mechanism, as well as shocks or ionization from old post-AGB stars. Usually, in the optical lines, good tracers of the photoionization state of the gas are the [OIII] and [NII] normalized to the nearest balmer series line (Hβ and Hα, respectively). In particular, these two ratios can be compared to construct the BPT diagram (Baldwin et al., 1981) which is plotted in Fig. 1.10. The diagram is constructed from a sample of nuclear spectra taken from the SDSS and shows two characteristic wings. The left wing of the BPT diagram represents line ratios consistent with photoionization from stars, while the right wing embraces ratios consistent with other ionizing sources.

In between there is a region of superimposition of the two sequences where the ionization field is low and the source uncertain. As it can be seen in Fig. 1.10, two lines are plotted: the dashed curve was calibrated by Kauffmann et al. (2003) and separates the AGN and HII region sequence; the dotted curve is the one of Kewley et al. (2001) who found the upper limit for the photoionization curve using modern synthesis and photoionization models for starburst galaxies. Following the models for photoionization by Kewley et al. (2001), Kauffmann et al. (2003), and Rich et al. (2011), at fixed metallicity the position on the BPT is determined by the ionization parameter which decreases following the left wing from left to right. Along with the BPT, other (similar) diagnostics have been studied such as the diagram that includes the [OI] line

(sensitive to shocks) instead of the [NII]. Also in this case, models are able to reconstruct the typical ratios as a function of ionization factors and metallicity.

1.3.4 Star formation

The emission lines of the ionized gas are a sensitive probe of the young stellar population and the flux from recombination lines such as Hα can be converted in a star formation rate (SFR). The conversion factor is usually computed using evolutionary synthesis models. Only stars with masses $> 10\mathrm{M}_{\odot}$ and lifetimes < 20 Myr contribute significantly to the integrated ionizing flux. Therefore the emission lines provide a nearly instantaneous measure of the SFR (Kennicutt, 1998). Using the calibrations of Kennicutt et al. (1994) and Madau et al. (1998) it is possible to derive the SFR from the Hα line luminosity following:

$$SFR\ (M_{\odot}\ yr^{-1}) = 7.9 \times 10^{-42} L(H\alpha)\ (ergs^{-1}). \tag{1.5}$$

The SFR can be extrapolated also from bright forbidden lines such as the [OII]λ3727-doublet although such measure is affected by large uncertainties (Kennicutt, 1998) mainly because its relation was calibrated with Hα but the [OII]/Hα ratio shows a great scatter. Another approach is to measure the SFR from specific windows of the UV continuum where the population of young stars ($t < 10^8 Myr$) completely dominates the spectrum and the SFR scales linearly with luminosity. Because of its direct relation to the photosphere of young massive stars, is one of the best instrument to probe SF. Nevertheless it cannot be observed from the ground and is highly affected by extinction which is distributed irregularly and is difficult to model (Kennicutt, 1998).
Nevertheless dust is heated by hot young stars and it reemits in the FIR. Such emission provides a very good estimate of the SFR. However the calibration of the SFR on the FIR flux are affected by some uncertainties because a fraction of the dust in some galaxies can be heated even by the old stars radiation field.

On average, ETGs have low to null levels of SFR while LTGs are characterized by high SFRs. Nevertheless, among LTGs, the SFR is not strongly correlated with the Hubble type and shows a great scatter within a single class. However Kennicutt, in 1989, was able to determine an underlying relation between gas and SFR which is independent of Hubble type, hence showing that the large dispersion in a single morphological class is attributable to a large

dispersion in the gas content in the same class. By comparing the SFR obtained from Hα observations of 62 disk galaxies to the averaged gas densities evaluated from Hα, HI and CO observations, Kennicutt was able to determine that the star formation in disk galaxies follows

$$\Sigma_{SFR} \propto \Sigma_{gas}^{\alpha}, \tag{1.6}$$

the Kennicutt-Schmidt law, where $\alpha \sim 2$ and Σ_{SFR} and Σ_{gas} are the superficial densities of SFR and gas, respectively.

More recently the work of Gavazzi & Scodeggio (1996) and Gavazzi et al. (1996) unveiled an anticorrelation between the SFR per unit mass (namely the specific star formation rate, sSFR) and stellar mass. By evaluating the SFR from nuclear spectra of galaxies of the SDSS and extrapolating the global SFR guided by the optical color of galaxies, Brinchmann et al. (2004) evaluated the star formation rate for a large sample of local galaxies and found that, intriguingly, galaxies separate in different region of the SFR vs M_* plane: most galaxies lie on an almost linear relation of proportionality between SFR an stellar mass, called the main sequence (MS) of star forming galaxies; above this relation lie the starburst galaxies, objects characterized by an extraordinary elevated star formation rate; finally below the relation fall passive galaxies (ETGs) or galaxies that are caught in the act of becoming passive (green valley galaxies).

Such distribution has been observed at high redshift as well as in the local Universe and, unlike starburst galaxies, normal star-forming galaxies inhabit the main sequence at all redshifts (e.g., Noeske et al. 2007, Elbaz et al. 2011). However, among local main-sequence galaxies, the exact dependence of the star formation rate on the stellar mass is still debated in the literature. In other words, it has not yet been determined whether the specific star formation rate (sSFR) decreases with increasing stellar mass (a process also known as *mass quenching* or *downsizing*, Cowie et al. 1996; Gavazzi et al. 1996; Boselli et al. 2001, Fontanot et al. 2009; Gavazzi 2009; Huang et al. 2012) or whether these two quantities are nearly proportional at all masses (e.g., Peng et al. 2010). A broader consensus exists instead on the quenching of massive main-sequence galaxies at higher redshift, where massive galaxies are seen to evolve more rapidly (e.g., Whitaker et al. 2014; Ilbert et al. 2014) than their less-massive counterparts. However, some tension remains between the observations and the current models and simulations of galaxy evolution (Fontanot et al. 2009;

Weinmann et al. 2009, 2012; Henriques et al. 2013; Boylan-Kolchin et al. 2012; Hirschmann et al. 2014) emphasizing that the physics of the quenching of star formation is still not fully understood and in particular the nature of the physical processes responsible for this mass quenching is still under debate (Peng et al. 2012, Lilly et al. 2013).

1.4 Kinematics - Longslit Spectroscopy and IFUs

The distribution of the baryonic (stars+gas+dust) and dark mass determines the potential well of the galaxy that univocally determines the motion of its constituents. How matter distribute depends on the way it was assembled therefore the assembly history can be deduced from the kinematics of galactic constituents.
Galaxies that we observe are divided in two categories: rotationally supported systems (i.e, rotating disks) and pressure supported systems (i.e, systems whose equilibrium is sustained by the chaotic motion of the stars in a triaxial geometry). Pressure supported systems form via violent mergers that scramble disks into ellipsoidals while disks form when the dark matter halo accretes slowly and unperturbed for a protracted time.
The kinematics of galaxies are in general unveiled with spectroscopy by subtracting the cosmological redshift and measuring the Doppler shift due to the relative motions of emission or absorption lines of their stellar and gaseous constituents. Typically, LTGs kinematics are observed by measuring the shifts of the bright emission lines of the gaseous component. Because the different components of galaxies distribute differently, their emission can probe the potential at different radii, sometimes larger than the optical radius.
The technique that allows to map the kinematics of galaxies at the largest radii from their center is the detection of the HI line at 21 cm, which is emitted by the component with the greatest scale length (HI, see Fig. 1.9).
ETGs are instead characterized by low to null amounts of gas hence their internal motions need to be traced by measuring the motion of the stellar component. This is done by measuring the width of the typical absorption lines of stellar atmospheres such as the H, K lines or the Na, MgII or CaII triplet.
In general, LTGs are rotating systems while, until recently, ETGs were ambiguous mainly because of the confusion among ellipticals and lenticulars in the morphological classification: face-on or slightly inclined disks projected

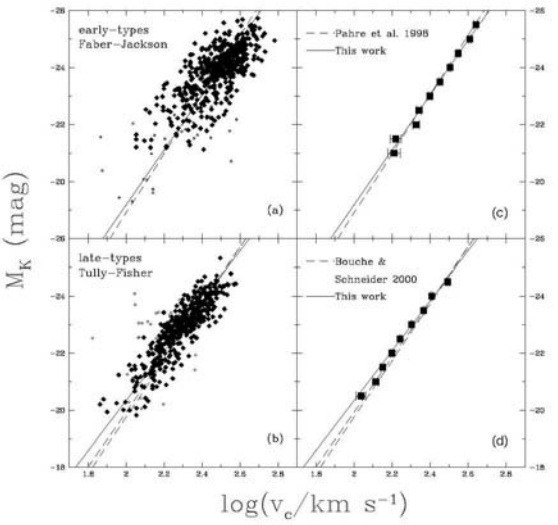

Figure 1.11: Faber-Jackson (Top) and Tully-Fisher (Bottom) relation for 2MASS galaxies with velocity dispersions and circular velocities drawn from the literature.

onto the plane of the sky are seen as ellipses therefore, in absence of disk features such as spiral arms or bars that would immediately identify them as disks, the morphological classification often fails in distinguishing rotating objects and elliptical galaxies. The separation is instead straightforward when the data of the kinematics are available for the whole galaxy, e.g. a measure of velocity at different radial steps from the center.

From the seminal work of E. Hubble that unveiled the extragalactic nature of nebulae, the optical spectroscopy technique has given a crucial contribution to our understanding of extragalactic objects. For instance, from optical and HI observations, Rubin et al. (1980) and Rubin et al. (1985) traced the rotational velocities as a function of their radius for a sample of local disk galaxies, providing important clues on the presence and distribution of dark matter in galaxies. In the same years, two fundamental empirical relations between the luminosity of galaxies and their kinematics, separately for rotating disks and dispersion dominated objects, were calibrated: the Tully-Fisher relation (Tully & Fisher, 1977) that showed the proportionality between the

luminosity of the galaxy in H band (best proxy for luminous mass) and their maximum rotational velocity (typically from HI); and Faber-Jackson relation (Faber & Jackson, 1976), that showed that in dispersion dominated galaxies the central velocity dispersion was proportional to the total H-luminosity of the galaxy.
In Fig. 1.11, from bottom to top, are shown the Tully-Fisher and Faber-Jackson relations, respectively. Both relations are determined by the relation between the overall potential well (dominated by dark matter), the luminous fraction of matter and how this moves in such potential. Moreover they provided a new method to extrapolate distances comparing the luminosity predicted by its kinematics and the observed flux.
Since these works, astronomers have developed new spectroscopic techniques that allowed to take multiple spectra at one time such as multiple slits spectrographs or fiber-fed spectrographs (i.e., the light of an object is convoyed to the instrument by an optical fiber carefully placed on the target). Such methods allowed for a simultaneous observation of a large number of spectra and allowed to tailor automated techniques for systematic spectroscopic surveys. Nevertheless none of these methods could accurately map an extended object while today this is possible using Integral Field Unit (IFU) spectrographs that are able to take simultaneously contiguous spectra of a given region, therefore producing 3D maps where the third dimension is the wavelength of the emission. The map of the kinematics was already possible using the HI line at 21 cm that nevertheless suffers two limitations: it cannot be used for ETGs and is characterized by a significantly lower spatial resolution. The modern IFUs (such as MUSE@VLT and soon the Cosmic Web Imager@Keck) combine an optimal spatial resolution (sub-arcsec) and good spectral resolution (R>1000).

An example of the tremendous potential of IFUs is represented by the results of the ATLAS^{3D} project: using the SAURON IFU mounted on the William Herschel telescope Cappellari et al. (2011) surveyed a sample of ≈ 300 ETGs extracting their kinematics and revealing that only a little fraction of galaxies are dispersion dominated systems. As a matter of fact $\approx 87\%$ of ETGs are dominated by rotation (called Fast Rotators, FR) and just a mere 13% of ETGs are truly pressure supported systems (Slow rotator, SR Emsellem et al., 2011), destroying the previous paradigm stating that ETGs

were mainly supported by their velocity dispersion. Also among LTGs, modern IFUs are changing the way that we look at galaxies. Such instruments give access to a huge amount of information, providing at the same time all the information needed to constrain the dynamical and physical state of both the gaseous (ionized) and stellar components.

1.5 Bars

Since the first observations, it resulted evident that selfgravitating disks can sustain characteristic structures such as spiral arms, and bars.
While spiral arms are density waves (i.e., they do not reflect a difference in the rotational or radial speed of stars) propagating with a differential angular velocity, bars are instead characterized by an actual motion of stars on almost radial orbits that precede coherently, as a rigid body.

Fig. 1.12 shows an evident stellar bar that connects the spiral arms to the center of NGC 986. A bar is characterized by an almost radial motion of stars that precede coherently as a rigid body with an angular precession velocity Ω_p. Stars in a disk can be thought on almost circular orbits characterized by an angular frequency Ω. For a star in a closed orbit, a small perturbation of the orbit induces a radial component to its motion, characterized by a typical frequency called epicyclic frequency (k). The angular velocities on orbits are determined by the potential and if the potential allows for orbits that at different radial distances show a constant $\Omega_p \sim \Omega - k/2$ (orbits that execute two radial excursions for every revolution) is called bar unstable, i.e. can sustain a bar.
In the epicyclic approximation orbits are characterized by the angular frequency and the radial frequency and an orbit is resonant if there are two integers l, m such that

$$lk + m(\Omega - \Omega_p) = 0, \tag{1.7}$$

where k is the epicyclic frequency, Ω and Ω_p the angular and precession frequency, respectively. The most important are the ones obtained for $m = -1$ $l = 2$ (Inner Lindblad Resonance, ILR, $\Omega_p = \Omega - k/2$), $m = 1$ $l = 2$ (the Outer Lindblad Resonance, OLR, $\Omega_p = \Omega + k/2$) and $l = 0$ (the corotation resonance, CR, $\Omega_p = \Omega$). Resonances gather large quantities of gas

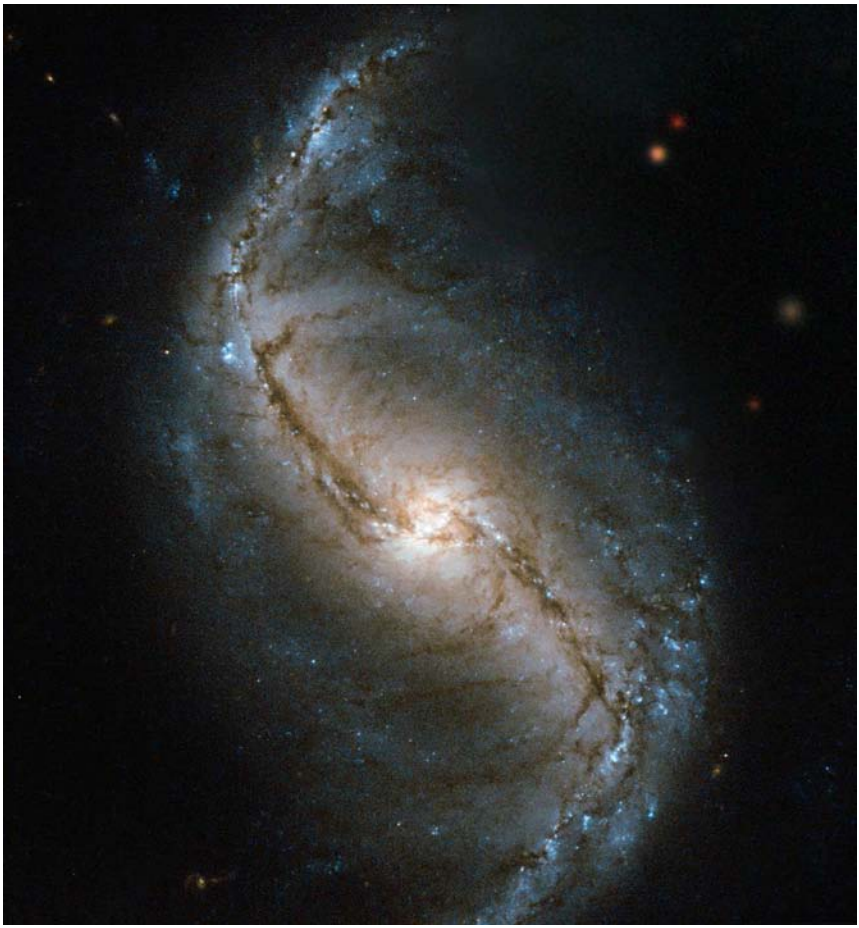

Figure 1.12: RGB image taken with HST of the barred galaxy NGC 986.

and sometimes are characterized by intense star formation. This aspect makes them sometimes easily recognizable as ring like structures characterized by a blue color. ILRs are typically observed as rings in the circumnuclear region of galaxies (few ~ 100 pc) while the corotation resonances are typically observed at the edge of the optical bar. OLRs are instead more difficult to observe and have dimensions even larger than the optical disk. In the RGB image of Fig. 1.12, for example, the blue ring-like structure surrounding the bar possibly represent the corotation resonance.

1.5.1 Consequences on the gas

Bars are transient objects: they form, evolve and dissolve. Their evolution is investigated with simulations that however still haven't reached a complete picture.
Many triggering mechanisms have been proposed such as satellite fly-bys, gas depletion, minor merging, but both simulations and observations, to date, have not reached a clear view of the bar-triggering phenomenon. However a plethora of simulations in the literature are available to put constrain on bar evolution.
Bars can be divided into weak and strong bars. The precise definition of bar strength is not unique and may change from observations to simulations. In general, the strength of the bar indicates the intensity of the non-axisymmetric forces that the bar exerts and is the ratio between tangential and radial forces. The efficiency and strength of the torques exerted by bars is different in different objects and also varies as a function of time (Athanassoula, 2013).
As soon as a potential can sustain a bar, stars occupy the elliptical orbits characterized by $\Omega_p \sim \Omega - k/2$ making the bar appear increasingly evident. During the growth of the bar, the bar become stronger until the strength of the bar reaches a maximum. Although this phase can be quite rapid ($\approx 10^9$ yr), the real timescales can vary significantly in different simulations (Athanassoula, 2013). After having reached the maximum the bars weakens and then settles on an almost constant value (secular phase).

Hydrodynamical simulations have made clear the impact that bars can have on the secular evolution of a galaxy (Athanassoula, 2002; Sellwood, 2014). In particular, it is now established that as a consequence of the non-

axisymmetric forces exerted onto the gaseous component of the galaxy, the gas within the corotational radius is rapidly funneled to the center of the galaxy, within the Inner Lindblad Resonance (see Kormendy & Kennicutt, 2004; Kormendy, 2013; Sellwood, 2014; Fanali et al., 2015), while the gas outside is confined to the outer disk (Sanders & Huntly, 1976; Shlosman, Frank & Begelman, 1989; Athanassoula, 1992; Berentzen et al., 1998; Regan & Teuben, 2004; Kim et al., 2012; Cole et al., 2014) and this process is more efficient in strong bars. In Fig. 1.12, for example, the inflow is testified by the evident dust lanes along the bar. In the center of the galaxy, the gas reaches high densities triggering a burst of star formation that rapidly depletes it, making the region inside the corotational radius gas-poor (Krumholz & McKee, 2005; Krumholz et al., 2009; Daddi et al., 2010; Genzel et al., 2010). However large cosmological simulations with sufficient resolution to resolve and properly reproduce the effects of bars on small scales are not available. Hence the overall impact on the evolution of galaxies remain elusive.
The strong inflow of gas has been also proposed as possible feeding mechanism of the central super massive black hole but is still not clear if this is possible (Emsellem et al., 2015).

In the end, the strong inflows of gas and the possible star formation bursts build a central concentration of mass within few Gyrs. Such bulge is often characterized by a thick disk like shape that rapidly rotates and is therefore different from the classical, pressure supported bulges (Kormendy, 2013). For this reason it is called pseudo-bulge.
Once the central component reaches a mass that gravitationally influences the orbits of stars in the bar, the bar weakens and eventually even dissolves (Shen & Sellwood, 2004). However, a comprehensive picture of the evolution of bars and host galaxies has not been reached yet.

1.5.2 Observational evidences

From an observational point of view, starting from the seminal work of E. Hubble who dedicated half of the world-famous tuning fork to barred disk galaxies (Hubble, 1936), bars have increasingly captured the interest for the understanding of galaxy evolution. As a matter of fact, bars redistribute the angular momentum within spiral galaxies and trigger gas inflows toward the

center that have been proposed as possible triggers of AGNs, rejuvenation of centers, and precursors of the disky pseudo bulges observed in many disk galaxies.
Throughout the years observations have enlighten the extremely high frequency of barred galaxies among spirals. Among local bright disk galaxies, $\sim 60\%$ (Knapen, 1999; Eskridge et al., 2000; Menéndez-Delmestre et al., 2007; Marinova & Jogee, 2007) are barred if observed in the near-infrared and about $\sim 40\%$ are barred if observed in the optical bands (Eskridge et al., 2000; Marinova & Jogee, 2007), which hints at bars as fundamental drivers of the evolution of late-type galaxies (LTGs).
If and how the bar fraction evolves across the cosmic time (Jogee et al., 2004; Sheth et al., 2008), along with the exact determination of the dependence of the bar frequency on stellar mass (especially at the faint end of the mass function) and galaxy environment, are still under debate (Thompson, 1981; Marinova et al., 2012; Skibba et al., 2012; Lansbury et al., 2014; Alonso et al., 2014). For example, Masters et al. (2012), Skibba et al. (2012), and Méndez-Abreu et al.(2012) all consistently report a bar fraction that increases with increasing mass. On the other hand, Barazza et al. (2008) recover a strong bar fraction that increases with decreasing mass while Nair & Abraham (2010) find a strong bar fraction that decreases from $\sim 10^9 M_\odot$ to $\sim 10^{10} M_\odot$ and increases again from $\sim 10^{10} M_\odot$ to $\sim 10^{11} M_\odot$.

An exact determination of the bar fraction can be reached only with an accurate morphology classification of barred galaxies. The visual inspection approach was adopted in works such as Nair & Abraham (2010) and the $Galaxy\ Zoo\ project$ while other authors have developed more objective criteria to detected barred galaxies.
An approach is to perform the two dimensional Fourier Analysis of the intensity distribution of the galaxy and look for a peak in the radial profiles of the m=2,4 Fourier components. Nevertheless the most common practice is to fit ellipses to the isophotes of galaxies and extrapolate the ellipticity and position angle (P.A) radial profiles. Indeed, as described in Jogee et al. (2004) bars produce specific features in the ellipticity and in the P.A. radial profiles of the isophotes. Along the bar, isophotes are neatly oriented with the same position angle and, if the galaxy is fairly face–on, their ellipticity is higher with respect to the disk (Jogee et al., 2004; Marinova et al., 2012). Hence in the ellipticity

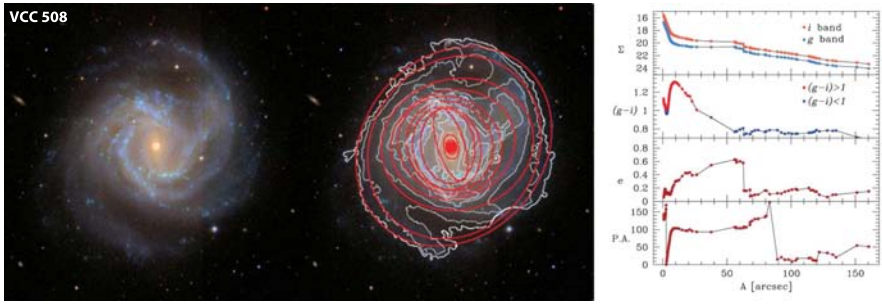

Figure 1.13: Example of isophotal fitting of the galaxy VCC 508. On the right the surface brightness, ellipticity, and position angle radial profiles are plotted.

radial profiles bars produce an evident peak while in the P.A. radial profile they produce a plateau (see for example Fig. 1.13).

The peak of the ellipticity profile is a good proxy of the strength of the bar (Laurikainen et al., 2007) and, in general, bars are called strong when they are long (with respect to the disk scale length) and massive (associated to large values of m=2,4 Fourier density component). On average, strong bars occupy $\gtrsim 30\%$ of the optical disk (Marinova & Jogee, 2007) and have typical ellipticity $e > 0.4$ (Marinova & Jogee, 2007; Laurikainen, Salo & Buta , 2004; Laurikainen et al., 2007).
It is still not clear whether there are evidences of a different evolution between bars in ETGs and LTGs although there are evidences of an enhanced bar fraction among red objects (Nair & Abraham, 2010; Masters et al., 2012). Similarly an increase of the bar fraction from gas poor to gas rich systems is observed (Masters et al., 2012). However, among ETGs, pressure supported systems cannot sustain bars and an accurate bar fraction among ETGs rotators demands an accurate morphological classification able to exclude the contribution of ellipticals from lenticulars.

A great work has been done with both simulation and observation to constrain the impact that bars have on the overall population of galaxies but, to date, the parameters that regulate the properties and the evolution of barred galaxies remain elusive and a comprehensive picture has still to be reached.

1.6 The environment

Many galaxies do not live in isolation during the cosmic epochs but gravitationally bind with other objects forming bigger structures such as groups and clusters of galaxies. Groups comprehend from two objects to few tens of galaxies while clusters count up to thousands of member galaxies. Galaxies are therefore distributed in the Universe inhomogeneously: long low density filaments of galaxies (Superclusters) embrace void regions and intersect in regions of high density (Clusters). In general, evolved clusters are spherically symmetric systems in virial equilibrium, sustained by the chaotic motion of member galaxies. The motion of galaxies provides an independent measure of the potential of the cluster. From the virial equilibrium, the dynamical mass of the cluster is linked to the velocity dispersion of galaxies by $GM_{cluster}/R^2 \approx \sigma^2$. Clusters span a range of masses going from $\sim 10^{13}$ up to $10^{15.5} M_{\odot}$ (Bahcall & Cen, 1993) and a corresponding velocity dispersion distribution ranging from ≈ 400 to 1500 $\mathrm{km\ s^{-1}}$ (Struble & Rood, 1991).

Historically, clusters were detected by eye and already in 1784, Charles Messier noticed the exceptional concentration of nebulae in the Virgo constellation and, in 1785, Herschel provided the first description of the Coma cluster. Later, in the last century, by examining high-quality photographic plates Abell was able to census more than 4000 clusters, recovering the first catalog of clusters. However visual inspection is a slow process and in modern large samples of galaxies, whenever spectroscopic observations are available, it is possible to quantify the density of galaxies parametrically. This is done by evaluating the projected density of galaxies from the three dimensional distribution of galaxies (R.A., dec, cz) using geometrical algorithms. The simplest way to quantify the local projected density is to count the number of galaxies inside cylinders centered on each galaxy and compare it to the average density of the sample. A good compromise for the cylinder dimension that is sensitive to both large and intermediate structures is a radius of $\approx$ 1Mpc and an half-length of c$z = 1000\ \mathrm{km\ s^{-1}}$. In this way the environment can be parametrized using

$$\delta_{1Mpc;100km/s} = \frac{\rho_{gal} - < \rho >}{< \rho >}, \tag{1.8}$$

where ρ_{gal} is the local galaxy density and $< \rho >$ the average density of the

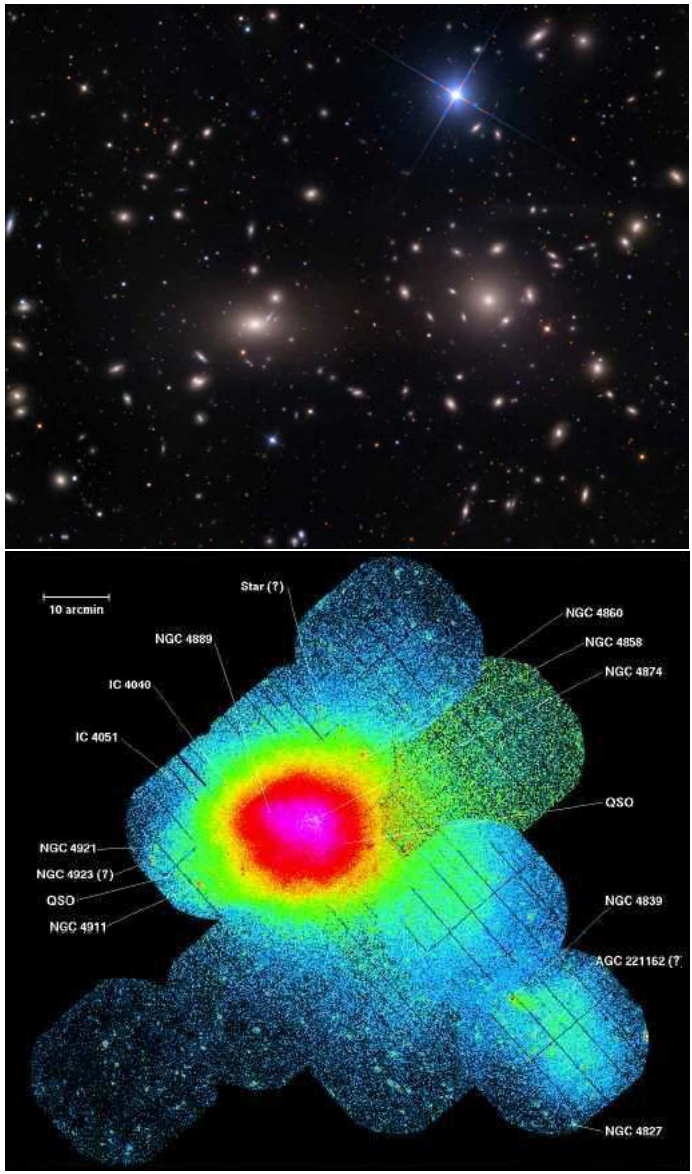

Figure 1.14: Top. RGB image of the core of the Coma cluster. Bottom. Xray map of the core of the Coma cluster.

field.

However one of the best tracer of clusters is represented by the huge amount of gas that fills their potential well. As a matter of fact, in the regions of high density such as clusters, the potential well created by the combined potentials of the galaxies forming the structure is filled with hot (T$\approx$ 10^{7-8}K) gas that emits Xrays due to thermal bremsstrahlung. An Xray image of the Coma cluster is shown in Fig. 1.14 and similarly beautiful X-ray maps of hundreds of clusters were made by the Einstein X-ray Observatory (Forman & Jones, 1982), ROSAT (Böhringer et al., 2004), Chandra, XMM-Newton (Arnaud, 2001) and X-ray blind surveys have been used to discover clusters. Moreover the Xray emission is particularly useful because it provides a probe of the gravitational potential as the mass and density of the gas (which dominate the baryon component) can be determined from it (Fabricant et al., 1980).
The hot gas filling the cluster is also responsible for a distortion in the CMB spectrum that is exploited to detect distant clusters. The hot gas of the cluster interacts with the CMB by scattering the photons and leaves a specific imprint in its spectrum which is independent from redshift. This effect, called Sunyaev Zeldovich effect, is therefore a powerful tool to detect high redshift clusters.

1.6.1 Evidences of environmental evolution

In Fig. 1.15 is shown the density-morphology relation found by Dressler (1980). The relation shows the fraction of spirals, lenticulars and ellipticals, respectively as a function of the projected density. It is clear that as the density rises the fraction of early type objects rises proportionally while the fraction of spirals decreases. This suggests that galaxies are sensitive to the environment in which they reside. They interact with the environment and evidences show that such interactions efficiently transform them from blue to red systems. Using the SDSS Gavazzi et al. (2010) have shown that the color-magnitude relation evolves from low density to high density regions in the Coma supercluster as shown in Fig. 1.16. In the lower left panel is displayed the relation for the lowest density bin: the red sequence (red dots) is almost absent while the blue cloud (blue dots) is crowded. The projected density increases counterclockwise and, as density increases, the red sequence populates while the blue cloud

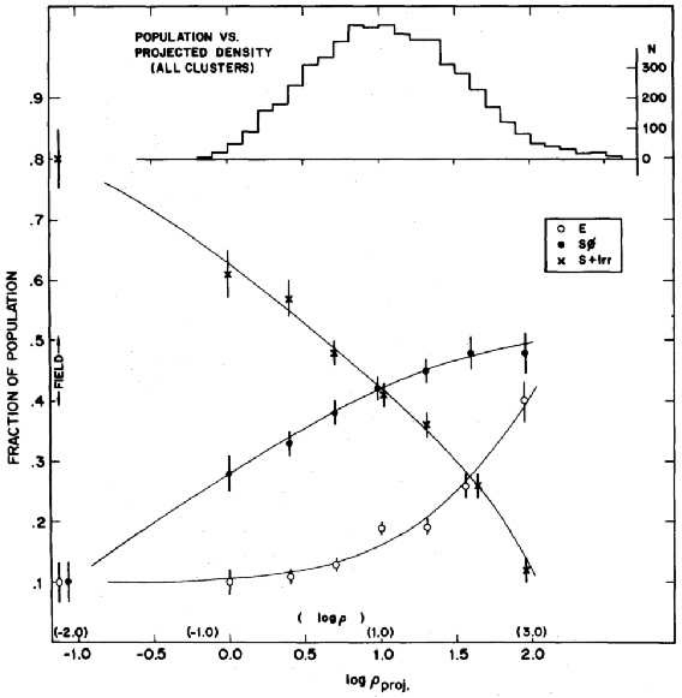

Figure 1.15: The density morphology relation as published by Dressler (1980).

fades. Among LTGs, Gavazzi et al. (2010) stress that the migration from blue to red systems in dense environments is more efficient at low mass compared to high mass. Therefore the processes that regulate the cluster-galaxy interaction depends on mass and is apparently more efficient at low mass.
In general, galaxies in dense environments appear mostly red and passive and this is consistent with their observed gas content and sSFR as demonstrated by Gavazzi et al. (2010). From Hα imaging observations of a sample of HI-selected galaxies from ALFALFA (Haynes et al., 2011) of the local supercluster including the Virgo cluster, Gavazzi et al. (2013a) derived the sSFR as well as the HI-deficiency as a function of the projected distance from M87. The deficiency increases as galaxies approach the highest density region (i.e., the center of the cluster, M87) while, conversly, the sSFR decreases. In other words, galaxy in clusters are redder, anemic and amorphous with respect to the field.
An imprint of the cluster influence on galaxy evolution is hidden also in the optical/UV luminosity functions (LF) of cluster galaxies when the contribution of early type and late type objects is separated. In general as shown by De Propris et al. (2003), the global luminosity function of clusters is steeper than in the field. Using different diagnostics for morphology, such as spectroscopic diagnostics and sersic indices, Madgwick et al. (2002), Yagi et al. (2002), and De Propris et al. (2003) consistently shown that the optical luminosity function of early-type objects in clusters is brighter and steeper ($\alpha \sim -1.49$) compared to the field ($\alpha \sim 1.04$), conversely the LF of LTGs appears similar. This suggests that such steepening is due to a higher percentage of low mass early type objects in clusters: low mass LTGs are transformed more efficiently in such environments (Boselli et al., 2008, 2014). Recently, owing to the complete multifrequency data available for the Virgo cluster, Boselli et al. (2011, 2014) found evidences of environmental transformations in the UV luminosity function confirming the strong influence of clusters in shaping galaxy evolution and stressing once again its higher efficiency at low masses. In general low mass galaxies are expected to be more affected by the cluster environment because of their loose gravitational potential with respect to higher mass galaxies. Using the SDSS data, Peng et al. (2010) proposed that the environment plays a role almost exclusively at $M_* < 10^{9.5} M_\odot$ however recent observations (Yagi et al., 2010; Boselli et al., 2016; Yagi et al., 2017) challenge this statement and a comprehensive view on the dependence on stellar mass of

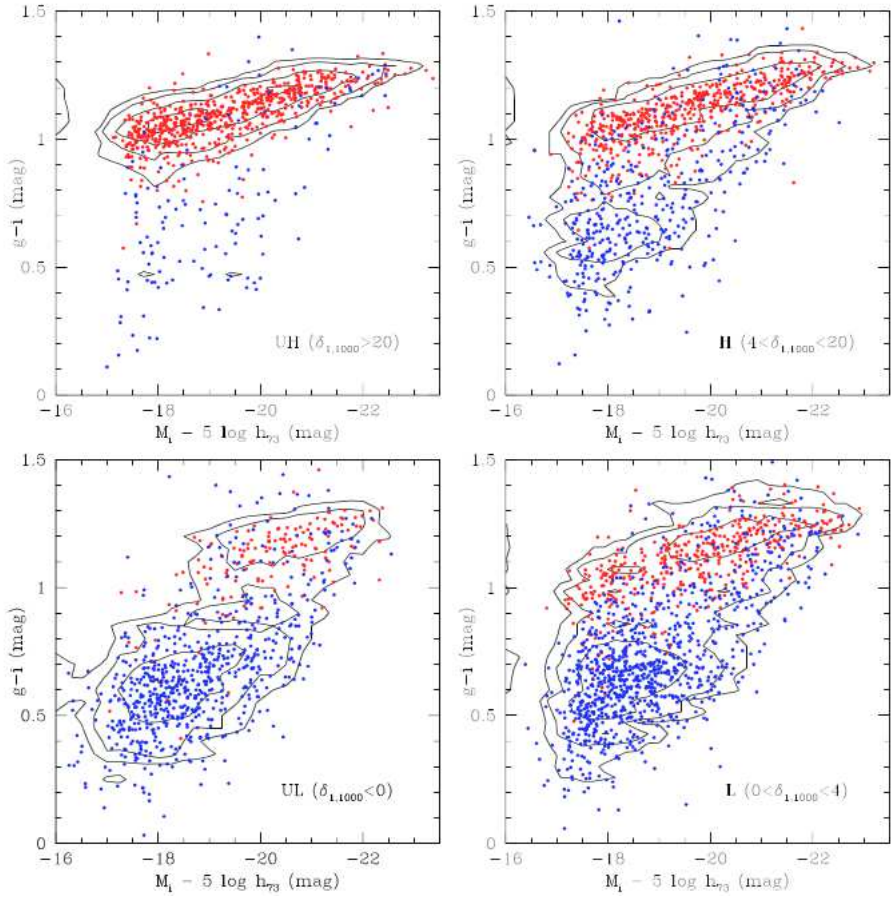

Figure 1.16: The color magnitude relation in four different bins of increasing projected density by Gavazzi et al. (2010). Blue dots represents LTGs while red dots are ETGs.

environmental processes has not been reached.

1.7 Environmental processes

From the observations emerges a scenario in which dense environments cause a migration of galaxies from star-forming to passive systems as testified by their morphologies, stellar populations, gaseous contents, and star formation rates. Many different processes driven by the interaction with other galaxies or with the ICM have been invoked to explain the observed transformations. These processes can be divided in two broad classes: tidal (i.e., merging and encounters between galaxies) and hydrodynamical (i.e., stripping phenomena) interactions. Nevertheless the exact interplay between such processes as a function of the galaxy properties and of local density is still poorly understood.

1.7.1 Tidal interactions

In high density environments tidal interactions between galaxy pairs can occur acting on all components of galaxies. In general, tidal interactions highly perturb the potential of galaxies modifying their morphologies. The degree of the perturbation depends on the ratio between the two interacting masses: when two massive galaxies of comparable mass merge produce evident stellar streams and tidal tails such as the one shown in Fig. 1.17 and eventually become an elliptical; in minor mergers, the more massive galaxy completely destroys the companion and possibly builds a classical bulge. However the efficiency of the transformation also depends on the relative distance between galaxies. Tidal forces act as M/R^3 and if the galaxy radii are not too small compared to the average separation between galaxies, tidal interactions can be efficient at removing matter from the galaxy (Boselli & Gavazzi, 2006). Nevertheless tidal interactions impact the SFR of galaxies only in their nuclei while in the disk it appears almost unaffected in both simulations and observations.
Despite the high density of objects in the core of clusters the efficiency of tidal interactions highly depends on the time of interaction. Therefore gravitational processes are less effective in the cluster environment where the relative velocities between galaxies reach thousands of $\mathrm{km\ s^{-1}}$ and only fast encounters

Figure 1.17: RGB image of the Antennae merging system.

can occur. On the contrary, in groups, the relative velocities between galaxies are low (few hundreds of $\mathrm{km\ s^{-1}}$) and allow for longer interactions that can significantly perturb galaxies.

It is also possible that galaxies interact with the tidal field of the cluster. Such interaction can induce an increase in nuclear activity but is not able to directly remove the gas from galaxies. However Moore et al. (1996) proposed that the combined effect of the tidal field of the cluster and of many high speed close (~ 50kpc)encounters between galaxies provides an efficient channel for transforming LTGs in ETGs in the cluster environment. This process, called "harassment", is particularly effective at low mass because of the shallower potential of these galaxies.

1.7.2 Hydrodynamical interactions

Hydrodynamical interactions do not perturb significantly the potential of the galaxies and leave the kinematics of stars unaltered. Nevertheless the gaseous component of galaxies is highly affected by the impact with the hot and dense ICM. As a matter of fact, the great amount of gas within the potential well

of the cluster can rapidly deplete the gas of a galaxy travelling at high speed through it. The wind caused by the relative motion between the galaxy and the ICM rips off the gas from the disk preventing future star formation. This is testified by many observations at different wavelengths of stripped gas in galaxies transiting clusters (see Fig. 1.18). As a matter of fact stripped tails of gas have been observed in HI (Chung et al., 2009), in Hα (Yagi et al., 2007, 2010; Fumagalli et al., 2011, 2014), and in the X-rays (Sun & Vikhlinin, 2005; Sun et al., 2007) in many galaxies at different redshifts.

In the last decades, hydrodynamical stripping processes are emerging as main drivers of the transformations occurring in dense environments and in particular in clusters. The most important process is ram-pressure stripping, first proposed by Gunn & Gott (1972): the gaseous component of a galaxy that travels at high speed within the ICM feels an external pressure that is proportional to the square of the relative velocity of the galaxy and to the local density of the ICM. In particular the pressure efficiently strip the gas if

$$P_{ram} = \rho_{ICM} v_{rel}^2 > 2\pi G \Sigma_{gas}(r) \Sigma_*(r), \tag{1.9}$$

where $\Sigma_{gas}(r)$ and $\Sigma_*(r)$ are the gas and stellar surface density of the galaxy within the radius r. Assuming typical ICM densities ($\approx 10^{-3} cm^{-3}$) and velocity dispersions ($1000 \mathrm{km\ s^{-1}}$) of clusters ram pressure is able to remove a considerable fraction of the ISM of galaxies on a timescale which is comparable to or less than their crossing time ($\approx 10^9$ yr). Simulations indicates that radial orbits are the most efficient because of their higher velocity and closer crossing to the cluster core (Abadi et al., 1999; Quilis et al., 2000; Tonnesen et al., 2007). Moreover, the efficiency of removal may depend on the geometry of the impact with the ICM with face-on impacts being more efficient.
In addition to ram pressure stripping, under certain circumstances, the stripping can be sustained also by other supplementary interactions such as turbulent viscous stripping proposed by Nulsen (1982): the ISM of a galaxy travelling in the ISM experiences a viscosity momentum transfer that can strip galaxies. The rate of the stripping depends on whether the motion of the gas is laminar or turbulent. The degree of turbulence is indicate by the Reynolds number defined as

$$R_e = 2.8 \left(\frac{r_{gal}}{\lambda_{IGM}} \right) \left(\frac{V_{gal}}{c_{IGM}} \right), \tag{1.10}$$

where c_{IGM} is the speed of sound in the ICM ($c_{IGM}=(k_B T_{IGM}/m_H)^{0.5}$) and λ_{IGM} (the mean free path of ions) is defined as

$$\lambda_{IGM}(kpc) = 11 \left(\frac{T_{IGM}}{10^8 K}\right)^2 \left(\frac{10^{-3} cm^{-3}}{\rho_{IGM}}\right). \quad (1.11)$$

If the mean free path of ions is lower than the radius of the galaxy so that classical viscosity can be applied and if $R_e \leq 30$ than the flux is laminar and the mass loss rate can be evaluated from

$$\dot{M}_{laminar} = \pi r_{gal}^2 \rho_{IGM} v_{gal} (12/R_e), \quad (1.12)$$

(Nulsen, 1982) where r_{gal} and v_{gal} are the radius and the velocity of the galaxy and ρ_{IGM} is the density of the IGM. On the other hand, if $R_e > 30$, the flux is turbulent and the mass loss rate is evaluated as

$$\dot{M}_{turbulent} = \pi r_{gal}^2 \rho_{IGM} v_{gal}. \quad (1.13)$$

From an observational point of view, the signatures of viscous stripping in the morphology of the gaseous component are very similar to the ones of ram pressure as well as its timescales ($\approx 10^7 - 10^8$ yr) thus it is difficult to disentangle the different contributions.

Despite the fact that stars are not affected by stripping processes, in the last years has emerged that the gas in the stripped tails can form stars possibly modifying the optical morphology of galaxies (see for example Fig. 1.18). Such possibility has been exploited to link the hydrodynamical interactions to a morphological category called Jelly-fish galaxies, i.e. galaxies with tentacles of stars emerging from their disks in a particular direction. They are typical of clusters and their optical morphologies are suggestive of the action of unilateral forces that may represent stripping phenomenon.

Another consequence of the the interaction between the galaxy and the ICM is starvation (Larson et al., 1980). As a matter of fact stripping phenomena remove the hot gaseous halo of gas from which galaxies receive their supply of gas from the cosmic web. As also shown by the simulations of Bekki et al. (2002) the gas in the halo of galaxies is almost completely removed within few Gyrs preventing further gas accretion and slowly quenching the star formation.

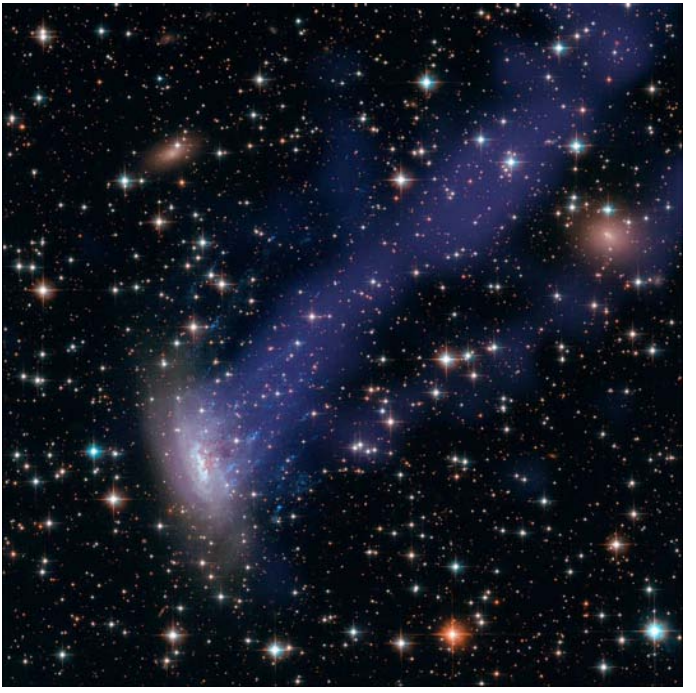

Figure 1.18: The Xray emission (in diffuse blue) superimposed to the optical RGB image of ESO 137-001 a galaxy under the action of ram pressure in the Norma cluster. Two evident Xray tails trails behind ESO 137-001 testifying the action of ram pressure on the gas of the galaxy. The optical image shows compact knots of young stars (associated to SF regions in the tails) distributed along tentacles emerging from the galaxy. ESO 137-001 is a posterchild of jellyfish galaxies.

Finally, as proposed first by Cowie & McKee (1977) thermal evaporation can also efficiently remove the gas from galaxies: when the temperature of the ICM is high compared to the galaxy velocity dispersion, at the interface between the ISM and the ICM the temperature rises steeply and the gas evaporates, escaping the gravitational field. However the real impact on the gaseous component and on the structural properties of cluster galaxies is very difficult to quantify.

Although these phenomena are typically observed in evolved clusters the environmental processes can start even before entering these structures. As

a matter of fact, clusters grow via the accretion of smaller groups. Because of the low relative velocities of group members tidal interactions can occur more easily within groups. At the same time, possible crossings and interaction between the gaseous haloes of group galaxies can trigger hydrodynamical interactions. The cumulative effect of gravitational and hydrodynamical interactions is called pre-processing and possibly strongly contribute to the build up of the passive, pressure supported systems population that is typically found in clusters.

1.7.3 A new golden-age

The direct observations of environmental interactions during the years has been often hampered by technological limitations. All multiwavelength studies based on the direct detection of environmental processes at play demand a high sensitivity as well as sufficient resolution. As a matter of fact, apart from striking merging events, shells and stellar streams triggered by mergers are tenuous features (see Duc et al., 2015) characterized by low surface brightness levels. Similarly also the diffuse gas stripped by hydrodynamical interactions is characterized by very low surface brightness (Boselli et al., 2016; Fossati et al., 2016).
The local Universe is obviously the best place to reach such sensitivities with the shortest integration time. However local galaxies have apparent sizes of several arcminutes, thus requiring large fields of view even just for mapping one object. Radio telescopes (such as Arecibo) or Xrays telescopes, that have large fields of view, suffer instead of a considerably lower spatial resolution compared to optical. Hence, for long years, the direct observations of the environmental interactions were limited to few targeted objects, preventing from a statistical analysis.

During this years we entered a new-era. In visible light, the large top-class telescopes now mount cameras with large FOVs ($\approx 1deg^2$) and are equipped with large interferometric filters. This have opened the possibility to map large portions of the sky at sufficient depth with reasonable integration times, thus enabling a statistical investigation. Indeed, using SuprimeCam mounted on the SUBARU telescope, Yagi et al. (2010), Yagi et al. (2017) could mapped the ionized gas emission of galaxies as traced by Hα in the Coma and Abell-1367 clusters with unprecedented spatial resolution and sensitivity. They un-

veiled that stripping phenomena are ubiquitous in cluster as a large fraction of LTGs (more than 40%) are observed loosing their ionized gas because of their hydrodynamical interaction with the ICM of these clusters. These galaxies show spectacular tails trailing in the opposite direction of the galaxy motion within the cluster.

More recently, Boselli et al. 2016, using the MegaCam mounted on the CFHT telescope, targeted with deep Hα observations a massive spiral in the Virgo cluster (NGC 4569) and unveiled a spectacular, 75 kpc long tail trailing behind the galaxy. These observations are particularly interesting because vividly show that ram pressure stripping may be very effective even in massive galaxies and in a still evolving intermediate mass cluster such as Virgo, suggesting an extremely high frequency of the phenomenon. In particular, such project has inspired an upcoming Hα survey (VESTIGE) of the Virgo cluster that will provide the first complete census of hydrodynamical interactions in a cluster up to its virial radius with such sensitivities.

However such "new era" is not limited to the possibility to perform statistical analysis on the environmental phenomena but is now giving us the chance to unveil the small physics that regulates those processes. As a matter of fact the advent of IFUs is taking to a whole new level the study of environment. As vividly shown by the recent studies of Fumagalli et al. 2014, Fossati et al. 2015, and Merluzzi et al. 2016, IFUs are able to recover with high spatial resolution the dynamics of both gas and stars and to provide all the spectroscopic information to fix the physical state of the ISM or of the stellar component. In the upcoming months/years many IFU follow-ups (already scheduled) of galaxies interacting in high density regions will put together sufficient statistic to highlight characteristic trends in the physical state of interacting systems.

1.8 Evolution

Observations consistently suggest an evolutionary path that takes galaxies from being gas-rich, star forming and blue to passively evolving, red, anemic systems. However such path is still poorly understood in the light of the modern cosmological picture settled by the ΛCDM paradigm (Peebles, 1982). It consists in a cosmology where the Universe is dominated by a dark energy component ($\approx 73\%$) driving the acceleration of the Universe (Carroll et al., 2004) while the remaining components are constituted by dark and baryonic

matter. The dark matter dominates the amount of matter of the Universe and baryonic matter moves driven by the dark matter potential. The small fluctuation present in the early homogeneous Universe grow and form the dark matter haloes in a bottom up scenario: smaller haloes form first and then merge forming bigger structures. These growing dark matter haloes form a potential well into which baryons fall and galaxies are forged in the core of such haloes where the gas cools and forms new stars.
During a protracted period of quiescent evolution after the initial collapse or subsequent mergers, gas and stars settle into a thin disk. In this period, the galaxy resembles its content following internal processes such as slow gas accretion, formation of bars and spiral instabilities. While actively forming stars, the young, massive stellar population of galaxies strongly contribute to the optical emission inferring a bluish color to the system. Once that a galaxy has stopped its star formation (SF) the old stellar population dominates its emission shifting it to redder colors. Apart from internal processes related to the dynamic of the galaxy (disk instabilities), galaxies host some of the most energetic astrophysical processes known, such as accretion on a supermassive black hole and supernovae explosions. These processes are thought to be responsible of the so-called black hole and supernova $feedback$, respectively. As a matter of fact, the large energy released by these processes can be transferred to the ISM, heating it and preventing its collapse (thus the SF) or even expelling it from the galaxy. These mechanisms were/are thought to be fundamental to reconcile the observations of the luminosity function with the one expected from the ΛCDM Universe. Modern cosmological simulations put in great relevance those effects that, however, have not been well constrained by observations despite the great effort of the last decades. Hence in this thesis, we concentrate the attention on other mechanisms responsible for major transformations in the evolution of a galaxy and discuss their relative relevance.

Following the potential of dark matter, galaxies gravitationally bind with other systems forming groups and clusters of galaxies. In high density regions, the deep gravitational potential allows to retain an elevated quantity of diffuse, hot gas, that we detect in the Xrays. As galaxies approach these regions of high density, environmental processes (ram pressure, harassment, encounters etc.) start to sum up to the internal ones heavily contributing to the consumption and ablation of the gaseous component, thus strongly contributing to the quenching

of their SF. Moreover, as large structure are thought to grow hierarchically via the accretion of smaller groups, the transition from the blue cloud to the red sequence may even begin outside the clusters inside compact groups.
Therefore galaxy evolution is regulated by a complex interplay between two broad classes of processes able to remove (or rapidly consume) their reservoir of gas quenching their SF activity: internal processes driven by the genetic (i.e., its mass) of the galaxy; and external processes that are driven by the environment in which the galaxy is embedded.

1.8.1 This work

This thesis aims at shading light on both internal and external processes in galaxies of the local Universe, where we can benefit from the best sensitivity and resolution given by the short distance. In particular, among internal processes, I have focused my research on a multiwavelength analysis of the impact that bars have on the star formation of disk galaxies. To this aim I have analyzed three different samples briefly describe in Chap. 2. The analysis can be divided in three steps:
i), from Hα observations taken during this work, In Chap. 3 will derive a refined SFR vs M$_*$ relation at $z = 0$ for local star forming galaxies and show that barred galaxies have their SFR suppressed in their central regions with respect to normal galaxies. This is interpreted within a single evolutionary scenario in which bars heavily contribute to the quenching of the star formation.
ii) I will further prove this point in Chap. 4, showing the influence on bar on the cold gas component as traced in FIR by the cold dust observed by the *Herschel* space telescope.
iii) In Chap. 5 and 6 I will gather evidences of such scenario in the optical imaging data of the SDSS of a much wider sample of thousands of galaxies in the Local and Coma superclusters. This part takes advantage of the algorithms and codes described in Appendix A.
In Chap 7, I will report the analysis of spectacular IFUs (taken with the MUSE IFU mounted on VLT-UT4) observations mosaicking UGC-6697, a massive spiral galaxy under the action of ram pressure during its transit in the nearby cluster Abell-1367. Finally results are summarized in the final chapter.

Chapter 2

Samples

The works presented in this thesis are based on three different sample of galaxies belonging to the local Universe that broadly overlap. In the first section I will describe the selection criteria for the SDSS sample that I will exploit to generate high-quality photometry from SDSS imaging in two filters (g and i) with an IDL-based (Interactive Data Language) procedure and study the color of galaxies in the local Universe. In a second section, I will describe the sample of the Hα3 survey from which I will derive a refined star formation versus M_* relation for the local Universe. Finally, I will briefly describe the Herschel Reference Sample from which we will check the FIR properties of barred galaxies.

2.1 The SDSS sample

A large part of this work is based on a sample of 6136 nearby galaxies in the spring sky selected from the SDSS as described in this section. The final sample is further split in two subsamples: i) the Local Supercluster ($11^h < RA < 16^h$; $0^o < Dec < 18^o$; $cz < 3000\,\mathrm{km\,sec^{-1}}$) containing 1112 galaxies and includes the Virgo cluster; ii) the Coma Supercluster ($10^h < RA < 16^h$; $18^o < Dec < 32^o$; $4000 < cz < 9500\,\mathrm{km\,sec^{-1}}$) containing 5024 galaxies and includes the Coma cluster. The two subsamples are displayed in Figure 2.1.

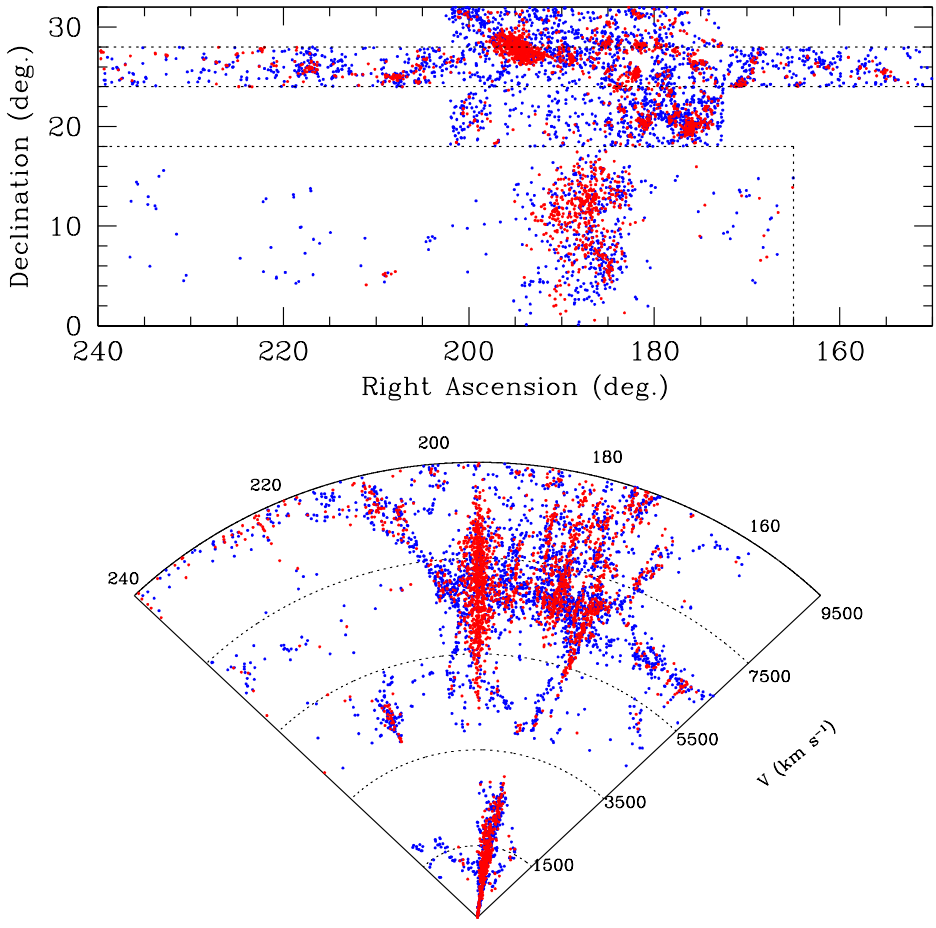

Figure 2.1: Sky projection (top) and Wedge diagram (bottom) of galaxies belonging to the sample studied in this work: the Coma supercluster ($\delta > 18^o$; $cz > 4000$ km s^{-1}) and the Local supercluster ($\delta < 18^o$; $cz < 3000$ km s^{-1}). Blue dots represent late type Galaxies (LTGs) while red dots stand for early type galaxies (ETGs). The dotted rectangular regions indicate the areas surveyed by ALFALFA.

Since galaxies at the distance of Virgo have apparent size often exceeding 5 arcmin, they are strongly affected by the shredding problem (Blanton et al. 2005) therefore our catalog cannot solely rely on the SDSS spectroscopic database. Thus, the Local supercluster sample is selected following the prescriptions of Gavazzi et al. (2012): in the area occupied by the Virgo cluster,the selection is based on the VCC catalog (limited however to $cz < 3000$ km sec^{-1}) down to its magnitude completeness limit of 18 mag (Binggeli et al., 1985). The object selection is furthermore limited to objects with surface brightness above the 1σ of the mean sky surface brightness in $i-$ band of the SDSS data (see Fig. 2.2). Outside the Virgo cluster the SDSS selection is complemented with objects taken from NED and ALFALFA (Haynes et al., 2011).

At the distance of the Coma supercluster the shredding problem is less severe and therefore we followed the selection of Gavazzi et al. (2010, 2013b). Briefly, galaxies are selected from the SDSS spectroscopic database DR7 (Abazajian et al., 2009) with $r < 17.77$ mag. To fill the residual incompleteness of the SDSS catalog for extended galaxies and due to fiber conflict, 133 galaxies from the CGCG catalog (Zwicky et al., 1968) with known redshifts from NED and 28 from ALFALFA are added, reaching a total of 5024 galaxies.

For these galaxies, I downloaded the SDSS images (using the on-line Mosaic service) in the $g-$ and $i-$band. In this work, I test the procedure exclusively on these two bands for mainly two reason: i) The u and z filters have lower signal-to-noise ratio (SN), ii) if compared to the $i-$band, the r filter have a central wavelength closer to the g filter central wavelength. Hence the g-i color is more sensitive to stellar population gradients and dust absorption. However only for 5753 (94%) targets the download process worked in both the $i-$ and the $g-$band [1]. Of these, 221 galaxies were discarded a posteriori because they lie too close to bright stars or they have too low surface brightness (see Fig. 2.2). The remaining analyzed sample is constituted of 969 (Local SC) + 4563 (Coma SC) objects, for a total of 5532 galaxies that can be considered representative of the nearby universe. Their morphological classification and diameters are taken from the public database GOLDMine

[1] the procedure is able to process all the SDSS bands images at the same time. Nevertheless, in this paper we present the analysis of only the $g-$ and $i-$band images. Obviously adding more bands affects the SN of the white image and therefore the detection performed by Source Extractor

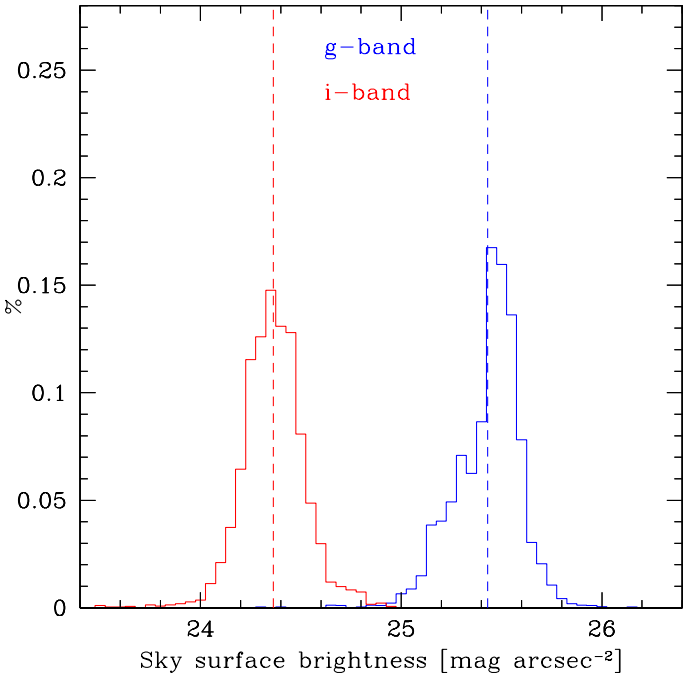

Figure 2.2: Sky surface brightness distributions in $g-$ (blue line) and $i-$ band (red line) for the sample analyzed in this work. The vertical dashed lines indicate the mean surface brightness in $g-$ and $i-$ band respectively $< \Sigma_i >= 24.36 \pm 0.16$ and $< \Sigma_g >= 25.43 \pm 0.17$ mag arcsec^{-2}.

(Gavazzi et al., 2003, 2014b).

Summarizing, the sample analyzed in this work coincides with the one presented by Gavazzi et al. (2013b, with the selection criteria given in Gavazzi et al. 2010, Coma supercluster) and Gavazzi et al 2012 (Local supercluster) except for 108 VCC galaxies that were excluded because their surface brightness (evaluated inside the radius at the 25^{th} B-band isophote reported in GOLDMine) is lower than the mean sky surface brightness in $i-$ band (Fig. 2.2). For the remaining 5532 galaxies the procedure developed in this thesis is aimed at obtaining more accurate photometry than reported in Gavazzi et al. (2012, 2013b).

2.2 The Hα3 sample

The Hα3 sample of local star forming galaxies is drawn from the wide catalog of source of the ALFALFA survey, not yet completed. In 2011, Haynes et al. (2011) released a comprehensive catalog containing 40% of the eventual final coverage of the survey. The surveyed area goes from R.A. 10^h to 16^h and declination from 24^o to 28^o and from 11^h to 16^h and 3^o to 18^o is shown in Fig. 2.1. The catalog covers the local supercluster including the Virgo cluster and a long strip of the Coma supercluster, including the Coma cluster.
The aim of the Hα3 survey was to follow-up with Hα imaging observations the ALFALFA sources in the region of the sky in the redshift interval $0<\mathrm{c}z<9000\ \mathrm{km\ s^{-1}}$. Observations were taken at the observatory of the Universidad Autonoma de Mexico (UNAM) at San Pedro Martir, Ensenada (Mexico), equipped with a set of interferometric filters of width $\sim 100\mathring{A}$, centered at different wavelengths. For each exposure, the continuum is evaluated with an R_{gunn} filter. Targets were selected from the ALFALFA catalog according to their signal-to-noise (S/N>6.5) as well as good match between the survey's two independent passes (Giovanelli et al., 2005). Moreover the selection is limited to objects with HI line flux densities $F_{HI} > 0,7\ \mathrm{Jy\ km\ s^{-1}}$. Such selection implies that at the distance of the Virgo cluster the limiting mass is $M_{HI} = 10^{7.7}\mathrm{M}_\odot$ while, at the distance of Coma, the limiting HI mass is $\approx 10^9\mathrm{M}_\odot$.
Hα3 was completed in 2014 (Gavazzi et al., 2014) and the continumm subtracted Hα fluxes of 1091 sources are published in Gavazzi et al. (2014). Data can be accessed via the website GOLDMine (Gavazzi et al., 2003).

2.3 The Herschel Reference Survey sample.

The *Herschel* Reference Sample consists in a statistically complete sample of 323 galaxies observed with the space-based observatory *Herschel*. The sample spans the region of the sky between 10^h17^m <R.A< 14^h43^m and -6 <dec< 60 and comprehend 65 ETGs and 258 LTGs spanning a stellar mass range $10^8 \lesssim \mathrm{M}_* \lesssim 10^{11}\ \mathrm{M}_\odot$.

Galaxies were selected according to three different criteria as reported in (Boselli et al., 2010). First, a volume limit is imposed. This is done by selecting all galaxies with recessional velocities of $1050\ \mathrm{km\,sec^{-1}}$ and $1750\ \mathrm{km\,sec^{-1}}$

that corresponds to a distance range of $15 \leq D \leq 25$ Mpc (with $H0 = 70\,\mathrm{km\,sec^{-1}\,Mpc}$). In such volume lies the Virgo cluster where peculiar velocities overcome the recessional velocities. Therefore in this region, the selection is different and embraces all galaxies with vel$< 3000\ \mathrm{km\ sec^{-1}}$ and belonging to the subgroups of the Virgo cluster with known distance lower than 25 Mpc (Gavazzi et al., 1999). Second, a 2MASS K-band magnitude limit is applied. The adopted limit is different between LTGs and ETGs: late type spirals are selected if K≤ 12 while, as passive galaxies are expected to be dust–poor and therefore hardly detected, Boselli et al. (2010) apply a more stringent limit of K≤ 8.7 for ETGs. Finally, to minimize the contamination from Galactic cirrus galaxies are selected at high galactic latitudes ($b > 5$). The selected galaxies are in good agreement with the global K-band luminosity function and can be thought as representative of the local Universe (Boselli et al., 2010).

The 22 μm from WISE and 100-500 μm from PACS and SPIRE images are available (Ciesla et al., 2014; Cortese et al., 2014) for the whole sample. All galaxies have been covered by the SDSS in its five (u,g,r,i,z) optical bands and have been followed-up with narrow-band Hα imaging observations (Boselli et al., 2015). All continuum-subtracted Hα images, as well as the FIR and optical images can be accessed and downloaded from the online database HeDaM (http://hedam.lam.fr/).

Chapter 3

Bar-quenching

This chapter reports the results obtained during this work of thesis and published in Gavazzi, G., **Consolandi, G.**, Dotti, M., et al. 2015, A&A, 580, A116. In a first section, we derive the star formation versus M_* relation for the local Universe owing to the Hα fluxes of the Hα3 survey sample (see Chap. 2.2). By comparing the present results with literature data at higher redshift, we reconstruct the star formation history of main sequence galaxies. The observed trends are then discussed in the light of a scenario in which bars drive the quenching of the inner regions of massive star forming galaxies.

3.1 Star formation rate at z=0

The sample of star-forming galaxies at z=0 used in this work consists of 1399 galaxies HI-selected primarily from ALFALFA (Haynes et al. 2011) in the regions of the Local Supercluster and in the Coma Supercluster. These are complemented with pointed HI observations of late-type galaxies taken at similar sensitivity in the region of the Coma supercluster not covered by ALFALFA (as listed in the GOLDMine database of Gavazzi et al. 2003, 2014). Gavazzi et al. (2008, 2013a) showed that ALFALFA selected galaxies are genuine star-forming objects (late-type galaxies, LTGs) with almost no contamination from S0s and S0as (see also Buat et al. 2014 for a discussion on the selection criteria of star-forming galaxies). Among these, 1091 were followed up with

Hα imaging observations to derive their global star formation rates (SFRs; Gavazzi et al 2015, Paper V). The Hα luminosity was corrected for Galactic extinction, deblending from [NII], and internal extinction following Lee et al. (2009).

In the Hα3 survey, stellar masses M_* and SFRs have been computed assuming a Salpeter Initial Mass Function (IMF), following the calibrations of Kennicutt (1998, see eq. 1.5). In this section, the results from our survey are compared with literature values. Therefore both stellar masses and SFR are recomputed assuming a Chabrier IMF, as commonly done in the modern literature. Specifically, the transformations applied to the Hα3 survey are $\mathrm{SFR_{Chabrier}} = 1.5 \times \mathrm{SFR_{Salpeter}}$ and $\log(M_*/\mathrm{M_\odot}) = -0.963 + 1.032\ (g - i) + \log(L_i/\mathrm{L_\odot})$, following Zibetti et al. (2009).

The Hα3 survey also includes galaxies in proximity and inside the rich Coma and Virgo clusters. The present study focuses on unperturbed galaxies, which we select to avoid environmental quenching effects (see Gavazzi et al. 2013b). To this purpose, we do not include in our analysis galaxies with HI-deficiency parameters (see eq. 1.4) greater than 0.3.

In addition to the cut based on HI deficiency, we wish to remove any possible residual environmental effects, such as sSFR quenching in high-density environments (e.g., Poggianti at al. 1999; Lewis et al. 2002; Balogh et al. 2004; Patel et al. 2009; Boselli & Gavazzi 2006, 2014). Following Gavazzi et al. (2010) I measured around all galaxies (in the Local and Coma superclusters irrespective of their type and HI content) a density contrast $\delta_{1,1000}$, computed as equation 1.8, and repeated the analysis shown in Figure 3.1 by including only galaxies with $\delta_{1,1000} < 20$, thus avoiding the cores of the rich clusters Virgo, A1367 and Coma. Except for a marginal decrease in the number of objects below $M_* = 10^{8.5}\ \mathrm{M_\odot}$, no differences are seen at high mass that could explain the observed decrease of the sSFR as being due to environmental mechanisms.

With this selection, and combining two local samples in the Local and Coma superclusters, the final sample obtained is composed by 864 galaxies. The derived star formation rates are plotted in Figure 3.1(a) and listed in Table 7.1 as a function of stellar mass.

The flux limit of ALFALFA translates into a selection effect in the HI mass, which depends on galaxy inclination (see Giovanelli et al. 2005). At the distance of Virgo, this limit is $\log(M_{\mathrm{HI}}/\mathrm{M_\odot}) = 7.25 - 7.54$, computed

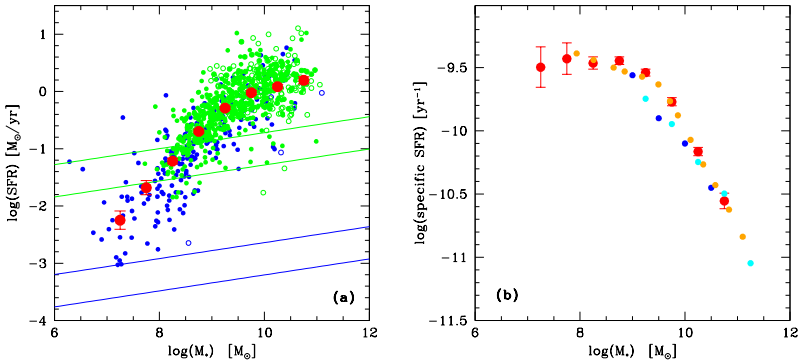

Figure 3.1: (Panel a) The star formation rate as a function of stellar mass at z=0 for HI non-deficient galaxies. Green symbols represent galaxies in the Coma supercluster; blue symbols are in the Local Supercluster. Red symbols are averages in bins of stellar mass. The derived star formation rate are computed from the Hα luminosity assuming a Chabrier IMF. The two green (blue) diagonal lines represent the selection bias on the SFR induced by the limited sensitivity of ALFALFA at the distance of Coma (Virgo), computed for galaxies with inclination of 10 and 45 degrees respectively. (Panel b): the specific star formation rate as a function of stellar mass at z=0. Average values from our local sample (Coma+Virgo) are given with red dots with error bars. Orange points are from Huang et al. (2012) and cyan points are from Brinchmann et al. (2004) (SDSS at z=0). The blue points are taken in the interval $0.05 < z < 0.08$ from Bauer et al. (2013). All sets of points show remarkable consistency above $10^{9.5}$ M$_\odot$.

for inclinations of 10 and 45 degrees, respectively. As discussed in Gavazzi et al. (2015), this selection threshold does not hamper the detection of normal gas-rich galaxies with typical stellar masses as low as 10^7M$_\odot$. This sensitivity limit is, however, 25 times worse at the distance of Coma, being $\log(M_{\rm HI}/{\rm M}_\odot) = 8.78 - 9.08$. Owing to this shallower selection, only an incomplete set of LTG galaxies at the distance of Coma are detected by ALFALFA and have been followed up by Hα3. The galaxies included in this study are therefore the most HI-rich objects, which means that the corresponding star formation rates are generally biased towards high values. The two diagonal lines in Figure 3.1(a) show this selection effect for Coma and for Virgo. Because of this bias, the slope of the SFR versus mass relation is significantly flatter for Coma than for the Local supercluster. Conversely,

one can note how this latter subsample is not hampered by the ALFALFA selection bias, but it suffers instead from an undersampling at the highest mass bin, owing to a lack of surveyed volume. However, the two subsamples are complementary, and the underlying SFR versus mass relation can be obtained by combining them together. The mean SFRs in bins of stellar mass for this combined sample is shown in Figure 3.1(a). Here, we also show that the star formation rate of star-forming galaxies (main-sequence galaxies) in the local Universe is inconsistent with a single power law (a slope of nearly unity), but shows a decreasing slope with increasing mass.

Figure 3.1(b) shows the specific star formation rate derived from the present data. Another set of local HI-selected galaxies in the entire ALFALFA survey by Huang et al. (2012) is shown. Although it is derived with a different SFR indicator based on UV luminosity corrected for IR, this second sample is remarkably consistent with our data. Additionally, Figure 3.1(b) shows a third sample of star-forming galaxies from Brinchmann et al. (2004), derived in the local Universe using SDSS data corrected for aperture effects. Finally the set of local data (obtained at $0.05 < z < 0.08$) from the GAMA survey by Bauer et al. (2013) is shown. Despite the different selections and indicators, all local determinations are in reasonable mutual agreement. Although not shown in Figure 3.1(b), we note that the SFR versus stellar mass relation derived by Peng et al. (2010) using SDSS data is inconsistent with that found in other local samples, mainly because it does not show a change of slope above some turnover mass. This is possibly due to the choice of Peng et al. (2010) to restrict their star-forming sample to galaxies showing strong emission lines in the nuclear spectra, thus biasing the selection towards starbursting objects. Similar inconsistency with Peng et al. (2010) is reported in Bauer et al. (2013) in their determination of the local SFR from the GAMA survey.

3.2 The star formation rate as a function of redshift

In this section the analysis to the star formation rate is pushed from z=0 up to $z \sim 4$. Figure 3.2 gives the SFR as a function of stellar mass in bins of increasing z. The local data from this work (red) are taken from Figure 3.1. Data at z=0.3 are from the GAMA survey by Bauer et al. (2013). Data in the 0.75, 1.25, 1.75, 2.25 redshift bins are from Whitaker et al. (2014), who selected star-forming galaxies using the UVJ diagram (Williams et al. 2009).

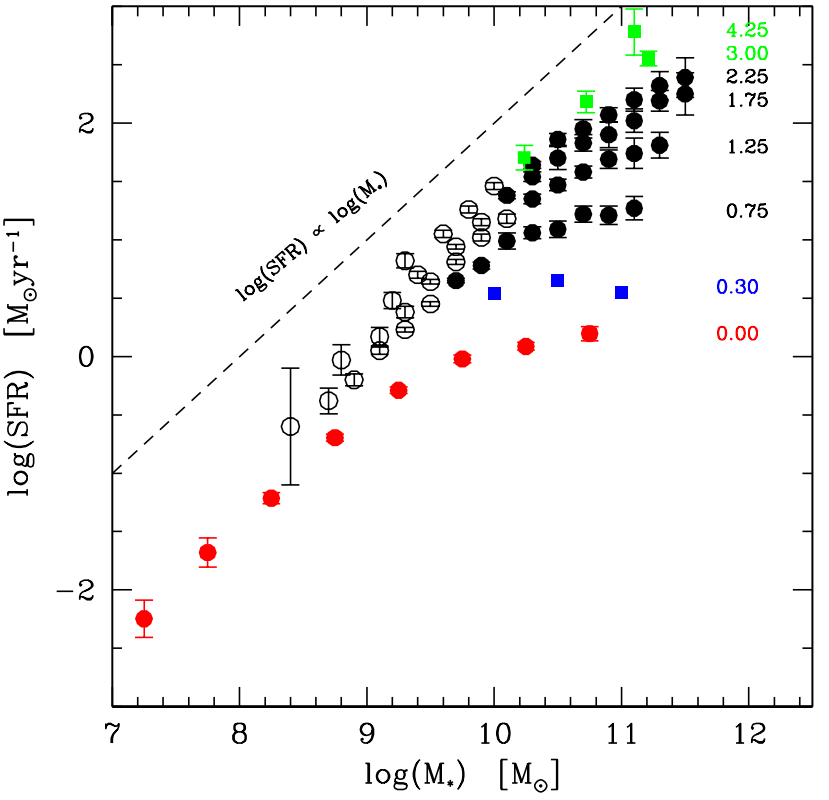

Figure 3.2: The star formation rate as a function of stellar mass in bins of redshift. Data at z=0 (red) are from this work (red symbols in Figure 3.1). Data at z=0.3 (blue) are from Bauer et al. (2013). Measurements in the interval $0.75 < z < 2.25$ (black) are from Whitaker et al. (2104) (empty circles are for mass bins where individual galaxies were stacked when deriving IR luminosities); the points at z=3 and z=4.25 (green) are from Schreiber et al. (2015). Whitaker et al. (2014) and Schreiber et al. (2015) data are plotted above their respective completeness limit.

Table 3.1: Star formation sequence at z=0. The associated uncertainties are Poissonian.

log M_* bin $M_\odot$	logSFR $M_\odot$ yr^{-1}	Error $M_\odot$ yr^{-1}
7.0 - 7.5	-2.247	0.159
7.5 - 8.0	-1.680	0.124
8.0 - 8.5	-1.214	0.047
8.5 - 9.0	-0.696	0.030
9.0 - 9.5	-0.290	0.027
9.5 - 10.0	-0.021	0.032
10.0 - 10.5	0.086	0.032
10.5 - 11.0	0.196	0.061

Their SFR are derived combining UV and IR luminosities from the deep CANDELS+3DHST surveys (Skelton et al. 2014) to account for obscured and unobscured star formation. This is currently among the best indicators of star formation at high-z (Wuyts et al. 2011). At even higher redshift (z=3 and z=4.25) we show the recent measurements by Schreiber et al. (2015), who adopt the same SFR indicator computed using FIR Herschel calibrated SFRs complemented by the UV luminosity from SED fitting. A line of proportionality between SFR and mass (exponential stellar mass growth) is given to guide the eye.

Figure 3.3 is derived from Figure 3.2 after computing the sSFR at each redshift. This figure highlights that in most redshift bins (except for z=2.25) the specific star formation rate is constant up to a characteristic stellar mass ($M_{\rm knee}$), beyond which it decreases steeply with increasing stellar mass (Kauffmann et al. 2003). In other words main-sequence star-forming galaxies above $M_{\rm knee}$ have their sSFR suppressed compared to the lower mass systems. Still, they remain classified as UVJ active galaxies, i.e., they are only partially quenched, and should not be confused with a passive population.

Similarly to the analysis by Whitaker et al. (2014), we fit to the sSFR versus mass relation a broken power law of the form

$$\log \mathrm{sSFR} = a[\log(M_*/M_\odot) - \log(M_{\rm knee}/M_\odot)] + b, \qquad (3.1)$$

where $a = a_{\rm low}$ for $M_* < M_{\rm knee}$ and $a = a_{\rm high}$ for $M_* \geq M_{\rm knee}$. In

Table 3.2: Parameters of the fit for the function $\log \mathrm{sSFR} = a(\log M_* - \log M_{\mathrm{knee}}) + b$

$< z >$	$\log M_{\mathrm{knee}}$	a_{low}	a_{high}	b
0.0	9.45 ± 0.08	-0.08 ± 0.04	-0.80 ± 0.06	-9.54 ± 0.10
0.75	10.06 ± 0.08	-0.02 ± 0.04	-0.71 ± 0.09	-9.07 ± 0.11
1.25	10.23 ± 0.11	-0.03 ± 0.05	-0.50 ± 0.09	-8.91 ± 0.14
1.75	10.40 ± 0.21	-0.03 ± 0.04	-0.43 ± 0.13	-8.75 ± 0.28
2.25	10.55 ± 0.18	-0.15 ± 0.04	-0.45 ± 0.10	-8.66 ± 0.24
3.00	10.75 ± 0.20	-0.02 ± 0.14	-0.25 ± 0.13	-8.54 ± 0.26

this equation, b represents the sSFR at $\mathrm{M_{knee}}$. During the fit a, b, and M_{knee} are kept as free parameters, and the best-fit value is given in Table 7.2. The resulting functions, which are plotted in Figure 3.3(a), are found to be consistent with the results of Whitaker et al. (2014), even though we have kept M_{knee} as a free parameter. Our approach allows for the study of the dependence of M_{knee} on redshift, which is found to be consistent with a scaling-relation $M_{\mathrm{knee}} \propto (1+z)^2$ as is shown in Figure 3.3(b)[1]. This implies that any quenching mechanism at work within the main sequence becomes effective above some mass threshold, which decreases by more than a factor of 10 from z=3 to the present. It is worth stressing that, by construction, this analysis is insensitive to quenching mechanisms that would remove galaxies from the star-forming sequence altogether, while it is sensitive to those mechanisms that perturb only in part the SFRs of main-sequence galaxies. Figure 3.3(c) shows how the sSFR evaluated at M_{knee} scales with redshift, implying that the typical sSFR of the main sequence depends on z at the 1.65^{th} power. In turn, this implies a decrease by more than one order of magnitude of the mean sSFR from z=4 to z=0 for normal (unquenched) galaxies. Figure 3.3(d) shows the dependence on redshift of the slope of the sSFR versus mass relation below (a_{low}) and above (a_{high}) M_{knee}. The parameter a_{low} is independent of redshift, while a_{high} increases as $(1+z)^{0.88}$: i.e., the main sequence of unquenched galaxies exists at all redshifts, but the effects of quenching are less severe with increasing redshift. This is in agreement with the findings of Whitaker et al. (2014).

[1] An independent study (Lee et al. 2015) has recently been found that shows a similar trend

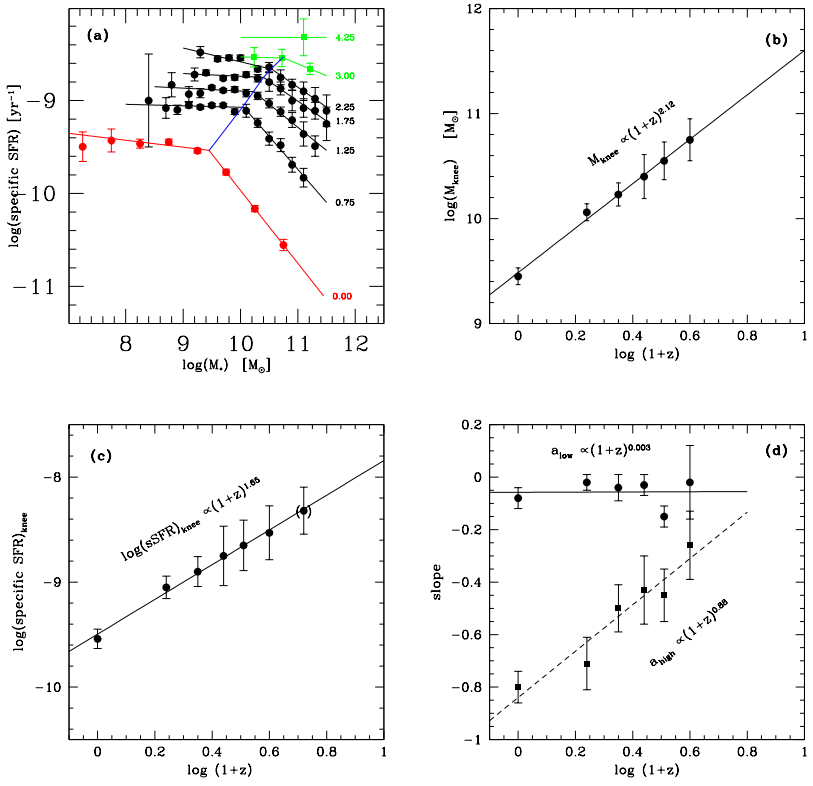

Figure 3.3: (panel a): the specific star formation rate as a function of stellar mass in bins of redshift. For all redshift bins the data are fitted with a broken power law with slope $a_{\rm low}$, holding below a critical mass ($M_{\rm knee}$), and $a_{\rm high}$ holding above $M_{\rm knee}$ (see Table 7.2). The blue line connects the loci of $M_{\rm knee}$ for the various redshifts. (panel b): the position of the $M_{\rm knee}$ as a function of log(1+z). (panel c): the specific star formation at $M_{\rm knee}$. (panel d): the slope below and above $M_{\rm knee}$ ($a_{\rm low}$ and $a_{\rm high}$). The position of $M_{\rm knee}$ and the specific star formation rate at $M_{\rm knee}$ increase approximately as $(1+z)^2$, while the mass quenching (given by $a_{\rm high}$) becomes less efficient with increasing redshift.

3.3 Strong bars and bulges as a function of M_*

The previous section shows that galaxies above a redshift-dependent mass threshold are progressively more quenched. It is necessary to study in greater depth what physical mechanism might have caused such an effect.

The first step is to take a closer look at the morphology of the studied galaxies below and above $M_{\rm knee}$, starting from the local sample. As discussed in the literature, it is quite challenging to produce a reliable morphological classification that distinguises disks from bulges and, possibly, classical from pseudo-type bulges (Wilman et al. 2013). The task is even harder as recent evidence indicates that the two bulge categories can even occur simultaneously (Erwin et al. 2015).

With these caveats in mind, we focused on the detection of "strong bars" (see Section 1.5.2). We instead refrain from classifying "weak" and even "intermediate" bars as "bars", because we expect that they produce only minor perturbations to the disk, making them difficult to recognize. The criteria used to visually identify strong bars include that the bar ellipticity must be larger than ~ 0.4, but we did not impose any constraint on the galaxy maximum inclination. Of course bars are easier to detect in face-on systems, although the presence of X-shaped, boxy, or peanut shaped bulges (Laurikainen et al., 2010) helps detect bars even in highly inclined objects. Secondary features such as rings near corotation, ansae, dust lanes, and ILR (mostly too small to be detected on SDSS images) are not mandatory features, but of course - if present - they help in identifying bars.

The visual classification of strong bars was performed by seven authors[2] who individually inspected and classified all 864 galaxies in our sample.

The classification was based on i-band SDSS images, not to be biased by the sSFR versus color relation, nor by dust attenuation effects. Following a template, the classifiers were called to distinguish i) barred, ii) unbarred galaxies hosting a bulge, and iii) disks without a bar or a bulge. Among class ii) we do not try to disentangle pseudobulges from classical bulges.

Despite the aforementioned difficulties, the robustness of the resulting classification is satisfactory overall: among the galaxies identified as hosts of a strong bar, agreement between more than four classifiers was reached in

[2] Giuseppe Gavazzi, Guido Consolandi, Massimo Dotti, Rossella Fanali, Matteo Fossati, Michele Fumagalli, Giulia Savorgnan.

92% of the cases; the level of agreement drops to 77% for bulges and to 85% for disks without bars or bulges. These percentages suggest that the main difficulty lies in the identification of bulges, reflecting the ambiguity in detecting the presence of bulges in face-on or poorly resolved disk galaxies when the color information is disregarded (see also Drory & Fisher 2007).

The result of this morphology classification is shown in Figure 3.4, which presents again the SFR versus stellar mass relation that is now color coded according to the morphological classification. The value of $M_{\rm knee}$ is indicated by the vertical dashed line. Histograms are also provided to highlight the relative frequency of each class in bins of mass and SFR.

Below $M_* = 10^{9.45}$ M$_\odot$, i.e., $M_{\rm knee}$ at z=0, the frequency of disks without bulge or bar, barred disks, and unbarred disks with a bulge is 87%, 8%, and 5% respectively. Above $M_* = 10^{9.45}$ M$_\odot$, instead, these frequencies become 28%, 27%, and 45%. The analysis reveals that the vast majority of low-mass galaxies are disks without bulge or bar, while more than half of the high-mass galaxies host either a bulge or a strong bar.

The top right panel shows the occupation fraction of visually classified strong bars of the whole sample as a function of stellar mass. This is in agreement with previous studies highlighting that the likelihood of having a bar in disk galaxies increases with increasing stellar mass. Skibba et al. (2011), Wang et al. (2012), and Masters et al. (2012) consistently find that the strong-bar fraction increases from 10% to 40% with increasing stellar mass from $M_* = 10^9$ to $M_* = 10^{11}$ M$_\odot$. Consistent conclusions are indirectly reached by Marinova et al. (2009) (who study the dependence on V luminosity). Moreover, focusing on the nearby Virgo cluster and using the early bar classifications by de Vaucouleurs et al. (1991, RC3) and by Binggeli et al. (1985) from high-quality photographic plates, in the Local and Coma superclusters the fraction of barred galaxies is lower than 20% below $M_* = 10^{9.5}$ M$_\odot$ and rises to 30-40% at high masses. Again, this is consistent with all results listed above.

On the other hand, two other results contradict this trend. Barazza et al (2008) and Nair & Abraham (2010) found bar fractions on the order of 30-40% above $M_* = 10^{10}$ M$_\odot$, consistently with all cited works, but their strong-bar fraction increases with decreasing mass, reaching 40-50% around $M_* = 10^{9.5}$ M$_\odot$. We note, first of all, that these authors did not include dwarf irregulars

in their study, but in fact these galaxies represent the majority in our sample among low-mass galaxies. We deliberately included them as they are gas-rich, star-forming main-sequence objects obeying the Tully-Fisher relation and this could explain the large discrepancies between our work and theirs. We stress that by selection, galaxies shown in Figure 3.4 include dIrrs but not dEs. This makes a direct comparison to other studies of the frequency of strong bars as a function of mass, such as Nair & Abraham (2010) and Barazza et al (2008), more difficult.

To further prove our point we checked against possible biases that could in principle artificially reduce the frequency of bars especially at low mass. These are traceable to the following cases: i) obscuration by dust; ii) galaxy inclination; and iii) limited spatial resolution (hampering the detection of bars in small galaxies and in gas-rich galaxies with patchy star formation).

Case i) It has been shown by several groups that 60% of bright disk galaxies are barred in the near-infrared (Eskridge et al. 2000; Laurikainen et al. 2004; Menendez-Delmestre et al. 2007; Marinova & Jogee 2007), while only 45% appear barred in the optical (Eskridge et al. 2000; Reese et al. 2007; Marinova & Jogee 2007), presumably due to dust obscuration. Our lack of bars at low stellar masses in Figure 4 could result from this dust bias if more obscuration associated with a larger dust fraction occurs at lower mass. However, first our bar selection band (SDSS i $\lambda = 7600\mathring{A}$) is closer to near-infrared than other bluer optical bands; second, we used a representative sample of the local universe (the HRS sample of Boselli et al. 2010) to compute the extinction coefficient as a function of stellar mass and (unsurprisingly, given the mass-metallicity relation) we found that it decreases with decreasing mass, such that for mass below $M_* = 10^9$ M$_\odot$ $A(i) < 0.2$ mag (Boselli et al. 2015), ruling out a strong obscuration at low mass, and consequently a possible bias in the ability to find bars at the low-mass end of the distribution.

Case ii) We found no significant bias related to the galaxy inclination and/or to the relative PA between the bar and the inclined galaxy. Qualitatively, while bars could be missed in very inclined systems, there is no reason to expect a higher incidence of bars in inclined systems at lower masses. More quantitatively, we computed the fraction of strong bars as a function of stellar mass in a subsample of face-on ($i < 45^o$) galaxies, and checked that the bar fraction remains unchanged as a function of mass. Actually, by adopting the same mass bins as used in Fig. 3.4 (from 8.5 to 11.0 in steps of 0.5 $\log(M_\star)$),

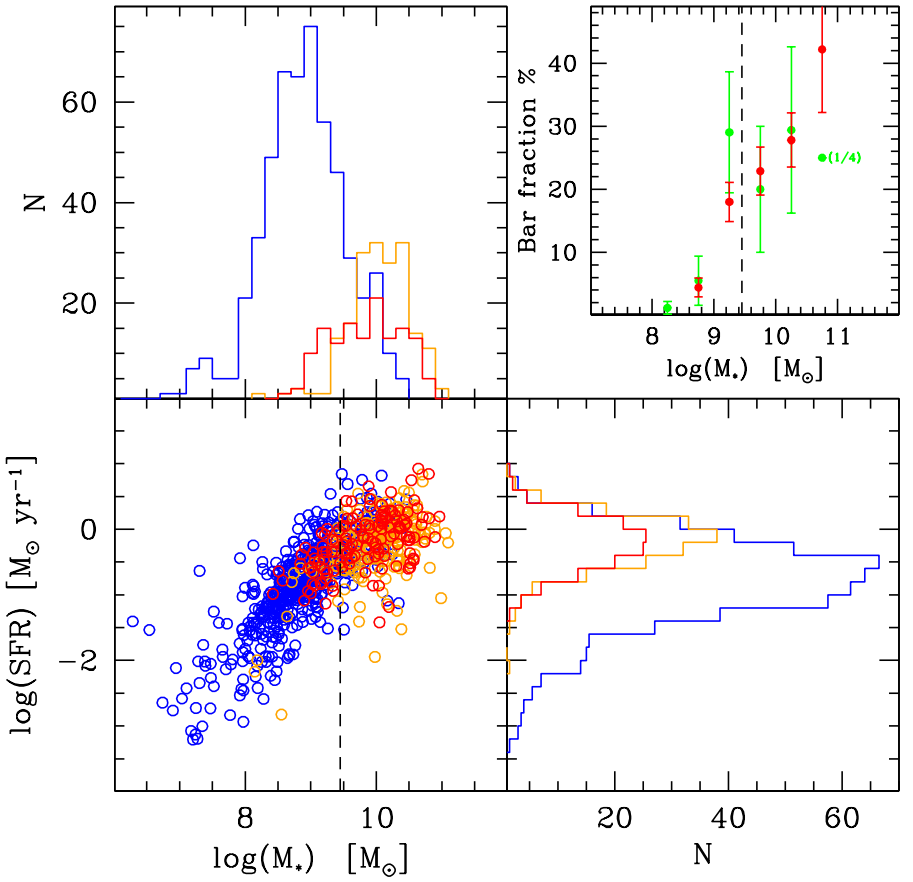

Figure 3.4: The SFR versus stellar mass for the local sample in Figure 1, but with symbols corresponding to the visual morphology: disks without bulge or bar (blue), barred disks (red), and unbarred disks with a bulge (orange). The vertical dashed line indicates $M_{\rm knee}$ at z=0. Within the same categories, distributions in bins of stellar mass and SFR are given in the top and right histograms. The top right panel gives the fraction of visually classified strong bars as a function of stellar mass, given separately for the whole sample (red), and for the local sample (within the distance of 40 Mpc, green). Owing to the small sampled volume, the third subsample lacks statistical weight at high mass (one barred galaxy over 4 objects in the highest mass bin), while the point at the low-mass end has the highest statistical significance (one barred galaxy over 85 targets).

the bar fractions become 4%, 11%, 25%, 26%, and 35%, which are consistent with the results obtained when analyzing the whole sample (4%, 17%, 23%, 28%, 42%), confirming that the results are not affected by any inclination bias[3].

Case iii) Our sample is limited to $z < 0.03$, but in the high-mass range it is dominated by objects with $z \sim 0.02$ (Coma Supercluster), while at low mass Local Supercluster galaxies dominate. The spatial resolution offered by SDSS images ($\sim$ 1.4 arcsec) corresponds to 0.7 kpc at the distance of Coma. As discussed by Barazza et al. (2008), the typical scale of strong bars at high mass (above 5×10^9 $M_\odot$) is 2 kpc, which does not hamper the bar detection at high mass. At low mass (below 10^9 $M_\odot$) our sample is instead dominated by dIrr in the Local Supercluster where the SDSS resolution element becomes ~ 110 pc, i.e., sufficient to resolve bars whose size is 10% of their optical diameter (Erwin et al 2005), which is typically 2.5 kpc. In order to test the robustness of the determination of the bar fraction with respect to the spatial resolution, we split the sample in two distance bins: within 40 Mpc (i.e., dominated by the Local Supercluster), and one between 40 and 100 Mpc (i.e., dominated by the Coma Supercluster). In Figure 3.4 we plot the bar fraction in the nearby subsample (green dots) separately from the total (red dots).

At low mass ($M_* < 10^9$ $M_\odot$), nine dwarf galaxies host a strong bar, while in the same mass range 312 objects are classified as unbarred. None of them appears to have a missed bar; however, among these 312 candidates, 7 galaxies received at least one bar-vote from one of the classifiers. This would bring the bar fraction below 10^9 $M_\odot$ to at most 5%, significantly below the frequencies measured by Barazza et al (2008) and Nair & Abraham (2010).

We finally check the dependence of the bar fraction on color. Given the known color-mass relation, e.g., more massive galaxies exhibit redder colors, it is not surprising that Skibba et al. (2011) and Masters et al. (2012) find that the bar fraction increases from 10 to 40% from blue to red, while Barazza et al (2008) and Nair & Abraham (2010) do not find such an effect. In our sample the bar fraction is 13%, 16%, 25%, and 21% with $g-i$ increasing from 0.25 to 1.25 in steps of 0.25. Above $M_{\rm knee}$, bars are undoubtedly associated with red regions, as vividly demonstrated by Figure 3.5, where a picture of the barred galaxy NGC 5921 is shown. Within the bar extent (red circle) the color index

[3]Our sample is also not biased by the relative PA as it does not affect face-on galaxies in any way.

is as red as the color of an early-type galaxy (ETG), while it is as blue as a typical massive LTG outside this radius. This color pattern is the same as the other massive barred galaxies in the local sample, as shown by the red lines in the right panel of Figure 3.5. These lines correspond to the median color profiles of barred galaxies with mass above $M_{\rm knee}$ and different inclination cuts. Profiles have been normalized to the bar length. Despite the projection effects that smear the sharp color gradient seen in NGC 5921 a change in the color profile is still visible near the bar edge because, even in face-on galaxies, the zone containing the bar often has a higher ellipticity and a position angle that is different from that of the galaxy as a whole, which is used to compute the color profile.

3.4 Bar-driven star formation quenching

In this section is proposed a simple model in which a forming or existing bar removes in few dynamical times most of the gas from the central region of the galaxy (i.e., within the bar corotational radius). As a consequence, after a short transient nuclear starburst, the inner region of the galaxy stops forming stars, and grows redder with time (see also Cheung et al. 2013). This model provides a simple and natural explanation of our observational evidence presented so far. We note, however, that our model applies only to isolated disk galaxies. Dynamically hot stellar systems, elliptical for example, would not form bars, and other environmental processes are known to act on galaxies in clusters (Boselli & Gavazzi 2006).

At first, in Section 3.4.1, we consider a single bar-unstable galaxy, and, through the comparison with a numerical simulation, we show that the main features of massive disk galaxies observed are nicely reproduced even with the most simplifying assumptions. Then, in Section 3.4.2, we make use of simple analytical considerations to demonstrate that the proposed model of bar-driven quenching reproduces the observed dependences of the sSFR on the galaxy masses and redshifts.

3.4.1 Comparison with hydrodynamical simulations

As a test-bed for the study of the effects of a strong bar on the gas on galactic scales we analyze one of the N-body/hydrodynamic simulations of isolated

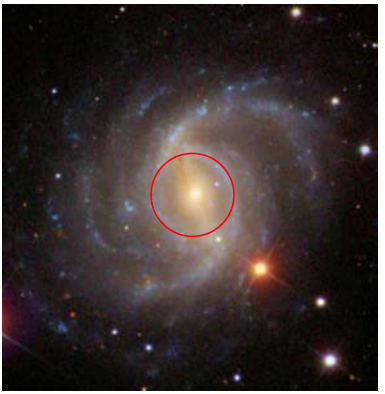

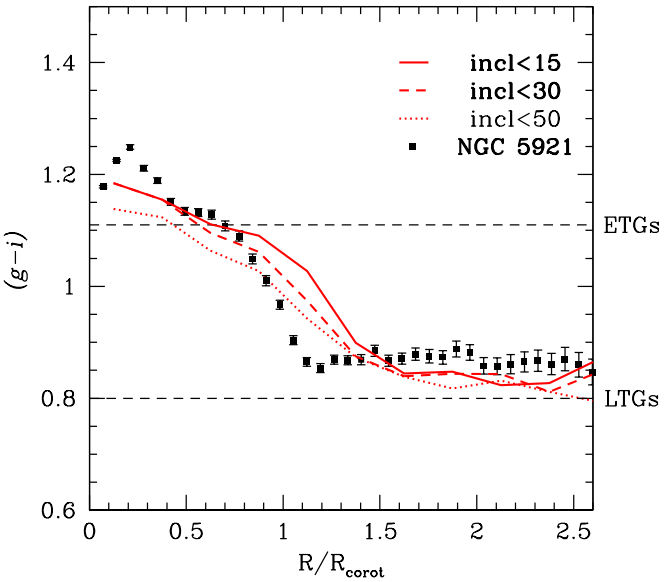

Figure 3.5: RGB image (SDSS) of the barred galaxy NGC 5921 (left panel). The bar extent is marked in red. Its $g - i$ color profile along the major axis in units of corotation radius (dots) is superposed to the median color profiles of barred galaxies with mass above $M_{\rm knee}$ and different inclinations ($<$15 deg, 30 deg, 50 deg). The two dashed horizontal lines mark the color of typical LTGs and ETGs above $M_{\rm knee}$.

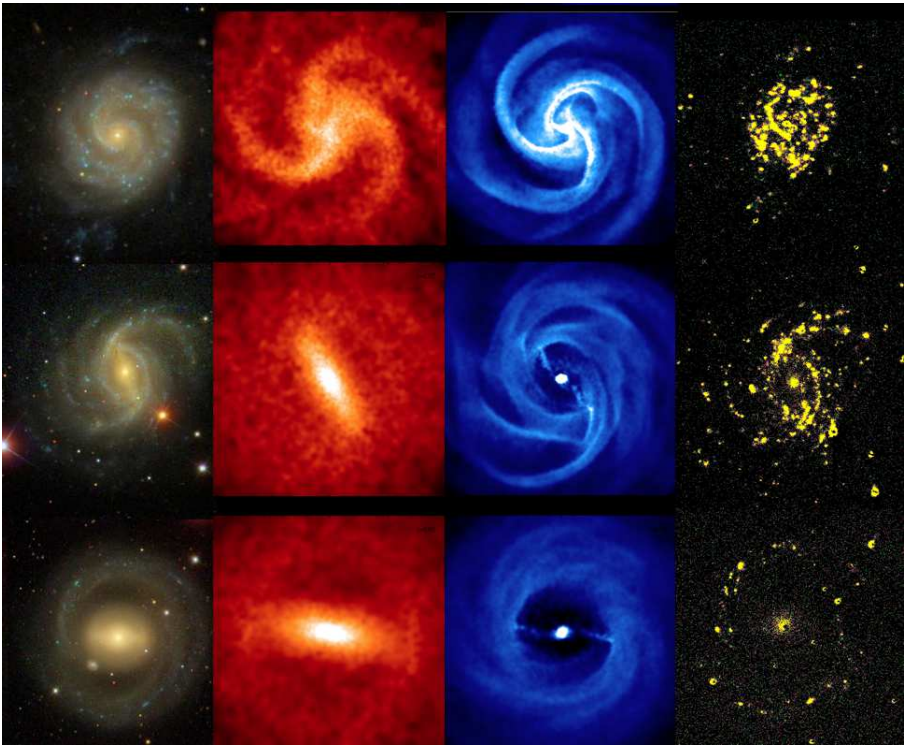

Figure 3.6: RGB images (SDSS) of three galaxies (left column) with increasing stellar mass (NGC 3596, NGC 5921, NGC 5701 from top to bottom) showing a regular spiral galaxy (top), a well-developed bar (middle), a barred ring (bottom). Face-on views of simulations of stars (second column) and gas densities (third column) from t=1 to t=4 Gyr showing a spiral disk galaxy (top) that becomes bar unstable (middle). Inside the corotation radius, the gas is conveyed towards the center and quickly consumed (except for little left along the bar). Outside the corotation radius, the gas is unperturbed and feeds peripheral star formation. At the latest time step (t=9 Gyr) the galaxy fully develops its bar and the central region is completely evacuated of gas. A ring of gas is left outside and feeds the star formation, as confirmed by the rightmost column showing our Hα images. When the bar is well developed (the two bottom panels) the star formation is suppressed inside the bar corotation radius, but it is ongoing in the outer parts. Even centrally quenched galaxies host some emission on a nuclear scale (rightmost column). However, we caution that this emission is dominated by [NII] with respect to Hα (common in LINERs) and so does not indicate solely ongoing star formation.

disk galaxies discussed in Fanali et al. (2015). In this run no star formation prescription or any kind of star formation/AGN related feedback has been implemented in order to allow for a clear identification of a dynamical quenching effect of the bar, if present. Reassuringly, despite the simple numerical techniques adopted in our calculation, the results discussed here are in line with the findings of other authors, as we will detail in the following.

The initial conditions of the run are equal to those described in Mayer & Wadsley (2004, model Lmd2c12), in order to reproduce an initially bulgeless bar-unstable galaxy. The stellar component of the galactic disk follows an exponential profile

$$\rho_*(R,z) = \frac{M_*}{4\pi R_*^2 z_*} \exp(-R/R_*)\mathrm{sech}^2(z/z_*), \tag{3.2}$$

where the radial and vertical scale lengths are $R_* = 3$ kpc and $z_* = 0.3$ kpc, respectively, and $M_* = 1.4 \cdot 10^{10}\mathrm{M}_\odot$ is the total stellar mass. The galactic disk has an additional gas component of mass $M_{\rm gas} = f_{\rm gas} \times M_*$, with a gas fraction $f_{\rm gas} = 0.05$. The gas follows the same surface density profile of the stars, and it is assumed to have a homogeneous temperature profile, with $T_{\rm gas} = 10^4$ K. The gas evolves isothermally during the system evolution. We will see that our simulation reproduces all the key features of massive disk galaxies that we need to test our model, even under such simple assumptions about the gas thermodynamics.

The composite stellar-gaseous disk is embedded in a larger scale dark matter halo, following a density profile

$$\rho(R) = \rho_H \frac{\delta_c}{(R/R_s)(1+R/R_s)^2}, \tag{3.3}$$

where $R_s = 10$ kpc, ρ_H is the critical density of the Universe today and $\delta_c = (200/3) \times \{c^3/[\ln(1+c) - c/(1+c)]\}$ depends only on the concentration parameter c, set equal to 12 for this galaxy (Navarro et al. 1995).

For each component (halo and disk) the particle positions are generated through a direct Monte Carlo sampling of the density profiles. Because of the complexity of the system, we do not generate the particle velocities by directly solving the collisionless Boltzmann equation. We instead enforce an approximate dynamical equilibrium for the system, following Hernquist (1993, H93 hereafter) and Springel et al. (2005). In detail, we make use of the Jeans

equation to compute the first and second moments of the velocity field as a function of the position, i.e., the bulk motion of the particles and the components of their local velocity dispersion. In the simpler halo case we assume an isotropic velocity field (i.e., no net rotation) and that all the components of the velocity dispersion tensor are equal. The three components of the velocity dispersion tensor as well as the rotational bulk velocity of the disk particles are obtained following the numerical procedure described in Section 2.2.3 in H93. The velocity components of each particle, then, are sampled through a Monte Carlo procedure, assuming that the local distribution function is Gaussian, in good agreement with the observational constraints (see the discussion in H93).

We sample the stellar disk with 9.5×10^5 particles, the gaseous disk with 5×10^4 particles, and the halo with 10^6 particles. We ensure that the particles in the disk all have the same mass, preventing any spurious relaxation and mass segregation. The softening length that sets the spatial resolution of the gravitational interaction in the run of each particle is 15 pc. The system is evolved using the smoothed particle hydrodynamics (SPH) code Gadget-2 (Springel 2005).

Three snapshots of the stellar and gas surface densities at different times are shown in the two central columns of Figure 3.6, together with three images of real galaxies taken from our sample for comparison (left columns). The simulated galaxy has a first evolutionary phase ($t < 1.5$ Gyr) during which it develops mainly spiral features (top panels in figure 3.6). At $t \sim 1.5$ Gyr a stellar bar forms, and during its growth and evolution it triggers strong gas inflows toward the galaxy center. Already at $t \sim 4$ Gyr (second row in in Figure 3.6) most of the gas in the central 4.5 kpc has been forced into the galactic nucleus, in accordance with previous observational (e.g., Sakamoto et al. 1999, Jogee et al. 2005, Sheth et al. 2005) as well as analytical and numerical studies (e.g., Sanders & Huntley 1976, Shlosman, Frank & Begelman 1989, Athanassoula 1992; Berentzen et al. 1998; Regan & Teuben 2004, Kim et al. 2012, Cole et al. 2014).

Although our simulation does not include any prescription for star formation, the extreme gas densities in the nucleus and its short dynamical time ensures that most of the gas mass is doomed to convert into stars in a burst of nuclear star formation (e.g., Krumholz et al. 2009, Krumholz & McKee 2005, Daddi et al. 2010, Genzel et al. 2010), likely resulting in the formation

of a pseudobulge.[4] After the short transient starburst event, the gas density (and, consequently, any expected star formation rate) drops. After 9 Gyr the stellar bar has swept the quasi-totality of the gas in the central 4.5 kpc (bottom row in in Figure 3.6), and our simulation nicely reproduces the properties of a centrally quenched galaxy as NGC 5701, but retains an evident external spiral structure (bottom left panel in Figure 3.6). Streams of low-density gas falling along the edges of the bar are still visible, both in the simulation and in the observations, where they are traced by dust filaments. The Hα images shown in rightmost column of Figure 3.6 show (from top to bottom) that normal star formation is taking place in the disk of the relatively lower mass NGC 3596, while when the bar fully develops (NGC 5921 and NGC 5701) the star formation activity is null inside the bar corotation radius, but remains conspicuous outside it. Some emission remains observable in the nuclear regions, hosting a star-forming cluster (in NGC 3596) or showing [NII] over Hα ratios suggestive of low ionization nuclear emission-line regions (LINERs, as in NGC 5921 and NGC 5701), as the nuclear spectra of these three galaxies indicate (Gavazzi et al. 2013c).

The comparison between our simulation and observations have been performed for more than three galaxies. We note that Figure 3.5 already demonstrates that the central regions of barred galaxies are, on average, quenched with respect to the corresponding outer parts. To further support this scenario with the observational data of nearby galaxies, we present in Figure 3.7 the color-mass diagram dividing the inner parts (within the bar extent) of barred galaxies from their outer parts. The $g - i$ colors, taken as a proxy for sSFR, have been corrected for Milky Way and internal extinction as in Gavazzi et al. (2013b). Non-barred LTGs in our sample and ETGs in the Coma and Local superclusters have been plotted for comparison. Figure 3.7 clearly demonstrates the significant central quenching caused by the bars in massive galaxies. We also note that the bar-driven gas removal cannot be the only quenching mechanism in place, as even the exteriors of massive barred galaxies are redder than lower mass counterparts. Our selection criteria, however, allow us to exclude a possible environmental nature of the additional quenching process. We note that the triggering of a strong gas inflow like the one observed in our

[4] The higher occurrence of strong episodes of nuclear star formation in barred galaxies has been extensively observed, see, e.g., Ho et al. (1997), Martinet & Friedli (1997), Hunt & Malkan (1999), Laurikainen et al. (2004), Jogee et al. (2005).

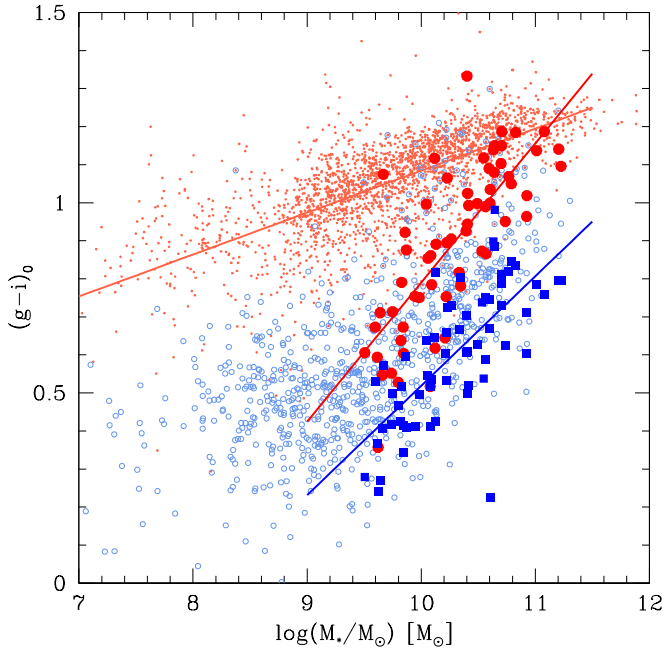

Figure 3.7: Color-mass diagram obtained with the $g-i$ color (corrected for extinction in the Milky Way and for internal extinction). ETGs in the Coma and Local Superclusters (small red points) are also shown for comparison. The LTGs are subdivided into galaxies with disks without a bulge or a bar (including dIrr and other blue dwarfs, light blues symbols) and galaxies that we classified as containing a strong bar. The colors of the latter are separately displayed as large red symbols within the corotation radius and with large blue squares outside the corotation radius. Fits to the colors of the inner and outer regions of barred galaxies (as well as for ETGs) are shown in the figure.

simulation is ubiquitously observed in many investigations, regardless of the particular type of code used (2D versus 3D, Eulerian grid based codes versus SPH, see Sellwood 2014 for a thorough discussion). As a final word of caution, we highlight that the main shortcut of our simulation is the lack of any feedback associated with star formation or to the possible onset of an AGN. This allowed us to firmly identify an independent – purely dynamical – bar driven quenching process. Stellar feedback could, however, eject a significant amount of the gas driven into the galaxy central regions by the bar. Because of the small angular momentum of such outflows, the gas would not re-enrich the quenched kpc size region. The ejected gas is instead expected to fall back towards the nucleus, leading to multiple episodes of intense and fast nuclear star formation (see the results of the high-resolution simulation including stellar feedback discussed in Emsellem et al. 2015).

3.4.2 Dynamical model for the sSFR-quenching cosmic evolution

In the previous section we discuss how the presence of a bar results in the removal of gas in the central region of a galaxy, explaining its red colour within the corotation radius and the lower sSFR of the whole galaxy. Figure 3.3, however, clearly indicates that the bar-driven quenching is not effective in low-mass galaxies. More specifically, the observational data are indeed consistent with strong bars forming only in massive spiral galaxies, with $M_* > M_{\rm knee} \sim 10^{9.5}$ M$_\odot$ at $z = 0$, where $M_{\rm knee}$ is an increasing function of redshift. We stress that the trend of $M_{\rm knee}$ with redshift fits with the results of studies on the strong bar frequencies in large observational samples. As an example, Sheth et al. (2008) analyzed the COSMOS 2 deg^2 field finding a decreasing bar fraction moving toward higher redshifts. They also comment on the fact that the strong bar fraction of low-mass $M_* \lesssim 10^{10.5}$ M$_\odot$ spirals declines significantly with redshift beyond z=0.3, while it remains roughly constant out to $z \sim 0.84$ in more massive, luminous spirals. This is consistent with the seminal results of Jogee et al (2004), obtained analyzing galaxies out to $z \sim 1$ observed with the Hubble Space Telescope Advanced Camera for Surveys (ACS). Later on, similar results were discussed in Cameron et al. (2010) who reported that the strong bar fraction for massive systems ($M_* > 10^{11}$ M$_\odot$) does not change between $z = 0.2$ and z$= 0.6$, while it falls for lower mass systems. More recently, Melvin et al. (2014), on the basis of

visual classifications provided by citizen scientists via the Galaxy Zoo Hubble project, also find that the overall strong bar fraction decreases from 22 $\pm$5% at z=0.4 to 11$\pm$2% at z=1.0. In addition, they confirmed that this decrease in the bar fraction is most prominent at low stellar masses.

A simple model that explains the existence of a redshift-dependent $M_{\rm knee}$ above which the sSFR declines can be built on the observational evidence that the dynamical state of galactic disks depends on their masses and redshifts (e.g., Sesana et al. 2014 and references therein). We start noticing that dynamically hot galactic disks are stable against bar formation, while colder disks can form bars in few dynamical times (e.g., Athanassoula & Sellwood 1986). We define hot disks those with Toomre parameter

$$Q \sim \frac{\sigma_* \Omega}{G \Sigma_*} \gtrsim 1, \tag{3.4}$$

where σ_* is the stellar velocity dispersion, Ω is the angular velocity and Σ_* is the stellar surface density. The Toomre parameter can be rewritten as

$$Q \sim \left(\frac{v_{\rm rot}}{\sigma_*}\right)^{-1} \left(\frac{v_{\rm rot}^2 r}{G M_*}\right) \sim \left(\frac{v_{\rm rot}}{\sigma_*}\right)^{-1}, \tag{3.5}$$

where $v_{\rm rot}$ is the rotational velocity of the disk, r is a proxy for the disk extension, and $(v_{\rm rot}^2 r)/(GM_*) \sim 1$ because of the virial equilibrium of the rotating stellar disk. Using Eq. 3.5 we can translate the critical value of the Toomre parameter $Q_{\rm crit}$, distinguishing between bar stable and unstable systems, into a critical value of the $v_{\rm rot}/\sigma_*$ ratio.

A growing number of studies (e.g., Förster Schreiber et al. 2009; Law et al. 2009; Gnerucci et al. 2011; Kassin et al. 2012; Wisnioski et al. 2011; Epinat et al. 2012; Swinbank et al. 2012; Newman et al. 2013; Wisnioski et al. 2015) finds that the $v_{\rm rot}/\sigma_{\rm gas}$ in disk galaxies increases as a function of the galaxy mass M_* and decreases with redshift. A similar trend in $v_{\rm rot}/\sigma_*$ is required to reproduce the observed evolution of the fraction of galactic bars and of the sSFR discussed above (as already noted by e.g., Sheth et al. 2008). As a note of caution we stress that the above cited studies focus on the gas dynamics instead of the stellar one, and that the gas component, being subject to additional forces of radiative and hydrodynamical nature, could have a different dynamics with respect to the stars. This, together with the very limited number of galaxies in the samples listed above and the large observational uncertainties in $v_{\rm rot}/\sigma_{\rm gas}$ prevents us to perform a more quantitative analysis.

Recently Kraljic et al. (2012) have studied the occurrence of bars in disk galaxies of $10^{10} \lesssim M_*/\mathrm{M}_\odot \lesssim 10^{11}$ in high-resolution cosmological simulations. They presented a physically motivated scenario in which long-lived bars form when galaxies stop being battered by frequent minor mergers, which tend to keep the host galaxies dynamically hot (see also Romano-Diaz et al. 2008). In the mass range they studied, the bar fraction is ≈ 0 at $z \gtrsim 1.5$, $\approx 10\%$ at $z \approx 1$, and $\approx 80\%$ at $z \approx 0.5$, in reasonable agreement with our model and with the value of $M_{\rm knee}$ we find for those masses. An observational confirmation of the model should pass through an estimate of the fraction of galaxies of a given mass undergoing a minor merger within a given redshift. This exercise has been already performed in the literature (e.g., Jogee et al. 2009, Lotz et al. 2011). The results depend on the different tracers used to identify galaxy mergers and the different assumptions underlying the estimates of the merging frequency, and do not always agree with the theoretical predictions, calling for a critical revision of both the observational and theoretical approaches (as discussed in Lotz et al. 2011). Even so, assuming the maximum number of mergers within the last 7 Gyr ($z \approx 0.8$) reported in Jogee et al. (2009) and Lotz et al. (2011), about half of the galaxies with $M_* > 10^9 M_\odot$ did not undergo any minor merger, leaving sufficient time to develop a bar in their central regions.

We conclude by commenting that the $M_{\rm knee} \propto (1+z)^2$ fit to the observational data (Figure 3.3, panel b) implies that $v_{\rm rot}/\sigma_*$ does not depend on two uncorrelated variables (M_* and z), but only on $M_*/(1+z)^2$, decreasing the dimensionality of the problem. This prediction can be tested by future accurate measurements of $v_{\rm rot}/\sigma_*$ in larger samples of galaxies of different masses and redshifts.

3.5 Discussion

The results of this observational study together with simple numerical and analytical arguments, demonstrate the relevance of bars in quenching the central regions of about 25% of the field main-sequence galaxies with $M_* > M_{\rm knee}$ in our sample. In this section we speculate further, depicting a physical scenario in which the mass quenching of the vast majority of the massive field galaxies is caused by the occurrence of a bar.

In section 3.3 we visually classified the galaxies in our sample either as

pure disks or as hosts of strong bars or bulges. A significant fraction ($\sim 40\%$) of the galaxies above $M_{\rm knee}$ do not show a prominent bar, but rather host a central bulge. First, we assume that the most of the observed bulges are not classical, but rather boxy/peanut bulges and/or pseudobulges. Such an assumption is not unrealistic for isolated disk galaxies (Weinzirl et al. 2009), but we stress again that it is highly challenging to classify reliably the different bulge morphologies (e.g., Graham et al 2008; Wilman et al. 2013). The task is even harder as recent evidence indicates that the two bulge categories can even occur simultaneously (Erwin et al. 2015). Given the speculative nature of this section, we will work under this assumption anyway, for which pseudobulges originate from bars. In fact, there is a growing evidence (e.g., Combes et al. 1990; Kormendy & Cornell 2004; Athanassoula et al. 2005, 2008) that non-classical bulges represent the late evolutionary stage of stellar bars, due to the buckling of the central part of the bar itself (boxy/peanut bulges) and to nuclear star formation fueled by bar-driven gas inflows (pseudobulges). The formation of a central gas concentration that could result in the formation of a pseudobulge is present in the simulation previously discussed (section 3.4.1). We further note that at the very end of the simulation the bar develops a thicker rotating stellar structure in its center, consistent with a boxy/peanut shape bulge, depending on the assumed line of sight (see Figure 3.8). Meanwhile, although still present, the bar becomes harder to identify in the stellar surface density distribution. For a detailed theoretical and observational description of the bar/pseudobulge interplay I refer the reader to the work of Raha et al. (1991), Kormendy & Kennicutt (2004), Kormendy (2013), and Sellwood (2014).

While it is well established that pseudobulges and boxy/peanut bulges can indeed form from the evolution of a bar, we cannot prove that our bulge category does not include a significant fraction of classical bulges. A detailed study of the nature of the bulges would require a wealth of additional information, including observational constraints on the dynamical state of the bulges (e.g., through long slit or integral field spectroscopy), and is beyond the scope of this paper. However, we can discuss some additional properties of the bulge population that hint to a physical link with the population of bar-hosting galaxies.

Figure 3.4 shows a sharp separation between pure disks and bars or bulges across $10^{9.5}$ $M_{\odot}$. A Kolmogorov-Smirnov test gives a null probability that the

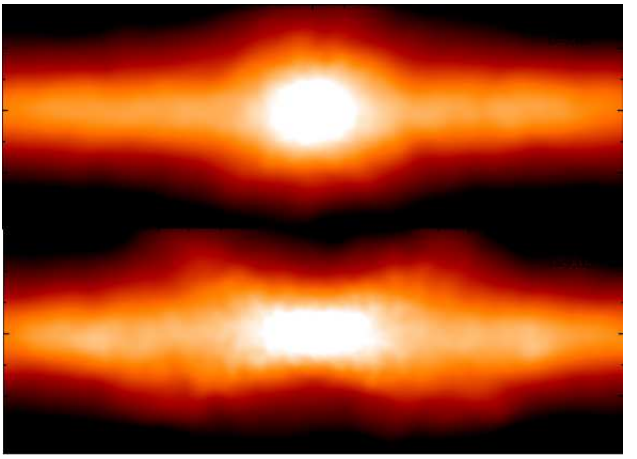

Figure 3.8: Edge-on view of the same object at the t=9 Gyr step of the simulation in Figure 3.6. The azimuthal angle of the bar is along (perpendicular to) the line of sight in the top (bottom) panel. In both cases we would classify it as pseudobulge.

distributions of pure disks and galaxies hosting bars or bulges are derived from the same parent population. Bars and bulges, instead, have almost identical SFR distributions (>99% K-S probability, see the right panel of Figure 3.4), supporting a scenario in which bars and bulges are physically associated. Bars and bulges also show similar mass distributions (upper panel in Figure 3.4). In this last case, however, they do not perfectly match, probably because of the ambiguity in the classification of objects in the transition regime between bulges and disks near $10^{9.5}$ $M_{\odot}$.

An additional independent hint comes from the study of the nuclear activity of galaxies with bars and bulges. Observations confirm that indeed many barred galaxies have dense central concentration of gas and enhanced central star formation (Sakamoto et al. 1999; Laurikainen et al. 2004; Jogee et al. 2005; Sheth et al. 2005; Ellison et al. 2011; Kormendy et al. 2013). We strengthen this point by performing an analysis of the nuclear activity of the galaxies in our sample, making use of the classification given in Gavazzi et al. (2013c). We find that among massive barred galaxies ($M_* > 10^{9.5}$ $M_{\odot}$) at $z = 0$, 61% of nuclei show line ratios typical of HII regions, 12% are strong

AGNs (mostly type 2), and 11% are either passive (2%) or retired (9%) [5]. The remaining galaxies (15%) are classified as LINERs. Very similarly, among massive spirals showing bulges, 53% have HII-like nuclei, 14% are strong AGNs, 23% are LINERs, and 9% are passive or retired. The large fraction of star-forming nuclei and strong AGNs in the two samples hints at large gas concentrations, and the similar fractions further hint to a common physical origin of bulges and bars. As a check the same exercise is performed among 954 E+S0, selected in the Local and Coma superclusters with stellar masses greater than $10^{9.5}$ $M_{\odot}$. Of these, only 5% show line ratios common to HII regions, 2% are strong AGNs, while 13% are LINERs and the remaining 80% are either passive or retired. In summary, the population of galaxies with strong bars is indistinguishable from that hosting bulges as far as their nuclear properties are concerned, while the E+S0 class (supposedly dominated by genuine classical bulges) does not show any significant central activity whatsoever.

In conclusion, the arguments discussed so far support a possible evolutionary scenario in which, at a given redshift, galaxies above $M_{\rm knee}$ undergo a bar instability (section 3.4.2). The bar forces the gas within the corotational radius to fall toward the center in few dynamical times. The forming central gas condensation is immediately consumed by a vigorous burst of star formation (and/or AGN activity), resulting in the formation of a pseudobulge. After a few rotations, the bar sweeps all the gas within its corotational radius, quenching the SF in the central region of the galaxy. Consequently, this region grows redder and redder with time, decreasing the global sSFR of the galaxy (see also Cheung et al. 2013). With time the central region of the bar undergoes a buckling instability (e.g., Sellwood 2014 and references therein): the bar becomes less and less visible, while a thicker but still rotationally supported stellar condensation (i.e., a boxy/peanut bulge) becomes clearly observable, often with a pseudobulge hosted in its very center. The common origin of pseudobulges and boxy/peanut bulges from bars justifies i) the significant fraction of galaxies hosting bulges observed in our sample above $M_{\rm knee}$ and ii) the similarities between their masses, SFRs, and nuclear activity distributions and those describing their barred counterparts.

[5] "Retired galaxies" is a denomination proposed by Stasińska et al. (2008) to describe nuclei that have stopped forming stars and are ionized by "hot post-AGB stars".

Chapter 4

The effect of bars on gas as seen by *Herschel*

In order to test the scenario described in the previous chapter, in this chapter we aim at mapping the distribution of gas in barred and unbarred galaxies. Untill now, the direct detection of inflows of cold gas in barred galaxies was performed only in few galaxies (Sakamoto et al., 1999). Therefore we aim at unveiling inflows of cold gas in a statistically significant sample of galaxies.

The most direct probe would require the direct imaging of molecular and neutral atomic gas. Unfortunately, such information is available only for a very limited sample of galaxies, and is often affected by either a too low angular resolution or a very limited field of view. However these problems can be overcome because the molecular gas distribution correlates strongly with the distribution of the cold dust component (Boselli et al., 2002). We take full advantage of such leverage by using the far–infrared (FIR) images from the *Herschel* Reference Survey (HRS, Boselli et al., 2010). We compare the *Herschel* data with the optical images from the Sloan Digital Sky Survey (SDSS, York et al., 2000). We study the correlation between the occurrence of bars in optical images and of either bar-like structures or central zones of no emission in the HRS. We further measure the extent of such optical and infrared structures and check whether they are correlated. For galaxies showing both an

optical bar and an infrared bar-related structure we link their morphology to the star formation distribution as traced by Hα images (Kennicutt, 1998). Finally a qualitative comparison to the few available HI-maps tracing the atomic gas distribution is accomplished owing to the high resolution maps from the VIVA survey (Chung et al., 2009).

All results are published in Consolandi, G., Dotti, M., Boselli, A., Gavazzi, G., Gargiulo, F. 2017, A&A, (in press).

4.1 The *Herschel* Reference Sample

The galaxies analyzed in this work have been extracted from the *Herschel* Reference Survey (Boselli et al., 2010) that is briefly described in section 2.3.

Since the present work aims at performing a visual comparison of the ISM and of the stellar morphology in the HRS galaxies, we need a sufficient spatial resolution in both the IR and the optical images as well as a good sensitivity and little dust obscuration in the optical band. For this purpose we characterize the morphological properties of the stellar component and of the ISM using the SDSS images in the i-band (Cortese et al. 2012) and the 160 μm maps obtained with the PACS instrument (Cortese et al. 2014), respectively. At 160 μm the resolution is FWHM = 11.4 arcsec, while the pixel size of the reduced maps is 2.85 arcsec pixel^{-1} (Cortese et al. 2014). This photometric band has been chosen among those available for the whole sample galaxies (22μm from WISE, Ciesla et al. 2014; 100-500 μm, Ciesla et al. 2012; Cortese et al. 2014) as the best compromise in terms of sensitivity, angular resolution and dust temperature. At this frequency the FIR emission gives the distribution of the cold dust component, which is a direct tracer of the molecular gas phase of the ISM (e.g. Boselli et al. 2002) from galactic to sub-kpc scales (Corbelli et al., 2012; Smith et al., 2012; Bolatto et al., 2013; Sandstrom et al., 2013). On the optical side, the i-band is only little affected by dust and is the best SDSS tracer of the stellar mass of a galaxy, and is preferred to the z-band for its higher sensitivity, while the Hα data are taken from Boselli et al. (2015). The SDSS, PACS and Hα images are available on the HeDaM database (http://hedam.lam.fr/).

Further on, we limited the analysis to the 261 late-type galaxies of the sample in order to avoid contamination from slow rotators (namely ellipticals, which do not develop bars, Sellwood, 2014) and from early-type disks (includ-

ing S0s) that have too little cold gas to test the bar-related quenching process (Boselli et al., 2014). Finally we exclude galaxies with an axis ratio lower than 0.4 to avoid a major inclination bias in our morphology classification and measures, leaving a final subsample of 165 late-type face-on galaxies.

4.2 Results

For each galaxy we visually inspect the i-band SDSS images and look for the presence of an evident stellar bar. Separately we also visually inspect the PACS images looking for a central carved region with little to no emission that, if present, is distributed along a bar-like component (see Fig.4.1, HRS208) or in a small nuclear region surrounded by a ring-like structure (see Fig.4.1, HRS220). In Fig. 4.1, from left to right, we show three illustrative cases representing the infrared morphologies possibly associated with optical bars (column one and two, HRS 208 and 220) and a normal spiral galaxy (last column, HRS 254). For each galaxy we give from top to bottom the SDSS RGB, the $160\mu\mathrm{m}$, the continuum subtracted Hα images and the HI map from the VIVA survey (Chung et al., 2009) that unfortunately overlaps our sample only with few galaxies.
We find 51 barred galaxies ($\approx$ 30% of the sample) in the i-band, out of which 75% show in the corresponding $160\mu\mathrm{m}$ images an elliptical/circular area where the only emission is distributed on a bar- or ring-like structure. On the other hand, we find 63 galaxies ($\approx$ 38% of the sample) hosting the described morphologies in the $160\mu\mathrm{m}$ images out of which 38 ($\approx 65\%$) galaxies are found barred in the corresponding optical image. The frequency of galaxies hosting an infrared feature that also show a corresponding optical bar, and the occurrence of optical bars showing an infrared feature are $\approx$ 65% and $\approx 75\%$, respectively. These percentages rise to $\approx 85\%$ and $\approx 96\%$ if we include 16 galaxies classified as barred by other literature classifications found in the NASA Extragalactic Database (NED). These are mostly weak bars that are difficult to recognize visually and whose extent is difficult to quantify. For this reason we exclude these objects from our further analysis. In order to quantitatively relate the region of star formation avoidance to the presence of an optical bar, we measure the size of these structures visually in the optical and in the $160\mu\mathrm{m}$ and then do the same using ellipse fits to isophotes. The two approaches are useful because the eye can effectively recognize features

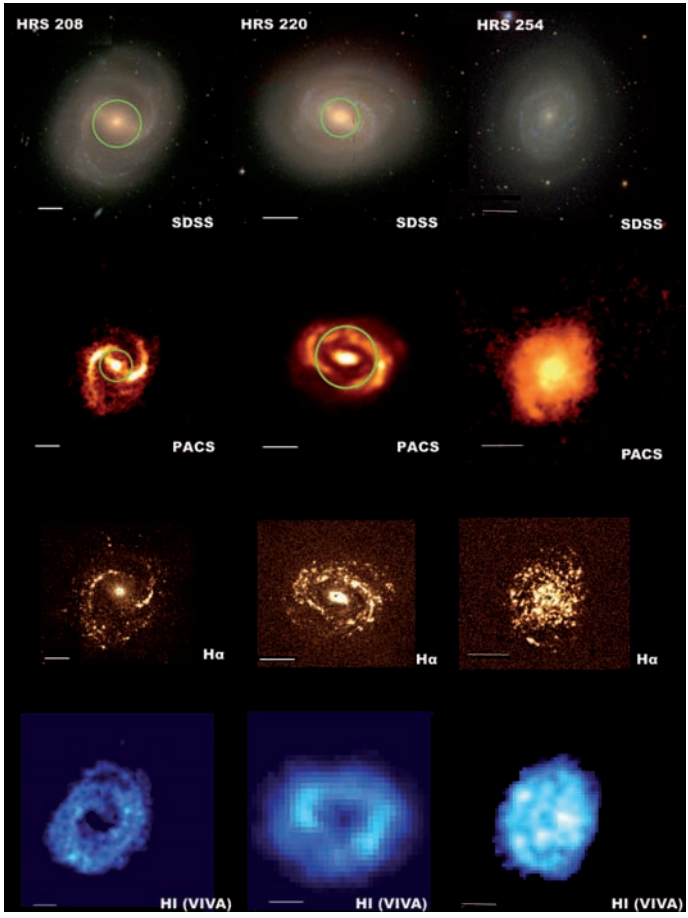

Figure 4.1: Examples for the categories classified in this work. From left to right: NGC 4548 (HRS-208), NGC 4579 (HRS-220), NGC 4689 (HRS-256). The top row shows the SDSS RGB image of the galaxy while the second row shows the corresponding PACS images. Green circles illustrate qualitatively the circular region used to measure the extensions of structures. In the third row is reported the Hα image and in the fourth the HI map from the VIVA survey. In each frame a 1 arcminute scale is given.

and their extent even if somewhat subjective, while ellipse fits are objective measures that nevertheless can be strongly affected by other structures in the galaxies. Four of the authors (GC, MD, FG, GG) manually evaluated the extent of optical bars by measuring the radius of the circular region circumscribing the bar, avoiding possible HII regions at the end of it. On the other hand, in the 160μm images, when an infrared bar is present we measure the radius of the circle circumscribing the bar while, when no clear bar is discernible, we measure the inner semi-major axis of the ring-like structure surrounding the depleted region (as depicted in Fig. 4.1). For the optical bars showing the region of avoidance in the 160μm images we also visually inspect the continuum subtracted Hα images finding similar morphologies and repeat the same measure.

Using IRAF[1] task $ellipse$, ellipticity (ϵ) and position angle (P.A.) radial profiles of the isophotes of each sample galaxy in each considered band. In optical broad-bands, it is well tested that the radius at which there is a peak in the ellipticity profile and a related plateau in the P.A. profile is a good proxy for the extension of the bar (Jogee et al., 2004; Laurikainen et al., 2010; Consolandi, 2016). Following this procedure we extract a radius of the bar in the i-band for each galaxy and, we deduce the bars strength following (Laurikainen et al., 2007) from the peak of the ϵ profile in the i-band. We find that $\approx 95\%$ of galaxies that we classified as barred harbor strong bars ($\epsilon > 0.4$). Although this quantitative method has not been applied to far-IR data previously, ellipse fits can nevertheless be derived for the 160μm images and the ϵ and P.A. profiles examined for a bar signature. Since we are trying to measure a region of decreased emission possibly surrounded by a ring-like emitting structure, we also extract a radial surface brightness profile from concentric elliptical apertures centered on the galaxy and ellipticity fixed to the outer infrared isophotes. The derived surface brightness profile therefore has a relative maximum in correspondence of the ring-like structure. In the cases where no infrared bar is discernible, the radius at which this occurs is a good proxy of the extension of the non emitting region.
In the 160μm images, this method succeeds at extracting the radius of the non emitting region or of the bar in 75% of the barred galaxies. Because of the irregular and clumpy distribution of light at 160μm the fit of the isophotes

[1]IRAF (Image Reduction and Analysis Facility) is a software for the reduction and analysis of astronomical data.

does not converge in 25% of the galaxies. Therefore, in order to preserve the statistics of our already limited sample, we plot in Fig. 4.2 the radius obtained averaging the measures of the optical bars made by the authors versus those from the 160μm data (black empty dots) and those from the continuum subtracted Hα images (red empty dots). All radii are normalized to the i-band 25^{th} mag isophote radius of the galaxy, taken from Cortese et al. (2012), and errors are evaluated from the standard deviation of our measurements. The black and red dashed lines indicate the bisector fit (Isobe et al., 1990) to the data respectively for the 160μm (slope $\sim 0.89 \pm 0.11$) and the Hα data (slope $\sim 1.35 \pm 0.08$). The slope of the fit relative to the optical versus Hα data is strongly influenced by the extremely deviant point (associated to HRS 322) visible in Fig. 4.2. This outlier is characterized by a very small error, as all the authors consistently measured the same radius with very little scatter. We stress, however, that the semi-major axis of this galaxy in the Hα distribution is perpendicular to the optical bar thus the important discrepancy is mostly due to projection effects. If we exclude this point from the fit, the slope becomes 0.79 ± 0.11. Finally, in green, we plot the best linear fit of the comparison of optical versus 160μm radii measured with IRAF (slope $\sim 0.87 \pm 0.10$). All fits show a strong consistency between them even when evaluated with independent methods. To further check a possible bias due to inclination, we derived the same fits for a subsample of galaxies with axis ratio greater than 0.7 ($\approx 40\%$ of the sample), finding fully consistent results.

4.3 Discussion and conclusions

The study and comparison of frequencies of occurrence of bar related features in the optical and FIR, as traced by the stellar continuum and by warm dust emission, respectively, results in a fraction of galaxies hosting an optical bar of $\sim 30\%$ while a zone of avoidance with or without an infrared bar is found in 38% of the 160μm images. The percentages of common occurrence suggests that FIR images are an effective way of identifying the presence of a bar in a galaxy.

For the galaxies hosting both an optical bar and a central zone of avoidance in the 160μm images, we measured the angular size of both structures with independent methods, finding a good correspondence. First, we measured the extent of bars in optical images, while in the FIR images we measured the

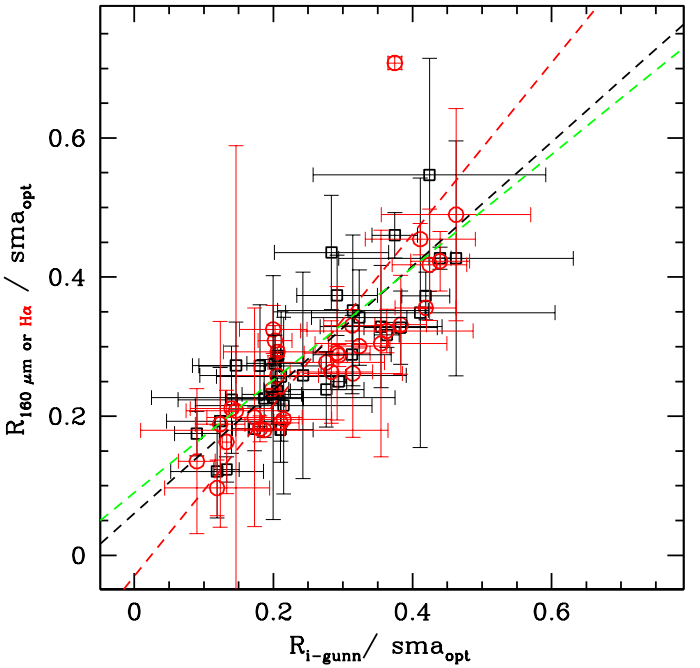

Figure 4.2: Comparison between the radii of bars in the i-band and the radii of the central zone of avoidance of the 160μm (black dots) and continuum subtracted Hα (red dots) images. The black and red dashed lines represent the bisector regression to the i-band versus 160μm and i-band versus Hα data, respectively. The green dashed line is the linear fit to the i-band versus 160μm radii measured using $ellipse$ in IRAF for 75% of the sample. All radii are normalised to the optical diameter of the galaxy taken from Cortese et al. (2012).

extent of the bar-like structure, if present, or of the inner semi-major axis of the ring-like structure. In the latter case, we stress that the projected angular sizes of the optical bar and the radius of non-emitting zone may differ significantly[2] depending on the bar orientation. In 75% of the barred galaxies we successfully ran the IRAF task $ellipse$ to objectively measure the extent of these structures in both the i-band and 160μm images, using the derived ellipticity, P.A. and surface brightness profiles. The goodness of the correlation strongly hints at a physical connection between the presence of an optical strong bar and a gas-depleted/quenched region where little SF is still possible. Only in the very center (where the bar conveys the gas originally within its reach) or along the bar is SF found. Such an effect is consistent with what we see in the continuum subtracted Hα images of the sample. SF is indeed distributed mainly in the nuclear region of galaxies and/or along the bar (consistent with Verley et al. (2007); see Fig. 4.1) and shows a morphology similar to the one observed in the FIR.

We conclude that the FIR morphologies are similar to the Hα morphologies (consistent with Verley et al., 2007) and that both are consistent with bar-driven inflows of gas inside the corotation radius as predicted by simulations (Sanders & Huntley, 1976; Athanassoula, 1992). Fig. 4.1 qualitatively show that also the HI emission, when available, show similar mophologies. The impact on the cold gas component, as derived from the FIR, is consistent to what has been observed in few galaxies (Sakamoto et al., 1999) and affects the star formation of barred galaxies (Verley et al., 2007; Gavazzi et al., 2015, and see chapter 3): as soon as a bar starts growing, the gas is initially perturbed and compressed along the bar, where it forms stars while gradually losing its angular momentum; as the time goes by, the gas is swept by the bar into sub-kpc scales, leaving a gas-depleted and SF quenched region of the size of the bar itself, with or without a central knot of SF depending on the consumption timescale of the originally infalling gas.

[2]Up to a factor of ≈ 2.5 for the maximum inclination of $B/A = 0.4$ allowed in our sample.

Chapter 5

Galaxy colors in the local Universe

The advent of the Sloan Digital Sky Survey (SDSS, York et al. 2000) represents a revolution in many fields of observational astronomy. The final SDSS catalog consists of about 500 million photometric objects in five bands with more than 1 million spectra. This huge amount of publicly available data has given the community the unprecedented opportunity to study galaxy properties from a statistical point of view in many different regimes of local density and cosmic epochs.

However the SDSS pipeline was optimized for the extraction of photometric parameters of galaxies at the median redshift of the survey ($z \sim 0.1$). Large nearby galaxies, often exceeding the apparent diameter of few arcmins were obviously penalized by this choice. One longstanding problem that affects the identification of extended sources (Blanton et al., 2005) is the so-called shredding of large, bright (in apparent magnitude) galaxies by the automatic pipelines, leading to wrong detections and incorrect magnitude calculations. Moreover, restrictions due to fiber collisions dictate that no two fibers can be placed closer than 55 arcsec during the same observation (Blanton et al., 2003) which affects the spectroscopy of crowded environments and introduces incompleteness at $z < 0.03$ where many local large scale structures exist, namely the Local and the Coma superclusters (see Fig. 2.1).

Nevertheless, galaxies of the local universe are, at fixed luminosity, the brightest as well as the best spatially resolved objects of the sky. Therefore, within the SDSS, local galaxies can be analyzed down to a mass limit that cannot be reached at higher redshift and, in addition, their structures and morphology are easier to constrain. In fact the median resolution of the SDSS, given by the median point spread function (PSF ~ 1.4 arcsec, in the r-band), corresponds to a physical scale of ~ 600 pc at the distance of the Coma cluster (~ 95.38 Mpc) and ~ 80 pc at the distance of Virgo (~ 17 Mpc, Gavazzi et al., 1999; Mei et al., 2007). This resolution is sufficient to resolve even small structures such as nuclear disks in galaxies.
Henceforth local galaxies are a natural test-bed for studies on the evolution of structures at higher redshift. The Local and Coma superclusters contain thousands of galaxies and are a perfect laboratory for studying the leading processes that transform galaxies from star forming objects into red and dead structures. Moreover the nearby Universe contain a wide range of environments that have been broadly studied by many groups at different wavelengths (Haynes et al., 2011; Boselli et al., 2011; Gavazzi et al., 2010, 2012). These regions are therefore perfect to constrain the properties of galactic structures in different environments at different wavelengths, with the SDSS magnitudes playing a fundamental role in the panchromatic description of these structures. Both areas of the sky have been fully covered by the SDSS in its five optical filters (u, g, r, i, z) and the data have been first published in the data release 4 (DR4) for (Virgo, Adelman-McCarthy et al., 2006) and in the DR7 (Coma, Abazajian et al., 2009). Unfortunately, the data of the local and Coma clusters as given by SDSS are affected by the aforementioned difficulties of the SDSS pipeline and, despite the good quality of the data, many galaxies are not included in the catalogs or, if present, have in some cases unreliable photometry. Despite the fact that the worst photometric discrepancies affect only $\sim 10\%$ of the whole sample (see section 5.1.1), these happen to coincide with the brightest galaxies in the Virgo and Coma clusters, thus affecting the high mass-end determination of the luminosity function that is already hampered by the lack of sampled volume.

In this context, my work aimed at automatically generate high-quality photometry from SDSS imaging in two filters (g and i) for the SDSS sample (see Chap. 2.1). The procedure developed is not limited to the magnitude extraction but performs aperture photometry and isophotal fitting in each considered

band as well. The technical details of the procedure are described in appendix A.

Owing to our automatic method (see appendix A), in this chapter, we will investigate in detail the color magnitude relation of the local Universe in the light of the results describe in Chap. 3. In section 5.1.1 we compare the magnitudes automatically extracted by our method with the SDSS database, the Extended Virgo Cluster Catalog (Kim et al., 2014) and measurements from Gavazzi et al. (2012) and Gavazzi et al. (2013b). We test quantitatively the efficiency of the SDSS pipeline in these local clusters, while demonstrating the exquisite quality of our guided extraction. Sections 5.1.2, 5.2.1, 5.3 focus on the color-mass distribution of galaxies within our sample and on the properties of the different galactic components traced by non-tilted radial color profiles as a function of mass and morphology. The results of this first analysis is discussed in section 5.4. All results are published in **Consolandi, G.**, Gavazzi, G., Fumagalli, M., Dotti, M., & Fossati, M., 2016, A&A, 591, A38.

5.1 Photometry

For the galaxies of the SDSS sample (see Chap. 2.1) analyzed with our procedure, we compute g and i Petrosian magnitudes, surface brightness profiles and $(g - i)$ color profiles truncated at 1σ of the background. Petrosian AB magnitudes and colors are publishe in Consolandi et al. (2016) and are available via the online database GOLDMine (Gavazzi et al., 2003, 2014b).

5.1.1 Magnitudes

In the top panel of Fig 5.2, the Petrosian magnitudes extracted with the procedure described in Chap. A are compared to those downloaded from the data release 10 of the SDSS (Ahn et al., 2014). We found values for 5465 objects, while 383 ($\sim 7\%$) objects are missing in the DR10: 274 are from the Local supercluster and 113 from the Coma supercluster. Although a considerable fraction show an appreciable agreement (residuals have a $\sigma \sim 0.13$ in both the $g-$ and $i-$ band and median value of -0.05; $\sim 90\%$ of the data is in agreement within 0.4 mag, i.e. 3σ), about 20% of the SDSS magnitudes differs

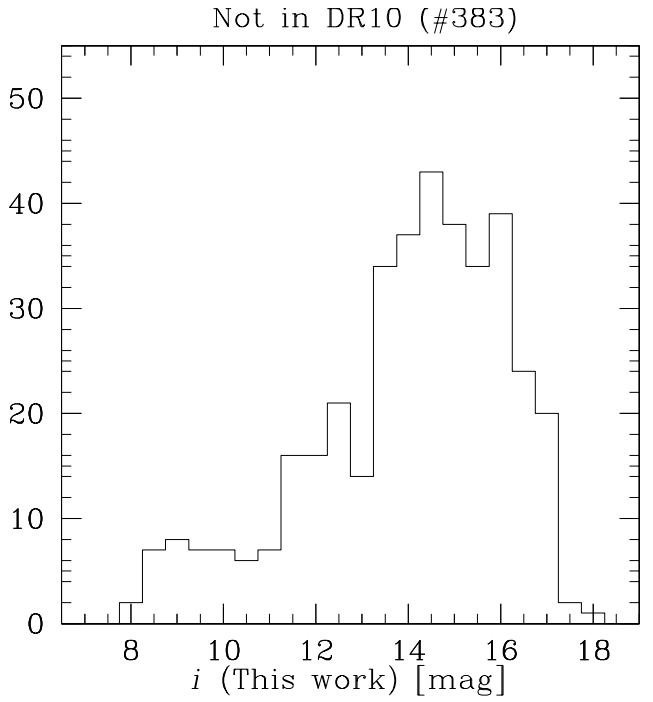

Figure 5.1: Distribution of magnitudes that are missing in the SDSS catalog as a function of the i-band apparent magnitude from this work.

of more than 0.3 mag from our determinations and about 2 % of the plotted magnitudes show up to 8 mag discrepancy in the SDSS DR10 database values.

One problem can be ascribed to the SDSS determination of the local background, i.e. by cutting all pixels above a certain sigma level and considering all remaining ones as being part of the background. For large, diffuse, extended objects this leads to a wrong local background determination that is used by the pipeline. The distribution of the residuals (bottom diagram of the top panels of Fig. 5.3, 5.2, 5.4) saturates at faint magnitudes indicating a systematic effect in small and low surface brightness systems (5th percentile at ~ -0.75 while the 95th percentile falls at ~ 0.05). We checked in the photometric catalog of the DR10 for possible causes of such an effect and found that the most deviant points are indeed low surface brightness, blue systems

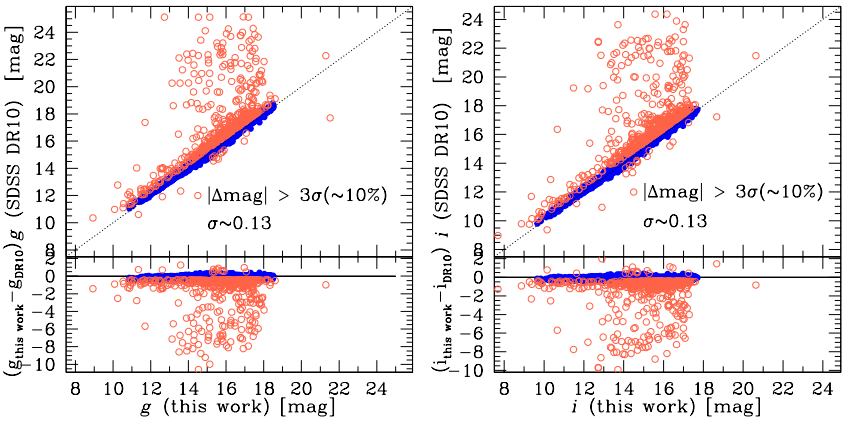

Figure 5.2: The g-band and i-band Petrosian magnitudes from this work compared to magnitudes from the SDSS Data Release 10 (Ahn et al., 2014), Blue points refer to the data within 3σ from the one to one correlation, while the orange points highlight the outliers i.e., galaxies with $\Delta mag > 3\sigma$ to the one-to-one relation (where sigma is the standard deviation of the residual distribution). In each panel we report the sigma of the residual distribution as well as the percentage of outliers. We stress that the brightest objects (42) are totally missing in the SDSS DR10. For each plot, the bottom panel reports the residual magnitudes between the two measurements.

that are flagged as NOPETRO by the SDSS pipeline. This means that their Petrosian radius could not be measured by the pipeline in the $r-$ band (because of their low SN, Lupton et al., 2001; Strauss et al., 2002) and it is set to the PSF FWHM, thus deriving PSF magnitudes for objects which are indeed extended. The other (less extreme) deviant points are again irregularly shaped, blue galaxies all reporting photometric flags indicating problems either with the raw data, the image or the evaluation of the Petrosian quantities (Lupton et al., 2001; Strauss et al., 2002) such as: DEBLENDED_AS_PSF (deblending problems), DEBLEND_NOPEAK, MANYPETRO, [1] etc. In these cases, the SDSS pipeline underestimates the Petrosian radius and hence the aperture for the photometry. Henceforth we stress that our procedure is not affected by this problem because it measures the Petrosian radius in the white image which has an improved SN ratio. This allows us to derive reliable mag-

[1] In irregular low surface brightness systems there may be more than one Petrosian radius, Lupton et al. (2001)

nitudes even in low surface brightness systems and, in general, systematically measure a larger Petrosian radius (hence Petrosian flux) if compared to the SDSS r-band Petrosian radius. Nevertheless we stress that, the fact that the Petrosian flux is taken within two Petrosian radii ensures that both apertures gather substantially the same Petrosian flux for the vast majority of the sample (Graham & Driver, 2005), i.e., the total flux. Moreover, DR10 lacks almost completely the brightest and most extended galaxies ($g \lesssim 11$, $i \lesssim 10$), as demonstrated by the distribution of the 383 objects that are not included in the SDSS database shown in Fig. 5.1.

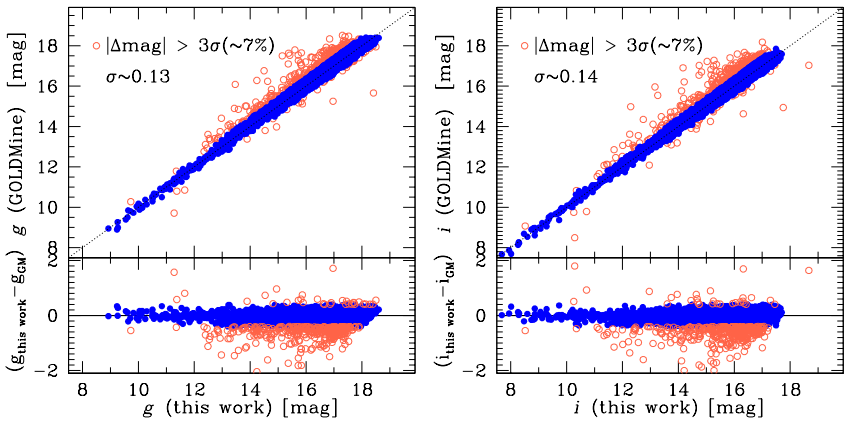

Figure 5.3: The g-band and i-band Petrosian magnitudes from this work compared to magnitudes published in Gavazzi et al. (2012, 2013). Blue points refer to the data within 3σ from the one to one correlation, while the orange points highlight the outliers i.e., galaxies with $\Delta mag > 3\sigma$ to the one-to-one relation (where sigma is the standard deviation of the residual distribution). In each panel we report the sigma of the residual distribution as well as the percentage of outliers. We stress that the agreement with Gavazzi et al. (2012, 2013b); Kim et al. (2014) is satisfactory, in particular for the brightest objects (42), that are totally missing in the SDSS DR10. For each plot, the bottom panel reports the residual magnitudes between the two measurements.

In fact, considering both discrepant and missing magnitudes, $\sim 9\%$ of the SDSS data are either unreliable or missing. In particular, in the Local supercluster, the percentage of missed galaxies of the DR10 is around 26% and, if we consider objects below 11 magnitudes, it reaches a dramatic 95%, reflecting the difficulties of the SDSS pipeline when dealing with nearby extended

objects. Moreover, the few (12) bright galaxies ($g < 11$ mag) included in the DR10 deviates more than 3σ from the one-to-one correlation in Fig.5.2. On the other hand, in the Coma supercluster, the percentage of missing and unreliable galaxies drops to 3% thanks to the smaller angular size of the objects.

To overcome the above discrepancies, about 400 galaxies of the Local supercluster have been manually measured using IRAF/QPHOT by Gavazzi et al. (2012). Moreover, for nearly 5000 galaxies in the Coma Supercluster the magnitudes were derived from the SDSS DR7 by Gavazzi et al. (2013b). We compare our automatically extracted magnitudes with those from Gavazzi et al. (2012, 2013b) (which are publicly available via the online database GOLDMine Gavazzi et al., 2013c, 2014b) obtaining a satisfactory agreement (median difference of ~ -0.025 mag), as shown in Fig. 5.3 (middle panels), especially below 11 mag. At the faint end there is less agreement, as $\sim 15\%$ of galaxies show a residual between the two measurements that exceeds 0.3 mag. The 5th percentile of the residuals distribution is ~ -0.45 mag while the 95th percentiles is ~ 0.2 mag, indicating that the systematic effect at low surface brightness affecting the DR10, affects the Gavazzi et al. measurements too. In fact, despite Gavazzi et al. checked the reliability of the magnitudes taken from the SDSS database of the magnitudes of the DR7, these were not re-calculated and therefore suffer similar problems as the DR10 data. As a matter of fact, the most discrepant objects are once again mainly blue and low surface brightness and are flagged in the SDSS photometry as problematic data. Hence, we believe that the observed discrepancies are again to be attributed to a bad evaluation of the Petrosian radius by the SDSS pipeline among some irregular and low surface brightness systems.

More recently, Kim et al. (2014) released the new Extended Virgo Cluster Catalog (EVCC) which covers an area 5.2 times larger than that of the VCC catalog (Binggeli et al., 1985). It includes 676 galaxies that were not included in the original VCC catalog. Similarly to our work, the EVCC is based on SDSS DR7 images, but it includes all the five SDSS bands $u\ g\ r\ i\ z$ determined using Source Extractor with parameters that are tailored by inspection of the individual galaxies.

We found 844 galaxies in common with the EVCC and we compared their g and i magnitudes with our results. The resulting correlation is plotted in Fig.5.4 (bottom panels) and shows a more than satisfactory agreement (median residual of -0.009 mag, $\sigma \sim 0.07$) between the two measurements. In

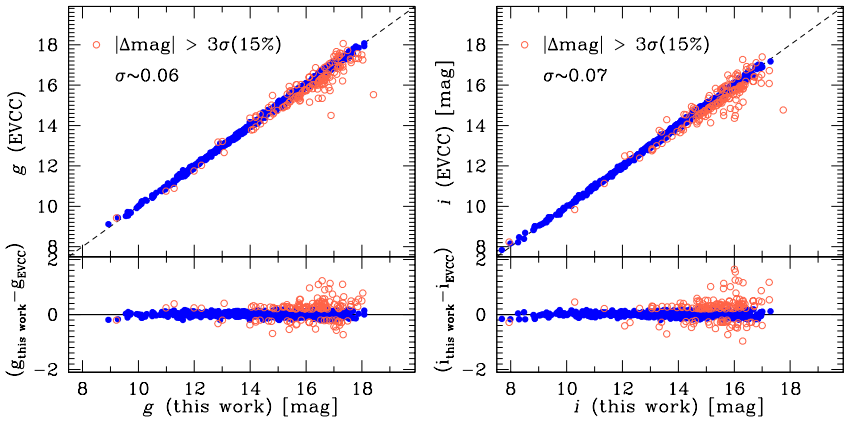

Figure 5.4: The g-band and i-band Petrosian magnitudes from this work compared to those published in the Extended Virgo Cluster Catalog (Kim et al., 2014). Blue points refer to the data within 3σ from the one to one correlation, while the orange points highlight the outliers i.e., galaxies with $\Delta mag > 3\sigma$ to the one-to-one relation (where sigma is the standard deviation of the residual distribution). Bottom panel reports the residual magnitudes between the two measurements.

particular, we remark the good agreement reached below 14 mag indicating that, unlike the SDSS photometric pipeline, neither the shredding problem nor the aperture radius measurement affect the results of both semi-automated methods. Moreover, 85% of the galaxies differs by less than 0.2 mag between the two studies. The Kim et al. (2014) magnitudes are measured by Source Extractor within an aperture with radius equal to k times the Kron radius (Graham & Driver, 2005) of the galaxy, where k is the Kron factor and is set to $k = 2.5$. This value is chosen because is expected to recover more than 94% of the total flux (Bertin & Arnouts, 1996). Therefore the agreement further demonstrate that the aperture radius set to two times the Petrosian radius evaluated in the white image recovers efficiently the total flux of the galaxy. Despite the overall excellent agreement, 6% of galaxies above mag ~ 15 display a difference between our and their measurements that exceeds 0.3 mag ($\sim 5 \times \sigma$) and, in two cases, the two determinations differs of ~ 3 mag. The vast majority of these discrepant objects appear significantly fainter in our analysis and are low surface brightness systems that lie very near to bright sources (e.g., stars, interacting galaxies etc.). We re-measured these magni-

tudes with IRAF/QPHOT and concluded that some contaminating light has likely not been fully masked by Kim et al. (2014).

5.1.2 The color magnitude diagram

After computing the observed magnitudes, we correct them for Galactic extinction, following the 100 micron based reddening map of Schlegel et al. (1998), re-calibrated by Schlafly & Finkbeiner (2011). Furthermore, colors of late-type galaxies are corrected for internal extinction using the empirical transformation (Gavazzi et al., 2013b)

$$(g-i)_0 = (g-i)_{mw} - 0.17([1-\cos(incl)][\log(\frac{M_\star}{\mathrm{M}_\odot}) - 8.17]), \quad (5.1)$$

where $(g-i)_{mw}$ is the color corrected for Milky Way Galactic extinction, $M_\star$ is the mass computed with eq. 5.2 using the uncorrected color and $incl$ is the inclination of the galaxy, computed following Solanes et al. (1996).
Stellar masses are derived from the i magnitudes and the inclination corrected color $(g-i)_0$, assuming a Chabrier IMF via the mass vs i-band luminosity relation

$$\log\left(\frac{M_\star}{\mathrm{M}_\odot}\right) = -0.96 + 1.13(g-i)_0 + \log\left(\frac{L_i}{\mathrm{L}_\odot}\right) \quad (5.2)$$

published by Zibetti et al. (2009), where L_i is the i-band luminosity of the galaxy in solar units.

Fig. 5.5 (top panel) shows the observed color-mass diagram of the Local and Coma superclusters before the inclination correction is applied. The sharp oblique density contrast in the figure occurring around $10^8\mathrm{M}_\odot$ is caused by the SDSS selection ($r < 17.7$) at the different distances of the Local and Coma superclusters (respectively $\sim$ 17 Mpc ad $\sim$ 95 Mpc) and by the mild dependence on galaxy color of the mass-luminosity relation. The Local supercluster is indeed less populated due to the lack of sampled volume and is undersampled at high masses. Nevertheless, owing to its proximity, the SDSS selection allows us to include in the analysis galaxies down to masses as low as $\sim 10^{6.5}\mathrm{M}_\odot$. On the contrary, the selection restricts the Coma color-magnitude relation to $\gtrsim 10^{8.5}\mathrm{M}_\odot$ making the blue cloud relation appear steeper than the local one (see Tab. 5.1).

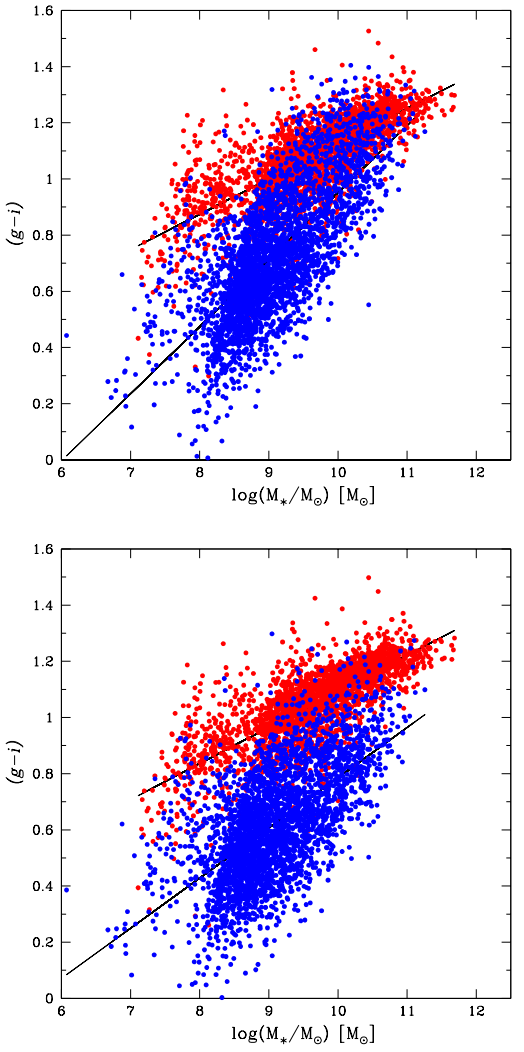

Figure 5.5: Top: Color magnitude diagram of the observed colors displaying the well known bimodal distribution for late type galaxies (blue cloud, blue dots) and early type galaxies (red sequence, red dots) selected accoridng to the morphological classification available in GOLDMine. Bottom: the color magnitude diagram after the inclination correction has been applied. The red sequence and the blue cloud are well separated at all masses.

Table 5.1: Slopes of the linear fits $(g-i) = a + b \times \lg(M_*)$ of the blue cloud and red sequence for the Local supercluster (Lsc), the Coma supercluster (Csc) and the whole sample (All).

Sample	b_{LTG}	b_{ETG}
Lsc	0.148 ± 0.007	0.121 ± 0.005
Csc	0.214 ± 0.005	0.150 ± 0.004
All	0.184 ± 0.004	0.131 ± 0.002

Early-type galaxies (dE,dS0, E, S0 and S0a; red dots) form the red sequence while late-type galaxies (from Sa to Irr, blue dots) follow the blue cloud that overlaps with the red sequence at high masses, as highlighted with early SDSS data by Strateva et al. (2001),Hogg et al. (2004). The morphological cut is based on the morphological classification available in GOLDMine (Gavazzi et al., 2003, 2014b). After the internal extinction correction is applied, as in Fig. 5.5 (Bottom panel), the color magnitude preserves its bimodality, with less overlap at high masses. At this point a note of caution is required: the selection bias that affects the more populated Coma sample prevents us from reliably extract a general slope. Therefore we constraint our fit to the deeper data of the local Universe and find that the slope of the blue cloud remains steeper than that of the red sequence even after the corrections. As a matter of fact, the local blue cloud best fit changes from $(g-i)_{LTG} = 0.18 \times \log(M_*) - 0.87$ in the uncorrected plot to

$$(g-i)_{LTG;0} = 0.15 \times \log(M_*) - 0.64 \tag{5.3}$$

when the correction is applied, where $(g-i)_{LTG}$ and $(g-i)_{LTG;0}$ are respectively the blue cloud uncorrected and corrected color and the error over the slope is as low as $\sim 3 \times 10^{-3}$ in both relations. As expected, since no inclination correction acts on ETGs, the red sequence fit remains consistent in both relations:
$(g-i)_{ETG} = 0.13 \times \log(M_*) - 0.12$.

5.2 Radial Color profiles

For each object of the sample, our procedure yields a radial color profile. In this section, we discuss the color profiles extracted by taking a closer look to some prototypical cases. Then we describe more quantitatively the general properties of color profiles along the Hubble sequence creating a set of radial color profile templates of different morphological classes in different mass bins.

In general, the color is a good tracer of the specific SFR: regions actively forming stars have bluer colors than regions of quenched SFR and profile shapes generally correlate with the Hubble type. Early type galaxies (e.g., Es and S0s) typically have almost flat and red profiles, common among the red and dead objects (Tamura & Ohta, 2003; Wu et al., 2005). Differently from the ETGs, irregular galaxies are characterized by an almost flat blue profile reflecting their lack of dust and their ongoing SF activity at all radii (Fig. 5.6, bottom row). Finally spiral galaxies have a composite profile that is blue at large radii and becomes redder only toward the center in correspondence with structures such as bulges or bars (e.g., VCC-1690 in Fig. 5.6, see also Gavazzi et al., 2015, for a detailed discussion), consistent with the conclusion drawn by Fossati et al. (2013) who compared the distribution of the star formation from Hα imaging flux with the stellar continuum.

Strong deviations from the typical color profiles can be induced by strong dust absorption, as in the case of the highly inclined galaxy VCC-873 shown in Fig. 5.6. The strongest deviations are observable in the nuclear regions of galaxies, where, for example, nuclear dusty disks are detectable as clear deviations toward a redder color (see, e.g., VCC-1154 in Fig. 5.6, *top-left*). On the other hand, unobscured HII regions, dominated by young stars, can cause strong deviations towards the blue in the color profiles. The barred spiral galaxy VCC-508 (Fig. 5.6, *top-right*) is the perfect posterchild of this class of objects, with a color profile deviating towards the blue on a scale of 3 arcseconds ($\sim$ 300 pc), in correspondence with a star-forming ring (vividly shown in the HST archival image), and possibly in correspondence of the bar Inner Lindblad Resonance (ILR, Kormendy & Kennicutt, 2004; Comerón et al., 2010; Font et al., 2014). Similar nuclear blue spikes can be associated to unobscured AGNs and Post Starburst (PSB) nuclei. An example of galaxy hosting a PSB nucleus is VCC-1499 (shown in Fig. 5.6), a member of the dEs of the Virgo cluster

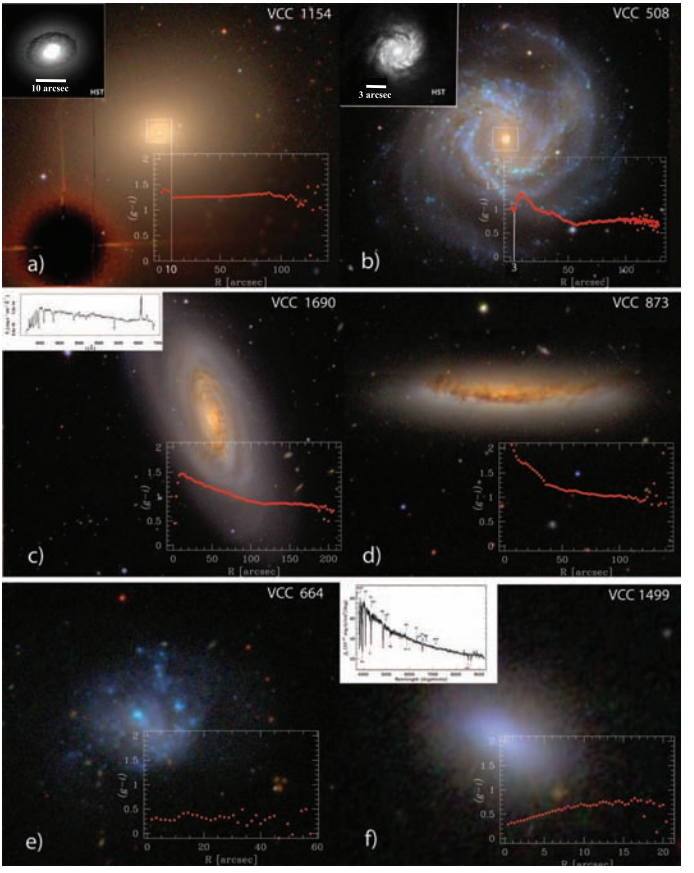

Figure 5.6: RGB SDSS images and (g-i) extracted color profiles of six galaxies belonging to the Local supercluster sample: (a) VCC 1154 is an S0 galaxy with a circumnuclear dusty disk of ~ 800 pc as shown by an archival HST image. The presence of these structures is easily spotted by a clear deviation towards the red on circumnuclear scale in the (g-i) profile at 3" as indicated by the vertical white line. (b) The barred spiral galaxy VCC 508. Its circumnuclear star-forming disk (highlighted in the inset) produces a deviation towards blue in the color profile at ~ 10" as indicated by the vertical white line. (c) VCC-1690 (Boselli et al. 2016), spiral galaxy with a strong blue AGN nuclear (g-i) color. Its nuclear spectra (shown in the inset) exhibit the key signatures of Post Starburst galaxies. (d) Late-type galaxy VCC-873. The AGN activity is strongly obscured by dust and its color profile reaches extreme values. (e) Irregular galaxy VCC 664 and its blue, nearly flat color profile. (f) The low mass galaxy together with its PSB-like nuclear spectrum. Its central emission strongly deviates towards bluer colors with respect of the outermost region of the galaxy.

that display blue nuclei (Lisker et al., 2006). To better test the good quality of our profiles in Fig. 5.7 we show the comparison between color profiles extracted in this work with the ones derived from the surface brightness profiles published by McDonald et al. (2011) for six galaxies of different morphological types: VCC1632 (E), VCC 2095 (S0), VCC0596 (Sc), VCC1555(Sc), VCC1356(Sm), VCC1499(dE). The agreement is good indicating once again the good quality of the photometry produced by our automatic pipeline. Nevertheless small differences appear especially in late type galaxies in Fig. 5.7. We ascribe these effects to the fact that the profiles of McDonald et al. (2011) were extracted with an isophotal fitting procedure (i.e., ellipticity and PA of the ellipses are allowed to vary) contrary to ours. In fact the greatest deviations are displayed in VCC0596. VCC1555, VCC1356 that are three late type galaxies, respectively an Sc, Sc and Sm. In these objects, isophotes twists in correspondence with non axisymmetric structures.

5.2.1 Templates

This section is devoted to a more quantitative analysis of the color profiles and of their correlations with stellar mass and morphology, focusing only on Local supercluster galaxies, which are resolved on scales of ~ 100 pc. Moreover, in this way, we are not affected by the selection bias discussed in chapter 2. Template profiles allow us to investigate the average properties of color profiles in our sample as a function of mass and morphology. After normalizing each profile to the Petrosian radius and correcting for Galactic extinction, we create template profiles in different bins of stellar mass and morphology with a radial step of 0.05 R/R$_{pet}$. Further on we correct the profiles for internal extinction. Despite the fact that we cannot obtain radial extinction profiles, Holwerda et al. (2005) show that on average the radial extinction profiles of spirals are flat within the given errors, except for the very central region ($R \lesssim 0.2\ R_{25}$) where extinction can be significantly more severe with respect to the external parts. It is impossible to correct for dust extinction this region relying solely on the optical data and to implement a precise galaxy-to-galaxy dust correction for the whole sample is way beyond the scope of the present study. Therefore we correct the profiles applying the average correction evaluated for the total color of the galaxy. In addition, we did not include galaxies with $incl > 60^o$, in order to avoid contaminations from edge-on spirals whose

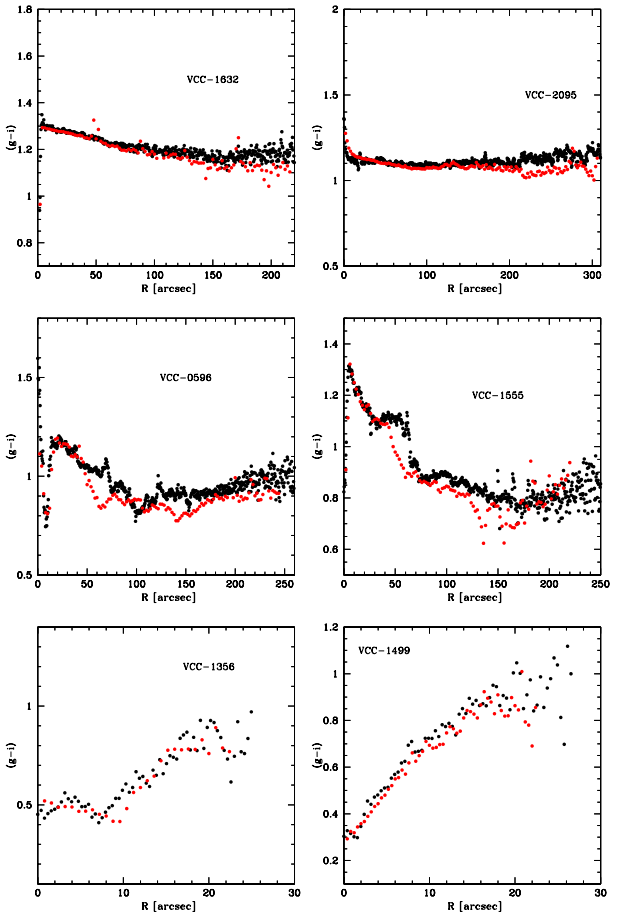

Figure 5.7: Comparison of our color profiles (red dots) with the ones derived from McDonald et al. (2011) (black dots) for six galaxies matching the two samples of different types. From top left to right we plot VCC 1632, VCC 2095, VCC 596, that are respectively an E,S0,Sc (from NED). In the second row we plot VCC 1555, VCC 1356, 1499, respectively an Sc an Sm and a dE. There is an overall good agreement but the profiles display some differences especially in late type galaxies. We ascribe these effects to the difference in the isophotal fitting technique and the one adopted in this work to extract the profiles. McDonald et al. (2011) are indeed sensitive to twists of the isophotes occurring in the presence of spiral arms, bars and even in bright HII regions in irregular galaxies.

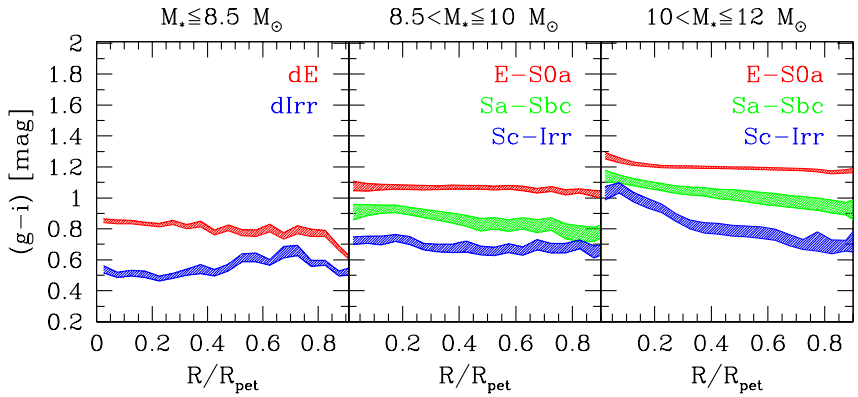

Figure 5.8: Template color profiles in different bins of mass and morphology. Left panel: low mass bin (M$\leq 10^{8.5}$M$_\odot$) where red stands for dwarf ellipticals (dE) and blue for dwarf irregulars (dIrr). Central panel: intermediate mass bin ($10^{8.5}$M$_\odot$ <M$\leq 10^{10}$M$_\odot$) where red dots are for the ETGs (from E to S0a) template, green dots for Spirals (from Sa to Sbc) and blue dots for Sc−Irr LTGs. Right panel: high mass bin (M$> 10^{10}$M$_\odot$) where the color code is the same as the intermediate mass bin. In both the high-mass and the intermediate-mass bins, we did not take into account galaxies with $incl > 60^o$.

internal and external colors are dramatically reddened by the dust extinction through the disk plane (see Fig. 5.6d). We defined three equally populated mass bins:

- a low mass bin containing galaxies with $M_* \leq 10^{8.5}$ M$_\odot$,
- an intermediate mass bin, in which $10^{8.5} < M_* \leq 10^{10}$ M$_\odot$,
- a high mass bin, in which $10^{10} < M_* \leq 10^{12}$ M$_\odot$.

In the intermediate and high mass bins we identified three morphological classes: the first class contains elliptical galaxies, S0s and S0a; the second bin includes late type galaxies from Sa to Sbc while the last bin Sc and irregulars. The cut is based on the morphological classification taken from GOLDMine (Gavazzi et al., 2003, 2014b) which, in the Local Universe, is mainly based on the morphological classification performed by de Vaucouleurs et al. (1991) and Binggeli et al. (1985) on photographic plates of exquisite quality.

Galaxies with masses lower than $10^{8.5}$ $M_{\odot}$ are either classified as dwarf ellipticals or dwarf irregulars. The resulting template profiles are shown in Fig. 5.8, separately for each morphological bin.
Summarizing, early type galaxies do not show significant gradients, irrespective of their mass. Late type galaxies show instead flat profiles in the low mass bin while, at higher masses, their profiles show evident color gradients, implying the presence of a red component in their central region whose importance increases with mass. Focusing on the highest mass bin, spirals are as red as ellipticals in their central parts and as blue as dIrrs in their outskirts. In other words, given the well known color-sSFR relation, spirals are primarily quenched in a central region whose importance is a function of mass while their outermost regions remain star forming (Fossati et al., 2013).

5.3 Dissecting the color-magnitude relation

Inspecting Fig. 5.8 with the aim of further investigating properties of color gradients, we identified three non-overlapping zones of interest of the color profiles:

- the nuclear (or innermost) region going from the center of the galaxy up to approximately $1\mathrm{kpc}$.

- an intermediate region defined by $0.2\mathrm{R}_{Pet} \leq \mathrm{R} \leq 0.3\mathrm{R}_{Pet}$;

- an outer, disk-dominated, zone with $\mathrm{R} \geq 0.35\mathrm{R}_{Pet}$.

Fig. 5.9 shows the galaxy color as a function of the total stellar mass for each of the three zones, all corrected for Galactic extinction, with the disk-dominated zone also corrected for inclination. Overall, galaxies belonging to the red sequence are insensitive to this decomposition and show a consistent gradient in all three mass-color diagrams traced by each zone. Instead late-type galaxies populate a blue cloud that show three different distributions for each of the three zone analyzed. While the outer region of late type galaxies follows a relation almost parallel to the red sequence, the inner zones lie on much steeper color-mass relations.

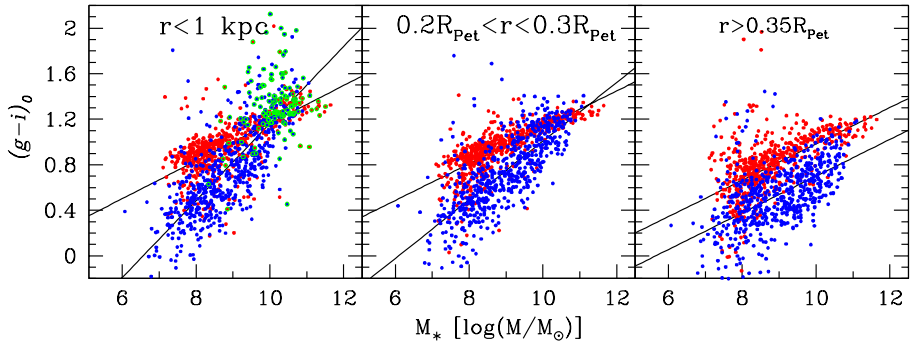

Figure 5.9: Color-magnitude diagram of three different zones where red dots are ETGs and blue dots are LTGs: (left panel) inner zone, where open green dots are galaxies hosting an active galactic nucleus of different kinds (LINERs, Seyfert, AGN) classified on the basis of nuclear emission lines; (central panel) intermediate zone; (right panel) outer, disk-dominated zone.

5.3.1 Nuclei

In the left panel of Fig. 5.9 we plot the color mass diagram of the inner kpc of galaxies in our local supercluster sample. Early type galaxies form a well defined red sequence while late type galaxies lie on the blue cloud. Comparing this diagram to the classical color-magnitude, the red sequence slopes are consistent. Nevertheless, considering nuclear colors, late type galaxies scatter around a much steeper relation that crosses the red sequence at about 10^9 $M_\odot$, displaying color indices even greater than those for typical early types at $M_* > 10^{9.5-10} M_\odot$. Furthermore, in the mass range 10^9-$10^{12} M_\odot$, we highlight galaxies with ongoing nuclear activity, such as AGNs, LINERS and Seyfert (green dots in the left panel in Fig. 5.9). The adopted nuclear activity classification is based on the ratio of nuclear Hα and [NII] emission lines according to the WHAN (Cid Fernandes et al., 2011) diagram. Nuclear emission lines were taken from the SDSS spectroscopic database Data Release 12 (Alam et al., 2015), complemented with spectra available in NED and other measured by Gavazzi et al. (2013c). Overall we find the nuclear classifications for 91% of the galaxies.

As it can be seen in figure 5.9, these objects, highlighted in green, deviate

from the relations followed by the red sequence and the blue cloud and reach the most extreme red values of color indices at any given mass.
To further investigate how the color inside the nuclear region is linked to its nuclear activity we define an index of "central/nuclear reddening" :

$$Q_{red} = (g-i)_{nuc} - (g-i)_0, \tag{5.4}$$

where $(g\text{-}i)_{nuc}$ is the nuclear-scale color corrected for Galactic extinction and $(g\text{-}i)_0$ is the mean color of the galaxy. Q_{red} estimates the deviation of the nuclear color from the average color of the galaxy. Fig. 5.10 shows the distribution of Q_{red} for four different categories of nuclear activity: in orange, we plot the distribution of the RETIRED (galaxies that stopped their star formation and have their gas ionized by old stellar populations, Stasińska et al., 2015) and Passive nuclei galaxies; in red are displayed LINERs, AGNs and Seyfert; blue represents Post Staburst (PSB) galaxies and green is for HII region-like nuclei.
The identified categories distribute quite differently: Passive and Retired galaxies show a quite tight distribution peaked at $Q_{\rm red} \sim 0$; Active Galactic Nuclei are undoubtedly associated with colors that are redder than the average of the galaxy. The vast majority ($\sim 91\%$) have values of $Q_{\rm red} > 0.0$ and only 9% of AGNs display a bluer nucleus with respect to the galaxy color. Moreover, if we consider galaxies reaching the more extreme deviations, i.e. $Q_{\rm red} > 0.3$, they represent the 45% of the AGNs population. This effect is possibly due to dust absorption associated with the gas fueling the nuclear region, although a contribution from the AGN itself cannot be excluded based only on the optical data. Post Staburst (PSB) galaxies are, on the contrary, associated with nuclei that are bluer with respect to the galaxy color since in 80% of cases PSBs display a $Q_{\rm red} < 0$; HII-region like nuclei have instead the most widespread distribution of nuclear colors, with respect to the galaxy color. The evidence of a bluer nucleus in PSBs and the fact that they are preferentially found in higher density environments is consistent with a picture where these objects are transitioning from the blue cloud to red sequence quenching their star formation in an outside-in fashion due to a ram pressure stripping event (Gavazzi et al., 2010).
Moreover, if we consider low and high mass galaxies separately (Fig. 5.10, *bottom panel*), the distribution is bimodal: HII region-like nuclei in massive galaxies are always redder than the galaxy itself while, at low masses, the dis-

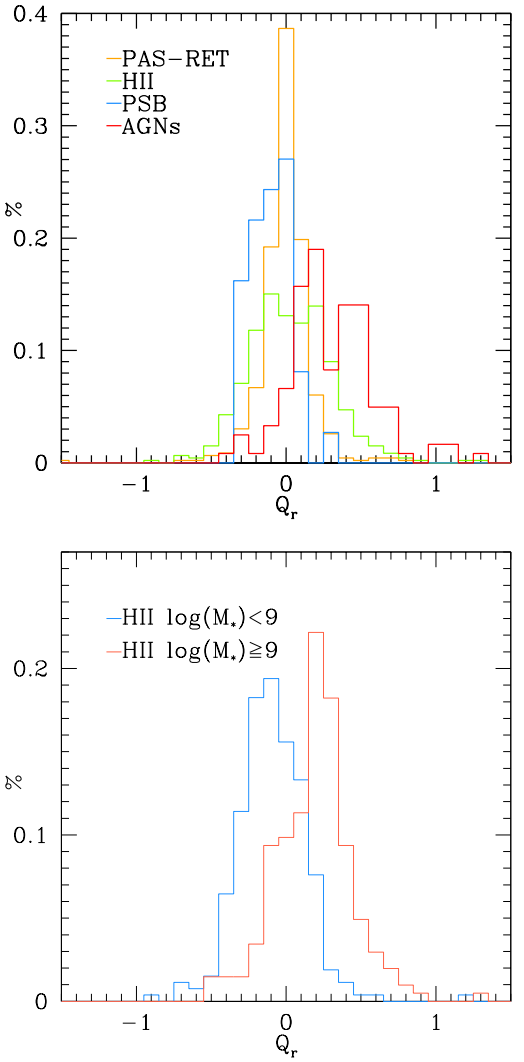

Figure 5.10: (Top) Normalized distributions of the nuclear reddening Q_r indices for different classes of nuclear activity (computed following Cid Fernandes et al., 2011) color coded as follows: AGNs are represented by a red line; the (PSBs) distribution is traced by the blu line; the green line stands for HII-like nuclei and the orange for PASSIVE and Retired galaxies. (Bottom) Normalized distributions of HII-like nuclei above (red) and below (blue) $10^9 M_\odot$.

tribution is dominated by galaxies showing a nucleus that is bluer with respect to the average color of the galaxy.
This is consistent with a picture where nuclei of small galaxies are more likely to be caught in a bursting act and have little or no dust absorption (Holwerda et al., 2005) while, massive galaxies have on average a redder nucleus with respect to the galaxy color possibly due to dust extinction. Nevertheless, our optical data cannot exclude a contribution from an underlying older stellar population.

5.3.2 Bulges, Bars and Disks

Focusing on the second and third panel of Fig. 5.9, we highlight the intermediate and disk zone contribution to the color-magnitude diagram. The red sequence is once again consistent between the two plots. Indeed, the slopes determined with a least squared fit of the red sequence in the two diagrams are consistently 0.17 ± 0.01 and 0.16 ± 0.01 mag dex^{-1}. On the other hand, the blue cloud differs significantly: its slope varies from 0.34 ± 0.01 mag dex^{-1} in the innermost region to 0.28 ± 0.01 and 0.18 ± 0.01 mag dex^{-1} respectively in the intermediate and disk-dominated regions.

Therefore, in the intermediate zone, the blue cloud displays a steep relation although not as steep as in the innermost region. Nevertheless, the blue cloud completely overlaps the red sequence at $M_* > 10^{10} M_\odot$. This behavior drastically changes in the disk-dominated zone (right panel of Fig. 5.9). Indeed, the outer-zone color magnitude diagram is composed of two well separated distributions: the blue cloud increases its color with mass following a slope that is almost identical to the red sequence.
In the intermediate zone, above a threshold mass, LTG galaxies have therefore suppressed SF and assume color values typical of ETGs. On the contrary, they mostly appear as normal star forming objects in their outer disks.

Moreover, the growth of the red component and the color contamination from the star forming disk (with bluer colors) in this zone can be approximately traced by the color difference between the intermediate and the outer zone shown in Fig.5.12, where this difference is plotted as a function of mass. Despite a significant scatter, a Kolmogorov-Smirnov test confirms that the distributions of ETGs and LTGs are not drawn from the same parent sample ($P \lesssim 10^{-3}$). Red and blue lines connect the average difference between the

intermediate and outer regions inside bins of 1 $\log(M_*/M_\odot)$ separately for ETGs (red) and LTGs (blue). This diagram shows that early type galaxies display an average mild gradient of approximately $\lesssim 0.1$ mag from low to high mass galaxies.

Late type galaxies are instead characterized by a gradient between the two zones whose importance increases with mass. This is consistent with a picture where galaxies develop a red and dead, quenched structure in their central regions, the relevance of which depends on mass. In their disks, instead, late type galaxies preserve their star formation almost unaffected. Nevertheless, even the outer regions, which are occupied by SF structures and are therefore blue, still display an increasingly red color with increasing mass (see Fig 5.9, right panel). As a note of caution, we remind that the correction for internal extinction is not radially dependent and although it is a good approximation, some small residual contribution of the dust absorption might still affect the profiles. Nevertheless, visual inspection of many images and profiles support the idea that the main cause of the red color observed is due to different stellar populations instead of dust extinction.

5.4 Discussion

Our method successfully led to a set of final optical color-based parameters that trace some properties of nuclei, bulges and disks among our Local sample. In our analysis, we searched for systematic gradients in $(g - i)$ color profiles in different galaxy types. Here we compare our results with literature studies and discuss their implications for galaxy formation and evolution.

We investigated color gradients with two different techniques: in section 5.2.1 we built color profiles templates for different morphological classes in three bins of increasing mass; in section 5.3 we relate the galaxy total stellar mass versus the average color of three different, non-overlapping regions in which respectively nuclei, bulges (and/or bars) and disks are the dominant structure. As a general result, regardless of the binning used, colors show a mass dependency, with more massive galaxies harboring redder structures with respect to their lower mass counterparts (see Fig. 5.9), confirming different literature results.

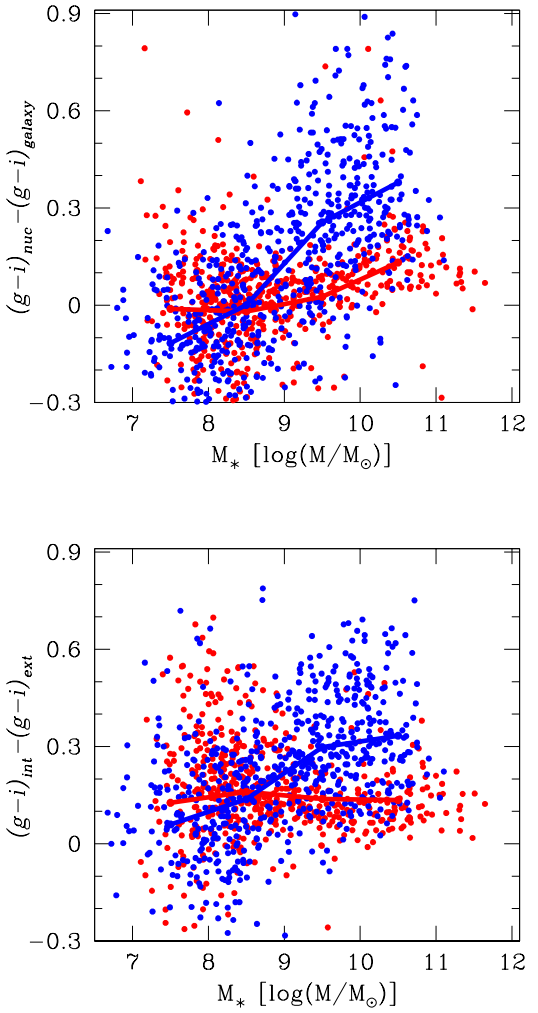

Figure 5.11: Top:Distribution of the difference between the color indexes of the nuclear zone and the color of the galaxy plotted against the total stellar mass. Bottom:Distribution of the difference between the color indexes of the intermediate zone and those of the disk-dominated zone plotted against the total stellar mass. In both panels, the blue and red small dots stand for respectively the blue cloud and the red sequence galaxies. The blue (red) line connects the average value in 4 bins of $10\log(M/\mathrm{M}_\odot)$ from 10^7 to 10^{11} $\mathrm{M}_\odot$ for LTGs (ETGs).

5.4.1 Nuclei

Our investigation of nuclear regions confirms the tight correlation existing between the color of nuclei and the luminosity/mass of the host-galaxy that has been consistently observed in detailed studies of massive Virgo cluster galaxies by the ACS Virgo cluster survey (Côté et al., 2006) and of fainter galaxies of the Virgo and Fornax clusters (Lotz et al., 2004). We find that the correlation holds for both faint and bright galaxies although it shows a large scatter in the bright end of the distribution. Consistently, Côté et al. (2006) have shown that the brightest early type galaxies show a considerable scatter in the nuclear color magnitude. Nevertheless, a note of caution is required: the scale that defines our innermost region extends up to 1kpc, which is approximately ten times the scale length of the nuclei studied in the ACS Virgo cluster survey and by Lotz et al. (2004) both relying on HST data. In particular, we note that our innermost region extends to the typical distance within which dusty structures such as the one in Fig. A.1(a) are found. In the ACS these represents $\sim 20\%$ of the ETGs and therefore at least for these early type galaxies, the high reddening is likely dominated by the presence of structures of dust instead of their underlying stellar populations. Nevertheless we still find evidences of the results drawn by Lotz et al. (2004) and Côté et al. (2006): all nuclear regions of bright ETGs are redder than their harboring galaxy (Côté et al., 2006) while, at the faint end of the red sequence, nuclear colors are more scattered and often bluer than the color of their host galaxy (see top panel of Fig. 5.12).

LTGs show similar trends although strongly amplified compared to the ETGs. Intriguingly, among the high mass, scattered population of both ETGs and LTGs, it appears to be a correlation between the color in the innermost region and the AGN activity of the nucleus: nuclei of active galaxies are found on average to be redder than their non-active counterparts (see Fig. 5.9). Nevertheless, given the large extension of our innermost region, we refrain from considering the AGN as main contributors to the color of the nuclei in these galaxies, as such effect could be related to the extinction caused by the dust dragged by the gas that occupies the region and fuels the AGN. Our analysis is consistent with the stellar population study presented by Côté et al. (2006) who find an old/intermediate stellar population component in the nuclear regions of all bright galaxies (ETGs and LTGs). These still follow a color

magnitude relation despite the scatter at high mass that suggests that, at least for the most deviant population, the nuclear chemical enrichment was governed by internal/local factors. The presence of disky dusty structures even in evolved systems such as Es and S0s suggests that the region is periodically refurbished with gas and dust. For example, secular disk instabilities or mergers can funnel the gas and the dust toward the very center of the galaxy. Consequently the strong degeneracy between absorption and stellar population age on such scales prevents from a unique interpretation of the history of these structures relying solely on optical data (Driver et al., 2007). Further on, as it is shown in the faint end of the two distributions in Fig 5.12 (*Top*), many LTGs have nuclei that are bluer compared to the galaxy color (Taylor et al., 2005) and, despite a considerable scatter, many ETGs also display blue nuclei consistently with Lisker et al. (2006). Our spectroscopic analysis revealed that a fraction of the population of blue nuclei is possibly populated by PSB galaxies (see Fig 5.10) which have recently experienced a recent, sudden shut down of star formation and by nuclei that retain some residual SF activity (HII-like) despite the poor HI content of the host galaxy. These systems are undergoing an outside-in quenching of the star formation in the Virgo cluster hinting at physical processes such as harassment (Moore et al., 1996) and ram pressure stripping (Gunn & Gott, 1972) as possible causes of such evolutionary paths.

5.4.2 Bulges, Bars & Disks

Despite the considerable scatter in both colors and color gradients (Peletier & Balcells, 1996; Taylor et al., 2005; Roediger et al., 2011a), the tight correlation between color and stellar mass of the host galaxies holds true in both the region identified as intermediate and outer in section 5.3. ETGs form a tight red sequence (see Fig. 5.9) for both regions and show an average inside-out gradient of ~ 0.1 mag (Fig. 5.12, *bottom*). LTGs form instead two different distributions: the blue cloud of the intermediate (or bulge/bar) region becomes red (i.e., it reaches the red sequences) above 10^{10} $M_{\odot}$ while the outer, disk-dominated region never overlaps completely the red sequence. Still, more massive disks are redder than their lower mass counterparts but the difference between the colors of the outer and the intermediate region increases with respect to the total stellar mass. This can be possibly induced by the growth of a red and dead structure in the center of massive disks, i.e. that the central part of galax-

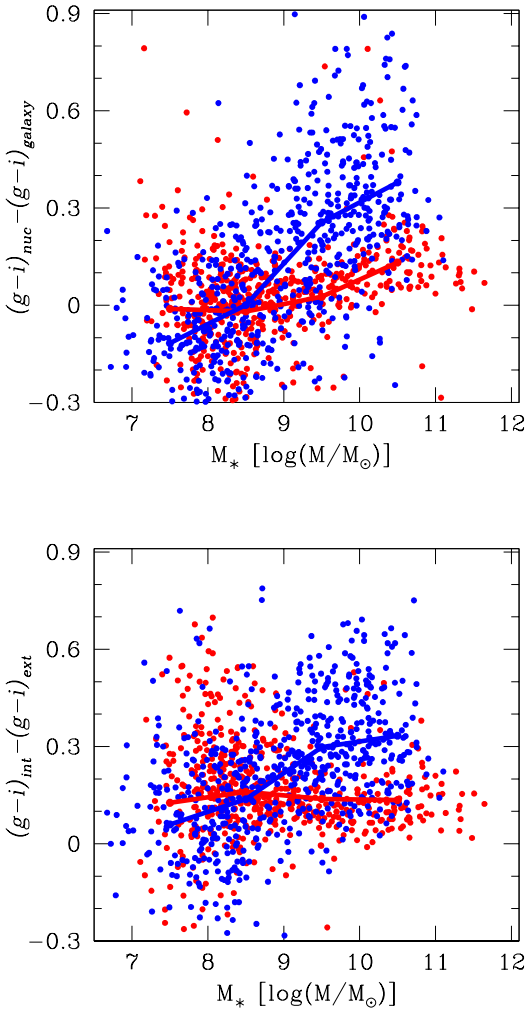

Figure 5.12: Top:Distribution of the difference between the color indexes of the nuclear zone and the color of the galaxy plotted against the total stellar mass. Bottom:Distribution of the difference between the color indexes of the intermediate zone and those of the disk-dominated zone plotted against the total stellar mass. In both panels, the blue and red small dots stand for respectively the blue cloud and the red sequence galaxies. The blue (red) line connects the average value in 4 bins of $10\log(M/\mathrm{M}_\odot)$ from 10^7 to 10^{11} $\mathrm{M}_\odot$ for LTGs (ETGs).

ies underwent a star formation quenching process that turned them red. Our results on the average properties of color profiles broadly agree with literature data. For example MacArthur et al. (2004) have shown that the radial profile of the average ages of the stellar populations decreases from inside out and that the steepness of the decrease is a function of morphological type. Color templates shown in Fig. 5.8 exhibit a radial behavior fully consistent with the average age profiles shown by MacArthur et al. (2004). We find there is also a good agreement with the (g-H) color profiles published in Roediger et al. (2011a) for almost all the morphological types, although in their median profiles of early disks they find positive color gradients (and consistently positive age population gradients in their stellar population analysis, Roediger et al., 2011b) that we do not see. Roediger et al. (2011b) do not find any direct link between galaxy morphologies and the observed stellar population gradients. On the contrary, the results of Chap. 3 and studies such as Cheung et al. (2013) show that the bar occupation fraction rises steeply above $10^{9.5}$M$_{\odot}$ (as also confirmed by the works done by Skibba et al., 2012; Masters et al., 2012) and that, above this mass,galaxies are progressively more quenched (red) in their centers, while their disks still sustain SF and hence are blue. These results therefore highlight that the presence of structures such as bars can indeed produce the color gradients that we observe and likely also the stellar population gradients. These authors thus conclude that a secular bar drives the quenching of the star formation in the central kiloparsecs of galaxies. Moreover massive galaxies undergo bar instability earlier than their lower mass counterparts and thus have more time to grow redder than low mass systems. Moreover, Méndez-Abreu et al. (2012) on a study of the Virgo bar fraction have shown that this rises up to more than 50% above 10^{10}M$_{\odot}$, adding a further link between color/stellar populations radial gradients that we observe and structures such as bars (Laurikainen et al. 2010). We stress, however, that disk instabilities can also rejuvinate the central stellar population by, e.g., triggering central star formation in correspondence of the ILRs of spirals or bars (an example could be the one of VCC 508 in Fig. A.1 (a)).
Both MacArthur et al. (2004) and Roediger et al. (2011a), also observe a positive gradient in low mass galaxies. Among these galaxies we find only a mild gradient in the template profile of dIrr in Fig. 5.8. From Fig. 5.12 we are taken to conclude that positive gradients can be found in low mass galaxies especially if we consider the most internal regions (Lisker et al., 2006;

Fossati et al., 2013) in contrast to the external parts but that the severe scattering occurring at low mass in our parameters prevents from extracting a robust general trend. This could be related to the fact that the low mass population may be composed of objects with different formation processes (van Zee et al 2004; Lisker et al. 2008). In our sample, positive gradients are most noticeable in the nuclear region (Fig. 5.12, Top) while in the comparison between the color of the intermediate region with the color of the disk-dominated region their difference is consistent with zero.

Chapter 6

The colors of bars

In the previous chapter we found evidences for the growth of a red central component in LTGs from low to high mass galaxies. In order to investigate if the presence of a bar can be responsible for such a trend, we ran over the same sample the isophotal fitting task described in appendix A and then, the bar-finder algorithm described in A.3. Limitations, pureness, and completeness of the automatic classification are discussed in section 6.2 by comparing the final selection to other classifications found in the literature. In section 6.3 the resulting bar fraction versus mass relation is compared to other published results. Finally, the results are discussed in section 6.4 and the bar-quenching scenario described in chapter 3 is tested by creating a set of templates of color profiles of barred galaxies in different bins of mass. These are also compared to the template color profiles discussed in chapter 5.2.1.

The results of this chapter have been published in **Consolandi, G.** 2016, A&A, 595, A67.

6.1 The automatic classification

In order to account only for systems that can develop non-axisymmetric structures in the barfraction estimate, a morphological cut is applied to exclude pressure supported systems. The morphological classification of all the galax-

ies of the sample is found in the online public database GOLDMine (Gavazzi et al., 2003, 2014b). Nevertheless this classification is purely visual (Binggeli et al., 1985) and probably does not accurately separate slowly rotating systems (elliptical galaxies) and fast rotators (namely S0s), preventing a robust estimate of the bar fraction when including early-type disks. Therefore I give the results separately for the sample of late-type disks (from S0a to Sm and Irr) and the sample that includes S0s. The procedure performed the extraction over a subsample of 922 face-on ($B/A > 0.7$) late-type galaxies (LTGs, from S0a to Sm and Irr) and over 447 S0s and dS0s. The sample including early-type disks therefore accounts for 1365 members. In the late-type disks sample 365 galaxies received a positive vote (442 including early types) and, thus, have been highlighted to be possible bars. A visual inspection of all galaxies revealed that above vote$= 4$ (227 galaxies) the sample of bars extracted can be considered more than 95% pure while below $vote = 1$ (557 galaxies) only ~ 20 barred galaxies were erroneously classified as unbarred ($3 - 4\%$). The $votes$ =2,3,4 categories (106) comprehend about 10% of bad detections and $\sim 9\%$ of ambiguous cases in which, even after visual inspection of both images and profiles, it is very hard to speak a final word on their real morphology. This is summarized in Tab. 7.1, which indicates that selecting galaxies with $vote \geq 2$ defines a satisfactory $\sim 90\%$ (considering as intruders both bad and uncertain cases) pure sample of barred galaxies, which maximizes the overall bar fraction of our sample ($36\% \pm 2\%$).

6.2 Comparison with visual classifications

To further test the efficiency of the extraction of barred objects, I compared this classification to that performed by Binggeli et al. (1985) for galaxies of the Virgo Cluster Catalog (VCC). Among the VCC, face-on LTGs with a $B/A > 0.7$ and a $cz < 3000 kms^{-1}$ are 56, out of which 20 are classified as barred. Among VCC bars, 80% have also been consistently classified as barred by my automatic method which, on the other hand, classifies 16 more galaxies (among which there is VCC 508, see Fig. A.1a) as barred and misses 4 barred galaxies from the VCC, thereby implying an overall accordance between the present classification and Binggeli of $\lesssim 70\%$. Nevertheless, among the objects classified as barred by the automatic pipeline and unbarred by the VCC, 50% are instead classified as barred in the RC3 (de Vaucouleurs et al.,

Table 6.1: Frequencies of bad, uncertain, and confirmed detections after visual inspection of the 922 face-on late-type galaxies. Bad detections are the missed bars, in the category with a vote lower than 0, or, in the other groups, the unbarred galaxies considered as barred.

	N_{gal}	Bad classification	Uncertain
vote ≤ 0	557	22	10
vote > 0	365	30	25
vote = 1	32	10	4
vote = 2	24	3	4
vote = 3	66	5	4
vote = 4	16	2	2
vote ≥ 2	333	18	21
vote ≥ 4	227	10	11

1991), which indicates that the bar extraction efficiency of the pipeline is better than what we can deduce from the accordance with VCC. The remaining 50% (9 galaxies) are either classified as peculiar objects or weakly barred; these are mostly low surface brightness systems with some degree of perturbation and asymmetry. Only 4 galaxies do not show any bar component and are classified as normal late-type galaxies by both RC3 and VCC.

A more recent classification based on SDSS images was performed over a sample of about 500 galaxies in the Virgo cluster by Méndez-Abreu et al. (2012) and over a different sample of about 200 galaxies in the Coma cluster by Méndez-Abreu et al. (2010). I found a sample of 452 objects in common with the sample of this work and those of Méndez-Abreu et al. (2012). Performing our selection cut in their sample leads to a test sample of 29 galaxies out of which 14 are barred in the Méndez-Abreu et al. (2012) classification. Among these, 12 have been consistently voted as barred galaxies by my automatic procedure, while 2 galaxies where erroneously considered unbarred and another 2 are not classified as barred in the Méndez-Abreu et al. (2010, 2012) classifications. If we instead include the analysis of S0s, we find a test sample of 50 galaxies. In this case Méndez-Abreu et al. (2010) finds 23 barred objects while the automatic procedure extracts a total of 18 bars. Overall, 17 galaxies were classified as barred by both works, while 6 galaxies were missed by

my automatic procedure. The overall agreement in the classification of the 50 objects selected is $\sim 82\%$.

Finally we compare the classification with that extracted in the GZ (Lintott et al., 2008; Willett et al., 2013), selecting objects with pbar > 0.5 and that have been voted by more than 28 citizens (Melvin et al., 2014). In total I found a GZ classification for 727 late-type galaxies with $BA > 0.7$ out of which 180 barred (25%). On the contrary our procedure finds 285 barred galaxies ($\sim 39\%$) including 80% of the galaxies classified as barred by the zoo. The objects that are not found barred in the GZ project are mostly (62%) galaxies with $M_* < 10^{9.5}$ $M_\odot$. In these cases, the procedure is sensitive to the non-axisymmetric distribution of bright HII regions and clumps in these irregular galaxies, leading to wrong or ambiguous detections that overestimate the fraction in the low mass systems. On the other hand, among brighter galaxies, it was possible to find an independent classification of the RC3 and/or VCC catalogs, indicating $\sim 30\%$ of the objects voted unbarred in the GZ are in fact barred. This indicates the good performance of the procedure at higher luminosities. Moreover about 50% of the remaining galaxies have a pbar between 0.35 and 0.5, indicating that they were nearly recognized as barred in the GZ. Therefore there is evidence that the present procedure overestimates the fraction at low mass but performs very well at higher masses, for an overall agreement with this classification of $\sim 78\%$.

In spite of the aforementioned difficulties of this automatic method at low mass, the overall agreement among the classifications is satisfactory but with an high source of uncertainty coming from bars detected in low mass systems. These are often low surface brightness with poorly resolved structures that, even after visual inspection of their images and ellipticity profiles, it is very difficult to say if they harbor bars (see Fig. A.1, the galaxy SDSSJ140127.3+240751).

A further demonstration comes from the comparison with the visual classification performed in Chap. 3.3. In total, I could compare the classification of 229 galaxies out of which 51 were classified as barred in that chapter. In this work the procedure was able to spot $\sim 80\%$ of the bars classified Chap. 3.3 but, on the other hand, the procedure classifies 60 more bars. Of these, the 68% are once again low-mass ($M_* < 10^{9.5} M_\odot$) irregularly shaped systems. Of the remaining more massive galaxies that were not classified as bars by the classification of Chap. 3.3, 33% are confirmed to host a bar by other indepen-

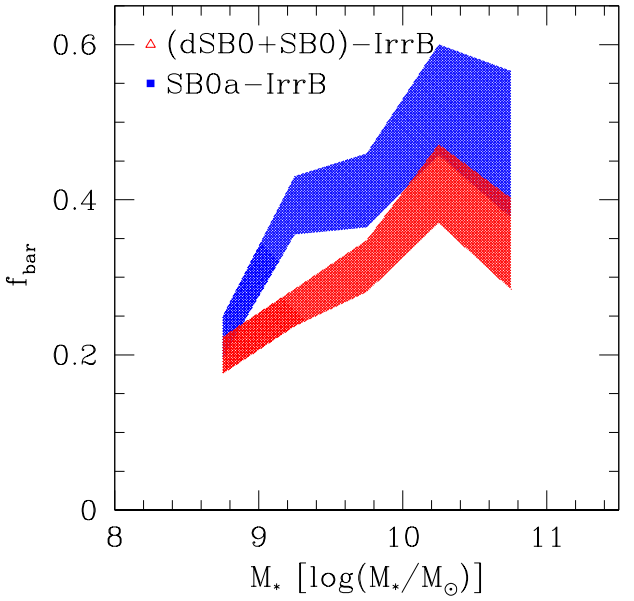

Figure 6.1: Optical local bar fraction as a function of stellar mass given separately for the sample that includes galaxies from S0a to Irr (blue) and the sample that accounts for SB0s (red). The width of the shaded area gives the poisson uncertainty in each bin.

dent classifications found in NED that corroborate the result of this method. Once again, the procedure shows a good capability in spotting bars in high luminosity systems, while having more difficulty at low mass.

6.3 The local bar fraction

In the past section we described our selection and showed that the procedure selected a reliable sample of barred galaxies. In chapter 5.3 we showed that spiral galaxies above some threshold mass are undoubtly redder then their lower mass counterparts and that this phenomenon is more evident in their central parts. I now test the consistency of the evaluated bar fraction with

the bars extracted by Méndez-Abreu et al. (2012) and in chapter 3.3 and then check whether the presence of a bar can indeed produce the trend in color profiles with mass that we observed in chapter 5.3 by building a template color profile of barred galaxies.

The overall local bar fraction evaluated in the present analysis is 36%, while if we include S0s it becomes 28%. The agreement with Jogee et al. (2004), Marinova & Jogee (2007), Barazza et al. (2008), Nair & Abraham (2010), Oh et al. (2012), and chapter 3.3 is satisfactory. Figure 6.1 shows the local bar fraction as a function of mass obtained separately for late-type galaxies and late-type galaxies plus S0s and dS0s. This has been evaluated in five bins of 0.5 dex from $10^{8.5}\mathrm{M}_{\odot}$ to $10^{11}\mathrm{M}_{\odot}$. The bar fraction increases evidently with increasing mass in both relations confirming the results of chapter 3 and many literature results (Méndez-Abreu et al., 2012; Masters et al., 2012; Skibba et al., 2012; Cheung et al., 2013). Nevertheless there is a clear separation between the sample containing lenticular galaxies and the LTG-only sample. Compared to the bar fraction of Fig. 3.4, the fraction at low mass is considerably higher. As discussed in the previous section, the automatic pipeline is very sensitive to irregular structures in low mass galaxies and may produce an higher fraction at low mass. In this sense, the low mass end of this bar fraction could be considered an upper limit. Nevertheless, the steep relation between the total stellar mass and the bar occupation fraction is preserved.

6.4 Tilted color profiles of barred galaxies

Maintaining the selection onto late-type galaxies and excluding S0s, I constructed a template $(g-i)$ color profile in three different bins of mass: i) below $M < 10^{9.75}\mathrm{M}_{\odot}$ ii) $M > 10^{9.75}\mathrm{M}_{\odot}$ and $M < 10^{10.25}\mathrm{M}_{\odot}$ iii), and $M > 10^{10.25}\mathrm{M}_{\odot}$. The bins were selected to guarantee that more than 50 galaxies contribute to each template profile. Color profiles are good tracers of the specific SFR and works such as MacArthur et al. (2004); McDonald et al. (2011), and the work in chapter 5.2 highlight the good correspondence between average age of the stellar population as a function of radius and color radial profiles. Moreover, using the technique of template profiles, in chapter 5.2.1 we showed that massive spiral galaxies develop a red and dead component, the importance of which increases with mass. Using the same technique

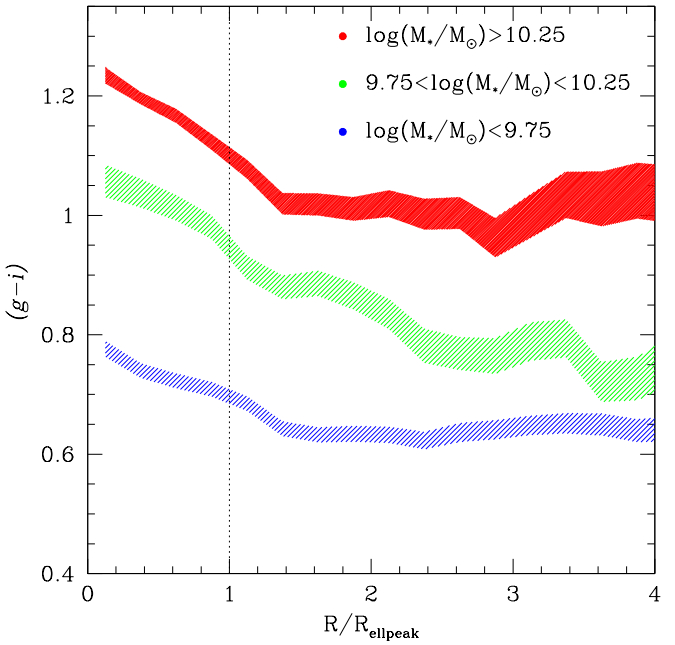

Figure 6.2: Color profiles templates of barred galaxies automatically extracted in this work in three bins of increasing mass. Radii are normalized to the radius at which the ellipticity peak is found in the profile.

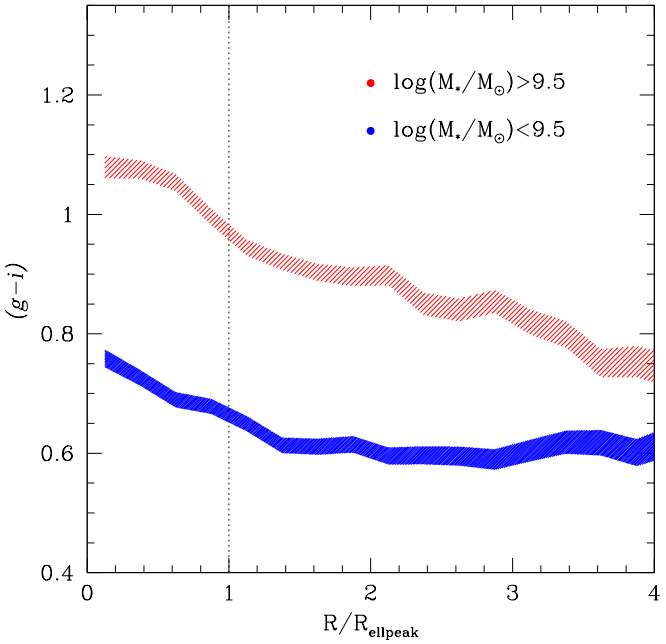

Figure 6.3: Color profiles templates of barred galaxies automatically extracted in this work in two bins of increasing mass: above (red) and below (blue) $M_{\rm knee}$, the threshold mass found in chap. 3.2. Radii are normalized to the radius at which the ellipticity peak is found in the profile

on the tilted color profiles of the subsample of barred galaxies extracted in this chapter, we test whether the central red and dead component is consistent with the presence of a bar-like structure in the center of galaxies. The template profiles for barred galaxies are shown in Fig.6.2 with each radius normalized to the radius of the selected ellipticity peak ($R_{ellpeak}$), which is a good proxy for the bar length and corotation radius (Laurikainen et al., 2010), with a radial step of 0.1 $\mathrm{R/R_{ellpeak}}$.

The template profiles evolve significantly from low to high mass. In the lowest mass bin, the color profile is blue over all radii, with possibly only a mild gradient toward red inside the bar radius. Things change clearly in the intermediate mass template profile: the outer disk (R/Rpeak > 1) is blue and, in the outermost regions, it overlaps with the lowest mass bin profile, while inside the corotation radius (R/Rpeak < 1) the color profile is red as an elliptical of the same mass. The bar has already reached the red sequence and, on the contrary, the disk is still on the blue cloud. In the highest mass bin, the red component once again has the typical color of the red sequence in the same range of mass. The disk is still bluer in the outer region but displays an average color of the disk that is redder than the respective average blue cloud values of the same mass. Moreover in Fig.6.3 we show the template radial color profiles of barred galaxies for two samples above and below the threshold mass found in chap. 3.2 ($\mathrm{M_{knee}}$), the mass above which bars have quenched the region inside the corotation radius. In order to quantify the average extension of the region that is under the bar influence, we correct the radius of the ellipticity peak for projection effects using the measured P.A with respect to its galaxy that is considered to have the P.A. of the last fitted isophote. The distribution of the ratio of the deprojected bar semi-major axis and the galaxy semi-major axis is plotted in Fig 6.4. This distribution peaks at 0.3 consistently with others results, such as that published in Marinova & Jogee (2007) and Barazza et al. (2008). The bars that we extracted are primarily strong bars (e> 0.4, Laurikainen et al., 2007, 2010) and weak bars represent only $\sim 9\%$ of the bars extracted which is again consistent with the proportion observed in Marinova & Jogee (2007).

Figure 6.2 allows us to deduce that bars are on average redder structures when they are compared to their associated disks. Fig 6.1 reveals that especially at high mass bars are extremely common and likely have a big impact on the average photometric properties of the galaxy population. Therefore

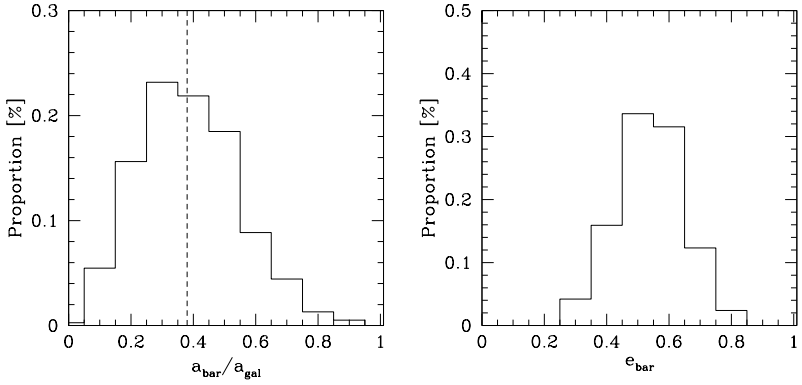

Figure 6.4: (left) Distribution of the ratio between the deprojected semi-major axis of the bar and the semi-major axis of the galaxy. The dashed line indicates the average value of the distribution equal to 0.38. (right) The distribution of the ellipticity of the bars extracted in this work.

bars are strong contributors of the trends in color shown in the template color profiles of chapter 5 especially for high mass objects. Moreover a further clue comes from the distribution of the ratio between a_{bar} and a_{gal} (Fig. 6.4). This indicates that the average optical extension of the bar is ~ 0.3 a_{gal}, which is consistent with the extension of the intermediate/internal zone identified in the average color radial profiles of chapter 5.3 that is on average redder than the outer disk zone.

A possible explanation for such a correspondence between the presence of the bar and the color of the galaxy is that proposed in chapter 3.4.2 to explain how the sSFR of main-sequence local galaxies have a downturn at high mass. Summarizing, the torque exerted onto the gaseous component by the bar funnels the gas inside the corotation radius to the very center of the galaxy where it is rapidly consumed by a burst of star formation. The region within the bar extent is therefore gas depleted and grows redder with time (see also Hakobyan et al., 2016) and this phenomenon can occur earlier in more massive disks, which are dynamically colder. On the contrary, the gas outside the corotation radius is held in place and keeps feeding the star formation maintaining the disk blue. Nevertheless the bar fraction versus mass relation, along with the well-known color-mass relation, implies that there is a higher frac-

tion of bars among more massive galaxies with redder total colors; however, we stress that these are still star-forming spiral galaxies. This is consistent with previous works such as Masters et al. (2011), Alonso et al. (2013), and Alonso et al. (2014), who consistently find an increasing bar fraction in redder galaxies.

I found a difference between the bar fraction evaluated among all LTGs (ty>1) and the bar fraction that embraces lenticulars. As a matter of fact when lenticulars are taken into account the bar fraction decreases at all masses. At this point, a note of caution is required: the morphology selection relies only on visual morphological classification (Binggeli et al., 1985), which cannot disentangle the small population ($\sim 13\%$ of ETGs, Cappellari et al., 2011; Emsellem et al., 2011) of slow rotators (pure ellipticals) from the much wider population of fast rotators (disks that should have been taken into account when calculating the bar fractions; see chap. 1.4). Therefore this estimate of the bar fraction of the joint population of LTGs and S0/dS0s could be biased by the morphological classification. Nevertheless, the proportion that stands between fast and slow rotators (respectively $\sim 87\%$and $\sim 13\%$ of ETGs, Emsellem et al., 2011) implies that the bar fraction could be even lower, as many fast rotators have been likely classified as ellipticals and therefore excluded from the bar fraction determination. The lower bar fraction can possibly arise from two different scenarios: first, S0s are older systems with respect to other disk galaxies and have already undergone buckling instability that weakened the bar and, second, given the well-known density-morphology relation (Dressler, 1980), S0s populate dense environments which prevents them from growing bars because of tidal interactions or fast encounters. Nevertheless, other results suggest that intermediate/high density environments, such as groups, can indeed enhance the possibility of growing a galactic bar (Skibba et al., 2012).

As a final note, I would like to highlight that in the highest mass bin the bar fraction is lower. This feature has a low statistical significance but it can be seen also in other works, such as Nair & Abraham (2010), Méndez-Abreu et al. (2012), which show the bar fraction as function of mass. Although this feature has a low significance, such a decrease is possibly consistent with other two possible scenarios. First, more massive disks develop a bar at earlier times with respect to their lower mass counterparts and therefore undergo buckling instability earlier and dismantle the bar at earlier epochs. Second, more mas-

sive disks have a different merger history with respect to the low mass population and this may induce a different bar fraction. In the future it would be possible to investigate these hypotheses with the advent of new cosmological simulations at sufficient resolution.

Chapter 7

Ram Pressure stripping: U6697

UGC-6697 (Nilson 1973) (aka CGCG-97087, Zwicky et al. 1968) is the second brightest spiral/Irr member (cz=6727 kms^{-1}) of the nearby cluster Abell-1367 ($< cz >$=6595 kms^{-1}). It is located at R.A.11:43:49.03 ; Dec:+19:58:05.5, at a projected distance of 462 kpc in the NW direction from the X-ray center of A1367 (RA: 11:44:36.5; dec: +19:45:32, according to Piffaretti et al., 2011), well within the virial radius of the cluster (2.13 Mpc; Girardi et al. 1998). A smaller companion (CGCG-97087N) with a recessional velocity of cz=7542 kms^{-1} lies at$\sim$ 20 arcsec in the NE direction from UGC-6697, while NGC 3842 (cz=6247 kms^{-1}), one of the two giant E galaxies of A1367, lies at $\sim$ 3.5 arcminutes in the E direction. [1]
UGC-6697 and CGCG-97087N have a stellar mass of $10^{10.5}$M$_\odot$ and $10^{9.1}$M$_\odot$ respectively, as computed from the i-band luminosity and the (g-i) color following Zibetti et al. (2009).

UGC-6697 was pointed to our attention owing to the head-tail morphology of the radio continuum source associated with it (Gavazzi 1978). This morphology, generally found in clusters associated with elliptical galaxies, was not yet found attached to a spiral galaxy, and suggested that the galaxy is under the action of ram-pressure (Gunn & Gott 1972) during its high velocity, edge-on transit through the cluster IGM. The interpretation of this ob-

[1] At the assumed distance of 94.8 Mpc of A1367, 1 arcsec separation corresponds to 0.463 kpc, one arcmin to 27.8 kpc.

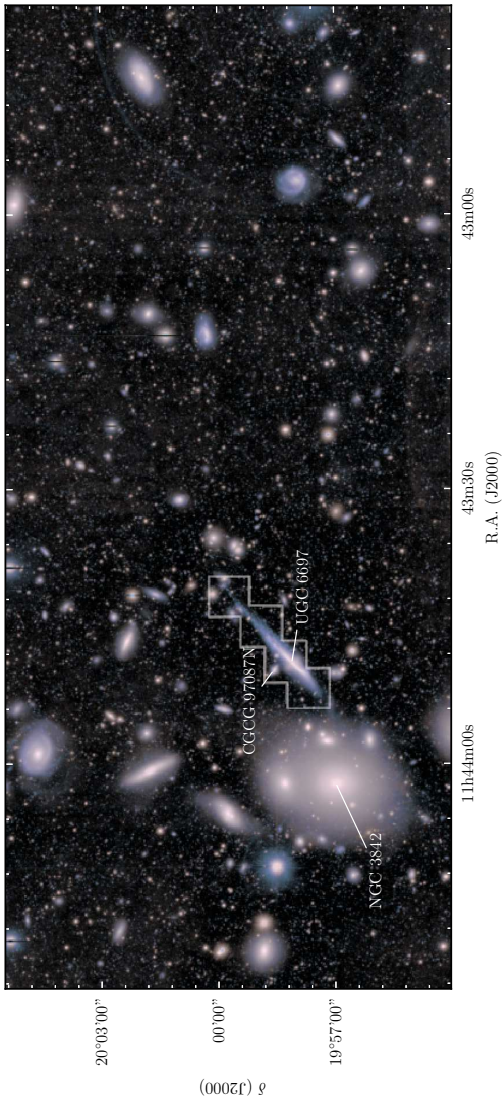

Figure 7.1: RGB (IRB) image of the central region of A1367 containing, among other fainter galaxies, NGC 3842, one of the two giant E galaxies in this cluster (left), the highly inclined UGC-6697 and its faint companion CGCG-97087N, which are the subject of the present investigation. The observations were taken with the Subaru observatory by Yagi et al. (2017). The image is rotated by 90 degrees: N is left.

ject based on the ram pressure scenario reinforced while more multifrequency data were gathered during the years, such as the Hα measurements of Kennicutt, Bothun & Schommer (1984) or the radio-optical data by Gavazzi et al. (1984). Moreover Gavazzi & Jaffe (1987), using VLA maps at 1415 MHz and CCD optical material, stressed once more the cometary appearance of UGC-6697 bringing to 50 kpc the length of the radio continuum tail, and Gavazzi (1987) using the Arecibo 305m telescope found evidence for moderate HI deficiency (Def_{HI}=0.24), supporting once again the ram pressure stripping scenario in its early phase. Later on, Gavazzi et al. (1995) found evidences for enhanced star formation and confirmed the asymmetric radio continuum appearance consistent with ram pressure stripping in a multifrequency (NIR, optical imaging and spectroscopy, radio continuum) study of this galaxy and also the HI profile was found asymmetric in subsequent Arecibo observations (Gavazzi 1989): most of the HI flux lies in the receding NW side of the galaxy. The small offset between the velocity of UGC-6697 and of the cluster suggests that the galaxy is crossing A1367 close to perpendicular to the line of sight. On the contrary, the velocity of CGCG 97087N suggests that its motion is almost along the line of sight.

Sun and Vichlinin (2005) observed UGC-6697 with the Chandra observatory. They detected significant X-ray diffuse emission from it, showing a morphological asymmetry similar to the one reported in the radio, stressing once more the ram pressure scenario. Nevertheless, a variation on the ram pressure scenario has been proposed by these authors inspired by the early work of Nulsen (1982) who noted that the geometry of the impact of the galaxy with the ICM (edge-on) should disfavor the ram-pressure as the main hydrodynamical process responsible for the stripping that causes such asymmetric emissions. As reaffirmed by Sun & Vikhlinin (2005), Kelvin-Helmholtz instabilities and viscous/turbulent stripping may be the principle hydrodynamical processes that are ripping the gas from UGC-6697.

In contrast with the HI and optical distribution, Boselli et al (1994) presented maps of the CO (1-0 and 2-1) lines, showing a symmetrical appearance that was later confirmed by Scott et al. (2013). This was interpreted as an evidence that CO is more centrally embedded in the stellar potential than HI, making it less easy to strip by ram pressure.

Other variations on the ram pressure scenario were also proposed: Gavazzi et al. (1984), who measured for the first time the rotation curve of UGC-6697,

Table 7.1: Details of the observing blocks composing the mosaic of UGC-6697 ordered in right ascension from E to W.

OB	RA	Dec	Obs date	T exp	AM	Seeing
	h m s	o ' "	dd mm yy	sec		arcsec
11	11 43 51.46	19 57 42.5	29 02 16	2x2190	1.48-1.57	0.77-1.07
1	11 43 48.70	19 58 16.8	10 02 16	2x2190	1.40-1.45	1.01-1.36
7	11 43 48.70	19 58 16.8	10 02 16	2x2190	1.51-1.62	0.72-1.95
2	11 43 45.00	19 58 53.0	10 02 16	2x2190	1.40-1.44	1.00-1.90
8	11 43 41.85	19 59 40.0	29 02 16	2x2190	1.40-1.43	1.02-1.43

pointed out the existence of a high-velocity component in the Hα emission and obtained the redshift of its fainter companion (CGCG-97087N). They speculated that a possible collision between the two galaxies might have occurred, causing a flow of gas to emerge from UGC-6697. They proposed that the detection of ionized gas between the two galaxies could eventually provide support for this model. They admitted that the weakness of this hypothesis consists in the absence of distortion in the optical morphology of both galaxies. In a more recent study of the velocity field of UGC-6697 using both long-slit and Fabry-Perot spectroscopy, Gavazzi et al. (2001) found a sharp kinematical discontinuity between the SE and the NW side of galaxy, leading them to speculate that the complex morphology and kinematics of the galaxy was the result of the merging of two different systems: an older component comprising the SE side of UGC-6697 and another younger object composing the NW star forming side of the galaxy.

Recently, Yagi et al. (2017), using the 8m Subaru telescope, obtained a deep Hα image of A1367, including UGC-6697. They discovered that its low surface brightness Hα cometary trail extends to the NW up to 100 kpc. Surprisingly they also found clear evidence of a faint gaseous double-tail that emerges perpendicularly from the disk of CGCG-97087N and connects to the disk of UGC-6697, supporting the scenario proposed by Gavazzi et al. (1984). The region of the cluster inhabited by UGC-6697 is shown in the Subaru field of Fig. 7.1.

7.1 Observations

UGC-6697 and its companion CGCG-97087N were observed with MUSE on VLT (UT4) on February the 10^{th} and 29^{th} 2016, as part of proposal 096.B-0019(A) (PI G. Gavazzi). A mosaic of the five MUSE pointings is shown in Fig. 7.2, taken at the coordinates listed in Table 7.1. They cover from the optical front of the galaxy (South East of the mosaic) up to 54 kpc outside the optical extent of the galaxy in the NW direction where the Hα tail extends. Each observation consisted of two 21.5 minutes exposures obtained rotating the instrument by 90 degrees, interspersed by an empty sky exposure of 4 min duration, taken at the coordinates $\alpha = 11^h43^m41^s$; $\delta = +19^o54'52"$. The central pointing that covers the center of UGC-6697 and its companion CGCG-97087N was repeated (OB1 and OB7) in order to reach a higher signal to noise in the area of a possible interaction between them. Observations were conducted while the galaxy was transiting at airmass ~ 1.5 in clear sky conditions and seeing ranging from 0.7 to 1.9 arcsec, using the Wide Field Mode with nominal wavelength coverage (4800-9300 $\mathring{A}$). Flux calibration is achieved by means of observations of the standard star GD153 exposed 160 seconds.

7.2 Data reduction & analysis

The final datacube mosaic was obtained using the MUSE data reduction pipeline (v 1.2.1) and a set of Python based codes that we designed in order to improve the quality of the illumination correction and of the sky subtraction for the observed field.
For each exposure composing the mosaic as well as for each sky and standard star frames, the first step was to create a master bias, master dark, a master flat and a wavelength solution within the MUSE pipeline. These were applied to each science, sky cubes and to the standard star (GD153). After computing and applying the telluric correction spectrum within the MUSE pipeline, we reconstruct the final cubes for each exposure. In order to produce a mosaic containing 5 different pointings we construct an astrometry reference frame building a regular 2D-WCS grid that maps all the exposures of the final mosaic. Starting from the WCS information contained in the reference WCS frame, we build for each exposure a regular 3-D WCS grid with a 0.2" spatial

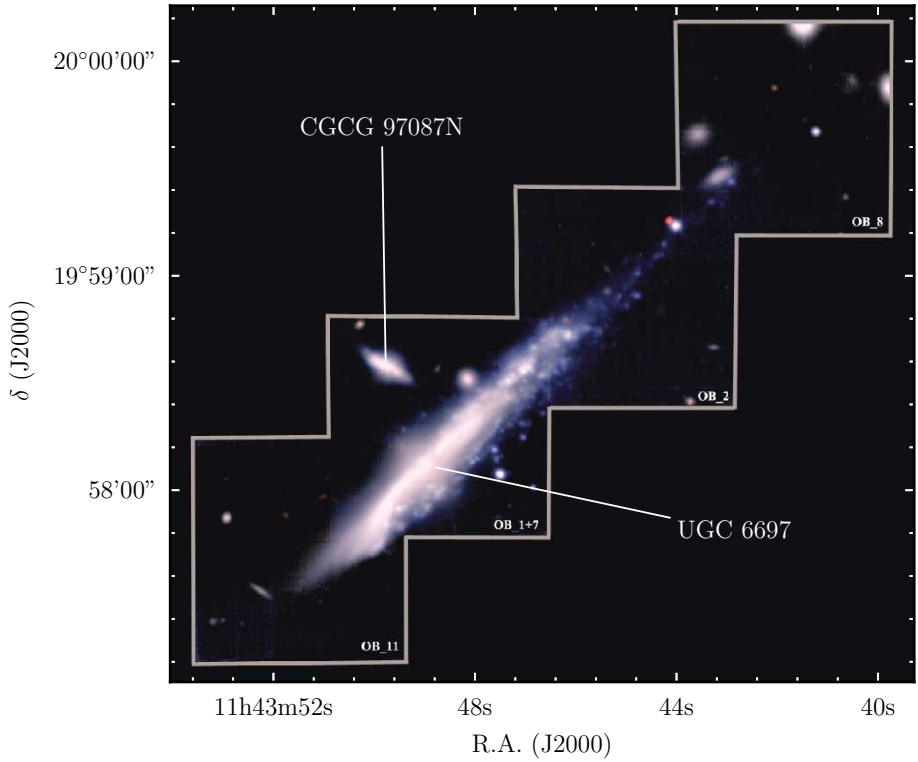

Figure 7.2: RGB (gri) image of the 5 mosaiched MUSE pointings that covers UGC-6697. Its companion galaxy UGC-6697N lies at $\sim$ 20 arcsec projected distance in the NE direction. Each RGB channel was constructed from the reduced MUSE data cube by projecting the cube respectively in the g, r and i SDSS bands.

pixel scale and a 1.25 $\mathring{A}$ spectral step from 4750 $\mathring{A}$ to 9300 $\mathring{A}$. All science exposures are projected onto their 3-D grid owing to the MUSE pipeline task *muse_scipost*. Every reconstructed cube of each exposure is mapped onto the same lambda and with the same pixel scale.
The reconstructed cubes exhibit a residual variation in the illumination of each IFU that depends on the wavelength at which the FOV is observed.

In order to perform a robust sky subtraction that minimizes the residuals (Fumagalli et al. 2014) we apply to each sky and science exposure an illumination correction. This was computed using in-house Python codes that evaluate, after masking bright contaminating objects, the illumination correction as a function of wavelength by computing the response of each IFU compared to the average response of the field in chunk of 500 $\mathring{A}$. The details of the illumination correction are presented in the appendix C

After correcting the illumination of each sky and science fields, we obtain a master sky spectrum by collapsing onto the lambda axis the single sky exposure which is free of contaminating sources and properly masked. To construct a correct model of the sky spectrum that accounts for both the time dependency of air glow line and continuum fluxes we take advantage of SKYCORR (Noll et al. 2014) as suggested in Fossati et al. (2016). The sky model is then subtracted from each spaxel interpolating the spectrum on the wavelength axis with a spline function. The uncertainties are appropriately added to the variance extension of the datacube.

After sky subtraction, a single datacube for each pointing is created by combining the respective exposures and the final datacube is assembled following the mosaic map. The final result is shown in the RGB (constructed by projecting the datacube in the SDSS gri filters) of Fig.7.2. The noise backgorund, in the central field covered by 4 expositions, has a 1-sigma limiting surface brightness around the redshifted Hα line ($\lambda \sim 6680 - 6750$) of $\approx 5. \times 10^{-19}$erg s^{-1} cm^{-2} arcsec^{-2} Å^{-2}. In the other fields the sky surface brightness reaches $\approx 9.5 \times 10^{-19}$erg s^{-1} cm^{-2} arcsec^{-2} Å^{-2}. Around the redshifted Hβ line ($\lambda \sim 4930 - 5015$) these values become $\approx 1. \times 10^{-18}$erg s^{-1} cm^{-2} arcsec^{-2} Å^{-2} and $\approx 2. \times 10^{-18}$erg s^{-1} cm^{-2} arcsec^{-2} Å^{-2}, respectively.

In order to characterize the properties of the ionized gaseous component

Table 7.2: Emission lines considered in this study. Column (1) is the name of the emission lines and column (2) the respective wavelengths in air. Column (3) represent the surface brightness limits at 5σ from the central cube covered by four exposures and the surface brightness limits at 5σ for the other cubes.

Line	λ	μ_{min}
	$\mathring{A}$	erg s^{-1} cm^{-2} $\mathring{A}^{-1}$ arcsec^{-2}
Hβ	4861.33	$\approx 2.3 - 4.0 \times 10^{-18}$
[OIII]	4658.81	$\approx 3.0 - 3.8 \times 10^{-18}$
[OIII]	5006.84	$\approx 3.0 - 3.8 \times 10^{-18}$
[OI]	6300.30	$\approx 3.8 - 4.3 \times 10^{-18}$
[NII]	6548.05	$\approx 1.6 - 2.6 \times 10^{-18}$
Hα	6562.82	$\approx 1.6 - 2.6 \times 10^{-18}$
[NII]	6583.45	$\approx 1.6 - 2.6 \times 10^{-18}$

of the galaxies we extract flux maps of the emission lines listed in Table 7.2 while, in order to trace the kinematics of the stellar component, we fit the Ca II triplet line at $8542.09\mathring{A}$. To robustly estimate emission line fluxes, we have to account for the stellar absorptions underlying the Balmer emission lines falling in the MUSE spectral window: Hα and Hβ. Therefore we take advantage of the code GANDALF (Sarzi et al., 2006) complemented by the Penalize Pixel-Fitting code (Cappellari & Emsellem, 2004) to simultaneously model the stellar continuum and the emission lines in individual spaxels with $S/N > 5$. The stellar continuum is modeled with the superposition of stellar templates from the MILES library (Vazdekis et al., 2010) convolved by the stellar line-of-sight velocity distribution, whereas the emission lines and kinematics are modeled assuming a Gaussian profile. In each spaxel, the modeled stellar continuum spectrum is subtracted from the observed spectrum obtaining a final datacube of pure emission lines, free of stellar absorption.

7.2.1 Emission line measurements

The complex kinematics of the ionized gas of UGC-6697 is known since the longslit spectroscopy of Gavazzi et al. (2001). In order to account for more complex kinematics along the line of sight we designed a Python fitting code called $QBfit$. $QBfit$ allows to fit groups of emission lines (or line sets) at

once, such as Hα and [NII] $\lambda\lambda 6548, 6584$Å, by fitting 1D Gaussian functions with relative velocity separation of the lines kept fixed according to the wavelengths listed in Table 7.2. The fit of [OIII] and [NII] line sets assume the ratio between the [OIII] lines and between the [NII] lines fixed to the values published in Storey & Zeippen (2000). The continuum is evaluated with a flat power-law during the fit and the S/N ratio of the Hα is evauated making use of the "stat" extension of the datacube. Moreover $QBfit$ allows the fit of an additional lineset with a different velocity component by fitting simultaneously the same lineset two times with a shift in lambda. In the end it returns kinematic, flux, sigma and error maps separated for a low velocity and an high velocity component.

QBfit was ran on the continuum-free datacube median smoothed 10x10 in the spatial dimension. We fit the emission lines in the continuum free datacube, assuming a systemic redshift of $z_{sys} = 0.02243$ for UGC-6697 and after a median smoothing of 10x10 spaxel (2 arcsec) in the spatial dimension to increase the S$/$N ratio per pixel. We do not perform any smoothing along the spectral dimension.
During the fitting procedure, sky line residuals and spaxels where the S/N at the Hα line is lower than 5 are masked. Further masking is applied to spaxel in which the line centroid or the line width are extremely deviant or showing an error greater than 50 $\mathrm{km\ s^{-1}}$.

The double velocity component fit is not necessary across the whole galaxy extension but the procedure recognizes the spaxels that show double velocities by fitting a single velocity component and by using the sigma of the emission line as a proxy for multiple velocity components. The sigma is evaluated after taking into account the instrumental width of the line, evaluated from the MUSE spectral resolution function. As an example, Figure 7.3 shows the spectrum around the Hα emission line of a spaxel clearly showing two velocity components (as testified by the double horn profile of the Hα and [NII] lines) fitted with a single velocity component (top) and with two velocity components (bottom) by $QBfit$. The fit that accounts for just one velocity component finds a solution with a very large velocity dispersion (≈ 125 km s^{-1}) because it fits both lines as one. In fact a better fit is obtained when two velocity components are considered. We set the sigma threshold to discriminate when a double velocity fit may be needed to 35 km/s, that is the typical veloc-

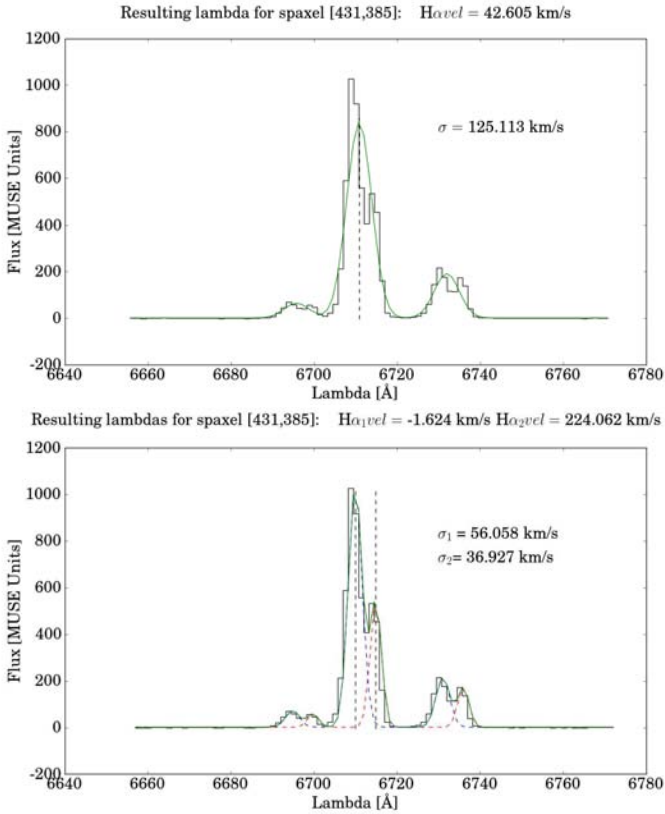

Figure 7.3: Spectrum around Hα of a spaxel clearly showing two velocity components. In the top panel, the single velocity fit to this data is shown in green while in the bottom panel the sum of the two velocity component fit is shown in green while the individual velocity components are displayed with the blue and red lines.

ity dispersion of the gaseous component in galaxies at $z \sim 0$ (Wisnioski et al., 2015).
After a double velocity component fit is performed $QBfit$ performs further checks in order to limit false or ambiguous detections: the two component must be separated of at least $1.25\mathring{A}$, which is the spectral step of the spectrum; both components must have S/N> 5 in order to represent a detection of a velocity component. In each spaxel, if the solution does not satisfy these conditions or if the double velocity component fit does not converge, the result of the single velocity component fit is stored instead. As a rule, $QBfit$ always stores the single velocity solution as part of the high velocity final results.

7.2.2 Absorption line measurement

Kinematics from the Ca II triplet TBD

7.3 Results - Flux and Kinematics of gas and stars

In the first part of this section we discuss the kinematics of stars and gas as evaluated respectively from the Ca II absorption lines and the Hα+[NII] emission lines. In this section we explore the results of the two velocity component fit performed assuming the systemic redshift of UGC-6697 for the whole frame (hence CGCG 97807N is not centered at 0 $\mathrm{km\ s^{-1}}$). In order to test the robustness of our double component fits these were compared to the fit of the galaxy resulting from KUBEVIZ (see Fossati et al., 2016), globally finding consistent results. Our results are divided in two maps: one of low-velocity and the other of high-velocity (see Fig. 7.4). The fit for the stellar component is also shown. The distribution of the spaxels that contain two velocity components is traced by the low velocity component, while the high velocity map contains the spaxel fitted with one velocity as well.

As it can be seen in the first two panels, the gas distribution of UGC-6697 extends in the NW direction twice as much the extent of the stellar component traced by the grey contours of the continuum in the r filter. The extent and orientation of the tail suggests that UGC-6697 is traveling edge-on (with respect to the ICM) at high speed, almost in the plane of the sky, through

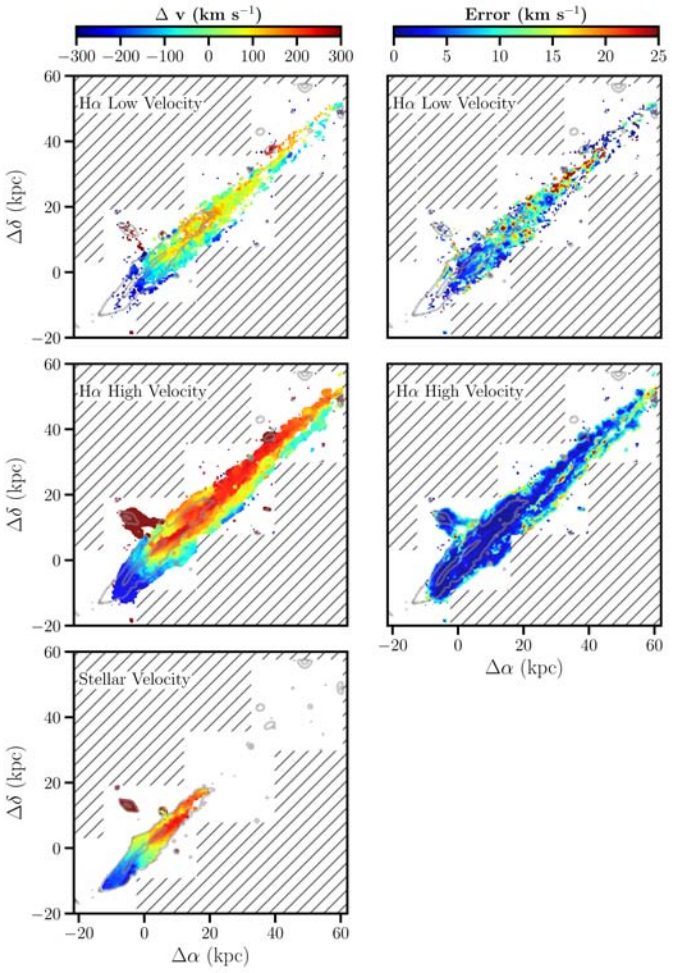

Figure 7.4: The MUSE field centered on UGC-6697 smoothed 10x10 has been fitted with the [NII]+Hα+[NII] lines (double velocity component). The first two top panels show the velocity field of the low and high velocity component of the gas derived from the Hα line. The top right panel shows the stellar velocity map derived from the fit of the Ca II line. The two bottom panels, from lefy to right, show the errors on the velocity of the low and high velocity component, respectively. The cross in all panels marks the stellar kinematical center, which coincides in position with the bright HII region at $\alpha = 11^h43^m49^s$; $\delta = +19^o58'07"$. The extent of the stellar continuum is given by the gray contours that represents the $\sim 23^{th}$ mag arcsec^{-2} and the $\sim 20^{th}$ mag arcsec^{-2} isophotes in the SDSS r-band image obtained from the datacube. Notice that the SE tip of the galaxy does not show any line emission.

Abell 1367 from NW to SE suffering the hydrodynamical interaction with the hot intacluster medium (ICM). In the SE front of the stellar component of the galaxy, the gas is absent and no emission line is detected. The tail extends approximately for 50 kpc, including many HII regions, seen preferentially on the upper edge of the tail.

The companion galaxy, CGCG 97087N, is losing gas while traveling almost perpendicular (from SW to NE) to the motion of UGC-6697 as suggested by the double tail emerging from the galaxy and connecting to the gas distribution of UGC-6697. Similarly to UGC-6697, also CGCG 97087N has a "depleted front" where we do not detect any gas emission but, differently from its massive companion, its tail splits in two and completely lacks HII regions. For UGC-6697, the integrated Hα flux in the low velocity map is 1.16×10^{-13}erg s^{-1} cm^{-2} and 5.2×10^{-13}erg s^{-1} cm^{-2} in the high velocity frame. CGCG 97087N instead has an Hα flux as low as 6.9×10^{-16}erg s^{-1} cm^{-2} and 1.23×10^{-14}erg s^{-1} cm^{-2} in the low and high velocity maps respectively. The sum of the fluxes of the two component is in good agreement with the independent values published by Yagi et al. (2017), obtained from the narrow-band imaging with the Subaru telescope. By Assuming the distance of Abell 1367 with respect to the CMB (94.8 Mpc), we derive the star formation rates of our targets from the Hα luminosity following **?**. UGC-6697 produces 5.3 $\mathrm{M}_\odot$ yr^{-1}, in full agreement with the previous estimate by Kennicutt et al. (1984) and Donas et al. (1990). CGCG 97087N exhibits instead a star formation rate of only ≈ 0.1 $\mathrm{M}_\odot$ yr^{-1} .

7.3.1 Velocities

The top panels of Fig. 7.4 show the velocities of the ionized gas, separated in low and high velocity components, and of the stellar component along the line of sight after subtracting the systemic velocity of UGC-6697. Both galaxies are seen nearly edge-on with clear evidence of a rotation curve in both the gas (left and central panels) and the stars (right panel). The rotation curve of stars as traced by the CaII triplet is smooth and fairly symmetric in both galaxies. UGC-6697, the most massive of the two galaxies, rotates with a velocity of ≈ 250 km s^{-1} (at a radius of ≈ 14 kpc) while its smaller companion shows a rotational velocity of ≈ 100 km s^{-1} (at a radius of ≈ 3 kpc). The rotation curve appears fairly regular and this disfavoures a scenario in which the two

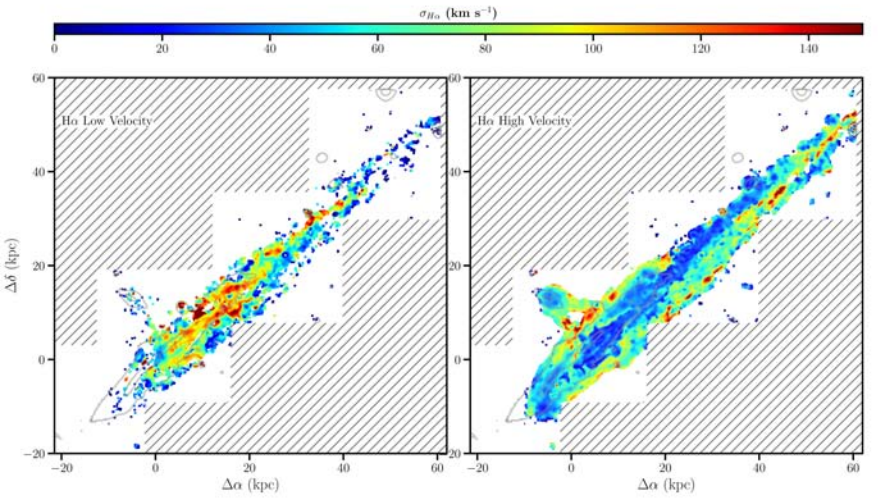

Figure 7.5: Velocity dispersion map derived from the Hα line, fitted with a double velocity component. In the left panel we plot the low velocity component and in the right panel the high velocity component. Gray contours represent the $\sim 23^{th}$ and the $\sim 20^{th}$ mag arcsec^{-2} isophotes in the SDSS r-band image obtained from the datacube.

galaxies have been interacting tidally. However a mild asymmetry is present in the NW edge of the stellar component of UGC-6697.

On the other hand, the interaction between the ISM and the ICM causes the gaseous component to leave UGC-6697 in the NW direction. Since the motion of the galaxy through the cluster is believed to be almost in the plane of the sky, the drag due to ram pressure does not decelerate the gas along the line of sight, thus its effects on the measured kinematics are negligible. In this geometry, the stripped gas would preserve its pre-stripping dynamical status. In other words the redshift of the stripped gas would remain close to the value it had before stripping, i.e. when it was attached to the stars, thus preserving the shape of the stellar rotation curve. We do observe traces of gas at negative velocity up to 50 kpc away from their original location (as deduced from the stellar velocity), implying that we can reconstruct the original location of the gas in the far tail by measuring its line-of-sight velocity and comparing it with the stellar velocity.

In the velocity space, the tail of UGC-6697 is divided in two substructures

sharply separated by ≈ 200 km s^{-1}: the upper layer of the tail (in orange in the central map) connects to the NW edge of the stellar component and its velocity is around 250 km s^{-1}; the lower layer of the tail (in green/blue in the central map) is at much lower velocities (-100 - 0 km s^{-1}) and connects to the central and SE-front part of the galaxy. Such a difference of velocities suggests that, similarly to 97087N, also the gas stripped from UGC-6697 is distributed along two tails. These are on the same plane (perpendicular to the plane of the sky) and are seen almost in perfect superposition. As a matter of fact, in correspondence of the upper layer of the tail, in the low velocity map, we are able to trace the underlying low velocity gas possibly associated to the lower layer of the tail. Intriguingly all the HII regions that we detect in the NW tail are univocaly associated to the gas with the highest velocity that connects to the NW edge of the galaxy. Moreover, the velocity dispersions of the two components are displayed in the maps of Fig. 7.5. Far in the NW tail, where the HII regions are formed, the gas displays low velocity dispersions with respect to the surrounding gas, contrary to the low velocity gas which retains higher values of velocity dispersion hence more turbulent kinematics. As a matter of fact, the observed velocity dispersion of the gas outside the HII regions in the disk and in the tail is broadened up to $\approx$ 150km s^{-1}, i.e. approximately five times higher than the expected value for a spiral galaxy at $z \sim 0$ (Wisnioski et al., 2015). Figure 7.6 sketches our cartoon model for UGC-6697, including the presence of double velocity components. In this model, the galaxy is represented in its fast motion through the ICM and is observed along an almost edge-on view. Its front (shaded) has been already completely gas depleted (the presence of PSB spectral features in this region testifies an abrupt truncation of the star formation). As the line of sight approaches the central region we detect gas at increasing velocity following the rising rotation curve of the stars. More to the NW, most lines of sight will cross regions containing multiple velocities: those "on board" the stellar rotation curve (marked 200) are blended with those containing stripped gas (marked -50) that originate in the SE and retain the kinematics of their places of origin. The spectrum shown in the lower corner of the Figure shows a typical double horned profile of Hα and N[II] with separation exceeding 200 km/s, as observed mainly in the down-stream half of UGC-6697. Fig. 7.7 shows the velocity field of 97087N for its stellar and gaseous component separately. For the gaseous component, we plot the high velocity component since we detect only few spaxels in the low velocity

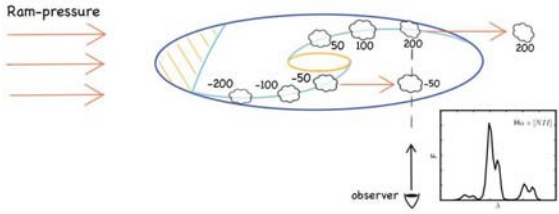

Figure 7.6: Cartoon of UGC-6697 under the action of ram pressure due to its fast motion through the ICM. Its front (shaded) is already completely gas depleted. The velocity of the gas is shown following the velocity curve of the stars. Velocities are given normalized to zero in the center. Some gas originally belonging to a central region has been displaced to the NW by ram pressure, retaining its original velocity (-50 km/s). This cloud overlaps spatially with another gas cloud on-board the background arm, with a velocity of 200 km/s. An observed who looks at the galaxy almost edge-on collects a spectrum carrying multiple velocity components in most spaxels along the NW tail.

component and these represents a negligible percentage of the flux belonging to CGCG-97087N. The map shows the gas being dragged out of the galaxy by the ram pressure from NE to SW. Its lower rotational speed is consistent with the low mass measured by Consolandi et al. (2016) and the high recessional velocity with respect to the cluster suggests a motion through the cluster with a significant component along the line-of-sight.
The stellar component rotation curve is fairly smooth with only a mild velocity gradient. On the contrary the map of the gas looks rather different. The ionized gas is stripped along two tails that are separated spatially and kinematically: the southern (S) tail and the northern (N) tail. Along the N tail we detect velocities that are very similar to the velocities of the stars (between -100 and 100 $\mathrm{km\ s^{-1}}$). Oppositely, the S tail shows a much steeper velocity gradient: the velocity of the gas from the S edge of the galaxy continuously decreases down to $\approx$ -400 $\mathrm{km\ s^{-1}}$. Such gradient is not consistent with the velocities displayed by the velocity curve of the stars. Instead, such a significant deceleration of the gas could be caused by the drag induced on the ISM by the cluster ICM. In this case however a similar deceleration should show up in the N tail too. However we tend to exclude that the gas that we observe at

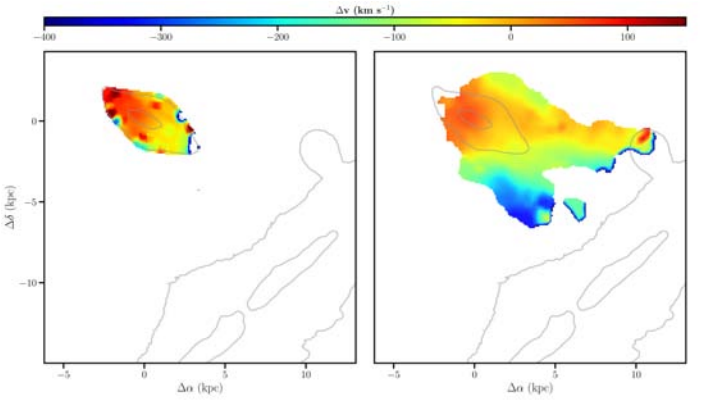

Figure 7.7: Velocity maps centered on CGCG 97087N of the stellar component as derived from the Ca II lines (left) and of the gaseous component (right) as traced by the Hα. Gray contours represent the $\sim 23^{th}$ and the $\sim 20^{th}$ mag arcsec^{-2} isophotes in the SDSS r-band image obtained from the datacube.

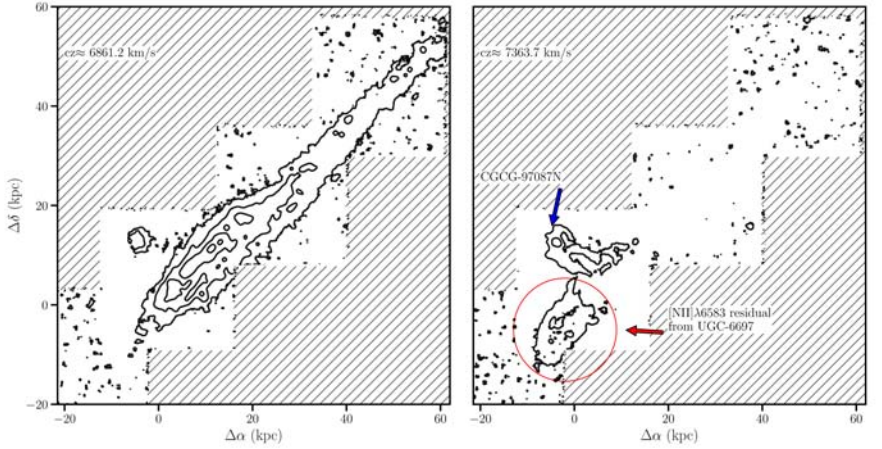

Figure 7.8: Contour maps at increasing velocity along the line of sight of the continuum subtracted Hα flux of the tails of UGC-6697 (panel 1 to 5) and CGCG-97087N (see panel 6). In panel 6, we the red circle indicates the contours arising from the residual flux of the [NII]λ6583 emitted by UGC-6697. Area not observed are shaded in gray.

-400 $\mathrm{km\ s^{-1}}$ belongs instead to UGC-6697 (which would support a possible direct interaction between the two galaxies). There is in fact a gap of more than 500 $\mathrm{km\ s^{-1}}$ between the lowest velocity in the N tail and the velocity of the gas unambiguously belonging to UGC-6697 observed near the region of putative crossing. Nevertheless, the flux of both tails eventually connect to the gas distribution of UGC-6697 (see also Fig. 7.4) but there is no evident continuity in the velocity distributions. However, looking at Fig. 7.5 we note that the dispersion in the tails of CGCG-97087N seem to form a continuum with the high velocity dispersion gas belonging to UGC-6697 in its upper periphery, suggesting at a possible physical connection between the two galaxies.
It is therefore interesting to test the possibility that a fast hydrodynamical interaction occurred between the two galaxies, possibly enhancing the ram pressure acting on CGCG-97087N. Signal from the tails of CGCG-97087N is detected from 7245 to 7647 km/s. In absence of a precise 3-D distance indicator it is of course impossible to establish if the gas trailing behind CGCG-97087N is just projected on UGC-6697 (either on the foreground or on the background) or has indeed crossed the disk of the main galaxy. If projected it would indicate that CGCG-97087N is under the action of ram pressure stripping by the ICM of A1367, conversely it would be the combined action of the ICM and the ISM of UGC-6697. In either cases, CGCG-97087N would be a member of A1367 and not a background object. In order to find evidences of a past interaction between the two galaxies we need to detect gas that is deeply embedded in the signal coming from UGC-6697. In principle, once that the continuum is properly subtracted, the difference in redshifts of the two galaxies should automatically separate the fluxes of the two galaxies. Unfortunately, the difference in redshift of the two galaxies is such that the Hα emission of the tails of CGCG-97087N falls at the wavelengths of the [NII]λ6583 line of UGC-6697. Moreover the tails cross eachother at the position where the emission from UGC-6697 is at its maximum, so that the [NII]λ6583 line outshines the faint signal of the Hα line belonging to the tail of CGCG-97087N. In these regions the signal of UGC-6697 is also characterized by double velocity component both brighter than the signal from CGCG-97087N, hence the double velocity component fit is insensitive to a possible third component.
In order to solve this problem and detect the desired signal, we use a non-parametric method to model and subtract the continuum and isolate only the emission of the Hα line. In each individual spaxel, the procedure starts from

the first element on the λ dimension and, for each spectral step it derives a redshift (z) and assumes the flux (F(λ)) at each wavelength (λ) to represent [NII]λ6548. Under these assumption it examines the flux at $\lambda_2 = \lambda + \Delta\lambda_{[NII]} \times (1 + z)$ and if F(λ_2) $> 3\times$ F(λ) it accounts it as belonging to [NII]λ6583. The procedure then subtracts the F(λ) and, at wavelength λ_2 subtracts $3\times$F(λ).
This procedure successfully recognizes the [NII] lines and the subtraction is satisfactory, although not perfect especially in the wings of the emission line. In the regions where the [NII] lines are very bright the subtraction is performed at $\approx 5\%$ level. In Fig. 7.8 we show the contour map of the channel at the velocity where the Hα of CGCG-97087N is found. The flux of the Hα line that we plot represent fluxes of $\approx 3.3 \times 10^{-19}, 3.8 \times 10^{-18}, 3.8 \times 10^{-17}, 3.8 \times 10^{-16}$erg s^{-1} cm^{-2} arcsec^{-2}. Intriguingly, the subtraction of the [NII] lines leaves a faint signal consistent with Hα emission belonging to CGCG-97087N elongating along the NW direction on the main body of UGC-6697. The appearance of this faint but well defined double tail naturally connecting with the ones observed outside the bright signal of UGC-6697 suggests that this embedded signal may not be an illusion, and that CGCG-97087N interacted hydro dynamically with UGC-6697.

7.3.2 Onboard and stripped gas

By comparing the gas properties of both the low and the high velocity component with the kinematics of the stars we attempt to separate the flux and kinematics of the stripped gas from the one that is possibly still onboard the galaxy. First we assume that the gas in projection outside the stellar distribution (as traced by the CaII lines) is stripped by definition. Second, we adopt a threshold of $\Delta v = |v_{gas} - v_{stars}| = 75$ km s^{-1} in each spaxel for the gas emission to be considered either bound to the galaxy ($\Delta v < 75$ km s^{-1}) or stripped ($\Delta v > 75$ km s^{-1}) [2]. Such threshold has been chosen to represent the quadratic sum of the maximum stellar and gas velocity dispersion expected (≈ 50 km s^{-1}) in local disk galaxies (Kregel et al., 2005; Wisnioski et al.,

[2]In spaxels where both the velocity components have a Δv greater than 75 km s^{-1} with respect to the stellar component we consider both belonging to stripped gas and we take into account the sum of the fluxes, and we average the velocities and the velocity dispersions

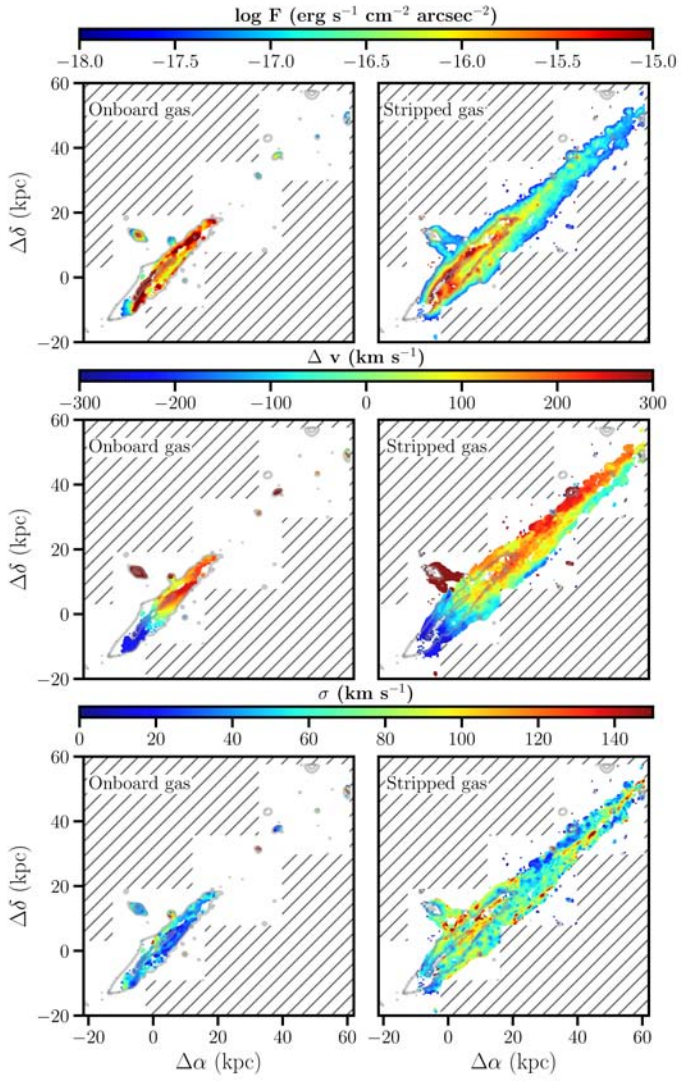

Figure 7.9: The MUSE field centered on UGC-6697 smoothed 10x10 has been fitted with two set of the [NII]+Hα+[NII] lines with different velocities along the line-of-sight. After adopting a δv threshold of 75 $\mathrm{km\ s^{-1}}$ between gas and stars to discriminate the gas emission aboard the galaxy and the stripped gas emission, we separate the inboard gas (left column) and the stripped gas (right column). The Flux, velocity and velocity dispersion maps are displayed from top to bottom and gray contours and the cross in each panel are the same as in previous figures.

2015).

Fig. 7.9 show the result of our attempt to separate the stripped gas from that remaining in the galaxy. In the first row of the image we display the flux maps from which we estimate that the flux still attached to UGC-6697 is $\approx 3.2 \times 10^{-13}$erg s^{-1} cm^{-2}, comparable with the stripped gas that has a flux of $\approx 2.8 \times 10^{-13}$erg s^{-1} cm^{-2}. As for CGCG 97087N, the flux splits in $\approx 9.2 \times 10^{-15}$erg s^{-1} cm^{-2} for the gas still associated with the galaxy and $\approx 3.63 \times 10^{-15}$erg s^{-1} cm^{-15} that is stripped away. The inboard gas is associated with the brightest regions of the continuum (see contours) and with the NW side of the galaxy.

The second and third rows of Fig. 7.9 show the kinematics (velocity and dispersion) as traced by the Hα line. It is remarkable that such a simple separation based solely on the velocity difference between stars and gas, with no further assumptions on the velocity dispersion, leads naturally to separate the high dispersion component from the low dispersion component. As a matter of fact, the gas considered inboard displays dispersions comparable to the expected values of Wisnioski et al. (2015), while the gas considered to be stripped shows much higher velocity dispersion. The only exception to this rule is in the upper layer of the tail, where most HII regions in the tail are found, that is characterized instead by low velocity dispersions (blue) similar to the gas bound to UGC-6697. Once again the velocity dispersion map of the tails of CGCG 97087N (bottom, right in Fig. 7.9) displays a structure that connects to the gas of UGC-6697, again suggesting a physical connection between the two galaxies.

Once the stripped gas was separated from the gas that remained bound to the galaxy, we quantify the mass of ionized gas that has been ripped from the galaxy. This can be estimated from the electron density by assuming a geometry for the Hα emission of the stripped gas. The electron density can be derived from the Hα luminosity using the relation

$$L(H\alpha) = n_e n_p \alpha_{H\alpha}^{eff} V f h \nu_{H\alpha} \tag{7.1}$$

(Osterbrock & Ferland, 2006), where $\mathrm{n_e}$ and $\mathrm{n_p}$ are the number density of electrons and protons, $\alpha_{H\alpha}^{eff}$ is the Hα effective recombination coefficient, V is the volume of the emitting region, f is the filling factor, h is the Planck's constant, and $\nu_{\mathrm{H}\alpha}$ is the frequency of the Hα emission line. Unfortunately

this estimate is affected by the high degree of uncertainty in its parameters. In particular the exact geometry of the tail is unknown and we can only approximate its structure assuming that the emitting region has a cylindrical shape of diameter equal to the height of the galaxy and length of ≈90 kpc. Because the morphology of the tail hints at a filamentary distribution containing high density clumps and compact knots, a filling factor lower than 1 is assumed. In particular, we assume $f = 0.1$, consistently with previous works that generally consider $0.05 < f < 0.1$. Moreover we assume that the gas is fully ionized, thus implying $n_e = n_p$ and $\alpha_{H\alpha}^{eff} = 1.17 \times 10^{-13}$ $\mathrm{cm^3 s^{-1}}$ (Osterbrock & Ferland, 2006). Assuming a distance of 94.8 Mpc, the resulting electron number density is of the order of 0.6 $\mathrm{cm^{-3}}$ which is in agreement with the density extrapolated by Yagi et al. (2007); Fossati et al. (2012, 2016). The implied mass of ionized gas dragged outside the galaxy is of $10^{9.1}\mathrm{M}_\odot$ and we estimate its recombination time to be ≈ 0.2 Myr using

$$\tau_r = \frac{1}{n_e \alpha_A}, \tag{7.2}$$

where α_A is the total recombination coefficient equal to 4.2×10^{-13} $\mathrm{cm^3 s^{-1}}$ (Osterbrock & Ferland, 2006).

By considering the projected separation between the stripped gas at lowest velocity in the NW tail and the region of the galaxy where stars have similar velocity, we can estimate a timescale since the gas has been stripped. Supposing that the gas is instantaneously accelerated to the cluster velocity, we estimate that these plumes have been stripped around ≈ 60 Myr ago, assuming that the galaxy travels at ≈ 1000 $\mathrm{km\ s^{-1}}$ in accordance with the upper limit for its velocity estimated by Sun & Vikhlinin (2005). Comparing this stripping timescale to the recombination time we conclude that some excitation mechanisms is necessary the to keep ionized the rarefied gas of the tail. Moreover, in the picture proposed by Nulsen (1982) and reaffirmed by Sun & Vikhlinin (2005), and given the orientation and geometry of the impact with the ICM of UGC-6697, mechanism such as viscous stripping and Kelvin-Helmholtz instabilities dominate the stripping of the gaseous component. Considering the density of the ICM ρ_ICM given by Sun & Vikhlinin (2005) equal to 4.5×10^{-4} $\mathrm{cm^{-3}}$, we can evaluate the time necessary to strip $10^{9.1}\mathrm{M}_\odot$ of ionized gas by Kelvin-Helmholtz instabilities if the galaxy traveling through the ICM

at ≈ 1000 km s^{-1} using:

$$\dot{M}_{K-H} \approx \pi r^2 \rho_{ICM} v_{gal}, \tag{7.3}$$

(Nulsen, 1982). The mass of ionized gas in the tail can therefore easily be stripped within $\approx 7 \times 10^7$ yr, which is consistent with the previous estimate of ≈ 60 Myr.

7.4 Excitation mechanisms

In order to constrain which ionizing processes are acting on the gas of the tail, we consider ratios of emission lines. In particular, we focus our attention to the BPT diagnostic diagram (Baldwin et al., 1981), considering lines that fall within the MUSE spectral window: H$\beta\lambda$4861, [OIII]λ5007, [OI]λ6300 and [NII]λ6584. The maps showing the distribution of the fluxes of all emission lines that we fitted are displayed in Fig. 7.10. The displayed flux is the sum of the two velocity component. Tthe [SII] lines are not considered because they fall at the wavelength of a strong sky emission line, preventing a robust determination.
Emission lines are detected along the main body of the galaxy while in the outer tail the distributions differ significantly. Hydrogen (Hα and Hβ) is found in both the diffuse gas and HII regions along the whole extent of the tail. The [OIII]λ5007 line is preferentially found in the HII regions of the tail and only little flux belongs to diffuse gas emission; conversely [OI]λ6300 is fainter and appears less important in HII regions.

The double velocity component fit to each lines keeps fixed the velocity and velocity dispersion of the two velocity components to the values evaluated during the fit of the Hα line. As a matter of fact, this ensures that all lines have been fitted with consistent kinematics fixed by the best resolved and brightest line available. Following the same criteria that we adopted to separate the onboard and stripped Hα, we split each line in an onboard and stripped component.

7.4.1 Line ratio maps

Line ratio maps are displayed in Fig. 7.11 and Fig. 7.12 for the onboard and stripped gas, respectively. The top-row of Fig. 7.11 shows the [NII]λ6584/Hα

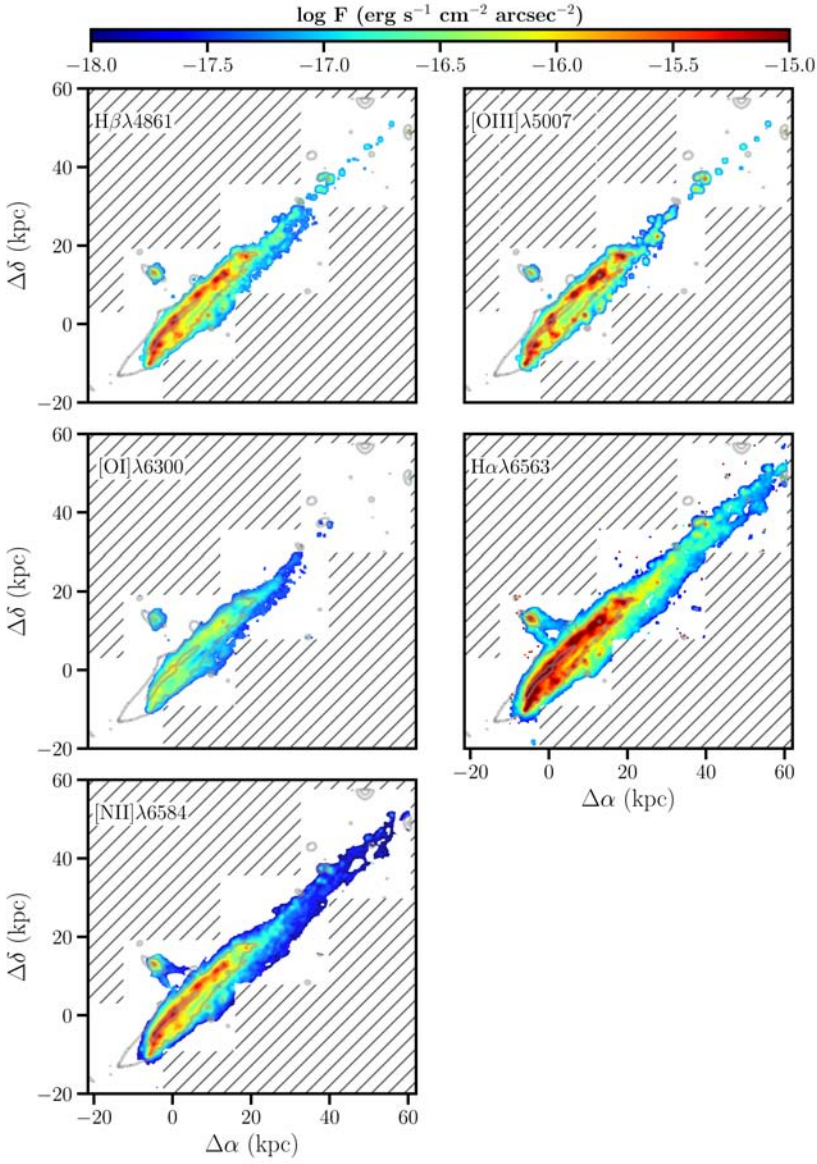

Figure 7.10: Emission line maps of UGC-6697. Panels are sorted by increasing line wavelength from left to right and from top to bottom. The solid contours represents the $\sim 23^{th}$ and the $\sim 20^{th}$ mag arcsec^{-2} isophotes in the SDSS r-band image obtained from the datacube. Areas not mapped by the MUSE mosaic are shaded in grey.

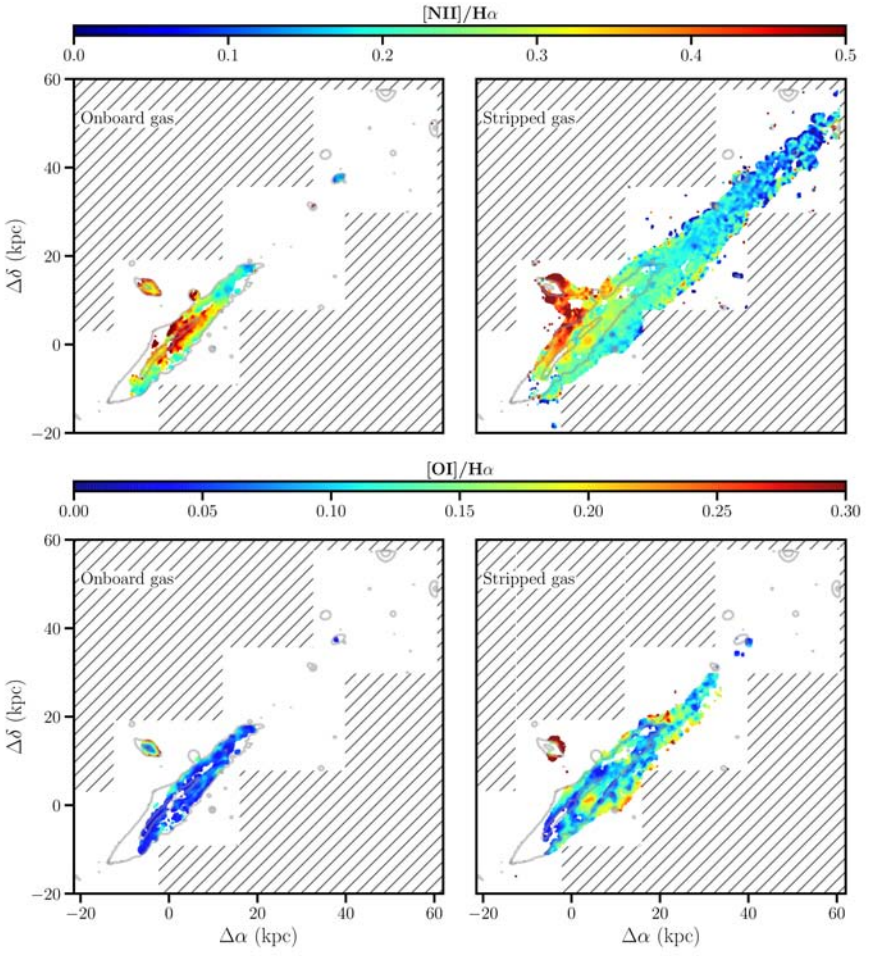

Figure 7.11: Maps of line ratios for the Onboard (left) and Stripped (right) components of the gase. From top to bottom, we plot the [NII]λ6584/Hα, [OI]λ6300/Hα, [OIII]λ5007/Hβ, and Hα/Hβ maps, respectively. Contours and gray shaded areas are the same as in previous figures.

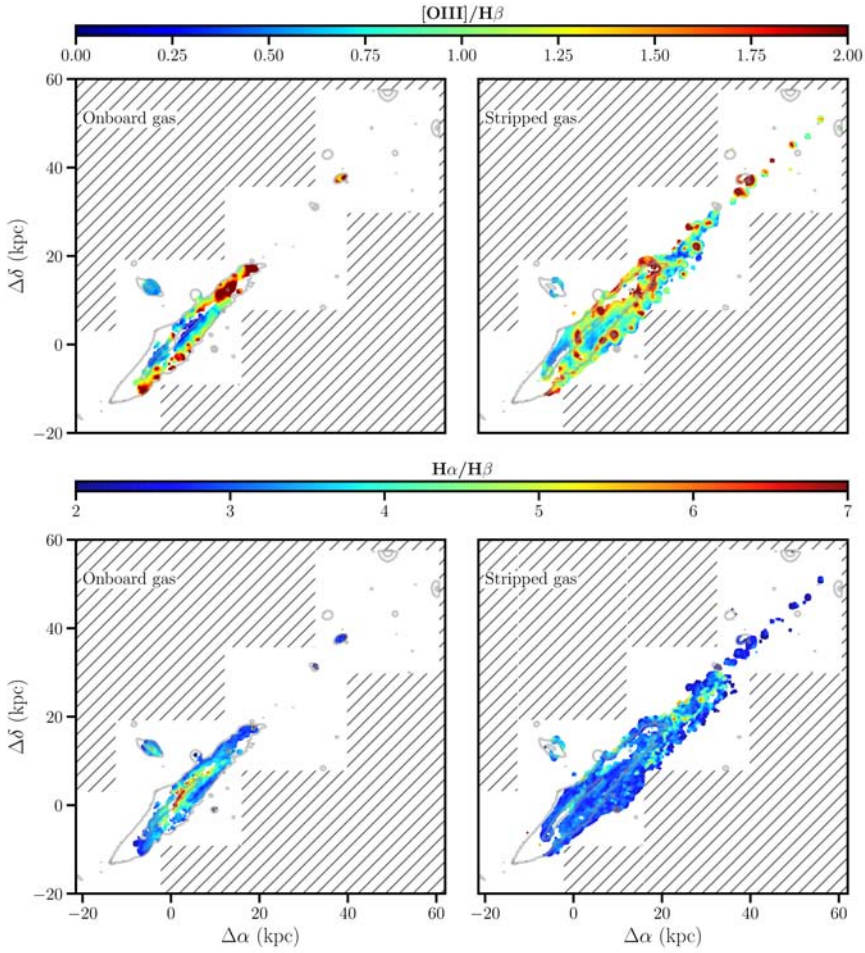

Figure 7.12: Maps of line ratios for the Onboard (left) and Stripped (right) components of the gase. From top to bottom, we plot the [NII]λ6584/Hα, [OI]λ6300/Hα, [OIII]λ5007/Hβ, and Hα/Hβ maps, respectively. Contours and gray shaded areas are the same as in previous figures.

maps. This ratio maintains modest values ($\sim 0.2 - 0.3$) on the main body of UGC-6697 and CGCG-97087N but its value varies dramatically in the CGCG-97087N tails where it is greatly enhanced and in the tail of UGC-6697 where it drops to values lower than 0.2. This ratio is enhanced by shocks (Kewley et al., 2001; Allen et al., 2008) and, in our map of the onboard gas, the highest values are found along an elongated central region of the main body of UGC-6697 and at the surface of contact where the tails of CGCG-97087N point. In the stripped gas maps, the highest values are in the wings and in the tails connecting CGCG-97087N to the galaxy. The gas characterized by high values of the [NII]λ6584/Hα ratio connects and mixes to the gas belonging to UGC-6697, suggesting once again a physical connection between the gas of the two galaxies. On the contrary, in the tail of UGC-6697 the ratio drops to values below 0.2.

A major difference between the gas still bound to the potential of galaxies and the gas stripped in the tails is visible in the [OI]λ6300/Hα map (second row of Fig. 7.11), another indicator of the presence of shocked gas. The gas belonging to the main body of both galaxies and to HII regions show very low ratio. On the contrary, the gas outside the two galaxies is characterized by much higher values, reaching the maximum in the two wings of CGCG-97087N and in the surface connecting to its tails similarly to what has been observed in the [NII]λ6584/Hα map, strongly hinting at an hydrodynamical interaction between the two systems.

The [OIII]λ5007/Hβ map is in the first row of Fig 7.12. The highest values of the ratio in both maps are found preferentially in regions that can be associated to the bright HII regions visible both in the Hα distribution and in the r-band image in the south direction and in the NW tail. This is consistent with an higher ionization factor (assuming a constant metallicity in the stripped gas) in those regions with respect to the surrounding gas.

In the central region of the stripped gas of UGC-6697, which shows modest values of the ratio, an extended blob is characterized by an high value of the [OIII]λ5007/Hβ ratio but cannot be associated to any clear compact knot of star formation.
The main body of both UGC-6697 and CGCG-97087N show onboard components with moderate [OIII]λ5007/Hβ values with the exception of the peripherical layer of UGC-6697, characterized by many HII regions. This is also true for the SE edge, in correspondence with the sharp cut in the ionized gas

distribution possibly associated to the front of the galaxy where the ISM impacts the hot ICM. In this case we would be probably looking at an enhanced star formation activity due to the compression of the front gas.

Finally we show the Hα/Hβ map in the bottom row of Fig. 7.12. This ratio is commonly used to infer the dust extinction, assuming an intrinsic ratio of 2.86 from case B recombination at $\mathrm{T} = 10^4\mathrm{K}$ (Osterbrock, 1989). In the onboard map, the main body of UGC-6697 display overall ratios that are consistent with being absorbed by the presence of dust. On the contrary the stripped gas is in line with the theoretical value of the ratio. Also the main body of CGCG-97087N is characterized by higher ratio values (≈ 4) consistent with a mild obscuration by dust. We stress that also UGC-6697 has higher values of Hα/Hβ where the continuum is maximum while in the tail the ratio settles around the theoretical value. The presence of dust along the line of sight is not surprising in the disk of edge on spiral galaxies but we refrain from interpreting the values in the tails, because other ionization mechanisms are at play and the assumption of an intrinsic ratio of 2.86 may not hold true in these regions.

7.4.2 Spatially resolved BPT diagrams

Next we build spatially resolved BPT diagrams for the onboard and stripped gas, separately. Unfortunately, the required simultaneous detection of four emission lines in each spaxel limits the analysis to the most bright spaxels and we cannot use the BPT diagnostic along the whole tail extent.
In the left panels of Fig. 7.13 (Top and Bottom) we show the BPT diagrams based on the H$\beta\lambda4861$, [OIII]$\lambda5007$, H$\alpha\lambda6563$ and [NII]$\lambda6684$ emission lines of the onboard and stripped component, respectively. Our points are color coded according to their minimum distance from the Kauffmann et al. (2003) curve that separate the regions of the plane associated to photo-ionization from the regions associated to other ionization processes (e.g. AGN and shocks). For each BPT panel, on the right, we display the map color-coded in the same way as the associated BPT digram in order to locate which region of the galaxy contribute to which points in the BPT digram. In both panels, we over plot three different photo ionization models at different metallicities (0.2,0.4,1 $\mathrm{Z}_\odot$) by Kewley et al. (2001). The contours are obtained from a sam-

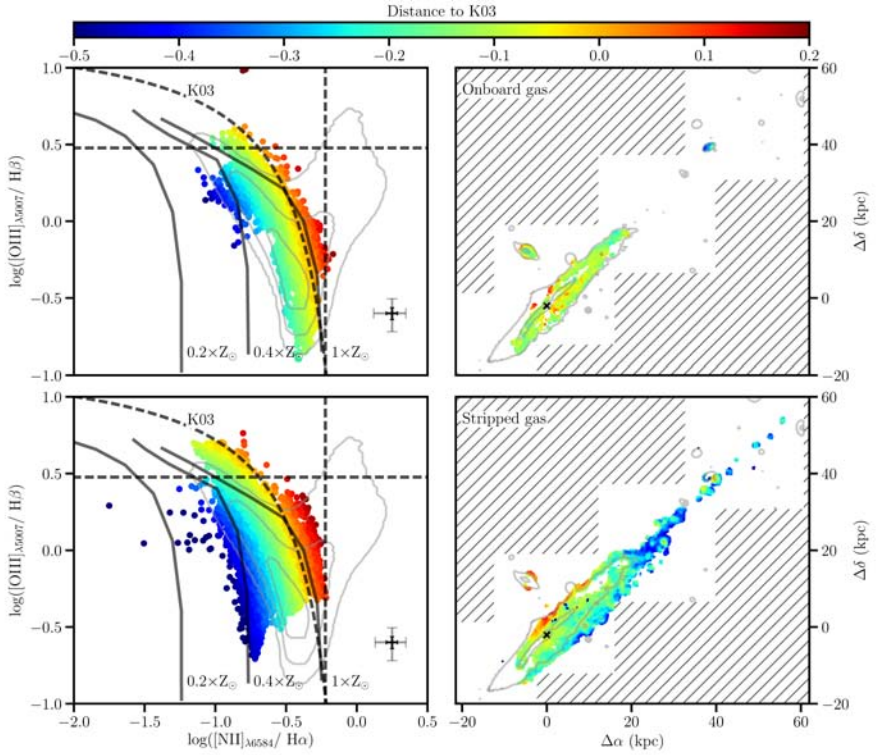

Figure 7.13: **Top.** Left: BPT diagram of the whole map of UGC-6697. The dashed curve separates AGN from HII regions and is taken from Kauffmann et al. (2003, K03). Data points are color coded according to their minimum distance to the K03 curve. The black and gray crosses indicate the typical error of the ratio of lines with S/N$\approx$ 15 and S/N$\approx$ 5, respectively. At higher S/N ratios, the error becomes comparable to the dots size. Thick solid lines show three different photo-ionization models at different metallicities (0.2,0.4,1 $Z_{\odot}$) by Kewley et al. (2001). The grey contours are obtained from a random sample of nuclear spectra of SDSS galaxies in the redshift range 0.01 - 0.1 and with masses spanning from 10^9 and 10^{11} $M_{\odot}$. Right: Map of UGC-6697 of the spaxel contributing to the BPT color coded as in the left panel. The black cross indicates the center of the galaxy while area of the sky not mapped by the MUSE mosaic are shaded in gray. **Bottom.** Same as in the Top panel but for the stripped component of the gas.

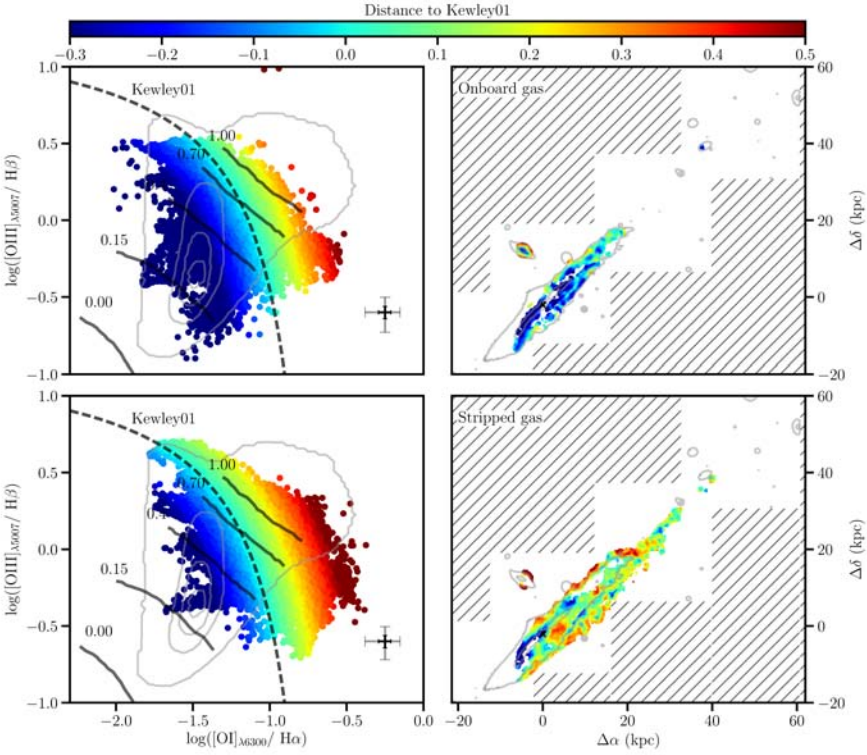

Figure 7.14: **Top.** Left: BPT diagram of the whole map of UGC-6697 using the O[I] to H α ratio. The dashed curve separates AGN from HII regions and is taken from Kewley et al. (2001, kewley01). Data points are color coded according to their minimum distance to the Kewley01 curve. The black and gray crosses indicate the typical error of the ratio of lines with S/N$\approx$ 15 and S/N$\approx$ 5, respectively. At higher S/N ratios, the error becomes comparable to the dots size. Thick solid lines show five different shock models by Rich et al. (2011) indicating five different fractions (from 0 to 1) of Hα flux contributed by shocks. The grey contours are obtained from a random sample of nuclear spectra of SDSS galaxies in the redshift range 0.01 - 0.1 and with masses spanning from 10^9 and 10^{11} $M_\odot$. Right: Map of UGC-6697 of the spaxel contributing to the BPT color coded as in the left panel. The black cross indicates the center of the galaxy while area of the sky not mapped by the MUSE mosaic are shaded in gray. **Bottom.** Same as in the Top panel but for the stripped component of the gas.

ple of nuclear spectra of SDSS galaxies in the redshift range $0.01 < z < 0.1$ and with masses $\mathrm{M}_* > 10^9 \mathrm{M}_\odot$. In the onboard component, our data mainly distribute along the HII region wing of the BPT: both the main body of UGC-6697 and the main body of CGCG 97087N are characterized by typical ratios for gas photoionized by stars.

The spaxels associated to the diffuse gas outside the galaxy (bottom of Fig. 7.13) exhibit instead a lower [OIII]λ5007/Hβ ratio compared to HII regions inside the galaxy. This deviation from the HII regions wing of the BPT can be interpreted as an effect of the lower metallicity of the peripherical gas of the galaxy. The photo ionization model with Z$= 0.4\mathrm{Z}_\odot$ of Kewley et al. (2001) falls in facts perfectly within our data. The (red) points in the BPT that lies just at the right of the curve of Kauffmann et al. (2003) are associated with the wings of CGCG-97087N and with the upper layer of UGC-6697, where the tails of CGCG-97087N intersects UGC-6697.

In Fig. 7.14, from top to bottom, we plot the BPT diagnostics based on H$\beta\lambda$4861, [OIII]λ5007, H$\alpha\lambda$6563 and [OI]λ6300 for the onboard and stripped component of the gas, respectively. Points and maps are color coded according to the minimum distance from the Kewley et al. (2001) curve that limits the region consistent with photoionization. We overplot five curves indicating the relative contribution of shocks to the ionization of the gas. The contours are again obtained from the same sample of nuclear spectra of SDSS galaxies previously described. In the top panel, the onboard gas is distributed mainly in the photoionization region of the diagram and the only points crossing the limit of Kewley et al. (2001) (dashed curve) are associated to the outer parts of CGCG-97087N and to peripherical regions of UGC-6697. A clear difference is observed instead in the diagram of the bottom panel: the majority of the points fall in the region at the right of the limit of photoionization of Kewley et al. (2001).

According to the models of Rich et al. (2011), roughly half of spaxels are consistent with 70% of the ionization coming from shocks. The regions with the highest contribution from shocks (up to 100%) to their ionization are associated with the diffuse gas at the periphery of the galaxy, while the main body of both galaxies appear consistently photo ionized by stars.

Taken together, Fig. 7.13 and 7.14 consistently show that the gas of the tails of CGCG 97087N and the gas of UGC-6697 to which they connect is

shocked (enhanced [NII]λ6684/Hα and [OI]λ6300/Hα). In the tail of UGC-6697, the gas is characterized by the lowest values of [NII]λ6684/Hα, possibly because of its low metallicity, but the high [OI]λ6300/Hα suggests that also this gas is shocked and turbulent. Hence all stripped gas show some evidence of shocks which might strongly contribute to the ionization of the gas. The fact that the strongest indications are found in the tails of CGCG 97087N and in the gas connecting the two galaxies hints at a physical interaction. We stress that the same (preliminary) conclusions were drawn also from the distribution of the velocity dispersion in this regions both in the single and in the double velocity component fit.

7.5 The HII regions

Compact knots of star formations lie outside the stellar disk along the northern and, to a lesser extent, southern periphery of the tail. Gas in and around these HII region is characterize by smaller velocity dispersions than the surrounding medium. It is therefore interesting to study in more details the properties of these compact knots. First, by visual inspecting the map of the [OIII]λ5007 (the faintest line of the BPT), we select the compact knots and extract the flux of the lines of the BPT in circular apertures containing the knots along with the average velocity and velocity dispersion of the Hα line inside the same apertures. In order to test whether these compact knots are associated also to an emission of the continuum, we collapsed the 5x5 smoothed MUSE cube on the lambda dimension and looked for counterpats first by visual inspection and then running SourceExtractor (Bertin & Arnouts, 1996). The automatic detection of the continuum is hard especially for the south HII regions embedded in the signal coming from the disk of UGC-6697. Such regions could not be disentangled within a single run of SourceExtractor but are clearly visible as spherically symmetric structures within the collapsed cube (also visible in Fig. 7.15, right panel). Outside the galaxy, SourceExtractor is more efficient and detects all regions visually selected from the [OIII] flux (26 regions) apart from 6 ($\approx 25\%$) HII regions.
Moreover, we cover the brightest regions of the main body of UGC-6697 and of CGCG-97087N with 7 circular apertures in order to characterize the properties of the star forming regions found inside the galaxy with respect to the

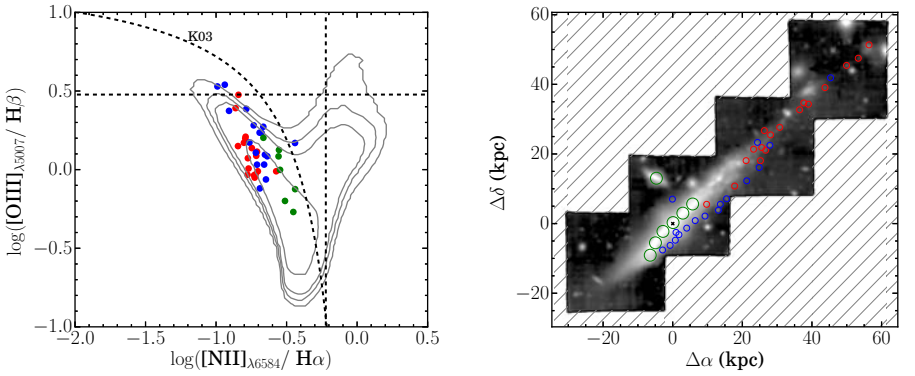

Figure 7.15: Left: BPT diagram of HII regions selected by visual inspection to the [OIII]λ5007 map. Right: the collapsed cube median smoothed 5x5 with circles indicating the position of the selected HII regions. HII regions that are part of the main body of galaxies are circled in green, while HII regions outside the bright disk of the galaxy are circled in blue ($v - v_{sys} < 100$ km s^{-1}) and red ($v - v_{sys} > 100$ km s^{-1}). Note that, by such division, HII regions that lie outside the galaxy are neatly distributed along two separate trails.

extra-disk knots. We measure the metallicity from the O3N2 ratio with the relation calibrated by Curti et al. (2016). The extinction is computed from the $\mathrm{H}\alpha/\mathrm{H}\beta$ ratio following the relation:

$$C(H\beta) = \frac{\log 2.86 - \log(\frac{f_{H\alpha}}{f_{H\beta}})}{f(H\alpha)}, \tag{7.4}$$

were f(H_α) = -0.297 is the selective extinction of Hα relative to Hβ from the Galactic extinction law of Cardelli et al. (1989) In Fig. 7.15 we show the BPT diagram of the HII regions identified by visual inspection. All appear as normal star forming regions in the diagram and we do not detect any remarkable difference between the HII regions in the main body of the galaxies and the external ones.

Mild differences between the extra-disk HII regions and the galactic HII regions are found in their metallicity and extinction. The gas ionized inside the disk has slightly higher metallicities compared to the ones outside the galaxy, consistent with the conclusions drawn for the tail of UGC-6697 from the low value of the [NII]/Hα ratio, consistent with the PHOT ionization models with $0.4\mathrm{Z}_\odot$ of Rich et al. (2011): in the disk the metallicity ($< 12 + \log(\mathrm{O/H}) > \approx 8.64$) is close to solar while in the HII regions outside the galaxy it ranges between 8.4 and 8.6, in agreement with the values extracted by Gavazzi et al. (2001). Also the extinction appear enhanced in the disk with respect to the HII regions in the tail where it is almost negligible ($< \mathrm{A}_\nu >= 0.2$). We find $< \mathrm{A}_\nu >= 0.8$ in the disk of UGC667 and CGCG-97087N, nevertheless in UGC-6697 the extinction associated to the two most internal regions visible in green in Fig. 7.15 is $\approx$ 1mag, while it drops to 0.4 in the outer regions of the disk.

In the velocity maps of Hα, most of the HII regions in the back tail are found at velocities larger than $100\ \mathrm{km\ s^{-1}}$. If we separate all HII regions with such velocities from the remaining ones we obtain the separation of red and blue symbols in Fig.7.15. Looking separately at the distribution of compact knots circled in blue and red, we note that these two are neatly positioned along two parallel paths running at the northern and southern boundary of the trailing gas. This suggests that there are two preferential streams along which star formation can occur in the stripped gas, that unfortunately we are seeing almost superimposed due to projection effects. This evidence hints at a physical mechanism able to funnel along preferential tracks the gas. Such

an effect has been proposed by (Dursi & Pfrommer, 2008) as due to cluster magnetic field draping.

7.6 Discussion

The present paper reports the results of the MUSE observations of UGC-6697 and CGCG-97087N, two galaxies belonging to the nearby cluster of galaxies Abell-1367. By fitting the emission lines in our final datacube we recover the line flux and kinematics with high precision down to a surface brightness of $F_{H\alpha} \approx 10^{-18}$erg s^{-1} cm^{-2} (see Fig. 7.4). At this depth, we detect an $H\alpha$ tail that extends continuously for at least $\approx$ 60kpc with a typical surface brightness of $F_{H\alpha} \approx 10^{-17}$erg s^{-1} cm^{-2}. In Fig. 7.16 we show the X-ray contours of Sun & Vikhlinin (2005) superimposed to our Hα map. The X-ray emission is coplanar to the Hα although it is by far shorter: at the front, where the ISM impacts the ICM, the contours compress forming a sharp edge that corresponds to the one observed in Hα; in the NW back both tails overcome the length of the optical galaxy.
In this section we present a comprehensive picture of the turbulent life of UGC-6697 in the cluster that we extrapolated from the analysis of the data, discussing it in the light of previous environmental studies.

7.6.1 Which process is driving the stripping?

UGC-6697. As discussed in Chapter 2, UGC-6697 has been under investigation since the early works of Gavazzi (1978) to the recent deep data of SUBARU and present MUSE observations. Through the years, the hydrodynamical interaction between the ISM ad the ICM has been invoked as the main responsible for the asymmetries in the young stellar distribution and in the gaseous distribution of UGC-6697.

Mainly because of the complex kinematics in the gaseous component of the galaxy, Gavazzi et al. (2001) proposed a different scenario in which UGC-6697 is a system of two merging galaxies. We tend to exclude this possibility since we can ascribe the complex gas kinematics to the super imposition of emitting gas with different velocities along the line of sight while being stripped from the SE and dragged to NW (see chap. 6, Fig. 7.6). Moreover, in the maps of the stelalr kinematics of UGC-6697 we do not find evidences of two kinematically separated systems. Hence

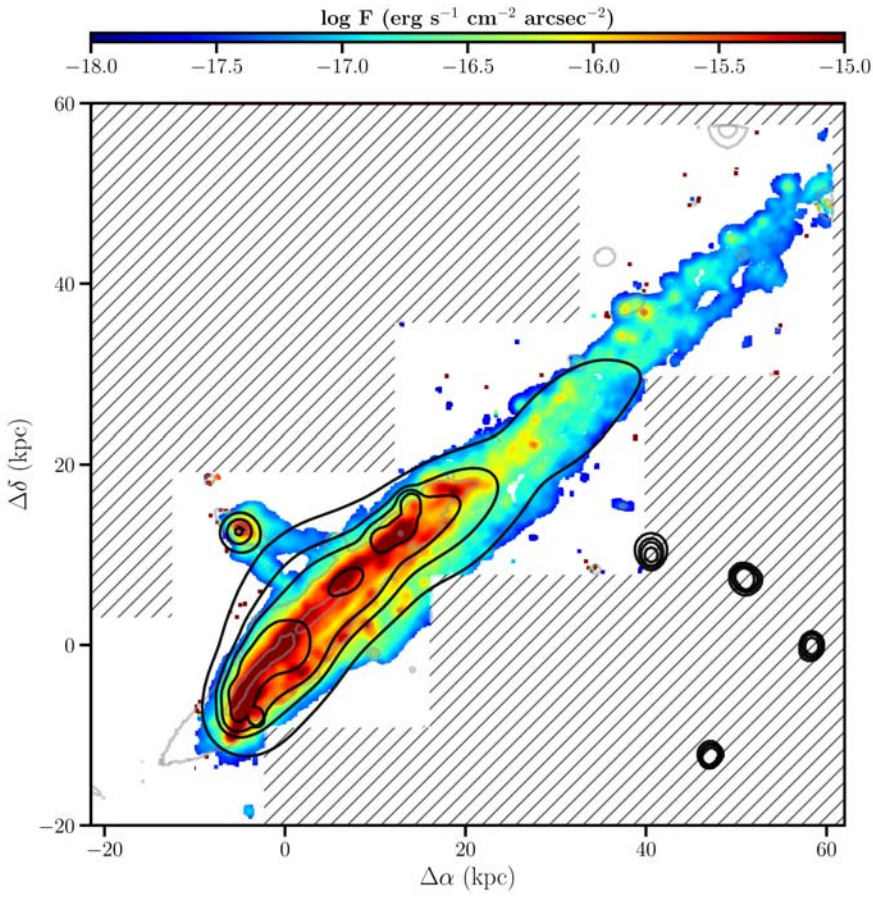

Figure 7.16: Same as Fig. 7.4 (left) but with the Chandra contours to show the region of the X-ray emitting gas. The X-ray map has been smoothed, but the X-ray front is at the same position of the Hα front. The X-ray tail appears co-spatial but shorter compared to the Hα tail.

we suggest that UGC-6697 is a single edge-on spiral galaxy suffering from the hydrodynamical interaction with the ICM.
Nevertheless, other gravitational interactions, i.e. with the giant elliptical NGC 3842, cannot be excluded $a\ priori$. As a matter of fact, the deep Subaru data (see Fig. 7.1) highlight the proximity of one of the two giant E galaxies of A-1367, CGCG-97095 (NGC 3842) whose recessional velocity differs from UGC-6697 of ≈ 500 km s^{-1}. This galaxy lies at a projected distance of $\approx 98kpc$ from the center of UGC-6697. In order to quantify the possible gravitational interaction between these two giant galaxies, we estimate the duration of a possible encounter. Nevertheless we stress that such estimate is highly affected by the great degree of uncertainty in the relative velocities of the two galaxies whose motion is in the plane of the sky as testified by the small differences in their recessional velocity with respect to the one of the cluster. In particular, the tail of UGC-6697 suggests a diagonal motion from NW to SE, while the bended jets of NGC-3842 (a Narrow Angle Tail, NAT, galaxy) hints at a W-E motion. Following

$$t_{enc} \simeq max[r_{UGC6697}, r_{NGC3842}, b]/\Delta V \tag{7.5}$$

where $r_{UGC6697}$ ($\approx$ 21 kpc) and $r_{NGC3842}$ ($\approx$ 30 kpc) are the optical radii of the two galaxies, b their separation and ΔV their relative velocity (Binney & Tremaine, 1987), the t_{enc} results equal to $\approx$ 200 Myr, sufficient to strip the amount of gas observed in UGC-6697. Moreover we can estimate the typical truncation radius for the two interacting galaxies using the relation (Read et al., 2006)

$$r_t \simeq b\big[\frac{m}{M(3+e)}\big], \tag{7.6}$$

where m and M are the masses of the galaxies, b their separation, and e the ellipticity of their orbit. All parameters are highly uncertain (especially the relative separation of galaxies) and we will assume the lower limit of $b = 98$kpc and the maximum ellipticity ($e = 1$). For this estimate we use stellar masses evaluated from the optical luminosity instead of dynamical masses because we do not have dynamical informations for NGC-3482. However, we stress that also the two masses evaluated from the optical luminosity are highly uncertain quantities, depending on the IMF and the galaxy color corrected for internal extinction, which depends on inclination and morphological type (Gavazzi et al., 2013b; Consolandi et al., 2016). In UGC-6697, because of its irregular shape and its almost edge-on geometry both the inclination and the morphological type are not well constrained and the galaxy color correction is probably highly uncertain. At the same time, the choice of the initial mass function (IMF) affects most the mass determination of blue galaxies. We adopt the mass estimate of Consolandi et al. (2016), who assumes a Chabrier IMF (Chabrier, 2003; Zibetti et al., 2009) and measured a stellar mass of $10^{9.8}$M$_\odot$ for UGC-6697 and $10^{11.5}$M$_\odot$ for NGC-3842.

The truncation radius of UGC-6697 therefore results $\approx 16.5\mathrm{kpc}$. Hence, from this analysis, although affected by highly uncertain parameters, we cannot completely exclude that a contribution from the tidal field of NGC 3842 is helping the stripping process as we also find mild asymmetries in the NW back of UGC-6697. However the absence of clear stellar streams, tidal tails, and shells in and around the galaxy discourages the idea that gravitational interactions are playing a major role in this process.

The asymmetric gas distribution of UGC-6697 is therefore to ascribe to the hydrodynamical action of the ICM onto the ISM that produces a tail of ionized gas of more than 60 kpc in projected length.
While the sharp cut in the gas distribution to the SE is almost certainly produced by ram-pressure, as pointed out by Nulsen (1982) and Sun & Vikhlinin (2005), the geometry of the impact of UGC-6697 with the hot ICM disfavors the pure ram-pressure stripping as the main process ripping the gas out of the galaxy. In particular, in the edge-on (with respect to the cluster) configuration of UGC-6697, turbulent viscous stripping with K-H instabilities is thought to be the most efficient channel for stripping the gas. We evaluated the mass loss from the Hα luminosity obtaining $\approx 10^9 M_\odot$ of ionized gas stripped. Such result is consistent with the mass loss of $\approx 10^9 M_\odot$ implied by the HI deficiency parameter (defHI=0.23; Giovanelli & Haynes 1985) measured by Gavazzi (1989). Following Nulsen (1982) and Sun & Vikhlinin (2005) we estimate that K-H instabilities can indeed strip $\approx 10^9 M_\odot$ in $\approx 10^7 yr$.

CGCG-97087N. The companion galaxy of UGC-6697, CGCG-97087N, is very close in projection to UGC-6697 ($\approx 14\mathrm{kpc}$) and, despite the early intuition by Gavazzi et al. 1984, only the recent deep SUBARU observations unveiled the double tail trailing behind the galaxy and connecting to the disk of UGC-6697. Also CGCG-97087N is detected in X-ray (although no tails are observed, see Fig. 7.16) by Sun & Vikhlinin (2005) who speculates that the X-ray emission may come from the gas heated by active star formation triggered by the tidal force of UGC-6697. In spite of a large difference in recessional velocity from UGC-6697 ($\approx 800\,\mathrm{km\,s^{-1}}$), Sun & Vikhlinin (2005) noticed that, at the projected distance of CGCG-97087N, this velocity is still lower than the escape velocity from UGC-6697, hence making t possible that the galaxy is still bound to UGC-6697. We evaluate the same quantities and we estimate that a possible encounter between the two galaxies lasted $\approx 25\mathrm{Myr}$ and, considering a $\mathrm{M}_* \approx 10^9 \mathrm{M}_\odot$ the truncation radius is comparable to its optical extent (≈ 3. kpc). The short duration of the encounter suggests that, if any, only a mild gravitational interaction occurred, consistent with the absence of stellar streams connecting the two galaxies along the gaseous tails. The gas distribution hence points to ram pressure stripping as the main driver of the observed gas outflow. We notice that the interaction with the ICM is similar to the one of UGC-6697 because also CGCG-97087N is

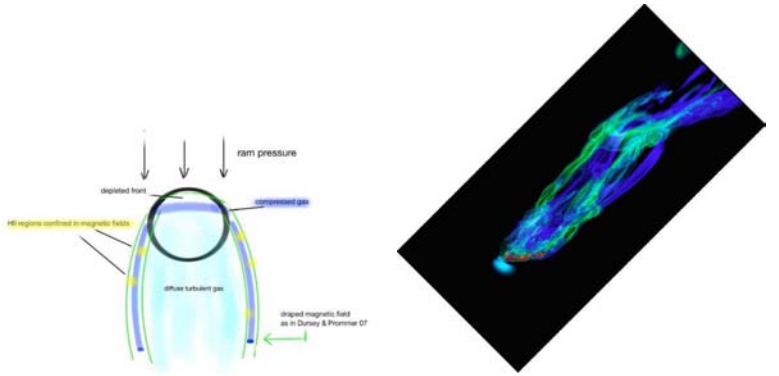

Figure 7.17: Cartoon of the derived toy-model for UGC-6697. On the right, an image taken from the magneto-hydrodynamical simulations of Ruszkowski et al. (2014)

crossing the cluster almost edge-on and therefore the main hydrodynamical process may be once more turbulent viscous stripping (Nulsen, 1982).
The shock and turbulence indicators such as σ_{gas}, enhanced [OI]/Hα and enhanced [NII]/Hα suggest a physical connection between the gas of CGCG-97087N and UGC-6697. Moreover our non-parametrical analysis of the Hα flux reveals that the tails of CGCG-97087N penetrate deeply in the signal of the main body of UGC-6697. In this scenario, we speculate that the enhancement of the shocks/turbulence indicators (σ_{gas}, enhanced [OI]/Hα and enhanced [NII]/Hα) in the gas connecting the two galaxies and at the surface of contact between the gas of UGC-6697 and the tails of CGCG-97087N are all caused by the hydrodynamical interaction between the ISM of the two systems.

7.6.2 The tail(s)

The recent images of the Coma and A1367 clusters, as well as the works on the Shapley and Norma Clusters have shown the possibility that the stripped gas collapses in the tail forming stars. Some of the gaseous tails of ram pressure observed during the years harbor compact knots of star formation while others don't. Tails of ram pressure harboring HII regions are seen in the ESO 137-001 galaxy in the Norma cluster (Fumagalli et al., 2014; Fossati et al., 2016), VCC 1217 (Fumagalli et al., 2011; Kenney et al., 2014), NGC4848 (Fossati et al., 2012), and in several galaxies of the Coma cluster sample of Yagi et al. (2010). The presence of HII regions in the stripped gas has been invoked for linking to ram pressure the so-called Jelly Fish galaxies (Ebeling et al., 2014; Poggianti et al., 2016), a morphology-related classification

based on the asymmetric optical morphology of these galaxies found in bright clusters, suggestive of unilateral external forces (i.e. ram pressure). The mechanisms regulating the possibility for the gas to collapse and form compact regions of star formation outside the galaxy, within the turbulent outflowing gas, are still poorly understood.

In our observations, both UGC-6697 and CGCG-97087N display evident tails of ionized material but the properties of the two are different. In particular, the tail of UGC-6697 harbors many HII regions neatly distributed along preferential trails while the tail of CGCG-97087N doesn't. Looking at the kinematics of the two tails, the striking difference between the two galaxies is the presence in the tail of UGC-6697 of a large fraction of gas that retains small velocity dispersions (< 50 km s^{-1}). As a matter of fact, the typical velocity dispersions in the double tails of CGCG-97087N are of the order $80 - 100$km s^{-1} while in UGC-6697 the gas associated to the trailing HII regions has typical velocity dispersions below 50 km s^{-1}. Hence, the star formation in the tail is associated to the less-turbulent component of the gas and this is confirmed by the line ratio diagnostics.

In the BPT diagrams of Fig. 7.13 the stripped gas from UGC-6697 is characterized by low values of [NII]/Hα and high values of [OI]/Hα. Taking into account the models at different metallicities of Kewley et al. (2001) we interpret the low values of [NII]/Hα as lower metallicity of the stripped diffuse gas. this is consistent with a picture where the turbulent stripping acted efficiently on the most external gas of the galaxy which is characterized by lower metallicities ($\approx 0.4 Z_{\odot}$), consistent with the metallicity gradients observed in spiral Sb-Sc galaxies (González Delgado et al., 2015). On the other hand, the high values of [OI]/Hα are suggestive of the presence of shocks heating the gas. In both BPT diagrams of Fig. 7.13 the gas stripped from CGCG-97087N is instead characterized by enhanced values of [OI]/Hα and [NII]/Hα, strongly suggesting that shocks are heating the gas in these regions (Rich et al., 2011; Fossati et al., 2016) and turbulence is dominating the dynamics.

Another difference is that the tail of CGCG-97087N splits while the tail of UGC-6697 doesn't, but this might result from projection effects due to the high galaxy inclination. A hint of this split is observable in the second and third contour maps of Fig. 7.8. The South trail of HII regions appears at lower velocities ($\sim 300\ km\ s^{-1}$) than the N trail that harbors HII regions (panel 5). Apparently, new stars are formed only along two preferential trails suggesting that in these regions cooling and collapse are favored possibly by an enhanced gas density and magnetic confinement.

In Fig. 7.17 (left panel) we plot a cartoon of our speculative view of the UGC-6697 system that we elaborated in the light of recent magneto hydrodynamical simulations.
UGC-6697 is traveling at high speed near the core of Abell 1367 in a nearly edge-on configuration. This configuration of impact disfavors ram pressure stripping with

respect to turbulent stripping (Nulsen, 1982) but, on the contrary, the stripping may be enhanced and favored by the scraping of the disk surface by the magnetic fields sliding past the ISM/ICM interface (Ruszkowski et al., 2014). As a matter of fact, this configuration of impact is similar to the ones explored by the simulations of Ruszkowski et al. (2014) from which we display an image in the right panel of Fig. 7.17. These simulations show that the presence of magnetic fields ensures a filamentary shape of the stripped material that otherwise appears more clumpy. In particular, two magnetized tails with enhanced gas density are clearly visible in the simulations (green filaments in the right panel of Fig. 7.17). The simulations show that along the two magnetic trails the gas density is enhanced, thus possibly favoring cooling and collapse with respect to the turbulent and less dense gas in the other filaments. We speculate that in UGC-6697 we are looking at a very similar phenomenon where the motion of the galaxy through the magnetized ICM drapes the magnetic fields lines (Dursi & Pfrommer, 2008) and produces two magnetized trails similar to the ones of Ruszkowski et al. (2014). At the front of the galaxy, ram pressure compresses the gas in the NW direction and leaves a depleted front. At the same time, along the body of the galaxy, at the surface of interface between the ISM and the ICM, K-H instabilities and magnetic scraping rip the gas from the disk and the wind of ramp pressure pushes it to the back of the galaxy. In the magnetized tails, the gas is compressed, cools and forms stars.
The weakness of this model is that magnetic fields should suppress disk instabilities (such as K-H instabilities), disfavoring the stripping of gas.

Chapter 8

Summary and conclusions

In this thesis, I have investigated two fundamental aspects of the evolution of galaxies: bar formation and ram pressure stripping. By studying the specific star formation rate of galaxies in the local Universe and comparing it with literature determinations at higher redshifts, in chapter 3 we found evidences of an evolutionary trend that can be ascribed to the present or past presence of a bar in massive LTGs. In particular, the inflow of gas triggered by the bar can rapidly quench the region within the corotation radius of the bar after a rapid burst of SF.
Investigating the FIR images of the Herschel reference sample that trace the dust cold component, thus the cold gas, in chap. 4 we find evidences of such inflows in barred local galaxies. In barred galaxies the FIR images show a carved region of little to no emission and such region has a radius that is on a one-to-one correlation with the radius of the optical bar. The continuum subtracted Hα images of the same sample show similar morphologies to the FIR images. We conclude that the central carved regions are gas–poor and the SF is suppressed because of the dynamical action of the stellar bar.

Since the region occupied by the bar is left gas–poor and quenched, it grows redder with time. I designed an automatic procedure able to perform exquisite integral and differential aperture photometry as well as isophotal fitting on g and i band SDSS images (see appendix A). The procedure was ran on a complete magnitude and volume limited sample of 5532 galaxies of the local Universe including the local and Coma Superclusters (see chap. 2). An accurate analysis of the color profiles of galaxies allowed to separate the contribution of different regions of galaxies to the global color magnitude (see chapter 5). We found that, on average, massive galaxies

($\approx M_* > 10^{10} M_\odot$) have their central regions redder than their outer disks. By running an automatic bar finder algorithm (see appendix A), in chapter 6 we showed that such trend can effectively be ascribed to the presence of a bar. However, all works find that an additional mechanism is required to quench the outer disks of massive spirals which follow a color magnitude in which more massive disks appear more quenched.

Finally in chapter 7 we reduced and analyzed the MUSE mosaic of UGC-6697 a massive spiral galaxy infalling in the nearby cluster A1367. The galaxy is under the action of hydrodynamical interactions with the ICM of the cluster as testified by the $\approx$ 60kpc long tail trailing behind it. By comparing the kinematics of stars and gas, we could separate the ionized gas in a stripped component and a component still attached to the potential of the galaxy. By comparing spatially resolved BPTs of the two different components we found that the stripped gas is mainly ionized by shocks between the ISM and the ICM while the onboard gas is consistent with photoionization by stars. The turbulence of the stripped gas is also testified by the large velocity dispersions found with respect to the onboard component. Moreover, we show that ram pressure stripping can act efficiently even in massive galaxies that are impacting the ICM in a edge-on configuration that should disfavor the stripping. In the tail of UGC6697, many HII regions can be observed and are neatly distributed along the only region of the stripped gas showing low velocity dispersion. In the NE direction from UGC-6697, CGCG-97087N shows a double gaseous tail that connects to UGC-6697 suggesting a past interaction.

In this chapter are summarized in details the results obtained in the previous chapters.

8.1 The bar quenching

In chapter 3 we tried to reconstruct the star formation history of main-sequence galaxies as a function of stellar mass from the present epoch (Section 3.1) up to $z = 3$ (Section 3.2). The local determination was based on the Hα narrow-band imaging follow-up survey (Hα3) of field galaxies selected from the HI Arecibo Legacy Fast ALFA Survey (ALFALFA) in the Coma and Local superclusters. The higher redshift measurements were taken from the recent literature.

A clear evolutionary trend was found indicating that star-forming galaxies had their star formation rate quenched above a certain threshold mass, which is a strong increasing function of redshift (Section 3.2).

To help identify what physical mechanism is responsible for this mass quenching, a set of hydrodynamical simulations of isolated disk galaxies was run to reproduce the formation of a bar (Section 3.4.1) and some dynamical considerations allowed us to highlight the joint dependence on mass and redshift of the Toomre conditions for bar

instability (Section 3.4.2).

The investigation highlighted five fundamental aspects underlying the global history of star-forming galaxies:
(i) there is a clear increase in the fraction of visually classified strong bars above some critical stellar mass $M_{\rm knee}$ that in the local Universe corresponds to $\sim 10^{9.5}$ $\mathrm{M}_{\odot}$;
(ii) above $M_{\rm knee}$ the bars are responsible for intense gas inflows that effectively trigger bursts of nuclear star formation that accelerate SF activity in the circumnuclear region, thus contributing to quenching the star formation in the longer run within the bar extent (on kpc scales) in agreement with Cheung et al. (2013);
(iii) the critical stellar mass $M_{\rm knee}$ is found to be strongly dependent on redshift, with only the most massive galaxies harboring bars at high redshift;
(iv) the specific star formation rate below $M_{\rm knee}$ (among normal main-sequence galaxies) strongly increases with redshift at least up to $z \sim 4$ (Madau et al. 1998);
(v) among centrally quenched galaxies, above $M_{\rm knee}$, the effects of quenching decrease significantly with increasing redshift.

Points (iv) and (v) may be caused by the cosmic evolution of galaxies, according to which higher redshift galaxies are progressively more gas-rich and are more often perturbed. Instead, results (i) to (iii) can be accounted for within a simple, physically motivated scenario, as detailed in section 3.4. In this picture, galaxies evolve from dynamically hotter structures to disks clearly dominated by their bulk rotation. More massive galaxies settle into dynamically cold configurations earlier, as supported by a growing wealth of observations (see references in section 3.4.2), with respect to less massive structures. As soon as a galaxy relaxes, the central part of the disk can undergo bar instability. The resulting bar sweeps away the gas within its corotational radius quenching the SF in the central region of the galaxy. This region, consequently, grows redder and redder with time, decreasing the global sSFR of the galaxy.

Actually, as presented in chap. 4, we indeed find evidences of strong inflows in the central regions of barred galaxies by investigating the SDSS optical, $160\mu\mathrm{m}$ and continuum subtracted Hα images of the Herschel Reference Samples. After a visual inspection and detection of barred galaxies, we measured the extent of bars in optical images, while in the $160\mu\mathrm{m}$ images we measured the extent of the bar-like structure, if present, or of the inner semi-major axis of the ring-like structure.

In 75% of the barred galaxies we successfully ran the IRAF task $ellipse$ to objectively measure the extent of these structures in both the i-band and $160\mu\mathrm{m}$ images, using the derived ellipticity, P.A. and surface brightness profiles. The goodness of the correlation between the extent of such structures strongly hints at a physical connection between the presence of an optical strong bar and a gas-depleted/quenched region where little SF is still possible. Only in the very center (where the bar conveys the gas originally within its reach) or along the bar is SF found. Such an effect is consistent with what we see in the continuum subtracted Hα images of the sample. SF is indeed distributed mainly in the nuclear region of galaxies and/or along the bar (consistent

with Verley et al. (2007); see Fig. 4.1) and shows a morphology similar to the one observed in the FIR.

FIR morphologies are similar to the Hα morphologies (consistent with Verley et al., 2007) and both are consistent with bar-driven inflows of gas inside the corotation radius.

As a note of caution we stress that, although bars play a significant role, some additional mass-driven quenching mechanisms are required to explain the "downsizing" of high-mass spirals. As shown in Figure 3.7, even the exteriors of massive barred galaxies are redder than lower mass counterparts. This could also be related to the evolution of galaxies in a cosmological context. Since the additional mechanisms are needed to quench the outer regions of field disk galaxies, we consider cosmological starvation (Feldmann & Mayer 2015, Fiacconi et al. 2015, Peng et al. 2015) to be a better candidate than SF/AGN feedback, for example, or any environmental effect. A complete understanding of this second quenching mechanism would require a more comprehensive study and is beyond the scope of this investigation.

The simple model outlined above has a number of testable assumptions and predictions: (i) Deep imaging can verify whether the central regions of quenched galaxies host bars/bulges at higher redshift, and if such structures are instead absent below $M_{\rm knee}$. This is already hinted at by observational studies of the cosmic evolution of the bar occupation fraction, e.g., Sheth et al. (2008). (ii) Our model predicts that the degree of "relaxation" of galaxies, as described by the $v_{\rm rot}/\sigma_*$ ratio, must depend on a specific combination ($M_*/(1+z)^2$) of the galaxy masses and redshift. Increasing the statistics and the accuracy of $v_{\rm rot}/\sigma_*$ measurements in mass and redshift bins will test such a prediction.

We conclude by speculating on the relevance of the bar-induced mass quenching for massive field galaxies. We believe that most of the massive galaxies that do not show a clear bar while hosting a central bulge can be associated with a late evolutionary stage of a previously barred galaxy. In this scenario most of the bulges in our classification would be either pseudobulges, formed during the bar-induced nuclear gas inflow, or boxy/peanut bulges, which are the results of the buckling instability that naturally develops in the central regions of the bar (e.g., Sellwood 2014 and references therein). As discussed in the literature, the bar buckling and formation of dense nuclear concentration of mass (e.g., the pseudobulge) modifies the dynamics of the stars in the bar. This can result in what is known as "bar suicide": the bar becomes less and less visible (Raha et al. 1991; Norman et al. 1996; Martinez-Valpuesta & Shlosman 2004; Shen & Sellwood 2004; Debattista et al. 2004, 2006; Athanassoula et al. 2005). A thicker but still rotationally supported stellar condensation (i.e., a boxy/peanut bulge) with a pseudobulge hosted in its very center would be the remaining traces of the dissolved bar. Such a speculative scenario is supported the similarities between the mass, SFR, and nuclear activity distributions of massive galaxies hosting bars and bulges.

8.2 The colors of Bar quenching

The results presented in the previous section lead to a scenario in which the central regions of disk galaxies grows redder with time and that such process must occur at earlier epochs in more massive LTGs. In chap. 5, we have presented the results of a semi-automated, IDL-based, procedure designed to perform photometric extraction on SDSS multi-band images. The procedure was used to analyze a magnitude and volume limited sample of 5532 galaxies in the Local and Coma superclusters. The procedure, unlike the SDSS pipeline, avoids the so-called shredding problem and successfully extracts total Petrosian magnitudes even for the largest objects of the sample, recovering 383 $g-$ (and $i-$) band magnitudes not included in the SDSS DR10 (Ahn et al., 2014). After the galactic and internal extinction correction is applied, we recover a refined color-magnitude diagram of the Local and Coma superclusters.

We attempted to dissect the color of galaxies in three distinct contributions: a nuclear region, an intermediate ($0.2\mathrm{R}_{Pet} \leq \mathrm{R} \leq 0.3\mathrm{R}_{Pet}$), and an external region. To this end, we analyzed the high quality color profiles that our routine has extracted for each galaxy, focusing on the objects of the Local Supercluster sample, with the best spatial resolution. Our analysis highlighted that:
Profiles are powerful tools for the detection of structures on nuclear scales (ILRs, dusty disks etc.) even when they are difficult to be visually spotted on SDSS images.
i) Nuclei of galaxies display the greatest deviations with respect to the galaxy color. This deviation correlates mildly with the nuclear activity of the galaxy. Passive galaxies do not deviate from the color of the galaxy while AGNs generally display very red nuclear colors. Star forming nuclei follow instead a bimodal distribution: Galaxies that are more massive than $10^9\mathrm{M}_\odot$ display redder nuclear color with respect to the galaxy while galaxies with $M < 10^9\mathrm{M}_\odot$ have bluer nuclei. Overall, a wide population of low mass galaxies display bluer nuclei with respect to their average color see Fig. 5.12 (*top*) although the high scatter does not allow the extraction of a general trend .
ii) Profiles of spiral galaxies reveal on average an intermediate zone that is redder with respect of the outer disk and this component is more important at high masses.
iii) The intermediate zone color of LTGs overlaps the red sequence already at $10^9\mathrm{M}_\odot$ and is completely superposed to it at $10^{10}\mathrm{M}_\odot$ (Fig. 5.9 and Fig. 5.12).
iv) The disks of spiral galaxies follow a distribution that does not overlap (and is almost parallel to) with the red sequence but that still displays an increasing color index with increasing mass.

From *i)* we conclude that a wide population of low mass galaxies undergo an outside-in quenching of their star formation consistent with an evolution driven by the environment on short timescales (Boselli & Gavazzi, 2006; Lisker et al., 2006; Fossati et al., 2013). Nevertheless this conclusion does not hold for the whole pop-

ulation at low mass, as testified by the large scatter in their photometric parameters in both ETGs and LTGs. From *ii)* and *iii)* we conclude that massive spiral galaxies develop a "red and dead" component, the importance of which increases with mass. Consistently to the result of chap. 3, *i)* and *iii)* lead us to conclude that this component must arise in a range mass between $10^9 M_\odot$ and $10^{10} M_\odot$ but that this component is not the only contribution to the slope of the global color-magnitude. In fact, *iv)* demonstrates that even after subtracting the "red and dead" component another process (such as strangulation, Peng et al., 2015; Fiacconi et al., 2015) is required to progressively quench the star formation in the outer regions of massive disks.

To ascribe to the possible presence of a bar the trend of point *ii)* and *iii)* we designed and ran an accessory routines of our procedure that performs isophotal fitting on the SDSS images and on the basis of the extracted radial ellipticity an P.A. profiles recognizes barred galaxies, thereby avoiding visual inspection of either the images or the profiles.

The main results can be summarized as follows. i) The procedure has extracted a fairly pure sample of barred galaxies among face-on LTGs and has led to the calculation of a bar fraction of $\sim 36\%$, which is consistent with other literature results (Jogee et al., 2004; Marinova & Jogee, 2007; Nair & Abraham, 2010) and with the fractions evaluated in chap. 3 and chap.4. ii) The bar fraction shows a strong mass dependency also obtained by previous works (also found in chap. 3) in the local volume and at higher redshifts (Marinova & Jogee, 2007; Nair & Abraham, 2010; Méndez-Abreu et al., 2012; Oh et al., 2012; Skibba et al., 2012). iii) The bars that we extracted typically occupy the central $\sim 30 - 40\%$ of the host galaxy and are typically strong ($\sim 90\%$ of times), consistently with the proportions observed by Marinova & Jogee (2007). iv) I constructed color average profiles of barred galaxies in different bins of mass and compared these profiles to the template profiles of chap. 5.

Points ii) and iii) imply that bars likely have a strong impact on the average color profiles created in chap. 5, where we observed in the template profiles of LTGs the growth of a red and dead component in an intermediate zone inside 0.3 Petrosian radii, whose importance increases with mass. From point iv) I was able to assess that bars are redder structures with respect to their disks and can indeed reproduce the upturn toward red of the templates profiles of chap. 5. This further links the presence of a bar to a decrease of the SFR in a disk galaxies as proposed by Cheung et al. (2013) and in chap. 3.

8.3 The stripping of UGC-6697

In chapter 7 we reported the results of the MUSE observations of UGC-6697 a massive ($M_* \approx 10^{10} M_\odot$) spiral galaxies of the nearby cluster Abell-1367 known to be under the action of ram pressure stripping. The galaxy has been mosaicked with 4 different pointings that included also its smaller companion CGCG-97087N lying at few arcminutes in the NE direction from the center of UGC-6697. Moreover UGC-6697 lies at ≈ 98kpc from CGCG-97095, a massive elliptical galaxy. The reduction has been performed with the MUSE reduction pipeline, complemented with in-house Python codes that improved the quality of the illumination correction and of the sky subtraction.

The emission line fitting is performed with KUBEVIZ (Fossati et al., 2016) and with $QBfit$, a code that I designed on purpose to automatically perform a more complex fit accounting for two velocity components along the line-of-sight. $QBfit$ is able to automatically choose whether two velocity components are needed to better represent the kinematics of the fitted line or if a single component fit is more appropriate.
We detect Hα emission distributed in a long tail that extends ≈ 60 kpc in the NW direction, well beyond the stellar distribution of the galaxy. The galaxy front, where the galaxy impacts the cluster, is completely depleted as testified by the sharp cut in the Hα emission at the SE edge of the galaxy. These signs are consistent with a strong ram pressure event that is ripping the gas out of the disk of UGC-6697. However we cannot completely exclude that a mild contribution might come from the gravitational field of CGCG-97095 as the small asymmetry in the NW edge of the galaxy suggests. CGCG-97087N is also suffering a stripping event as testified by the two tails of ionized gas trailing behind the galaxy and connecting to UGC-6697.

UGC-6697 is observed edge-on and because of the impact geometry, the stripped gas is seen superimposed along the line of sight to gas still attached to the potential of the galaxy. Running $QBfit$, hence accounting for two velocity components along the line of sight, we separated the ionized gas in an high-velocity and a low-velocity components. By comparing the kinematics of the different gaseous components to the stellar velocity field of UGC-6697 derived from the Ca II we were able to separate the ionized gas in a stripped component and a component still attached to the potential of the galaxy. By assuming a stripping process due to Kelvin-Helmotz instabilities the resulting mass of stripped gas is $\approx 10^9 M_\odot$ in agreement with other works and with the HI deficiency measured by Giovanelli & Haynes (1985). In general, despite the geometry of the impact with the ICM that should disfavor the stripping, it is remarkable that the process appears quite efficient in such a massive LTG.

We fixed the kinematics of the emission lines to the kinematics derived from the

Hα (and [NII]λ6584) and extracted the fluxes of Hβ, [OIII]λ5007, and [OI]λ6300 separately for the onboard and stripped components. To characterize the physical state of the two components, we build line ratio maps and spatially resolved BPT diagram.

The stripped gas is different from the onboard gas in both the kinematics and line ratios. The gas still onboard the galaxy, shows:
ia) velocity dispersions lower than 50 km/s, consistent with the expected values at $z \sim 0$ indicated by Wisnioski et al. (2015);
iia) low values of the shock indicators [OI]/Hα and [NII]/Hα. The [NII]/Hα appears mildly enhanced on the main body in the region where the signal connects to the tails of CGCG-97087N;
$iiia$) the average ionization state is consistent with photoionization by stars. The gas at the periphery of both galaxies, thus possibly at the surface of contact with the ICM, is the only consistent with being ionized by shocks.
The stripped gas shows instead:
ib) velocity dispersions as high as 100 km/s or more, which is more than four times the value expected for unperturbed disk galaxies at $z \sim 0$ (Wisnioski et al., 2015).
iib) High values of the shock indicators [OI]/Hα and [NII]/Hα. The most extreme values are found in the wings of CGCG-97087N and in the gas connecting the two galaxies.
$iiib$) On average, the average ionization state of the stripped gas evaluated from the BPT diagrams is consistent with a contribution by shocks up to 100%.

The stripped gas is therefore turbulent and is kept ionized by the shocks with the ICM while the gas onboard shows all the typical characteristics of local disks (i.e, low velocity dispersions and ionization mainly caused by stars). However in the stripped gas of UGC-6697, many HII regions are observed. These show physical properties in contrast with the average properties of the stripped gas. As a matter of fact, despite the fact that they belong to stripped gas they are univocally associated with dynamically cold gas showing ionization characteristics of normal HII regions. The correlation between dynamically cold gas and HII regions in the stripped gas is also observed in the stripped galaxy ESO137-001 (Fossati et al., 2016). The tails of CGCG-97087N, which are instead characterized by shocked and turbulent gas, lack completely of HII regions, indirectly confirming the tight correlation between the dynamic of the gas and the possibility to form stars in the stripped gas.

Appendix A

Automated photometry and isophotal fitting

In order to analyze a vast sample of galaxies such as the SDSS sample described in Chap. 2.1, I developed a set of routines to robustly extract magnitudes, surface brightness profiles and color profiles for g and i band images of the SDSS sample performing both aperture photometry and isophotal fitting. The work aims at robustly investigate the optical color gradients in galaxies to obtain clues on the evolution of local galaxies. In particular, our works aim at further investigate the possible signatures of the bar quenching scenario proposed in Chap. 3. In this chapter I present the routines and their limitations.

A.1 The method

The analysis code has been designed using IDL with the IDL Astronomy User's Library (Landsman 1993) and takes advantage of Source Extractor (Bertin & Arnouts 1996). It processes $FITS$ SDSS images in multiple bands that were downloaded using the IRSA and NVO image Mosaic service (Berriman et al., 2004; Katz et al. , 2011). The Mosaic interface returns science-grade SDSS mosaics that preserve fluxes and astrometry and rectify backgrounds to a common level. Furthermore, the photon counts are normalized to a common exposure time of 1 s and the zero point is set to 28.3 mag in every filter. Images are centered on the target galaxies and span approximately three times their major diameter at the 25^{th} magnitude arcsec^{-2} V-band

isophote as reported in GOLDMine (Gavazzi et al., 2003, 2014b). This ensures that a sufficient number of sky pixels exist around the targets for robust measurement of the sky background.

A.1.1 Image preparation, target detection and masking

The first step of the procedure is a preliminary estimate of the sky in each filter in a rectangular peripheral corona of width equal to one quarter of the full image size. This background mode value is subtracted from the images. The g and i sky-subtracted images are then averaged to create a higher signal-to-noise white frame that is analyzed using Source Extractor which detects and determines the photometric and geometric parameters of the objects in the field. We facilitated the Source Extractor detection enabling the filtering option of the routine. Each image is filtered with a Gaussian filter in order to smooth the image and avoid the detection of bright substructure inside the target galaxy as well as help the detection of the low surface brightness Local supercluster irregular galaxies. In the Source Extractor setup that we adopted (for the technical details about the implementation we refer the reader to Appendices we apply a 13x13 pixels smoothing filter. This value is obtained after that we tested that a finer filter does not cure the shredding problems while a larger filter drastically affects the deblending of overlapping objects.
Source Extractor succeeds in identifying the target galaxy as the central object in 96% of the cases. It also identifies all other objects in the field (overlapping or not with the target), discriminating between stars and galaxies through a continuum $CLASS\_STAR$ parameter that runs form 0 (galaxies) to 1 (stars). In this work, a lower limit of 0.8 has been adopted for an object to be considered a star. A mask of all the sources is then built and, in order to prevent from masking substructures inside a galaxy that are erroneously detected as overlapping sources, our procedure exploits the geometric parameters of the central galaxy as extracted by Source Extractor and define the area that it occupies. Henceforth we remove masks that are completely embedded within the central galaxy Kron radius (Graham & Driver, 2005)and with a $CLASS\_STAR$ parameter lower than 0.8 (non stellar). This avoids that structures such as spiral arms or bright HII regions are masked. Despite this geometric criterion, the masking of other sources with partial overlap with the main galaxy is preserved. Overall, this method fails to work in less than 4% of all cases, which, after inspection of the individual cases, are found to belong to three different classes: a) 45 large (A>5 arcmin) galaxies ($\sim 1\%$ of the sample) are still affected by a serious shredding problem. To overcome this problem we define an elliptical region for the target galaxy whose parameters (major, minor axes and PA) are taken from the UGC or the VCC. Within such elliptical shape Source Extractor finds and masks stars; b) 116 ($\sim 2\%$) targets suffer from insufficient masking from the halo, or spikes of bright stars in the field, or from the light of companion galaxies. These objects are masked manually;

c) In $\sim 1\%$ if cases, the target galaxies do not lie at the center of their respective images downloaded with Mosaic. This happens when the target coordinates were inaccurate or when Mosaic returns images displaced from the nominal coordinates. In these cases our code masks erroneously the galaxy as it does not recognize it as the primary target. These cases are repaired by manually cutting the frames around the target galaxy.
Altogether cases a+b+c, the only that requires human intervention, affect 220 objects out of 5532, a mere 4% of all cases. The remaining 96% are treated automatically. In this sense our procedure cannot be defined fully automatic, but quasi-automatic or guided. Once the mask is obtained the sky is re-computed (and re-subtracted) in order to remove the possible contamination by the sources within the corona used for preliminary background subtraction.

A.1.2 Petrosian radius and photometric extraction

For each target galaxy identified in the white image, Source Extractor provides a set of parameters (i.e., the center XWIN, YWIN, the position angle PA and the axis ratio B/A). Using these parameters or, in case of Source Extractor failure, those taken at the 25th magnitude isophote in B-band from GOLDmine (Gavazzi et al 2003, 2014) our procedure creates a set of concentric ellipses centered on the object and oriented at fixed PA, with a constant axis ratio B/A, evaluated at the 1.5 σ of the sky isophote by Source Extractor. In this work we choose to keep constant axis ratio and P.A. in order to keep a constant radial step between the elliptical annuli avoiding jumps due to the twist and overlap of the isophotes in galaxies hosting non-axisymmetric structures such as spiral arms or bars (Micheva et al., 2013). [1] The concentric ellipses define the elliptical annuli over which the surface brightness profile is evaluated as a function of the distance along the major axis, down to the Σ_{sky} surface brightness limit. Within the ellipses, the procedure evaluates the Petrosian radius r_p. This is defined as the radius at which the Petrosian ratio R_p, defined as

$$R_p(r_p) = \left(\frac{\int_{0.8r}^{1.25r} dr' 2\pi r' I(r')}{[\pi(1.25^2 - 0.8^2) r^2]} \right) \left(\frac{\int_0^r dr' 2\pi r' I(r')}{\pi r^2} \right)^{-1}, \qquad \text{(A.1)}$$

(Blanton et al., 2001; Yasuda et al., 2001) reaches 0.2, in line with the value adopted by the SDSS pipeline. The Petrosian flux (F_P) is defined as the flux within N_p Petrosian radii. We set N=2, once again consistently with the SDSS algorithm. For

[1] To speed up the procedure we set the step between adjacent ellipses (along the semi-major axis) as a function of the image dimensions: 1 pixel for images smaller than 300 pixels; 2 pixels for images greater than 300 pixels, up to 1000 pixels; 4 pixels for images greater than 1000 pixels.

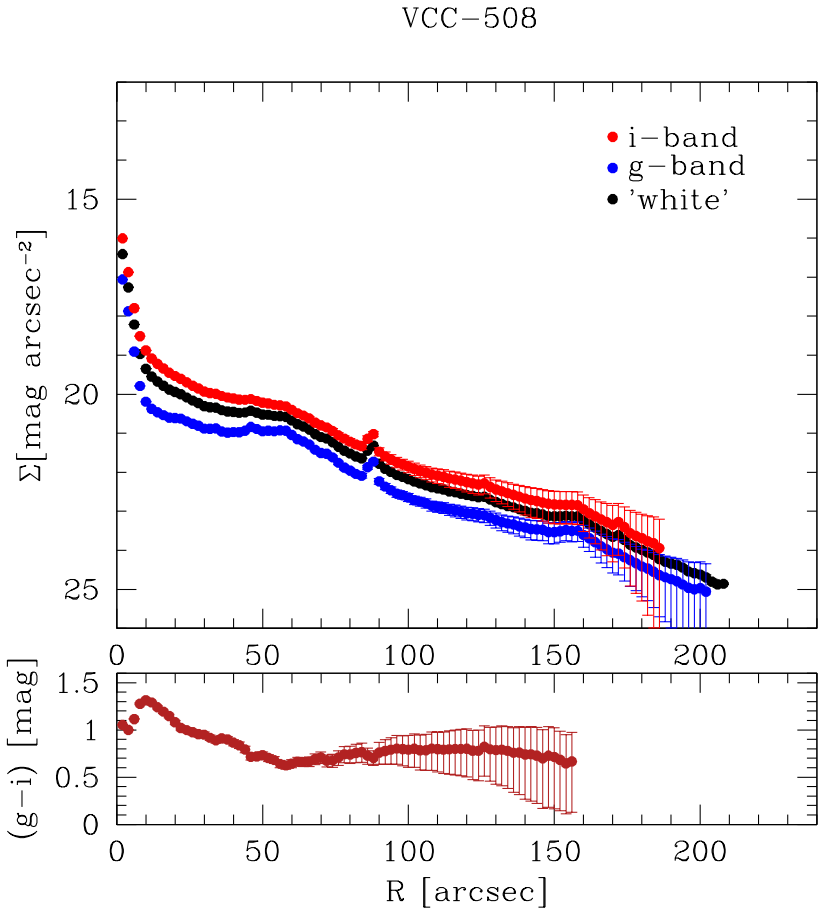

Figure A.1: Surface brightness profiles of the Virgo galaxy VCC-508. The g, i and white profiles are respectively show in blue, red and black in the top panel. All are traced down to $\Sigma_{\rm sky}$. In the bottom panel, the color profile is plotted.

consistency, Petrosian magnitudes are computed in both the g and i images within the the same aperture, determined in the white frame.
Similarly, the set of ellipses generated on the white image is used to evaluate both the g and i surface brightness profiles. Both are computed down to the Σ_{sky} surface brightness limit, see the example shown in Fig. A.1.
Finally, the $(g-i)$ color image is obtained performing the operation $Im_{(g-i)} = -2.5 \log \frac{Im_g}{Im_i}$, where Im_g and Im_i are respectively the g and i sky-subtracted image and $\mathrm{Im}_{(g-i)}$ is the color image. The color profile, truncated where the rms $\sim 1\sigma_{sky;(g-i)}$, is obtained subtracting the i- from the g-band surface brightness profile.

A.1.3 Errors

In order to evaluate errors on the surface brightness profiles, we take into account the Poissonian statistical noise ($\sqrt{S}$, where S are the counts) and the noise contributed by the statistics of the background, which has units of flux per area (i.e., surface brightness). This corresponds to the total observed individual pixel background σ integrated over the area A. Nevertheless, the MONTAGE software resamples the images of multiple SDSS fields building a mosaicked image of the target object with a generalized drizzle algorithm. The draw-backs are a Moirè pattern (Cotini et al., 2013), a slight image degradation (Blanton et al., 2011)and a mild correlation in the noise of pixels which can lead to an underestimate of the statistic of background. The Moiré pattern is in general non relevant (Cotini et al., 2013) and the degradation of the image is indeed very small (Blanton et al., 2011). Hence, following standard procedures (e.g., Gawiser et al. (2006) and Fumagalli et al. (2014)), we estimated the correlated noise that possibly affects our sky noise determination, especially within wide apertures. We compute an empirical noise model for the images, by measuring the flux standard deviation in aperture of n_{pix} pixels within sky regions empty of sources, according to the segmentation map. We fit the size-dependent standard deviation with the function

$$\sigma(n_{pix}) = \sigma_1 \alpha n_{pix}^{\beta}, \tag{A.2}$$

where σ_1 is the individual pixel standard deviation and α and β are the best-fit parameters that typically have a value of $\alpha \sim 1$ and $\beta \sim 0.56$ within our sample (where $\beta = 0.5$ means uncorrelated noise), implying a small but non-zero correlation in the pixel noise. The sky errors are therefore evaluated following the fitted function. Finally we consider an additional important source of error that comes from residual gradient of the flat field, which is estimated to be 10% of the rms in the individual pixel by Gavazzi (1993). This represents the dominant source of error in the low surface brightness regions and must therefore be taken into account. The total noise (N) is therefore estimated to be the quadratic sum of the the empirical noise model,

sky (corrected for the noise correlation) and flat fielding errors:

$$N = \sqrt{\frac{C}{G} + (\sigma^2)(\Delta A)^{1.12} + 0.1\sigma^2 A}, \tag{A.3}$$

where C are the counts, G the gain of the CCD, ΔA is the annuli area and A is the area of the aperture.
The magnitudes into the aperture are

$$m \pm \delta(m) = Zp - 2.5\log(S \pm N). \tag{A.4}$$

Errors on magnitudes in the profile can therefore be written as:

$$\delta m = -2.5\log(1 \pm \frac{N}{S}), \tag{A.5}$$

where S is the observed flux and N is the noise. In the $(g-i)$ color profiles, the noise $(N(g-i))$ is computed as the quadratic sum of the N_g and N_i which are the noise computed with equation A.3 respectively in $g-$ and $i-$band.

A.2 Isophotal fitting and tilted color profiles

Color profiles described in the previous sections are obtained from concentric ellipses that does not follow the galaxy's isophotes and keep instead fixed the global geometry of the galaxy (ellipticity and P.A.) as evaluated by Source Extractor. Isophotes can instead tilt and change ellipticity especially in correspondence of nonaxesymmetric structures such as bars. Hence, in order to properly get the color profile along a bar a tool for isophotal fitting is required.
Once again, in order to correctly evaluate color profiles, surface brightness profiles must be extracted over consistent apertures in the g and i bands. The ellipse fitting procedure is therefore performed on the white image that represents a high S/N reference frame common to all filters. For each galaxy, the procedure fits ellipses to the contours of the white light frame, which are built based on the *cgContour* routine of the IDL Coyote Library. The routine is set to extract 100 logarithmic levels ranging from $3 \times \sigma_{sky}$ to the maximum of the white surface brightness (non-tilted) profile, which was previously evaluated by the procedure described in C16. The *cgContour* routine returns the two-dimensional distribution of pixels of each contour level in the white frame. Starting from outside the galaxy and going toward the center, the procedure automatically fits each contour with the parametric formula of an ellipse rotated of a position angle (P.A.; each ellipse is fitted owing to the *mpfitellipse* procedure that is based on the *mpfit* routine, a non-linear least squares fitting program described in Markwardt, 2009). For each contour level I setup the initial guesses for

the ellipse-fitting assuming the center X_c, Y_c of the ellipse as the average X, Y pixel coordinates composing the contour level distribution. Further on the initial guesses for the semi-major and semi-minor axis are chosen as half the distance between the first (/half-path) pixel coordinates and the one at half-path (/three quarters), while the initial guess for the P.A. is taken as 0. Each fitted ellipse must not overlap the previously fitted ellipse. Once all contours are fitted, the routine checks and discards ellipses that are not centered. To this aim, the coordinates of the center previously evaluated by Source Extractor are not considered and are instead recomputed as the mode of the coordinates of the center of all fitted ellipses [2].
The procedure discards ellipses whose center are at a distance greater than ~ 15 arcsec from the galaxy center for Virgo galaxies and ~ 5 arcsec for Coma. Moreover, in some cases, especially among irregular galaxies, the most internal ellipses fits contours that follow patches of star formation that are not centered on the galaxy but are still within the tolerance distance adopted. To fix this, ellipses that have central coordinates at a distance to the galaxy center greater than their semi-major axis (*sma*) are not considered.
Finally, the surface brightness of each ellipse in the g and i band images are computed measuring the average surface brightness along the path of each fitted contour, and $(g-i)$ color profiles are consequently obtained making the difference between the g and i surface brightness profiles. Examples of the ellipses fitted and of the profiles extracted by the procedure are shown in Fig. A.1 for four different galaxies (three barred and one unbarred).

A.3 Bar detection

As it is described by Wozniak et al. (1995), Jogee et al. (2004), Marinova & Jogee (2007), Barazza et al. (2008), and Aguerri et al. (2009), and as can be seen in Fig. A.1, bars in face-on galaxies produce a peak in the ellipticity profile to which a plateau in the P.A. is associated, i.e., the P.A. is constant within $\pm 20^o$. The ellipse fitting method has been extensively tested by many authors to be efficient in extracting barred galaxies among wide samples (Jogee et al., 2004; Marinova & Jogee, 2007; Aguerri et al., 2009; Laurikainen et al., 2010). This fitting has two free parameters, Δe and $\Delta P.A.$. The first parameter is the difference between the ellipticity of the bar and that of the disk, while the second parameter is the interval within which the P.A. varies along the bar.
The procedure analyzes the properties of the ellipticity and P.A. profiles of each galaxy and hunts bars automatically extracting those objects that exhibit $\Delta e > 0.08$

[2] This choice was made because the coordinates evaluated by Source Extractor are referred to the ellipse that fits the external (at the $1.5\Sigma_{sky}$ isophote) geometry of the galaxy which does not always provide the correct barycenter of the internal isophotes

and $\Delta P.A. > 20^o$. These threshold values were tested by Aguerri et al. (2009) who showed that these values minimize the fraction of spurious/bad detections and simultaneously maximize the bar identifications. In order to automatically select galaxies on these bases, the procedure must correctly identify the ellipticity peak and the related P.A. plateau associated with the bar. Obviously both variations of the ellipticity and P.A. are more evident and easier to detect in face-on galaxies, where the contrast between the geometry of the galaxy and a bar is maximum. Hence we limited the extraction to galaxies with $B/A > 0.7$, where the axis ratio B/A is evaluated by the procedure itself as the average ratio between the semi-minor (B) and semi-major (A) axes of the four most external ellipses fitted. The blind extraction happens in three distinct phases: in the first phase (i), the procedure finds each ellipticity peak in the ellipticity profile and, for each of them, looks for a related plateau in the P.A. profile; in a second instance (ii), the ellipticity peaks associated with a plateau are compared and the most promising peak is extracted; and finally (iii), the geometry of the isophote associated with the extracted peak is compared to the galaxy geometry and the final word on the possible bar presence is made. We outline the steps of the procedure below.

Step (i): In order to identify the plateau, for each peak the routine considers all fitted isophotes in the neighborhood of each considered peak with P.A. within 20^o from P.A.$_{peak}$ an ellipticity within 0.1 from e_{peak}.

Step (ii): Peaks found in (i) are all thought to represent a possible bar and are therefore placed into competition. Each peak receive a positive or negative vote according to their ellipticity, Δe, length of the plateau, and number of fitted ellipses. In other words, the procedure gives the best votes to the peaks with the greatest ellipticity that 1)maximizes the ratio between the length of the plateau and the *sma* at which the peak is found; 2) minimizes the variations in the P.A. profile; and 3) is found in the region $0.05 < a_{peak}/a_{gal} < 0.95$. Eventually only the best ranked peak is considered and if two (or more) peaks get the same vote, the preference is given to the most internal peak [3].

Step (iii): Once that a single-peak is extracted, its vote is further boosted according to its values of Δe and $\Delta P.A.$, i.e., a peak that has $\Delta e \sim 0.4$ and $\Delta P.A. \lesssim 10$ receive a higher rank compared to a peak that has $0.1 \lesssim \Delta e \lesssim 0.2$ and $10 \lesssim \Delta P.A. \lesssim 20$.

[3] As a matter of fact, spiral arms can produce a peak in the ellipticity profile and a P.A. plateau that mimes the behavior of a bar, but when the bar is present they have larger scale length.

Appendix B

Single velocity component fitting

In the first two panels of Fig. B.1, we show the flux and velocity of the ionized gas as evaluated from the fit accounting for a single velocity component performed with KUBEVIZ. The stellar velocity along the line of sight after having subtracted the systemic redshift of UGC-6697, is plotted in the third panel for comparison to the gaseous velocity. This last map is the same as Fig. 7.4.

B.1 One component line ratios

For a comparison with the properties of the ionized gas fitted with a single velocity component we create line ratio maps that displayed in Fig. B.2. The first panel of Fig. B.2 shows the [NII]$\lambda 6684$/Hα map. This ratio maintains modest values ($\sim 0.2 - 0.3$) on the main body of UGC-6697 and CGCG-97087N but its value varies dramatically in the CGCG-97087N tails where it is greatly enhanced and in the tail of UGC-6697 where it drops to values lower than 0.2. This ratio is enhanced by shocks (Kewley et al., 2001; Allen et al., 2008) and, in our map, the highest values are found in the wings connecting the tails of CGCG-97087N to the galaxy. Intriguingly, the gas characterized by high values of the [NII]$\lambda 6684$/Hα ratio connects and mixes to the gas belonging to UGC-6697, suggesting once again a physical connection between the gas of the two galaxies.

A difference between the gas along the body of the two galaxies and the gas outside in the tails is visible also in the [OI]$\lambda 6300$/Hα map, another indicator of the presence of shocked gas. As a matter of fact, the gas belonging to the main body of both galaxies and to HII regions show very low value of the ratio. On the contrary, the gas outside the two galaxies is characterized by much higher values, reaching the

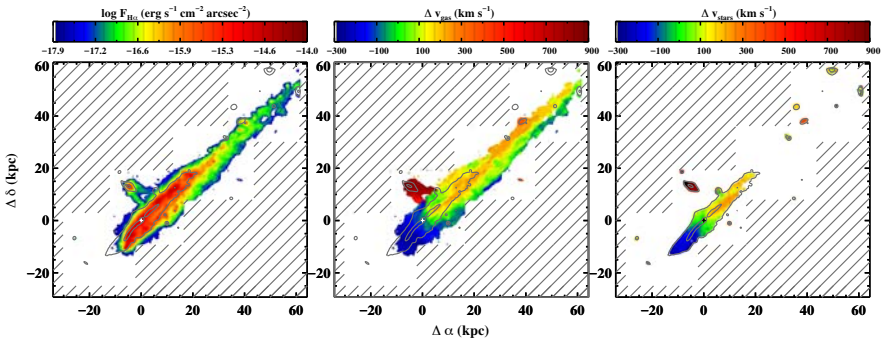

Figure B.1: The MUSE field centered on UGC-6697 smoothed 10x10 has been fitted with the [NII]+Hα+[NII] lines (single velocity component). The left panel shows the fitted flux. The central panel shows the velocity map derived from the Hα line. The right panel shows the stellar velocity map derived from the fit of the Ca II line. The cross in all panels marks the stellar kinematical center, which coincides in position with the bright HII region at $\alpha = 11^h43^m49^s;\ \delta = +19^o58'07"$. The extent of the stellar continuum is given by the black contours. Notice that the SE tip of the galaxy does not show any line emission.

maximum in the two wings of CGCG-97087N similarly to what has been observed in the [NII]λ6684/Hα map, strongly hinting at an hydrodynamical interaction between the two systems.

The [OIII]λ5007/Hβ map is displayed in the first panel of the second row of Fig B.2. The highest values of the ratio are found preferentially in regions that can be associated to bright HII regions, visible both in the Hα distribution and in the r-band image in the south direction and in the NW tail. Nevertheless, in the central region of UGC-6697, an extended blob is characterized by an high value of the [OIII]λ5007/Hβ ratio but cannot be associated to any compact knot of star formation and is instead found in a clear gap between the two bright structures of the stellar distribution.
This region is also characterized by high values in the Hα/Hβ map, and is thus associated with the presence of dust, whose presence is confirmed also by HST images. Nevertheless The main body of the two galaxies are instead characterized by low values of the ratios, with the exception of the SE edge, in correspondence with the sharp cut in the ionized gas distribution possibly associated to the front of the galaxy where the ISM impacts the hot IGM. In this case we would be probably looking at an enhanced star formation activity due to the compression of the front gas.

Finally we show the Hα/Hβ map in the second panel of the second row of Fig. B.2. This ratio is commonly used to infer the dust extinction, assuming an intrin-

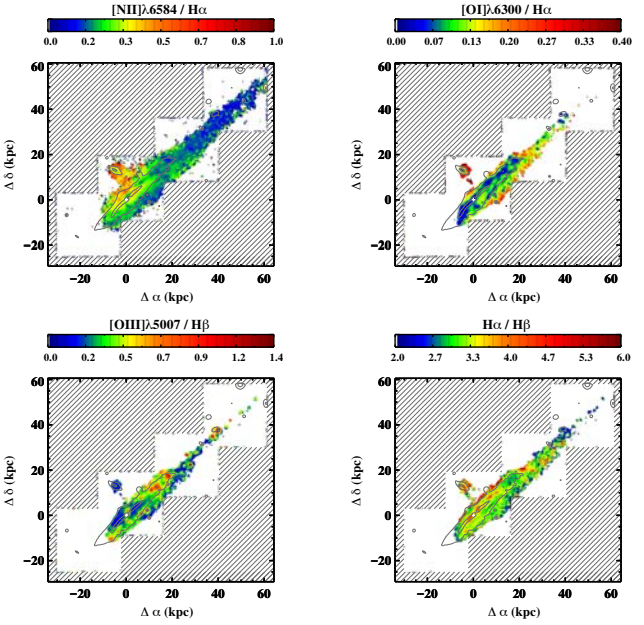

Figure B.2: Maps of line ratios: [NII]λ6584/Hα, [OI]λ6300/Hα, [OIII]λ5007/Hβ, Hα/Hβ. Contours and gray shaded areas are the same as in previous figures.

sic ratio of 2.86 from case B recombination at $\mathrm{T} = 10^4\mathrm{K}$ (Osterbrock, 1989). In this map, the main body of UGC-6697 display overall ratios that are in line with the expected value. Apparently, CGCG-97087N is characterized by slightly higher values especially in its two tails. We stress that also UGC-6697 has higher values of Hα/Hβ where the continuum is maximum and in the tail with respect to the disk. The presence of dust along the line of sight is not surprising in the disk of edge on spiral galaxies but we refrain from interpreting the high values in the tails as stripped dust, because other ionization mechanisms are at play and the assumption of an intrinsic ratio of 2.86 may not hold true in these regions.

Appendix C

Illumination correction details

In the Data reduction phase we perform an illumination correction for each IFU of the field by computing the average response of each IFU comapared to the average. To this aim the first step for each exposure is to map pixels that contain the signal coming from a single IFU.

The informations on the origin of the flux, such as it's (x,y) coordinates and which IFU received the signal, of each pixel is stored in the PIXELTABLE. The PIXELTABLE is also the raw file out of which the MUSE pipeline reconstructs the final datacube. By substituting the flux of each pixel with the number of the corresponding IFU, stored in the $origin$ extension of the PIXELTABLE, we reconstruct a cube where each pixel contains the number of the IFU contributing to the signal in that pixel. This cube, built taking advantage of the *muse_scipost_make_cube* task of the MUSE pipeline, maps the IFU on the FOV. After properly masking the bright sources in the field, we compute in chunk of 500$\mathring{A}$ the averge counts of each IFU and normalize it to the average counts of the field in the same wavelenghts chunk. This operation produces for each IFU a wavelength dependent correction of the flux.
As the final field-of-view (FOV) is obtained by interpolating the signal of the 24 IFUs onto a 3-D grid, there are regions where the signal is an interpolation of the signal coming from two adjacent IFUs. therefore, in the map, pixels belonging to these regions will contain a number ranging from IFU$_k$ to IFU$_{k+1}$. In order to properly correct these spaxels of overlapped signal we cannot apply the same correction adopted for pixels with signal belonging to a single IFU but we need a correction proportional to the contribute of each IFU to the signal of the spaxels.

Therefore we evaluate their corrections as the weighted mean between the corrections of two consequent IFUs. Calling n the number contained in these pixels in

the map of IFUs, weights (w_k and w_{k+1}) are evaluated as:

$$w_k = (\mathrm{IFU}_{k+1} - n); \tag{C.1}$$

$$w_{k+1} = (1 - w_k). \tag{C.2}$$

Bibliography

Aaronson, M., Persson, S. E., & Frogel, J. A. 1981, ApJ, 245, 18

Abadi, M. G., Moore, B., & Bower, R. G. 1999, MNRAS, 308, 947

Abazajian, K. N., et al. 2009, ApJS, 182, 543

Abraham, R. G., Tanvir, N. R., Santiago, B. X., et al. 1996, MNRAS, 279, L47

Abraham, R. G., van den Bergh, S., & Nair, P. 2003, ApJ, 588, 218

Adelman-McCarthy, J. K., Agüeros, M. A., Allam, S. S., et al. 2006, ApJS, 162, 38

Aguerri, J. A. L., Balcells, M., & Peletier, R. F. 2001, A&A, 367, 428

Aguerri, J. A. L., Méndez-Abreu, J., & Corsini, E. M. 2009, A&A, 495, 491

Ahn, C. P., Alexandroff, R., Allende Prieto, C., et al. 2014, ApJS, 211, 17

Alam, S., Albareti, F. D., Allende Prieto, C., et al. 2015, arXiv:1501.00963

Allen, M. G., Groves, B. A., Dopita, M. A., Sutherland, R. S., & Kewley, L. J. 2008, ApJS, 178, 20-55

Alonso, M. S., Coldwell, G., & Lambas, D. G. 2013, A&A, 549, A141

Alonso, S., Coldwell, G., & Lambas, D. G. 2014, A&A, 572, A86

Arnaud, M. 2001, New Century of X-ray Astronomy, 251, 154

Athanassoula, E., & Sellwood, J. A. 1986, MNRAS, 221, 213

Athanassoula, E. 1992, MNRAS, 259, 345

Athanassoula, E. 2002, Disks of Galaxies: Kinematics, Dynamics and Perturbations, 275, 141

Athanassoula E., 2005, MNRAS, 358, 147

Athanassoula E., Lambert J.C., Dehnen W. 2005, MNRAS, 358, 147

Athanassoula, E. 2008, Formation and Evolution of Galaxy Disks, 396, 333

Athanassoula, E. 2013, Secular Evolution of Galaxies, 305

Bahcall, N. A., & Cen, R. 1993, ApJ, 407, L49

Baldwin, J. A., Phillips, M. M., & Terlevich, R. 1981, PASP, 93, 5

Baldry, I. K., Glazebrook, K., Brinkmann, J., et al. 2004, ApJ, 600, 681

Balogh, M. L., Baldry, I. K., Nichol, R., et al. 2004, ApJ, 615, L101

Barazza, F. D., Jogee, S., & Marinova, I. 2008, ApJ, 675, 1194

Bauer, A. E., Hopkins, A. M., Gunawardhana, M., et al. 2013, MNRAS, 434, 209

Bekki, K., Couch, W. J., & Shioya, Y. 2002, ApJ, 577, 651

Bekki, K., & Couch, W. J. 2003, ApJ, 596, L13

Bell, E. F., Wolf, C., Meisenheimer, K., et al. 2004, ApJ, 608, 752

Berentzen, I., Heller, C. H., Shlosman, I. & Fricke, K. 1998, MNRAS, 300, 49

Berriman, G. B., Good,J. C., Laity, A. C., et al. 2004, Astronomical Data Analysis Software and Systems (ADASS) XIII, 314, 593

Bershady, M. A., Jangren, A., & Conselice, C. J. 2000, AJ, 119, 2645

Bertin, E., & Arnouts, S. 1996, A&AS, 117, 393

Binggeli, B., Sandage, A., & Tammann, G. A. 1985, AJ, 90, 1681

Binney, J., & Tremaine, S. 1987, Princeton, NJ, Princeton University Press, 1987, 747 p.

Blanton, M. R., Dalcanton, J., Eisenstein, D., et al. 2001, AJ, 121, 2358

Blanton, M. R., Lin, H., Lupton, R. H., et al. 2003, AJ, 125, 2276

Blanton, M. R., Schlegel, D. J., Strauss, M. A., et al. 2005, AJ, 129, 2562

Blanton, M. R., Kazin, E., Muna, D., Weaver, B. A., & Price-Whelan, A. 2011, AJ, 142, 31

Bliton, M., Rizza, E., Burns, J. O., Owen, F. N., & Ledlow, M. J. 1998, MNRAS, 301, 609

Böhringer, H., Schuecker, P., Guzzo, L., et al. 2004, A&A, 425, 367

Bolatto, A. D., Wolfire, M., & Leroy, A. K. 2013, ARA&A, 51, 207

Boselli, A., Gavazzi, G., Combes, F., Lequeux, J., & Casoli, F. 1994, A&A, 285,69

Boselli, A., Gavazzi, G., Donas, J., & Scodeggio, M. 2001, AJ, 121, 753

Boselli, A., Lequeux, J., & Gavazzi, G. 2002, A&A, 384, 33

Boselli, A. & Gavazzi, G. 2006, PASP, 118, 517

Boselli, A., Boissier, S., Cortese, L., & Gavazzi, G. 2008, ApJ, 674, 742-767

Boselli, A., Eales, S., Cortese, L., et al. 2010, PASP, 122, 261

Boselli, A., Boissier, S., Heinis, S., et al. 2011, A&A, 528, A107

Boselli, A., Cortese, L., Boquien, M., et al. 2014, A&A, 564, A66

Boselli, A., Voyer, E., Boissier, S., et al. 2014, A&A, 570, A69

Boselli, A., Fossati, M., Gavazzi, G., et al. 2015, A&A, 579, A102

Boselli, A., Cuillandre, J. C., Fossati, M., et al. 2016, A&A, 587, A68

Boylan-Kolchin, M., Bullock, J. S., & Kaplinghat, M. 2012, MNRAS, 422, 1203

Brinchmann, J., Charlot, S., White, S. D. M., et al. 2004, MNRAS, 351, 1151

Buat, V., Heinis, S., Boquien, M., et al. 2014, A&A, 561, AA39

Bundy, K., Georgakakis, A., Nandra, K., et al. 2008, ApJ, 681, 931

Cameron, E., Carollo, C. M., Oesch, P., et al. 2010, MNRAS, 409, 346

Cappellari, M., & Emsellem, E. 2004, PASP, 116, 138

Cappellari, M., Emsellem, E., Krajnović, D., et al. 2011, MNRAS, 413, 813

Cardelli, J. A., Clayton, G. C., & Mathis, J. S. 1989, ApJ, 345, 245

Carroll, S. M., Duvvuri, V., Trodden, M., & Turner, M. S. 2004, Phys. Rev. D, 70, 043528

Catinella, B., Schiminovich, D., Kauffmann, G., et al. 2010, MNRAS, 403, 683

Chabrier, G. 2003, PASP, 115, 763

Chester, C., & Roberts, M. S. 1964, AJ, 69, 635

Cheung, E., Athanassoula, E., Masters, K. L., et al. 2013, ApJ, 779, 162

Chung, A., van Gorkom, J. H., Kenney, J. D. P., Crowl, H., & Vollmer, B. 2009, AJ, 138, 1741

Cid Fernandes, R., Stasińska, G., Mateus, A., & Vale Asari, N. 2011, MNRAS, 413, 1687

Ciesla L., Boselli A., Smith M. W. L., et al. 2012, A&A, 543, A161

Ciesla L., Boquien M., Boselli A., et al. 2014, A&A, 565, A128

Clemens, M. S., Jones, A. P., Bressan, A., et al. 2010, A&A, 518, L50

Cole D. R., Debattista V. P., Erwin P., Earp S. W. F., Roskar R., 2014, MNRAS, 445, 3352

Combes, F., Debbasch, F., Friedli, D., & Pfenniger, D. 1990, A&A, 233, 82

Comerón, S., Knapen, J. H., Beckman, J. E., et al. 2010, MNRAS, 402, 2462

Conselice, C. J. 2003, ApJS, 147, 1

Consolandi, G., Gavazzi, G., Fumagalli, M., Dotti, M., & Fossati, M., 2016, A&A, 591, A38

Consolandi, G. 2016, arXiv:1607.05563

Corbelli, E., Bianchi, S., Cortese, L., et al. 2012, A&A, 542, A32

Cortese, L., Ciesla, L., Boselli, A., et al. 2012, A&A, 540, A52

Cortese L., Fritz J., Bianchi S., et al. 2014, MNRAS, 440, 942

Côté, P., Piatek, S., Ferrarese, L., et al. 2006, ApJS, 165, 57

Cotini, S., Ripamonti, E., Caccianiga, A., et al. 2013, MNRAS, 431, 2661

Cowie, L. L., & McKee, C. F. 1977, ApJ, 211, 135

Cowie, L. L., Songaila, A., Hu, E. M., & Cohen, J. G. 1996, AJ, 112, 839

Curti, M., Cresci, G., Mannucci, F., et al. 2016, arXiv:1610.06939

da Cunha, E., Charlot, S., & Elbaz, D. 2008, MNRAS, 388, 1595

Daddi, E., Elbaz, D., Walter, F., et al. 2010, ApJ, 714, L118

Debattista V.P.; et al., 2004, ApJ, 604, L93

Debattista, V. P., Mayer, L., Carollo, C. M., Moore, B., Wadsley, J. & Quinn, T. 2006, ApJ, 645, 209

De Propris, R., Colless, M., Driver, S. P., et al. 2003, MNRAS, 342, 725

de Vaucouleurs, G. 1959, Handbuch der Physik, 53, 275

de Vaucouleurs, G. 1961, ApJS, 5, 233

de Vaucouleurs, G. 1977, Evolution of Galaxies and Stellar Populations, 43

de Vaucouleurs, G., de Vaucouleurs, A., Corwin, H. G., Jr., et al. 1991, Third Reference Catalogue of Bright Galaxies. Volume I: Explanations and references. Volume II: Data for galaxies between 0^h and 12^h. Volume III: Data for galaxies between 12^h and 24^h., by de Vaucouleurs, G.; de Vaucouleurs, A.; Corwin, H. G., Jr.; Buta, R. J.; Paturel, G.; Fouqué, P.. Springer, New York, NY (USA), 1991, 2091 p., ISBN 0-387-97552-7, Price US$ 198.00. ISBN 3-540-97552-7, Price DM 448.00. ISBN 0-387-97549-7 (Vol. I), ISBN 0-387-97550-0 (Vol. II), ISBN 0-387-97551-9 (Vol. III).,

Donas, J., Milliard, B., Laget, M., & Buat, V. 1990, A&A, 235, 60

Dopita, M. A., & Sutherland, R. S. 1996, ApJS, 102, 161

Driver, S. P., Popescu, C. C., Tuffs, R. J., et al. 2007, MNRAS, 379, 1022

Drory, N., & Fisher, D. B. 2007, ApJ, 664, 640

Dressler, A. 1980, ApJ, 236, 351

Duc, P.-A., Cuillandre, J.-C., Karabal, E., et al. 2015, MNRAS, 446, 120

Dursi, L. J., & Pfrommer, C. 2008, ApJ, 677, 993-1018

Ebeling, H., Stephenson, L. N., & Edge, A. C. 2014, ApJ, 781, L40

Elbaz, D., Dickinson, M., Hwang, H. S., et al. 2011, A&A, 533, AA119

Ellison, S. L., Nair, P., Patton, D. R., et al. 2011, MNRAS, 416, 2182

Elmegreen, B. G., Bournaud, F., & Elmegreen, D. M. 2008, ApJ, 688, 67

Emsellem, E., Cappellari, M., Krajnović, D., et al. 2011, MNRAS, 414, 888

Emsellem, E., Renaud, F., Bournaud, F., et al. 2015, MNRAS, 446, 2468

Epinat, B., Tasca, L., Amram, P., et al. 2012, A&A, 539, AA92

Erwin, P. 2005, MNRAS, 364, 283

Erwin, P., Saglia, R. P., Fabricius, M., et al. 2015, MNRAS, 446, 4039

Eskridge, P. B., Frogel, J. A., Pogge, R. W., et al. 2000, AJ, 119, 536

Faber, S. M. 1973, ApJ, 179, 731

Faber, S. M., & Jackson, R. E. 1976, ApJ, 204, 668

Fabricant, D., Lecar, M., & Gorenstein, P. 1980, ApJ, 241, 552

Fanali, R., Dotti, M., Fiacconi, D., & Haardt, F. 2015, MNRAS, 454, 3641

Fasano, G., Vanzella, E., Dressler, A., et al. 2012, MNRAS, 420, 926

Feldmann, R., Gnedin, N. Y., & Kravtsov, A. V. 2012, ApJ, 747, 124

Feldmann, R., & Mayer, L. 2015, MNRAS, 446, 1939

Fiacconi, D., Feldmann, R., & Mayer, L. 2015, MNRAS, 446, 1957

Font, J., Beckman, J. E., Querejeta, M., et al. 2014, ApJS, 210, 2

Fontanot, F., De Lucia, G., Monaco, P., Somerville, R. S., & Santini, P. 2009, MNRAS, 397, 1776

Forman, W., & Jones, C. 1982, ARA&A, 20, 547

Förster Schreiber, N. M., Genzel, R., Bouché, N., et al. 2009, ApJ, 706, 1364

Fossati, M., Gavazzi, G., Boselli, A., & Fumagalli, M. 2012, A&A, 544, A128

Fossati, M., Gavazzi, G., Savorgnan, G., et al. 2013, A&A, 553, AA91

Fossati, M., Fumagalli, M., Boselli, A., et al. 2016, MNRAS, 455, 2028

Fruscione, A., & Gavazzi, G. 1990, BAAS, 22, 746

Fumagalli, M., Gavazzi, G., Scaramella, R., & Franzetti, P. 2011, A&A, 528, A46

Fumagalli, M., O'Meara, J. M., Prochaska, J. X., Kanekar, N., & Wolfe, A. M. 2014, MNRAS, 444, 1282

Gavazzi, G. 1978, A&A, 69, 355

Gavazzi, G., Tarenghi, M., Jaffe, W., Boksenberg, A., & Butcher, H. 1984, A&A, 137, 235

Gavazzi, G., & Jaffe, W. 1987, A&A, 186, L1

Gavazzi, G. 1987, ApJ, 320, 96

Gavazzi, G. 1989, ApJ, 346, 59

Gavazzi, G. 1993, ApJ, 419, 469

Gavazzi, G., Contursi, A., Carrasco, L., et al. 1995, A&A, 304, 325

Gavazzi, G., & Scodeggio, M. 1996, A&A, 312, L29

Gavazzi, G., Pierini, D., & Boselli, A. 1996, A&A, 312, 397

Gavazzi, G., Boselli, A., Scodeggio, M., Pierini, D., & Belsole, E. 1999, MNRAS, 304, 595

Gavazzi, G., Marcelin, M., Boselli, A., et al. 2001, A&A, 377, 745

Gavazzi, G., Boselli, A., Donati, A., Franzetti, P., & Scodeggio, M. 2003, A&A, 400, 451

Gavazzi, G., Giovanelli, R., Haynes, M. P., et al. 2008, A&A, 482, 43

Gavazzi, G. 2009, Revista Mexicana de Astronomia y Astrofisica Conference Series, 37, 72

Gavazzi, G., Fumagalli, M., Cucciati, O., & Boselli, A. 2010, A&A, 517, A73

Gavazzi, G., Fumagalli, M., Galardo, V., Grossetti, F., Boselli, A., Giovanelli, R., Haynes, M. P. & Fabello, S., Paper I, 2012, A&A, 545, A16

Gavazzi, G., Fumagalli, M., Fossati, M., Galardo, V., Grossetti, F., Boselli, A., Giovanelli, R.& Haynes, M. P., Paper II, 2013a, A&A, 553, A89

Gavazzi, G., Savorgnan, G., Fossati, M., et al. Paper III, 2013b, A&A, 553, AA90

Gavazzi, G., Consolandi, G., Dotti, M., et al. 2013c, A&A, 558, AA68

Gavazzi, G., Consolandi, G., Viscardi, E., Fossati, M., Fumagalli, M., Boselli, A., Giovanelli, R.& Haynes, M. P., Paper V, 2015, A&A

Gavazzi, G., Franzetti, P., & Boselli, A. 2014b, arXiv:1401.8123

Gavazzi, G., Consolandi, G., Dotti, M., et al. 2015, A&A, 580, A116

Gawiser, E., van Dokkum, P. G., Herrera, D., et al. 2006, ApJS, 162, 1

Genzel, R., Tacconi, L. J., Gracia-Carpio, J., et al. 2010, MNRAS, 407, 2091

Giovanelli, R., & Haynes, M. P. 1985, ApJ, 292, 404

Giovanelli, R., Haynes, M. P., Kent, B. R., et al. 2005, AJ, 130, 2598

González Delgado, R. M., García-Benito, R., Pérez, E., et al. 2015, A&A, 581, A103

Gnerucci, A., Marconi, A., Cresci, G., et al. 2011, A&A, 528, AA88

Graham, A. W., & Driver, S. P. 2005, PASA, 22, 118

Griersmith, D. 1980, AJ, 85, 1135

Gunn, J. E., & Gott, J. R., III 1972, ApJ, 176, 1

Haynes, M. P., & Giovanelli, R. 1984, AJ, 89, 758

Haynes, M. P., Giovanelli, R., Martin, A. M., et al. 2011, AJ, 142, 170

Hakobyan, A. A., Karapetyan, A. G., Barkhudaryan, L. V., et al. 2016, MNRAS, 456, 2848

Haywood M., Lehnert M.D., Di Matteo P., et al. 2016, A&A, 589, A66

Henriques, B. M. B., White, S. D. M., Thomas, P. A., et al. 2013, MNRAS, 431, 3373

Hernquist, L. 1993, ApJS, 86, 389

Hirschmann, M., De Lucia, G., Wilman, D., et al. 2014, MNRAS, 444, 2938

Ho L.C., Filippenko A.V. &

Hogg, D. W., Blanton, M. R., Brinchmann, J., et al. 2004, ApJ, 601, L29

Hollenbach, D., & Salpeter, E. E. 1971, ApJ, 163, 155

Holwerda, B. W., Gonzalez, R. A., Allen, R. J., & van der Kruit, P. C. 2005, AJ, 129, 1396

Huang, S., Haynes, M. P., Giovanelli, R., & Brinchmann, J. 2012, ApJ, 756, 113

Hubble, E. P. 1936, Realm of the Nebulae, by E.P. Hubble. New Haven: Yale University Press, 1936. ISBN 9780300025002

Hunt L.K. & Malkan M.A., 1999, ApJ,

Humason, M. L. 1936, ApJ, 83, 10

Ilbert et al. 2014, arXiv:1410.4875

Isobe, T., Feigelson, E. D., Akritas, M. G., & Babu, G. J. 1990, ApJ, 364, 104

Jáchym, P., Combes, F., Cortese, L., Sun, M., & Kenney, J. D. P. 2014, ApJ, 792, 11

Jogee, S., Barazza, F. D., Rix, H.-W., et al. 2004, ApJ, 615, L105

Jogee, S., Scoville, N., & Kenney, J. D. P. 2005, ApJ, 630, 837

Jogee, S., Miller, S. H.,

Kassin, S. A., Weiner, B. J., Faber, S. M., et al. 2012, ApJ, 758, 106

Katz, D. S., Berriman, G. B. Mann, R. G. in Reshaping Research and Development Using Web 2.0-based Technologies. Editor: Mark Baker, Nova Science Publishers, Inc.(2011)

Kauffmann, G., Heckman, T. M., White, S. D. M., et al. 2003, MNRAS, 341, 54

Kauffmann, G., White, S. D. M., Heckman, T. M., et al. 2004, MNRAS, 353, 713

Kenney, J. D. P., & Young, J. S. 1989, ApJ, 344, 171

Kenney, J. D. P., Geha, M., Jáchym, P., et al. 2014, ApJ, 780, 119

Kennicutt, R. C., Jr., Bothun, G. D., & Schommer, R. A. 1984, AJ, 89, 1279

Kennicutt, R. C., Jr., Tamblyn, P., & Congdon, C. E. 1994, ApJ, 435, 22

Kennicutt, R. C., Jr. 1998, ARA&A, 36, 189

Kewley, L. J., Dopita, M. A., Sutherland, R. S., Heisler, C. A., & Trevena, J. 2001, ApJ, 556, 121

Kim, W.-T., Seo, W.-Y., & Kim, Y. 2012, ApJ, 758, 14

Kim, S., Rey, S.-C., Jerjen, H., et al. 2014, ApJS, 215, 22

Knapp, G. R., Turner, E. L., & Cunniffe, P. E. 1985, AJ, 90, 454

Knapen, J. H. 1999, The Evolution of Galaxies on Cosmological Timescales, 187, 72

Kormendy, J., & Cornell, M. E. 2004, Penetrating Bars Through Masks of Cosmic Dust, 319, 261

Kormendy, J., & Kennicutt, R. C., Jr. 2004, ARA&A, 42, 603

Kormendy, J. 2013, Secular Evolution of Galaxies, 1

Kraljic, K., Bournaud,

Kregel, M., van der Kruit, P. C., & Freeman, K. C. 2005, MNRAS, 358, 503

Krumholz, M. R., & McKee, C. F. 2005, ApJ, 630, 250

Krumholz, M. R., McKee, C. F., & Tumlinson, J. 2009, ApJ, 699, 850

Landsman, W. B. 1993, Astronomical Data Analysis Software and Systems II, 52, 246

Lansbury, G. B., Lucey, J. R., & Smith, R. J. 2014, MNRAS, 439, 1749

Larson, R. B., Tinsley, B. M., & Caldwell, C. N. 1980, ApJ, 237, 692

Laurikainen E., Salo H. & Buta R., 2004,ApJ,607, L103

Laurikainen, E., Salo, H., & Buta, R. 2005, MNRAS, 362, 1319

Laurikainen, E., Salo, H., Buta, R., & Knapen, J. H. 2007, MNRAS, 381, 401

Laurikainen, E., Salo, H., Buta, R., Knapen, J. H., & Comerón, S. 2010, MNRAS, 405, 1089

Law, D. R., Steidel, C. C., Erb, D. K., et al. 2009, ApJ, 697, 2057

Lee, J. C., Gil de Paz, A., Tremonti, C., et al. 2009, ApJ, 706, 599

Lee, N., Sanders, D. B., Casey, C. M., et al. 2015, ApJ, 801, 80

Lewis, I., Balogh, M., De Propris, R., et al. 2002, MNRAS, 334, 673

Lilly, S. J., Carollo, C. M., Pipino, A., Renzini, A., & Peng, Y. 2013, ApJ, 772, 119

Lintott, C. J., Schawinski, K., Slosar, A., et al. 2008, MNRAS, 389, 1179

Lisker, T., Glatt, K., Westera, P., & Grebel, E. K. 2006, AJ, 132, 2432

Lisker, T., Grebel, E. K., & Binggeli, B. 2008, AJ, 135, 380

Lotz, J. M., Miller, B. W., & Ferguson, H. C. 2004, ApJ, 613, 262

Lupton, R., Gunn, J. E., Ivezić, Z., Knapp, G. R., & Kent, S. 2001, Astronomical Data Analysis Software and Systems X, 238, 269

MacArthur, L. A., Courteau, S., Bell, E., & Holtzman, J. A. 2004, ApJS, 152, 175

Madau, P., Pozzetti, L., & Dickinson, M. 1998, ApJ, 498, 106

Madgwick, D. S., Lahav, O., Baldry, I. K., et al. 2002, MNRAS, 333, 133

Marinova, I., & Jogee, S. 2007, ApJ, 659, 1176

Marinova, I., Jogee, S., Heiderman, A., et al. 2009, ApJ, 698, 1639

Marinova, I., Jogee, S., Weinzirl, T., et al. 2012, ApJ, 746, 136

Markwardt, C. B. 2009, Astronomical Data Analysis Software and Systems XVIII, 411, 251

Martinet L., & Friedli D., 1997, A&A,323,363

Martinez-Valpuesta I.; & Shlosman I.; 2004, ApJ, 613, L29

Masters, K. L., Nichol, R. C., Hoyle, B., et al. 2011, MNRAS, 411, 2026

Masters, K. L., Nichol, R. C., Haynes, M. P., et al. 2012, MNRAS, 424, 2180

Mayer, L., & Wadsley, J. 2004, MNRAS, 347, 277

McDonald, M.,Courteau, S., Tully, R. B., & Roediger, J. 2011, MNRAS, 414, 2055

Mei, S., Blakeslee, J. P., Côté, P., et al. 2007, ApJ, 655, 144

Melvin, T., Masters, K., Lintott, C., et al. 2014, MNRAS, 438, 2882

Mendel, J. T., Simard, L., Palmer, M., Ellison, S. L., & Patton, D. R. 2014, ApJS, 210, 3

Méndez-Abreu, J., Sánchez-Janssen, R., & Aguerri, J. A. L. 2010, ApJ, 711, L61

Méndez-Abreu, J., Sánchez-Janssen, R., Aguerri, J. A. L., Corsini, E. M., & Zarattini, S. 2012, ApJ, 761, L6

Menéndez-Delmestre, K., Sheth, K., Schinnerer, E., Jarrett, T. H., & Scoville, N. Z. 2007, ApJ, 657, 790

Micheva, G., Östlin, G., Bergvall, N., et al. 2013, MNRAS, 431, 102

Moore, B., Katz, N., Lake, G., Dressler, A., & Oemler, A. 1996, Nature, 379, 613

Morgan, W. W. 1958, PASP, 70, 364

Nair, P. B., & Abraham, R. G. 2010, ApJS, 186, 427

Nair, P. B., & Abraham, R. G. 2010, ApJ, 714, L260

Navarro, J. F., Frenk, C. S., & White, S. D. M. 1997, ApJ, 490, 493

Newman, S. F., Genzel, R., Förster Schreiber, N. M., et al. 2013, ApJ, 767, 104

Nilson, P. 973, Acta Universitatis Upsaliensis. Nova Acta Regiae Societatis Scientiarum Upsaliensis - Uppsala Astronomiska Observatoriums Annaler, Uppsala: Astronomiska Observatorium, 1973,

Noeske, K. G., Weiner, B. J., Faber, S. M., et al. 2007, ApJ, 660, L43

Noll, S., Kausch, W., Kimeswenger, S., et al. 2014, A&A, 567, A25

Norman, C. A., Sellwood, J. A. & Hasan, H. 1996, ApJ, 462, 114

Nulsen, P. E. J. 1982, MNRAS, 198, 1007

Obreschkow, D., & Rawlings, S. 2009, MNRAS, 394, 1857

Oh, S., Oh, K., & Yi, S. K. 2012, ApJS, 198, 4

Oppenheimer, B. D., Davé, R., Kereš, D., et al. 2010, MNRAS, 406, 2325

Osterbrock, D. E. 1989, Research supported by the University of California, John Simon Guggenheim Memorial Foundation, University of Minnesota, et al. Mill Valley, CA, University Science Books, 1989, 422 p.

Osterbrock, D. E., & Ferland, G. J. 2006, Astrophysics of gaseous nebulae and active galactic nuclei, 2nd. ed. by D.E. Osterbrock and G.J. Ferland. Sausalito, CA: University Science Books, 2006

Peletier, R. F., & Balcells, M. 1996, AJ, 111, 2238

Patel, S. G., Holden, B. P., Kelson, D. D., Illingworth, G. D., & Franx, M. 2009, ApJ, 705, L67

Peebles, P. J. E. 1982, ApJ, 263, L1

Peng, C. Y., Ho, L. C., Impey, C. D., & Rix, H.-W. 2010, AJ, 139, 2097

Peng, Y.-j., Lilly, S. J., Kovač, K., et al. 2010, ApJ, 721, 193

Peng, Y.-j., Lilly, S. J., Renzini, A., & Carollo, M. 2012, ApJ, 757, 4

Peng, Y., Maiolino, R., & Cochrane, R. 2015, Nature, 521, 192

Piffaretti, R., Arnaud, M., Pratt, G. W., Pointecouteau, E., & Melin, J.-B. 2011, A&A, 534, A109

Poggianti, B. M., Smail, I., Dressler, A., et al. 1999, ApJ, 518, 576

Poggianti, B. M., Fasano, G., Omizzolo, A., et al. 2016, AJ, 151, 78

Quilis, V., Moore, B., & Bower, R. 2000, Science, 288, 1617

Raha, N., Sellwood, J. A., James, R. A., & Kahn, F. D. 1991, Nature, 352, 411

Read, J. I., Wilkinson, M. I., Evans, N. W., Gilmore, G., & Kleyna, J. T. 2006, MNRAS, 366, 429

Reese, A. S., Williams, T. B., Sellwood, J. A., Barnes, E. I., & Powell, B. A. 2007, AJ, 133, 2846

Regan M.W. & Teuben P.J., 2004,ApJ, 600, 595

Reynaud, D., & Downes, D. 1998, A&A, 337, 671

Rich, J. A., Kewley, L. J., & Dopita, M. A. 2011, ApJ, 734, 87

Roberts W.W., Jr., Huntley J. M., & van Albada G.D. 1979, ApJ, 233, 67

Roberts, M. S., & Haynes, M. P. 1994, ARA&A, 32, 115

Roediger, J. C., Courteau, S., McDonald, M., & MacArthur, L. A. 2011, MNRAS, 416, 1983

Roediger, J. C., Courteau, S., MacArthur, L. A., & McDonald, M. 2011, MNRAS, 416, 1996

Romano-Díaz, E., Shlosman, I., Heller, C., & Hoffman, Y. 2008, ApJ, 687, L13

Rubin, V. C., Ford, W. K. J., & . Thonnard, N. 1980, ApJ, 238, 471

Rubin, V. C., Burstein, D., Ford, W. K., Jr., & Thonnard, N. 1985, ApJ, 289, 81

Ruszkowski, M., Brüggen, M., Lee, D., & Shin, M.-S. 2014, ApJ, 784, 75

Saintonge, A., Kauffmann, G., Kramer, C., et al. 2011, MNRAS, 415, 32

Salpeter, E. E. 1955, ApJ, 121, 161

Sánchez-Janssen, R., Méndez-Abreu, J., & Aguerri, J. A. L. 2010, MNRAS, 406, L65

Sandage, A. 1961, Washington: Carnegie Institution, 1961,

Sandage, A. 1975, Galaxies and the Universe, 1

Sanders, R. H. & Huntley, J. M. 1976, ApJ, 209, 53

Sanders, D. B., Solomon, P. M., & Scoville, N. Z. 1984, ApJ, 276, 182

Sandstrom, K. M., Leroy, A. K., Walter, F., et al. 2013, ApJ, 777, 5

Sarzi, M., Falcón-Barroso, J., Davies, R. L., et al. 2006, MNRAS, 366, 1151

Sakamoto, K., Okumura, S. K., Ishizuki, S., & Scoville, N. Z. 1999, ApJ, 525, 691

Scannapieco, E., Silk, J., & Bouwens, R. 2005, ApJ, 635, L13

Scarlata, C., Carollo, C. M., Lilly, S., et al. 2007, ApJS, 172, 406

Schawinski, K., Urry, C. M., Simmons, B. D., et al. 2014, MNRAS, 440, 889

Schechter, P. 1976, ApJ, 203, 297

Schlegel, D. J., Finkbeiner, D. P., & Davis, M. 1998, ApJ, 500, 525

Schlafly, E. F., & Finkbeiner, D. P. 2011, ApJ, 737, 103

Schreiber, C., Pannella, M., Elbaz, D., et al. 2015, A&A, 575, A74

Scodeggio, M., Gavazzi, G., Franzetti, P., et al. 2002, A&A, 384, 812

Scott, T. C., Usero, A., Brinks, E., et al. 2013, MNRAS, 429, 221

Sellwood, J. A. 2014, Reviews of Modern Physics, 86, 1

Sérsic, J. L. 1963, Boletin de la Asociacion Argentina de Astronomia La Plata Argentina, 6, 41

Sérsic, J. L. 1968, Cordoba, Argentina: Observatorio Astronomico, 1968

Sesana, A., Barausse, E., Dotti, M., & Rossi, E. M. 2014, ApJ, 794, 104

Shen, J. & Sellwood, J. A. 2004, ApJ, 604, 614

Sheth, K., Vogel, S. N., Regan, M. W., Thornley, M. D., & Teuben, P. J. 2005, ApJ, 632, 217

Sheth, K., Elmegreen, D. M., Elmegreen, B. G., et al. 2008, ApJ, 675, 1141

Sheth, K., Melbourne, J.,

Siudek, M. et al. 2016, arXiv:1605.05503

Shlosman I., Frank J., Begelman M.C., 1989, Nature, 338, 45

Simard, L. 1998, Astronomical Data Analysis Software and Systems VII, 145, 108

Simard, L., Mendel, J. T., Patton, D. R., Ellison, S. L., & McConnachie, A. W. 2011, ApJS, 196, 11

Skelton, R. E., Whitaker, K. E., Momcheva, I. G., et al. 2014, ApJS, 214, 24

Skibba, R. A., Masters, K. L., Nichol, R. C., et al. 2012, MNRAS, 423, 1485

Smith, M. W. L., Eales, S. A., Gomez, H. L., et al. 2012, ApJ, 756, 40

Solanes, J. M., Giovanelli, R., & Haynes, M. P. 1996, ApJ, 461, 609

Springel, V. 2005, MNRAS, 364, 1105

Springel V., Di Matteo T., & Hernquist L., 2005, MNRAS, 361, 776

Stasińska, G., Vale Asari, N., Cid Fernandes, R., et al. 2008, MNRAS, 391, L29

Stasińska, G., Costa-Duarte, M. V., Vale Asari, N., Cid Fernandes, R., & Sodré, L. 2015, MNRAS, 449, 559

Storey, P. J., & Zeippen, C. J. 2000, MNRAS, 312, 813

Strateva, I., Ivezić, Ž., Knapp, G. R., et al. 2001, AJ, 122, 1861

Strauss, M. A., Weinberg, D. H., Lupton, R. H., et al. 2002, AJ, 124, 1810

Strong, A. W., Bloemen, J. B. G. M., Dame, T. M., et al. 1988, A&A, 207, 1

Struble, M. F., & Rood, H. J. 1991, ApJS, 77, 363

Sullivan, W. T., III, Bates, B., Bothun, G. D., & Schommer, R. A. 1981, AJ, 86, 919

Sun, M., & Vikhlinin, A. 2005, ApJ, 621, 718

Sun, M., Donahue, M., & Voit, G. M. 2007, ApJ, 671, 190

Swinbank, A. M., Sobral, D., Smail, I., et al. 2012, MNRAS, 426, 935

Takamiya, M. 1999, ApJS, 122, 109

Tamura, N., & Ohta, K. 2003, AJ, 126, 596

Taylor, V. A., Jansen, R. A., Windhorst, R. A., Odewahn, S. C., & Hibbard, J. E. 2005, ApJ, 630, 784

Thompson, L. A. 1981, ApJ, 244, L43

Tonnesen, S., Bryan, G. L., & van Gorkom, J. H. 2007, ApJ, 671, 1434

Tonnesen, S., & Bryan, G. L. 2009, ApJ, 694, 789

Tully, R. B., & Fisher, J. R. 1977, A&A, 54, 661

van Driel, W., & van Woerden, H. 1991, A&A, 243, 71

van Zee, L., Barton, E. J., & Skillman, E. D. 2004, AJ, 128, 2797

Vazdekis, A., Sánchez-Blázquez, P., Falcón-Barroso, J., et al. 2010, MNRAS, 404, 1639

Verley, S., Combes, F., Verdes-Montenegro, L., Bergond, G., & Leon, S. 2007, A&A, 474, 43

Visvanathan, N., & Sandage, A. 1977, ApJ, 216, 214

Visvanathan, N., & Griersmith, D. 1977, A&A, 59, 317

Wadsley, J. W., Stadel, J., & Quinn, T. 2004, New A, 9, 137

Wang, J., Kauffmann, G., Overzier, R., et al. 2012, MNRAS, 423, 3486

Weinmann, S. M., Kauffmann, G., van den Bosch, F. C., et al. 2009, MNRAS, 394, 1213

Weinmann, S. M., Pasquali, A., Oppenheimer, B. D., et al. 2012, MNRAS, 426, 2797

Weinzirl, T., Jogee,S., Khochfar, S., Burkert, A., & Kormendy, J. 2009, ApJ, 696, 411

Willett, K. W., Lintott, C. J., Bamford, S. P., et al. 2013, MNRAS, 435, 2835

Williams, R. J., Quadri, R. F., Franx, M., van Dokkum, P., & Labbé, I. 2009, ApJ, 691, 1879

Wilman, D. J., Fontanot, F., De Lucia, G., Erwin, P., & Monaco, P. 2013, MNRAS, 433, 2986

Wisnioski, E., Glazebrook, K., Blake, C., et al. 2011, MNRAS, 417, 2601

Wisnioski, E., Förster Schreiber, N. M., Wuyts, S., et al. 2015, ApJ, 799, 209

Whitaker, K. E., Franx, M., Leja, J., et al. 2014, ApJ, 795, 104

Wozniak, H., Friedli, D., Martinet, L., Martin, P., & Bratschi, P. 1995, A&AS, 111, 115

Wu, H., Shao, Z., Mo, H. J., Xia, X., & Deng, Z. 2005, ApJ, 622, 244

Wuyts, S., Förster Schreiber, N. M., Lutz, D., et al. 2011, ApJ, 738, 106

Xue, Y. Q., Brandt, W. N., Luo, B., et al. 2010, ApJ, 720, 368

Yasuda, N., Fukugita, M., Narayanan, V. K., et al. 2001, AJ, 122, 1104

Yagi, M., Kashikawa, N., Sekiguchi, M., et al. 2002, AJ, 123, 66

Yagi, M., Komiyama, Y., Yoshida, M., et al. 2007, ApJ, 660, 1209

Yagi, M., Yoshida, M., Komiyama, Y., et al. 2010, AJ, 140, 1814

Yagi, M.,Yoshida, M., Gavazzi, G., et al. 2017, submitted to ApJ

York, D. G., Adelman, J., Anderson, J. E., Jr., et al. 2000, AJ, 120, 1579

Zibetti, S., Charlot, S., & Rix, H.-W. 2009, MNRAS, 400, 1181

Zwicky, F., Herzog, E., & Wild, P. 1968, Pasadena: California Institute of Technology (CIT), 1961-1968,